A GENERAL PURPOSE CONSTITUTIVE MODEL FITTING APPROACH USING INVERSE METHODS

by

Devon C. Hartlen

Submitted in partial fulfillment of the requirements
for the degree of Master of Applied Science

at

Dalhousie University
Halifax, Nova Scotia
November 2018

For Dad

Contents

List of Tables

List of Figures

Abstract

Computer simulation techniques such as finite element (FE) methods are used extensively to ensure functionality, reliability, and safety. The accuracy of these simulations is reliant on how accurately one can describe material behavior through the use of mathematical formulations known as constitutive material models. However, traditional methods of fitting constitutive material models are slow, tedious, and require a skilled researcher to perform correctly. In this thesis, an alternative fitting technique is investigated. Known as inverse material modeling (IMM), this technique couples experimental testing, FE modeling, and numerical optimization algorithms. Unlike traditional fitting techniques, IMM displays a high degree of automation, reducing the time and effort needed to fit constitutive material models without sacrificing accuracy. Moreover, as the FE model replicates the experiment being conducted, non-linearities such as irregular states of stress and specimen fixturing are accounted for; something which cannot be done with traditional fitting techniques.

This thesis is devoted to the development and use a custom-built IMM framework known as Compcam. To investigate the effectiveness of IMM and Compcam, two separate investigations were undertaken. In the first, five wrought alloys of varying composition and mechanical behavior are fit to four separate constitutive models. The goal of this study was to fit the stress-strain behavior of each material. In the second, twelve ferrous sintered powder metallurgy (PM) alloys consisting of four elemental compositions and three sintered densities are each fit to four constitutive models each. In addition to stress-strain behavior, the second investigation aimed to uncover how well said constitutive models and Compcam fit each alloy's densification behavior.

The results of these investigations show that Compcam is effective for the fitting of constitutive material models across a range of material behaviors and constitutive models for metals. However, there are limitations to Compcam's effectiveness. In particular, Compcam and IMM are unable to produce realistic fits for constitutive models which are not appropriate to describe the material behavior. However, this limitation can be overcome though appropriate selection of constitutive models by the user.

List of Abbreviations and Symbols Used

Acronyms

AISI	American Institute for Steel and Iron
COMPCAM	COnstitutive Model Parameters from CAmera Measurements
DACE	Design and Analysis of Computer Experiments
DIC	Digital Image Correlation
EGO	Efficient Global Optimization
FE	Finite Element
IMM	Inverse Material Modeling
MIKE	MATLAB Integrated Kriging Environment
MPIF	Metal Powder Industries Foundation
MSE	Mean Square Error
OO	Object-oriented
PM	Powder Metallurgy
PSO	Particle Swarm Optimizer
SPECS	Super Portable Extensomenter Camera System

Symbols

α	material porosity
α_0	Initial material porosity
$\bar{y}$	Mean of experimental dataset (coefficient of determination)
$\boldsymbol{\psi}$	Bias vector
$\tilde{\boldsymbol{\Psi}}$	Augmented correlation matrix
$\boldsymbol{x}^{(i)}$	i-th sampling point
δ_{ij}	Kronecker delta
$\dot{\epsilon}$	Strain rate
ϵ	Strain
ϵ^e	Elastic component of strain
ϵ^p	Plastic component of strain or effective plastic strain
ϵ_0	Initial yield strain
ϵ_N	Average strain at void nucleation (GTN Model)
ϵ_V	Volumetric strain
$\hat{\mu}$	Maximum likelihood estimate of the mean (Kriging derivation)
$\hat{\sigma}$	Maximum likelihood estimate of the standard deviation (Kriging derivation)
$\hat{s}$	Mean square error of the Kriging model
$\hat{y}$	Kriging interpolation at any point in space
μ	Coefficient of friction
μ	Statistical mean (Kriging derivation)
ν	Poisson's ratio
$\Phi(\cdot)$	Cumulative distribution function
$\phi(\cdot)$	Probability density function
ρ	Density

ρ_{rel}	Relative density
σ	Statistical standard deviation (Kriging derivation)
σ	Stress (in the context of material behavior)
σ'	Deviatoric component of stress
σ_0	Initial yield stress
σ_H	Hydrostatic pressure
σ_y	Yield strength or yield stress of a material
σ_{vm}	Von Mises stress
θ	Variable influence parameter (Kriging derivation)
A	Yield strength parameter (Johnson-Cook Model)
B	Hardening coefficient (Johnson-Cook Model)
C	Equation of state proportionality constant
E	Elastic (Young's) modulus
$E[I(\cdot)]$	Expected improvement function
E_P	Effective plastic modulus of the isotropic linear plasticity model
E_{tan}	Tangent modulus of the isotropic linear plasticity model
f^*	Effective void fraction (GTN Model)
f_c	Critical void fraction (GTN Model)
f_F	Void fraction at failure (GTN Model)
f_N	Nucleation void fraction (GTN Model)
K	Swift hardening coefficient
k	Number of free parameters (Kriging derivation)
L	Likelihood
N	Hardening factor (GTN model)
n	Plastic hardening exponent
P	Pressure used by equation
p	Variable smoothness parameter (Kriging derivation)
$P[I(\cdot)]$	Probability of Improvement function
P_e	Hydrostatic pressure at the material's yield point
P_s	Hydrostatic pressure when material reaches full density
q_1	Proportionality constant (GTN Model)
q_2	Proportionality constant (GTN Model)
R^2	Coefficient of determination
s_N	Standard deviation of strain at void nucleation (GTN Model)
V	Volume
$y^{(i)}$	Value at i-th sampling point
y_{min}	Smallest value of all sampled points (Kriging derivation)
$\mathrm{erf}(\cdot)$	Error function

Acknowledgements

A thesis may be the singular record of a student's work at an institution, but it is important to recognize that such work cannot be accomplished in a vacuum. To that end, there are many people to whom I need to extend my deepest gratitude.

To my supervisor, Darrel Doman, giving me the opportunity to pursue graduate studies, for his mentorship and understanding, and the giving me the freedom to do explore and investigate wild ideas, even when they weren't directly related to my thesis. I like to think that at least most of those schemes worked out in the end.

To Steve Corbin, Claver Diallo, and Allison Nolting for their insight, advice, and the use of their equipment.

To my colleague, Patrick Hennessy, for helping me out during a difficult time, interesting conversations, and most importantly, dominoes. I'm still trying to figure out we got into that last one.

And above all, to all my friends and family who have supported me all the way. The last two years have had some major highs and lows. You have no idea how much your support means to me during this time.

Chapter 1

Introduction

All models are wrong, but some models are useful.
George E.P. Box

Modern design and manufacturing methods rely heavily on computer simulation techniques such as finite element (FE) modeling to shorten the design cycle of a product, reduce manufacturing costs through process optimization, verify product functionality, and ensure consumer safety in extreme scenarios. The veracity of these modeling techniques is highly dependant on a number of factors, such as the appropriate discretization of the model and proper boundary conditions. In the case of FE models which incorporate the effects of plastic deformation, the largest factor which influences the validity of the simulation is how accurately the behavior of the material's behavior is captured.

In FE modeling, material behavior is described through the use of mathematical formulations known as constitutive material models. Given the wide range of materials, and hence material behaviors, there exist a very large number of constitutive material models. These model vary in complexity and application based on the material and situation they were developed to model. However, a challenge common to all constitutive models is the selection of appropriate input parameters that allow a given constitutive model to describe a material's behavior, a process known as model fitting, or simply fitting. Fitting is complicated by two key factors.

The first complication when fitting a constitutive model is the appropriate characterization of a material's behavior. While simple constitutive models may only require a single material test to garner enough information to describe a material's behavior, more complex constitutive models require a battery of tests to characterize a material's behavior under a range of conditions. A common example is the testing required to fit the Johnson-Cook model, a commonly used temperature and strain rate dependent plasticity model. The model's creators suggest a large test matrix which characterizes the material using three different material tests, a torsional test, a uniaxial tension test, and split Hopkinson bar test, at a range of temperatures and strain rates (Johnson and Cook, 1983). This large test matrix requires three different testing apparatus, a large number of test specimens, and trained personnel to carry out testing and data processing. This makes material characterization expensive from both a financial perspective, but also from the perspective of the amount of time and effort required.

The second complication to fitting is the constitutive model itself. With the exception of select constitutive models, fitting is made difficult by both the large number of parameters needed to fully describe a material and the issue that many of said parameters do not have analytic or semi-empirical means of determination. Further, as the complexity of constitutive models increases, there is a trend toward parameters which cannot be measured experimentally or are entirely non-physical. While the authors of some constitutive models do suggest methods or correlations to make fitting easier, the majority of authors do not. To that end, the majority of existing fitting techniques are iterative in nature and generally require manual intervention at each step. As a result, a skilled researcher is generally required, making such methods tedious and costly.

With the current drive from industry to develop new materials and manufacturing techniques to improve performance and reduce cost, coupled with the idea of digital prototyping to mitigate the cost of product design, the use for simulations techniques such as FE modeling is increasing. However, the process of fitting constitutive models remains a significant time and cost barrier to overcome. From an industrial perspective, the cost associated with model fitting reduces the incentive to adopt new material, manufacturing methods, or modeling approaches, slowing or stalling the widespread adoption of new advancements. From a research perspective, the process of fitting slows the exploration of new constitutive models which may improve the predictions of material behavior. To that end, there is a decided need for an efficient and accurate method to fit arbitrary constitutive material models to the behavior of arbitrary materials.

This thesis develops a software tool known as Compcam based on an alternative model fitting technique which overcomes many of the aforementioned challenges and limitations of traditional fitting methodologies. This tool, known as Compcam (COnstitutive Model Parameters from CAmera Measurements) utilizes a fitting technique known as inverse material modeling (IMM), which couples numeric optimization algorithms with FE modeling.

One common means of testing the quality of a fitted constitutive model is to create an FE model of the material test used to generate characterization data and assign it the fitted constitutive model. This allows one to directly compare the accuracy of the FE model to experimental data. Instead of using this method as a final validation, Compcam and IMM use the FE model from the start of fitting. By allowing numeric optimization algorithms to tune the parameters of the constitutive model inside the FE model, Compcam automatically determines material parameters which minimize the error between the response of the FE model and experimental data. Not only does IMM require no user interaction once optimization is started, phenomena which make traditional fitting difficult such as stress triaxiality and non-linearity in the experimental data are easily accounted for, as such phenomena are captured by the FE model.

The objectives of the work detailed in this thesis are threefold. First, to develop the aforementioned Compcam, a software tool that performs IMM. Second, to perform mechanical characterization of several types of materials, ranging from ferrous and non-ferrous wrought metals to sintered PM ferrous alloys. By exploring a wide breadth of materials, not only is a large dataset of material data generated and presented, but it allows for the effectiveness of IMM and Compcam to be tested under a variety of materials. Third, to fit several constitutive material models of varying behavior and complexity to all material tested and to generate a library of constitutive model parameters which can be used in future modeling tasks.

IMM and Compcam are not without their drawbacks. As optimization algorithms require the FE model to be evaluated a significant number of times, FE models which take a long time to solve or constitutive models with an excessive number of free parameters can make Compcam prohibitively expensive. Additionally, the effectiveness of IMM is maximized when the constitutive model being fit is a realistic description of actual material behavior. While Compcam and IMM can and will naively fit any constitutive model to any material's behavior, the quality of the final set of parameters and final model fit will suffer if inappropriate models are used.

To show the effectiveness of Compcam, this thesis presents the results of two investigations. In the first, four constitutive models were fit to the mechanical behavior of five ductile metals, specifically aluminum 2024-T351, C36000 brass, C10100 copper, AISI 4140 steel, and AISI 4340 steel. This work not only validated Compcam's development but also showed the effectiveness of IMM on a wide range of constitutive models and material behaviors. In the second investigation, four sintered, ferrous powder metallurgy (PM) alloys, each sintered to three final densities, were fit to four constitutive material models. In this case, not only is the material's stress-strain behavior of interest during fitting, but also the densification of each alloy in compression. In both investigations, Compcam proved to be an effective and accurate fitting tool, with certain caveats. Primarily, the constitutive model being fit must be a faithful representation of all material behaviors present in the target material. Should this not be true, Compcam can produce artifacts such as unrealistic parameters and poor model fits.

Chapter 2

Background and Literature Review

Owing to the breadth of subject matter covered in this thesis, a comprehensive background which covers several seemingly unconnected fields is required. In this background and literature review, the primary material test used in this work, the cold upsetting test, is introduced and discussed. Also presented is an overview of the optical measurement system used with all cold upsetting tests throughout this work. Following material testing, constitutive material modeling is introduced. This look at constitutive material models focuses exclusively on metal plasticity. Existing fitting techniques for material models are presented, with a focus on inverse techniques. Owing to the interconnectivity of inverse techniques and numerical optimization, an overview of optimization techniques is also presented, including local optimization and global search algorithms.

2.1 Material Testing Techniques

Various testing techniques exist to characterize the mechanical behavior of materials. One of the most ubiquitous is the uniaxial tensile test, made popular due to the simple equipment and methodology required. In addition, uniaxial tensile tests produce a state of stress which is predominantly tension with minimal non-linearities imparted by the test fixturing or specimen geometry, making it an effective means of characterizing a material's behavior, particularly for constitutive material models.

An alternative material testing method is the cold upsetting test, which involves the compression of a cylindrical specimen. Compared to the uniaxial tension test, cold upsetting has several advantages. Test specimens used in tensile tests need to be specially machined to allow the specimens to be gripped by the testing apparatus. The machining also ensures the stress in the specimen concentrates at a point away from the grips. By comparison, test specimens for cold upsetting tests are simple cylinders which can be parted off a length of bar stock without subsequent machining.

Owing to their simplicity, the testing equipment needed for cold upsetting tests is also simpler than tensile tests. Instead of the specialized grips required for tensile tests, cold upsetting merely requires hardened platens to compress the specimen. Further, compressive test frames are generally easier to design, build, and purchase. As a result, the overall cost associated with cold upsetting tends to be less than that of the uniaxial tension tests.

Another major advantage of cold upsetting is that a much larger cross-section of the material is placed under load compared to tensile tests (Chait and Curll, 1976). This advantage is particularly apparent when specimens undergo plastic deformation. While a tensile specimen of ductile material will experience a localized reduction in cross-section, a phenomena known as necking, a cold upsetting specimen's cross-section increases, maintaining and increasing the area under stress. This allows more of the material to be experiencing plastic deformation, potentially allowing researchers to measure more information about the material's behavior.

Despite these advantages, cold upsetting has seen limited application in material characterization for constitutive material models. In fact, its largest common use has been limited to the study of failure loci (Bao and Wierzbicki, 2004; Wierzbicki et al., 2005; Xue and Wierzbicki, 2009), as opposed to characterizing a material's behavior. The key reason for this is a phenomenon known as barreling. During testing, a cold upsetting specimen will expand radially due to the effects of Poisson's ratio. In theory, this expansion will be completely uniform if there is nothing constraining the specimen radially (Chen and Chen, 2000). However, friction between the platens and test specimens restricts the expansion of the specimen's top and bottom faces. This causes the specimen to bulge about its midplane, hence the name barreling.

In addition to causing non-uniform deformation, barreling introduces significant stress triaxiality within the specimen, particularly during plastic deformation. This triaxiality results in areas of compression, radial tension, and shear stress developing within a single specimen, as shown by Figure 2.1. The triaxiality which develops in a cold upsetting specimen prevents the isolation of a single state of stress, which is a general requirement when fitting constitutive material models analytically, as will be discussed later in Section 2.3. Several methods have been suggested to mitigate the effects of barreling in cold upsetting specimens, which would make the test more amenable to use in characterizing material behavior. The most common method is the application of lubricant between the specimen and platens, with the most common lubricants being PTFE sheets or molybdenum disulfide grease (ASTM Standard E9-09, 2012; Banerjee, 1985; Narayan and Rajeshkannan, 2012). Other methods involve specially machined specimens (Chait and Curll, 1976) which either trap lubricant or attempt to counteract barreling with specially shaped profiles. While these methods have been proven to reduce, although not eliminate, barreling in cold upsetting tests, they tend to add complexity to the testing procedure or expense to the manufacture of specimens.

An alternative solution to the problem of barreling was developed by Felling and Doman (2018). Instead of attempting to mitigate barreling through the use of lubricants or special specimens, Felling and Doman's solution was to track the development of barreling throughout a test. In a system known as SPECS (Super Portable Extensometer Camera System), Felling and Doman developed an optical measurement technique which performs two duties. First, it acts as a non-contact extensometer which tracks the vertical deformation of a specimen during a cold upsetting test. This allows a researcher to take a specimen to fracture without needing to stop a test to remove a contact extensometer. Second, it measures the barreled contour (the deformed radius at any point in the specimen's height) of the specimen throughout a test. By measuring the actual deformed radius of a specimen during a test, a researcher can calculate the bulk true stress in a specimen without relying on assumptions of volume consistency. Although digital image correlation (DIC) systems can achieve similar

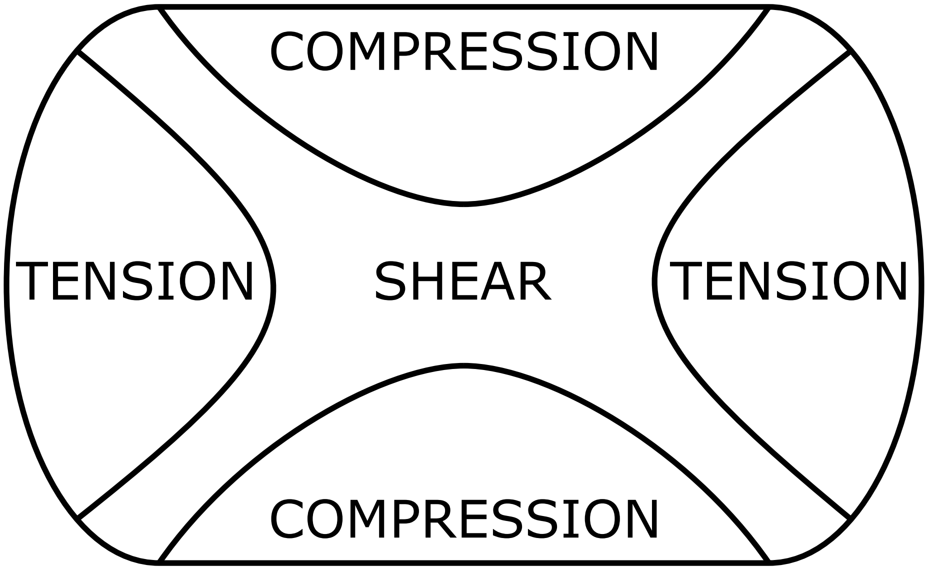

Figure 2.1: Stress states within a cold upsetting specimen undergoing plastic deformation

measurements, Specs is an order of magnitude less expensive than commercial DIC systems.

Specs utilizes a computer vision technique known as background subtraction. An image of the experiment's background is taken without fixturing or specimens installed prior to the start of testing. Test fixturing, with spherical targets for the optical system to read, is then installed. These targets are used to compute the vertical displacement, and hence strain, imposed on the specimen. During a test, images are taken of the specimen and test fixturing at an arbitrary frequency. In post-processing, each test image and the background image are broken into their constitutive color planes (red, green, and blue). For each color plane, the background image is subtracted from the test image. The resulting three images are then summed together to form a greyscale image which isolates the test fixturing and specimen from the stationary background. A binary thresholding operation is then applied, converting the greyscale image to a black and white image which specifically isolates the fixturing and specimen. Because the thresholding operation removes areas of the image, the threshold value must be carefully selected to ensure the edges of the specimen are not cropped. The effect of background subtraction is given in Figure 2.2, where a test image is shown in its processed and unprocessed state.

To account for distortion in the camera's optics as well as to convert the image's pixels to real-world dimensions, microplane calibration was applied. Developed by

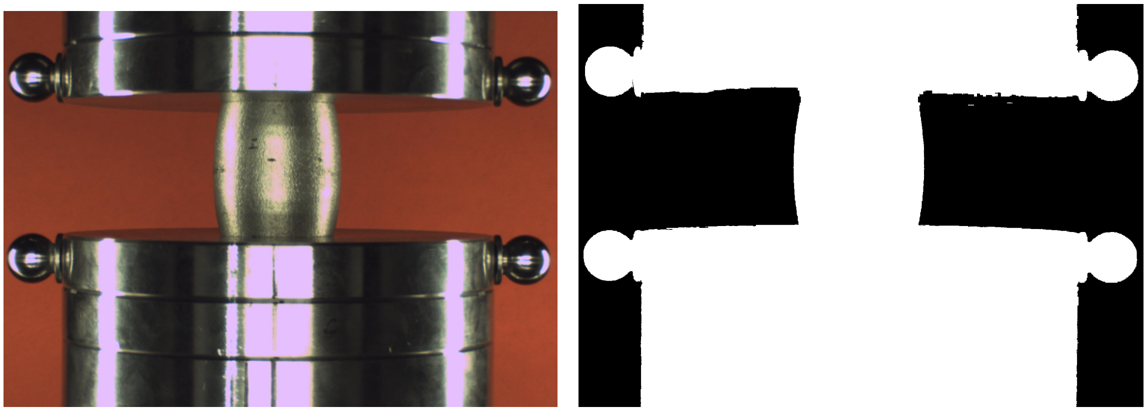

(a) Unprocessed Image (b) Final Processed Image

Figure 2.2: Before and after background subtraction technique is applied to a test image

National Instruments and available in LabView, this calibration technique removes distortion from images by analyzing a calibration image consisting of an array of dots of known spacing. By analyzing the spacing of the dots in the image, a mathematical map can be constructed to correct for any deformation as well as determine the size of a pixel in real-world units.

Information about specimen deformation is extracted from the calibrated, binary images through the use of two feature recognition techniques. First, a circle detection algorithm is run to determine the location of all spherical targets. As there are two targets per platen in the cold upsetting test, the average location of two targets is used. The difference between the location of the top and bottom platen provides a measure of the specimen's height and, therefore, vertical deformation. Next, a rake algorithm is performed to determine the edges of the deformed specimen, which allows Specs to calculate the barreled contour. The barreled contour can then be used to measure the extent of radial deformation or calculate mean deformed diameter. For more information on the operation of Specs, please refer to Felling and Doman (2018).

Barreling is caused by a combination of Poisson's effects and friction. While Specs provides the researcher with a rich dataset describing the progression of barreling throughout a test, there is still no closed-form method to analytically isolate the effects of friction and Poisson's ratio. Further, Specs does not aid a researcher in isolating a specific state of stress in the test specimen. However, the computational methods such as FE modeling can account for the combined effects of material behavior and sliding friction. The barreled contour measured by SPECS can allow a researcher to make direct comparisons to an FE model. This is a key point which drives the implementation of IMM used in this work. Further, SPECS allows one to take advantage of the triaxial state of stress in barreling to fit models which are sensitive to different states of stress without multiple tests.

2.1.1 Characterization of Friction in Compressive Testing

Characterization of friction is difficult as it varies based on lubrication, materials, surface finish, interface velocity, and a host of other factors. For this work, it was assumed friction is static in nature due to the quasi-static nature of the cold upsetting test.

To characterize the coefficient of friction between the specimen and the pressing platens the friction ring test was used. Pioneered by Male and Cockcroft (1964), the friction ring test makes use of the barreling phenomena to estimate the coefficient of friction between two materials. This is accomplished by the compression of a short ring of material. During compression, the outer diameter of the ring bulges outward while the inner diameter of the ring deforms inward. Using (2.1), where ΔD_i is the percent change in inner diameter (in units of percentage) and δH is the percent change in the ring's height (also in units of percentage). Both measurements are made after testing, so springback is accounted within the equations below.

$$\Delta D_i = m \ln \left(\frac{\mu}{0.055} \right) \tag{2.1}$$

where

$$\ln m = (0.044 \Delta H) + 10.6 \tag{2.2}$$

It is important to note that the results of the friction ring test are not exact, as there is no method available to analytically resolve coefficient of friction from deformation (Male and Cockcroft, 1964). The equations used here are approximations based on several assumptions of material deformation, and as such, the coefficients of friction determined through this method are approximate in nature. While some works do attempt more sophisticated mathematics to improve the accuracy of the friction ring test (Male and DePierre, 1970), the fact remains that there is no closed form solution to resolve friction from deformation.

Another consequence of the friction ring test is that it is incompatible with materials which exhibit compressible behavior. One of the key assumptions which underpin the analysis of friction ring tests is volume consistency. To that end, the sintered PM alloys used in this work cannot use the friction ring test.

2.2 Constitutive Material Models

Constitutive material models are the mathematics which describes how materials behave. It is a very broad term, as it can cover any type of material behavior, from thermal, to mechanical, to chemical. While the breadth of constitutive modeling is vast, this research focuses on the specific branch of that field. As such, for the purposes of this thesis, the term constitutive material model will refer exclusively to behavior related to mechanical deformation.

In their simplest form, constitutive material models which describe mechanical behavior can be given the general form seen in (2.3), where stress, σ, is a function of strain, ϵ, and any number of other inputs such as temperature, strain rate, state variables such as material damage or prior loads, and many others. However, owing to variations in the behavior of different types of materials, such as between polymers, metals, and powders, many different approaches to modeling material behavior are used. As such, this thesis once again narrows the definition of constitutive material model to limit itself to metals and metal plasticity.

$$\sigma = f(\epsilon, \dots) \tag{2.3}$$

This section begins with a brief introduction to the tensor mathematics which underlies metal plasticity. Following this introduction, a broad discussion of stress, yielding, and metal plasticity is presented. The definitions of the constitutive models used in this research are also discussed.

2.2.1 Tensor Notation

Prior to discussing metal plasticity and some of the other mathematics used in this work, it is important to introduce consistent mathematical formatting and notation. As stress states are inherently three dimensional, a complete mathematical description of stress or strain cannot be given in a single value. Instead, stress states (and strain states for that matter) are described using second-order tensors, as given in (2.4). Because stress states are generally computed in the material's coordinate system, stress tensors often use numeric subscripts instead of the traditional x, y, and z subscripts.

$$\sigma_{ij} = \begin{bmatrix} \sigma_{11} & \sigma_{12} & \sigma_{13} \\ \sigma_{21} & \sigma_{22} & \sigma_{23} \\ \sigma_{31} & \sigma_{32} & \sigma_{33} \end{bmatrix} \tag{2.4}$$

The use of tensor notation, particularly when discussing metal plasticity, provides one with the ability to create shorthand forms of matrix operations. Specifically, one definition of tensor notation is that repeated indices in one tensor or between two tensors indicates summation over the repeated index. For example, given the tensor σ_{ij}, the notation σ_{nn} represents the sum of all diagonal components of the tensor (an operation also known as the trace of a matrix). For the case of two matrices, the expression $\sigma_{ij}\sigma_{ji}$ represents multiplication of two second-order tensors and is equivalent to the longer expression shown (2.5). One interesting facet of tensor notation is that when multiplying two tensors, the number of repeated indices indicates the number of orders the solution is reduced by. For example, in the case of matrix multiplication, the two repeated indices indicated the answer must be a zero-order tensor or a scalar value. The reader is directed toward an excellent introductory text by Fung (1977) for a more detailed discussion of tensor mathematics.

$$\sigma_{ij}\sigma_{ji} = \sum_{i}\sum_{j} \sigma_{ij}\sigma_{ji} \tag{2.5}$$

2.2.2 Yielding and Metal Plasticity

The yield point of a material is the point at which the loads on a material will cause permanent or plastic deformation. Typically given in terms of stress, any loading incurred by the material below its yield strength, σ_y, will cause elastic deformation, meaning the material will return to its original configuration when unloaded. In most product design applications, the yield strength of a material is generally used as a failure criterion to determine if a component can safely withstand operating loads.

However, unlike the case of product design, there are many applications were permanent deformation is essential. Manufacturing is perhaps the most accessible example of where loading a material past its yield strength is not only acceptable but necessary. Operations such as stamping and forging require detailed knowledge of how a material behaves after yielding and permanent deformation occurs. Unlike a material's elastic behavior wherein stress and strain have a linear relationship, a material's plastic behavior can be highly complex and varied. The study of a metals' post-yield behavior is known as metal plasticity.

The most common metric used to determine yielding in metals is the von Mises yield criterion, also known as distortion energy theory. This criterion, given by (2.6) where σ_{ij} are the individual components of the Cauchy stress tensor given in (2.4), allows one to reduce a complex state of stress to a single value. This single value, formally known as the distortion energy failure criterion but more commonly referred as von Mises stress, can be compared to a materials yield strength to determine if yielding has occurred.

$$\sigma_{vm} = \sqrt{\frac{1}{2}\Big[(\sigma_1 - \sigma_2)^2 + (\sigma_2 - \sigma_3)^2 + (\sigma_3 - \sigma_1)^2 + 6(\sigma_{12}^2 + \sigma_{23}^2 + \sigma_{31}^2)\Big]} \tag{2.6}$$

Visualized in three dimensions in the stress tensor's principal axes, the von Mises yield criterion forms the cylindrical surface shown in Figure 2.3, known as the von Mises yield surface. This surface has its central axis along the $\sigma_1 = \sigma_2 = \sigma_3$ line. This line is referred to as the hydrostatic axis, as it represents the hydrostatic pressure or stress generated as a result of equal loading in all principal directions experienced by the material. Any state of stress which falls inside the yield surface will not cause a material to yield. An important consequence of this is that it implies that a hydrostatically loaded material cannot undergo yielding, even if the magnitude of the hydrostatic pressure exceeds the tensile yield strength of a material.

It is important to note that while the von Mises yield criterion is insensitive to hydrostatic pressure, some yield and failure criteria such as the Gurson-Tveergard-Needleman model presented later in this section, show a dependence on hydrostatic pressure. These models are necessary when a material's strength is dependant on the pressure exerted on it, such as the compaction of powders. As such, it behooves one to decompose the stress tensor in (2.4) into two components, as shown in (2.7), where δ_{ij} is the Kronecker delta. The scalar hydrostatic pressure (σ_H or P) controls how far up the hydrostatic axis a particular state of stress is. The deviatoric components (σ'_{ij}) account for all stresses which push the stress state off the hydrostatic axis and toward the yield surface.

$$\sigma_{ij} = \sigma_H \delta_{ij} + \sigma'_{ij} \tag{2.7}$$

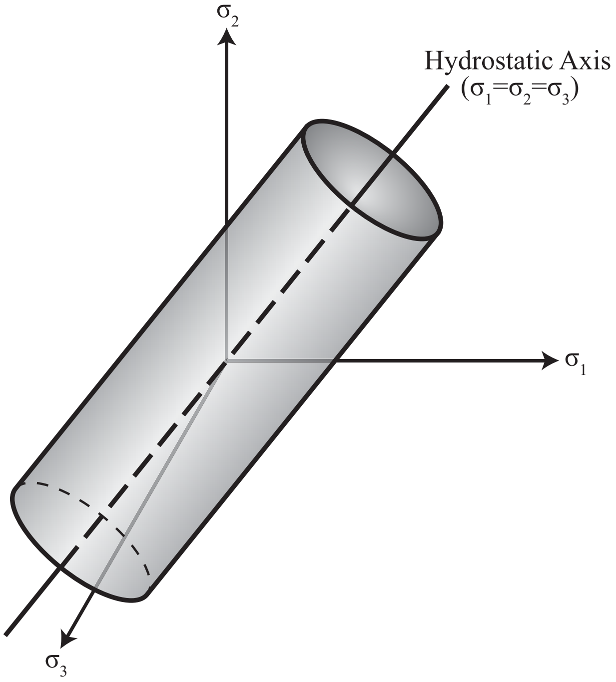

Figure 2.3: The von Mises yield surface visualized in three dimensions in the principal coordinate system.

where

$$\sigma_H = \frac{1}{3}\sigma_{nn} \tag{2.8}$$

$$\sigma'_{ij} = \sigma_{ij} - \sigma_H \delta_{ij} \tag{2.9}$$

It is important to note that the yield surface of a material represents the limiting stress which, at any instant in time, the material can withstand. This implies that while a material undergoes yielding when its state of stress intersects the yield surface, it is also true that the stress cannot exceed the yield surface. As such, as a material undergoes plastic deformation, the stress state must remain on the yield surface, for that particular loading and instant of time.

However, that most materials experience an increase in yield strength when plastically deformed, a process known as work or strain hardening. This phenomenon is modeled by altering the yield surface. The function which modifies the yield surface is known as the hardening rule. Broadly speaking, hardening rules fall under two categories; isotropic hardening and kinematic hardening. Isotropic hardening, which is used exclusively in this research, allow the yield surface to grow radially about the hydrostatic axis. Kinematic hardening also allows the yield surface to grow radially but shift the center of the yield surface off the hydrostatic axis. In the case of uniaxial loading, such as during a tensile test, and a material which exhibits isotropic hardening, the hardening rule can be observed as the plastic behavior experienced by the material.

Because the hardening rule is only active when a material is undergoing plastic deformation, it is convenient to decompose the total strain experienced by a material into the strain caused elastic deformation, ϵ^e, and plastic deformation, ϵ^p. This decomposition is formalized in (2.10).

$$\epsilon = \epsilon^e + \epsilon^p \tag{2.10}$$

An interesting consequence of the fact that stresses cannot exist outside the yield surface and that the yield surface itself can grow is that there is no closed form solution which simultaneously controls the growth of the yield surface and ensures that the stress in the material remains on the yield surface during plastic deformation. As such, a key aspect of constitutive material models used with finite element methods is an iterative procedure known as stress integration or return mapping (Simo and Hughes, 1998). These procedures ensure that the current stress in the material and the growth of the yield surface agree. While techniques vary across constitutive material models, the general procedure is the same. A trial stress is computed based on the material's current deformation. If the stress lies outside the yield surface, the return mapping algorithm starts. First, the hardening rule is evaluated to determine the extent to which the yield surface will grow. Then, based on a variety of criteria depending on the model, a trial attempt is taken to return the trial stress to the new yield surface. The algorithm repeats the process of adjusting the yield surface and attempting to map the stress onto the surface until the two converge. While computationally expensive, reliable and robust return mapping algorithms are critical for efficient and stable constitutive models.

2.2.3 Modeling Approaches for Sintered PM Alloys

In many cases, the behavior of sintered PM alloys can be treated as identical to wrought alloys, as most end uses of PM alloys, such as components in automotive gear trains, require a relative density approaching the theoretical full density of the alloys. However, in some cases, secondary shaping or forging processes are required to collapse the residual porosity in as-sintered components. One such processed used in the production of gears is gear rolling, where an as-sintered PM gear is placed between to large master gears. The PM gear is then rolled with radial force applied by the master gears, collapsing the surface porosity of the gear and bringing the gear into its final shape.

In efforts to understand the underlying operation of gear rolling as well as to perform process optimization, several researchers have turned to FE modeling. However, because the collapse of residual porosity within the gear during rolling, the von Mises yield criterion described in Section 2.2.2 is no longer valid, as this criterion cannot account for a material changing volume. To that end, alternative constitutive models and yield criteria are used in the literature.

Klocke et al. (2007) found good agreement between their modeling and experimental density gradients found in rolled gears. Additionally, they presented the results of a study which examined the effects of different process parameters on the final gear's surface densification and shape. However, the constitutive modeling approach used in this work was unclear and borderline contradictory, although it seems as though a bespoke constitutive model based on the Kuhn-Downey and Shima-Oyana models was used.

Yazici et al. (2008) attempted to model the densification process of both cold upsetting and gear rolling using the GTN model and the Gologanu-Leblond model. Both models attempt to recreate the growth, nucleation, and collapse of pores within a ductile metal. However, while the GTN model only considers spherical pores, the Gologanu-Leblond considers anisotropic pores, which allows for the model to account for pore shearing and ovalization (Gologanu and Leblond, 1997; Gologanu et al., 1993). While Yazici et al. found the Gologanu-Leblond model predicted the final density gradient of a cold upsetting specimen better than the GTN model, the computational expense was significantly greater. Yazici et al. did not present a comparison of the two models for gear rolling due to confidentiality reasons.

Cho et al. (2015) found good agreement between experimental and FE results using a Shima-Oyana model. However, they noted the difficulty associated with determining appropriate constitutive parameters. Cho et al. were also one of the only researchers to publish direct comparisons of the density gradients between their FE models and experimental results.

Regardless of the approach, it is clear that pressure-dependant constitutive material models are required to model the gear rolling process, and by extension, any forging or shaping operation of sintered PM alloys with residual porosity. But as noted by Cho et al., a key challenge associated with such models is the difficulty of determining appropriate constitutive parameters. Given that some parameters used by these models, particularly the GTN model, which is discussed below, and the Gologanu-Leblond model, are non-physical or cannot be measured experimentally, time-consuming iterative methods are generally used. However, it is important to note that none of the works detailed here discuss how parameters were fit, nor do any of the works present the parameters they used.

2.2.4 Overview of Models Used In This Work

Having covered the basics of metals plasticity and reviewed modeling approaches seen in the literature, we can now discuss the specific constitutive material models which will be used in this work. Each of these material models describes plastic deformation in a different manner. It is important to note that the specifics of the return mapping algorithm are not introduced. This is because each model presented here is a built-in model provided with the FE package used in this work (specifically Ls-Dyna R9.1.0), with little to no information provided as to how the return mapping is implemented. A key reason for the selection of these constitutive models over other models presented in the above literature review was their availability in Ls-Dyna R9.1.0 (LSTC, 2017a,b), as discussed later in this document.

2.2.4.1 Linear Isotropic Plasticity

Perhaps the simplest constitutive model which incorporate some form of hardening, linear isotropic plasticity models predict plasticity behavior using a single linear function. In general, this type of material model defines the slope of this hardening curve with a parameter known as the plastic or tangent modulus. The fact that only one parameter is needed to describe plastic behavior makes linear plasticity models simple to fit but can limit their use with certain materials.

As with all material models used in this work, a built-in material model from Ls-Dyna 9.1.0 was used. *MAT_PLASTIC_KINEMATIC, with all kinematic plasticity effects disabled, provides researchers with the ability to model linear isotropic hardening behavior by defining a single plastic parameter. The linear hardening rule is used in concert with a von Mises yield surface in this work.

*MAT_PLASTIC_KINEMATIC allows the user to define the tangent modulus, E_T, which is then used in concert with the Young's modulus of the material, E, to compute the plastic modulus E_P, as shown by (2.11). This modulus is then used to compute the flow stress, or stress incurred solely from plastic deformation, using the (2.12), where ϵ^p is the effective plastic strain. The user is also required to specify an initial yield strength for this material model.

$$E_P = \frac{E_{tan} E}{E - E_{tan}} \tag{2.11}$$

$$\sigma_y = \sigma_0 + E_P \epsilon^p \tag{2.12}$$

2.2.4.2 Swift Hardening Rule

A step up in complexity from linear plasticity, the Swift hardening rule (Swift, 1952) models plastic behavior using an exponential relationship, shown in (2.13) and was originally developed for use in modeling sheet metal stamping operations. The Swift hardening rule used in this work is implemented in Ls-Dyna as *MAT_POWER_LAW_PLASTICITY and allows the user to specify two plasticity parameters in addition to the initial yield strength of the material. These two parameters are the hardening coefficient K and hardening exponent n. The term ϵ_0 is the yield strain of the material computed from the material's Young's modulus and initial yield strength. As with linear plasticity, the Swift hardening law is used in concert with a von Mises yield surface.

$$\sigma_y = K(\epsilon_0 + \epsilon^p)^n \tag{2.13}$$

2.2.4.3 Johnson-Cook Model

The Johnson-Cook model (Johnson and Cook, 1983) has become a staple of constitutive material modeling owing to its ability to model large deformation, high strain rates, and thermal effects. The hardening rule used by this model, given by (2.14), consists of a power law hardening rule similar to the Swift hardening law, a logarithmic dependence on strain rate, and an exponential dependence on the temperature of the material. The yield surface of the Johnson-Cook model is controlled by the von Mises stress criterion. This model is given implemented in Ls-Dyna as *MAT_JOHNSON_COOK.

$$\sigma_y = (A + B(\epsilon^p)^n)(1 + c\ln\dot{\epsilon})(1 - T^{*m}) \tag{2.14}$$

Where T^* is the homologous temperature given by:

$$T^* = \frac{T - T_{room}}{T_{melt} - T_{room}} \tag{2.15}$$

While thermal and strain rate effects are a key part of the Johnson-Cook model, this model, as it is implemented in Ls-Dyna, was selected owing to its ability to use an equation of state.

Equations of state for metals are common when modeling extremely high rate events, when the hydrostatic pressure far exceed a material's yield strength, and when shock waves propagation is of interest. In these situations, the material's behavior is more accurately described as a fluid than a solid. Equations of state effect material behavior by directly controlling the hydrostatic component of the stress tensor, while the hardening rule and yield surface control the deviatoric components of stress. Equations of state are generally a function of the material volume, internal energy, temperature, or any combination thereof.

As already noted, the calculation of stress in most FE codes is decoupled into its hydrostatic and deviatoric components. This is advantageous for constitutive models, as most are pressure independent, such as those which use the von Mises yield criterion. In such cases, pressure and volumetric deformation are calculated based on the material's bulk stiffness and it is assumed that all volumetric deformation is elastic in nature. The use of an equation of state allows one to control the material's pressure behavior, allowing one to circumvent the pressure-independent nature of yield surface and add densification behavior to material models which otherwise be unable to do so. For a technical treatment of how equations of state are implemented in FE solvers, please refer to Appendix A. While any material models could be combined with an equation of state, in practice, the added challenge limits the number of constitutive models which can do so in most FE solvers. It is for this reason the more complex Johnson-Cook model is used for equation of state modeling instead of the similar and far simpler Swift hardening rule.

While work completed in this thesis does not include consideration of high rate and high energy deformation situations, an equation of state's ability to link hydrostatic pressure to volume, and hence material density provides an alternative means of modeling sintered PM alloys. The usage of an equation of state to model the small to moderate densification of sintered PM alloys under low strain rate has not been seen in literature prior to this work.

Two equations of state were used in this thesis. The first was a bi-linear equation of state implemented in Ls-Dyna as EOS_TABULATED_COMPACTION. As suggested by its name, this equation of state takes a list of proportionality constants, C_n, at various volumetric strains, $\epsilon_{V,n}$. These pairs form controls points which define the material's pressure-volumetric strain behavior, as shown in (2.16). While upward of eight control points could be selected, only three points were chosen for this work, providing bi-linear pressure-volume behavior. It was found that this combination provided a good trade-off of complexity and accuracy compared to higher and lower order piecewise curves.

$$P(\epsilon_V) = \begin{cases} C_1\epsilon_V + P_0 & \epsilon_V \leq \epsilon_{V,1} \\ C_2\epsilon_V + P(\epsilon_{V,1}) & \epsilon_{V,1} < \epsilon_V \leq \epsilon_{V,2} \\ \vdots & \\ C_n\epsilon_V + P(\epsilon_{V,n-1}) & \epsilon_{V,n-1} < \epsilon_V \end{cases} \tag{2.16}$$

The second equation of state used in this work is based on the $P - \alpha$ compaction curve. This curve, developed to model the dynamic compaction of ductile porous bodies (Herrmann, 1969), has several useful properties. Prime amongst them, the $P - \alpha$ compaction curve, where P is pressure and α is porosity (the inverse of relative density), prevents a constitutive model predicting impossible densification by increasing hydrostatic pressure asymptotically as a material approaches full density, as shown in Figure 2.4. This behavior allows the equation of state to behave like a

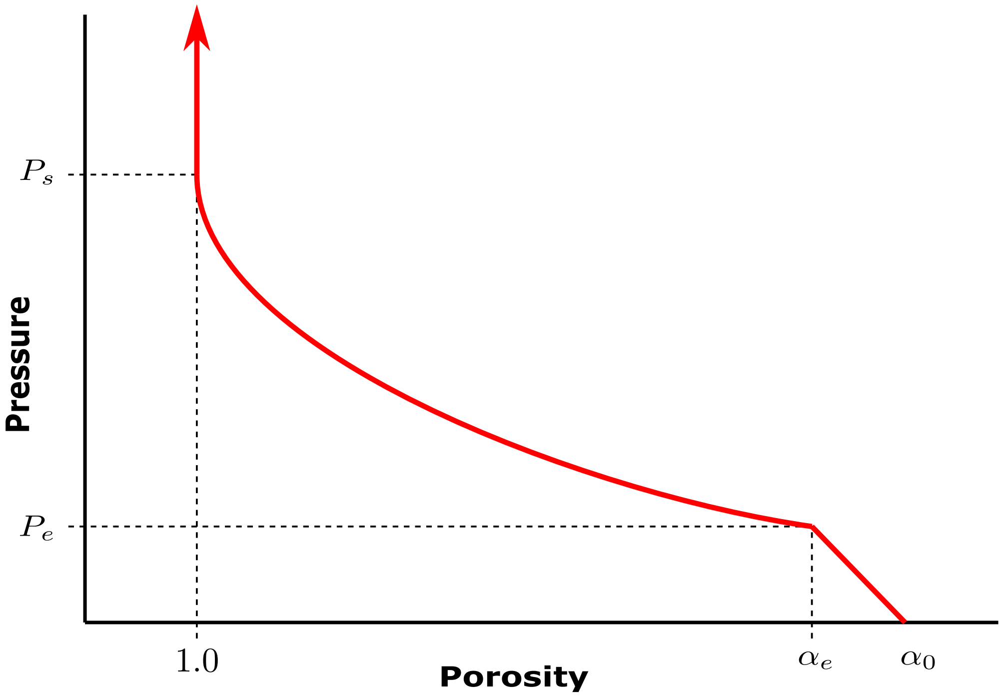

Figure 2.4: The $P - \alpha$ compaction curve

pressure-independent model at full density, something the bi-linear equation of state listed above would not be able to accomplish without a set of control points forcing near infinite pressure-volume behavior. It was found that forcing the bi-linear equation of state to attempt such behavior yielded significant numerical instabilities which were impossible to overcome.

The $P - \alpha$ curve used by Ls-Dyna is found in EOS_MIE_GRUNEISEN. While this equation of state does contain a Gruneisen-type component to deal with internal energy, the quasi-static nature of this work means that this component is not activated. Porosity and pressure are tied together using (2.17), were P is the current pressure, P_s is the hydrostatic pressure when a material reaches full density, P_e is the hydrostatic pressure at at the material's yield point, α_0 is the initial porosity of the material, and N is an exponential modifier.

$$\alpha = 1 + (\alpha_0 - 1)\left(\frac{P_s - P}{P_s - P_e}\right)^N \tag{2.17}$$

2.2.4.4 Gurson-Tvergaard-Needleman Model

The Gurson-Tvergaard-Needleman (GTN) model is a phenomenological model which attempts to models porous materials. Originally developed by Gurson (1977) to represent the growth and collapse of pores in a material, the model was expanded by Tvergaard (1981) and Chu and Needleman (1980) to account for the coalescence and nucleation of pores during plastic deformation. It is important to note that all work by Gurson, Tvergaard, and Needleman make the assumption that changes to porosity only occur under hydrostatic pressure, with no accounting for the deviatoric components of stress. The GTN model is implemented in Ls-Dyna as *MAT_GURSON.

Unlike the four material models already presented, the GTN model uses its own yield surface given by (2.18). The yield strength of the material used by the GTN model, σ_y, can either be a constant to model perfect plasticity or can be a function of effective plastic stress to model a material's hardening behavior.

$$\Phi = \frac{\sigma_{vm}^2}{\sigma_y^2} + 2q_1 f^* \cosh\left(\frac{3q_2\sigma_H}{2\sigma_y}\right) - 1 - (q_1 f^*)^2 = 0 \tag{2.18}$$

An important component of the GTN yield surface is the effective void fraction f^*, which models the degree of porosity in a material. Given by (2.19), the effective void fraction of the GTN model is dependant on the critical void volume f_c. When the void volume exceeds this critical void fraction, it becomes a function of the void fraction at material failure f_F, which helps account for material damage which occurs when porosity becomes excessive. It is important to note that under compression, the void fraction cannot exceed the critical void volume because existing pores will collapse.

$$f^*(f) = \begin{cases} f & f \leq f_c \\ f_c + \left(\frac{q_1^{-1} - f_c}{f_F - f_c}\right)(f - f_c) & f > f_c \end{cases} \tag{2.19}$$

Growth and contraction of the void fraction is computed incrementally using (2.20). The term $\dot{f}_G$ represents growth of existing voids and, as shown by (2.21), is solely dependant on the hydrostatic component of plastic strain. The nucleation of new voids, defined by $\dot{f}_N$, is a function of the term A, which attempts to model the probabilistic nature of void nucleation or the creation of new pores. As given by (2.23), the probability of void nucleation is assumed to be Gaussian in nature.

$$\dot{f} = \dot{f_G} + \dot{f_N} \tag{2.20}$$

$$\dot{f_G} = (1 - f)\dot{\epsilon}^p_{nn} \tag{2.21}$$

$$\dot{f_N} = A\dot{\epsilon}_p \tag{2.22}$$

$$A = \frac{f_N}{s_N\sqrt{2\pi}} \exp\left(-\frac{1}{2}\left(\frac{\epsilon^p - \epsilon_N}{s_N}\right)^2\right) \tag{2.23}$$

A major difference between the von Mises yield criterion and the GTN model is that the yield strength of the GTN model is dependant on both hydrostatic and deviatoric stress. This is seen in the flow function by the use of both von Mises stress (which is a measure of deviatoric stress) and hydrostatic pressure σ_H. Additionally, the yield surface of the GTN model is also highly dependant on the effective void fraction f^*. As the void fraction approaches zero, indicating there is little to no porosity in the material, the GTN model approaches the behavior of the von Mises yield criterion, where yielding is only caused by the deviatoric components of stress. However, as porosity increases and f^* increases above zero, yielding can also be triggered by hydrostatic pressure. This feature helps to model the collapse of pores in a material. The effect of void fraction on the GTN yield surface is shown in Figure 2.5 as a function of hydrostatic and deviatoric stress.

Owing to its dependence on both hydrostatic and deviatoric stress, the GTN model is appropriate for materials whose density and strength change as a function of hydrostatic pressure, including porous materials and powders to a certain degree. Further, the effective void fraction f^* can be used as a direct measure of the relative density of the material. The conversion between relative density and the effective void fraction is given in (2.24), where ρ_{rel} is defined as relative density.

$$\rho_{rel} = 1 - f^* \tag{2.24}$$

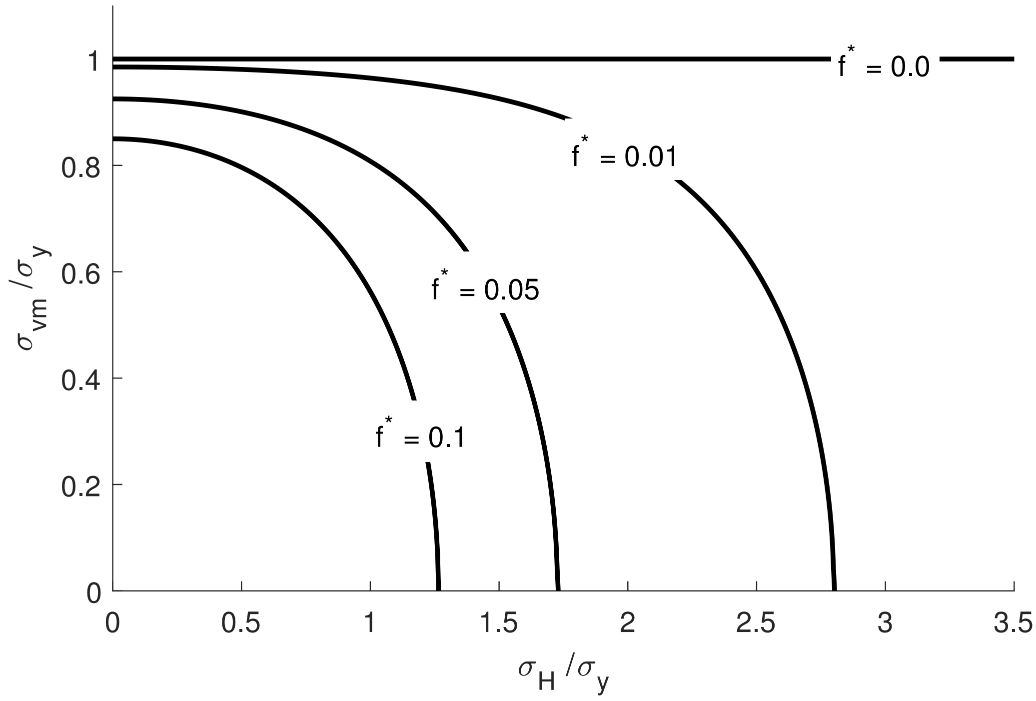

Figure 2.5: The effect of varying void fraction on the GTN model.

2.3 Model Fitting Techniques

Fitting is the process of choosing the input parameters of a constitutive material model that provide the best prediction of a material's real behavior. While this may sound like an easy proposition on paper, the fitting of material models is a major challenge in material characterization. This section details some traditional fitting techniques and their challenges before introducing the methodology used in this work, inverse material modeling.

2.3.1 Traditional Fitting Techniques

Traditional fitting techniques will be a term used in this document to denote a family of existing methodologies which have been used extensively to fit constitutive models. Techniques in this family include analytical solutions, successive iteration, and specially developed material tests and correlations provided by the creator of the constitutive material model.

The simplest traditional fitting technique is the determination of input parameters using analytic solutions of a constitutive model. A well-known example of an analytic solution is the determination of Young's modulus from a stress-strain curve. While analytic solutions make fitting very easy, they are uncommon. The primary reason for this is that constitutive material models are generally more complex than functions which consist of one or two parameters. Additionally, complex constitutive models tend to have model parameters which may not have physical meaning or cannot be measured. For example, the GTN model described in Section 2.2.4.4 has several parameters which cannot be measured, such as the void fraction at which pores begin to nucleate and the so-called critical void fraction.

For cases in which analytic solutions do not exist, the most common methodology is to manually fit the response of a material directly to the constitutive material model. Generally speaking, this methodology requires the constitutive material model to be coded external to the FE package in which it will be used, as the process of manual fitting tends to be iterative in nature. Externally coded material models can provide significant computational savings compared to manual iteration on an FE model. However, fitting using externally coded material models generally require material specific tests in order to isolate specific stress states and determine specific model parameters. Tests which causes significant triaxiality in the test specimen, such as the cold upsetting test, are not generally compatible with fitting using externally coded FE models.

A classic example of this method is the determination of parameters for the Johnson-Cook model. In their original paper, Johnson and Cook (1983) use three separate material characterization techniques, a split Hopkinson bar test, a tensile test, and a torsional test, to isolate specific tensile and torsional states of stress as well as to capture high rate and thermal effects. While not directly stated, Johnson and Cook likely used an iterative approach, particularly for the determination of the strain hardening parameter C as they state C was determined from torsional data by "numerically simulating" the test at high strain rates.

Another interesting factor in how Johnson and Cook recommend fitting parameters for their model is that a sequential fitting methodology should be adopted (1983). Specifically, they recommend fitting of the hardening parameters A, B, and n under quasistatic ($\dot{\epsilon}^p = 0$) and isothermal ($T^* = 0$) conditions prior to fitting thermal or strain rate effects. In the case of the flow rule developed by Johnson and Cook, this methodology makes sense, as the thermal and strain rate effects are somewhat modular in nature. However, there are several constitutive models for which sequential fitting is not an ideal method.

Some examples of sequential fitting include attempts to fit constitutive parameters for the GTN model. Oh et al. (2007) fit the failure parameters of the GTN model to API X65 steel starting with the nucleation void fraction, f_N before proceeding to fit the critical void fraction f_c and the void fraction at failure f_f simultaneously. Kiran and Khandelwal (2014) used a similar sequential methodology when fitting the GTN model to ASTM A992 steel, starting with nucleation parameters ϵ_N and f_N before proceeding to f_c and f_f. While Oh et al. do not specify the exact method used to select the final parameters they published, Kiran and Khandelwal used a series of parametric studies to determine the best input parameters. A final example presented here is the work of Cuesta et al. (2010) which sequentially fit GTN parameters using a tensile test to first determine elastic parameters, then a single punch test to sequentially determine nucleation parameters, the critical void fraction, then the void fraction at failure. Cuesta et al. made use of semi-empirical formula to aid in the determination of parameters.

The use of sequential fitting is not limited to the GTN model. Work on the Bamman model, a constitutive model for metals which accounts for high rate, thermal softening, and kinematic hardening effects, recommends a sequential fitting methodology starting with hardening parameters before proceeding to either rate or thermal effects (Bammann, 1990; Chuzhoy et al., 2003). Recent work with laminated composites, a complex, highly coupled material which is challenging to model constitutively, also advocates the sequential fitting of parameters to both ease the fitting process as well as to gain an understanding of how parameters interact (Qiao et al., 2017).

While it eases the fitting process, sequential fitting of parameters could present a major issue. As pointed out by Xue (2008) in a discussion of the GTN model, the highly coupled nature of that and many other material models makes calibration difficult. If two parameters are coupled, such as the hardening coefficient K and exponent n in the Swift hardening rule presented in Section 2.2.4.2, fitting K while holding n constant would drastically affect the quality of model fit, as both parameters have a coupled effect on model behavior.

Another issue with traditional fitting techniques is how the constitutive model is implemented. In many cases, the constitutive material model has to be implemented in an environment outside the FE package the model will eventually be used in. This is due to the expense of manually iterating on an FE model. In older works, such as Johnson and Cook and Bammann, externally coded models were required due to the expense of running a full FE model to fit parameters. However, externally coded material models may differ in implementation from their counterparts in the FE package. Finally, externally coded material models have difficulty dealing with complex states of stress which can develop due to testing conditions, such as the cold upsetting test discussed in Section 2.1. While newer works, such as Cuesta et al., Kiran and Khandelwal, and Qiao et al. iterate on an FE model, there is still the issue of sequentially fitting parameters in models which have highly coupled phenomena.

2.3.2 Inverse Material Modeling

Regardless of the fitting methodology selected, a common way of testing the accuracy of a constitutive model fit is to create an FE model of the experiment from which the experimental data was retrieved. This way, information such as force-displacement can be used to validate the model fit. While traditional fitting techniques generally produce an FE model which closely replicate the experimental data, there is generally subsequent tuning of parameters to deal with effects which cannot be accounted for analytically, such as specimen geometry, non-linearities in the experimental setup, or most commonly, differences in the implementation between the constitutive model used in the FE package and the externally coded version used for fitting.

Inverse material modeling (IMM) builds on the idea of tuning an FE model of the experiment to replicate experimental data. Instead of traditional fitting techniques involving external coding, IMM determines parameters for the constitutive model used in the FE package directly. Further, instead of manual iteration and sequential fitting, IMM fits all parameters simultaneously by coupling the FE model to numerical optimization techniques. These techniques adjust the input parameters of the constitutive model, and hence the FE model, to minimize the difference between the responses measured in the experimental test and FE model. Because the FE model simulates the entire experimental system, directly measured experimental data such as force-displacement can be used, which removes any reliance on computed values of true stress. The optimization techniques used for IMM vary across the literature, as will be shown below. While the following review notes the type of optimization technique used for IMM varies across the literature, an overview of numerical optimization algorithms is presented later in this chapter.

There are many good examples of IMM in literature. Springmann and Kuna (2005) used IMM to determine input parameters for the GTN model for StE 690 structural steel. Their experimental regime consisted of flat tensile tests from which a force-displacement curve was extracted. The material model was implemented in the bespoke FE code SPC-PMHP. Optimization was undertaken using a gradient-based algorithm. Springmann and Kuna were able to produce GTN parameters which matched experimental force-displacement curves including the capture of material failure.

The GTN model is a popular model to be fit using IMM owing to its complexity and it highly coupled nature. Table 2.1 highlights several examples of this. One will note that both the types of material test as well as the optimization techniques used vary between sources. As IMM is an inverse method, a standard material test technique does not necessarily need to be used to determine material parameters. Any test which can be effectively reproduced with an FE model and from which an appropriate response can be extracted can be used.

Table 2.1: Various IMM approach to fitting the GTN model

Reference	Testing Method	Optimization Technique
Vaz et al. (2015)	Deep drawing of sheet metal	Various (comparison of gradient-based, gradient-free and global search)
Abbasi et al. (2011)	Tensile test	Response surface modeling (statistical approach)
Muñoz-Rojas et al. (2010)	Tensile test	Global search (genetic algorithm)

In addition to fitting constitutive model parameters for plastic behavior, IMM has also been used extensively for the fitting of damage models. Cooreman et al. (2008) used IMM to fit Swift hardening parameters as well as parameters for a Hill 1948 yield and failure surface to DC06 steel sheet. Cooreman et al. used a bi-axial tension test in concert with digital image correlation (DIC) to make full-field strain measurements, allowing for the experimental strain contours to be used as responses during optimization. A Gauss-Newton optimization algorithm was used in this work.

Work by Roux and Bouchard (2010, 2015) also looked at hardening and damage model for sheet metal. However, unlike Cooreman et al., the work of Roux and Bouchard focused on the optimization techniques and challenges associated with fitting material parameters than on the final model fit. However, this focus does yield several important results. In a conference paper published in 2010, Roux and Bouchard demonstrated that a rich dataset is required to ensure that the final parameters determined by IMM are actually the best set to describe a material behavior. Using a Kriging Efficient Global Optimization (EGO) method, they determined that force-displacement data alone can produce several local solutions, allowing several parameter sets to describe material behavior (Roux and Bouchard, 2010). In an effort to isolate a global best set of parameters, data describing the progression of necking was included, which helped IMM produce a single best set of parameters. However, the methodology used to measure necking was not discussed.

Roux and Bouchard later extended their work to include the use of DIC for flat tensile tests (Roux and Bouchard, 2015), wherein they used the full-field strain measurements provided by DIC in concert with a force-displacement curve to determine a set of output parameters. While this work provided significant insight into some of the challenges associated with IMM, it is important to note that Roux and Bouchard limited the number of input parameters they work fitting. Specifically, the 2010 paper limited their work to two parameters while the 2015 article looked at only two and three free parameters, unlike many of the other works presented here attempt to optimize the full range of material parameters. In addition, while the 2015 article discusses DIC in depth, Roux and Bouchard do not actually make use of experimental data, instead relying on an FE model from which data similar to that measured with DIC was extracted. Regardless, their finding that a rich dataset is required to determine an appropriate set of input parameters is of critical importance as the number of parameters increases.

Primavera et al. (2015) presented a unique take on IMM to determine constitutive parameters for aluminum foam. Whereas work presented here has so far used responses gathered from a single test, Primavera et al. used three separate material tests to determine a single set of parameters. Specifically, they used compression, three-point bending, and Charpy tests to gather enough data to fully describe the material's responses. To accommodate the three material tests, three FE models were also used. Instead of combining the responses of the three tests into a single metric for optimization, as was done by Roux and Bouchard (2015), Primavera et al. used a multi-objective genetic algorithm. Unlike the gradient-based methods or EGO methods presented earlier, the use of a multi-objective genetic algorithm results in a very large computational expense, with the three FE models used in this work being evaluated several thousand times each.

Examples of IMM for various material types, testing methods, and optimization techniques can be found in the literature. Some of these works are summarized in Table 2.2. However, two conclusions from these works have greatly influenced this present research.

1. While various testing techniques have been used, none have used the cold upsetting test, or compressive testing in general with the exception of powder compaction documented in Wikman et al. (2006) or compression of aluminum foam by Primavera et al. (2015).
2. With the exception of Primavera et al. and Roux and Bouchard, all previous attempts have used a single metric for fitting, such as force-displacement, stress-strain, or force-time.

Table 2.2: Various IMM approach to fitting the GTN model

Reference	Material	Constitutive Model	Testing Method	Optimization Technique
Bondy et al. (2016)	Aluminum 6061-T6	Johnson-Cook	Tube cutting	Unspecified (LS-OPT package)
Umbrello et al. (2007)	AISI 316L	Johnson-Cook	Metal cutting	Gradient-based
Wikman et al. (2006)	Distalloy AE powder	Drucker-Prager	Single action compaction	Nedler-Mead type Gradient free
Morrow et al. (2010)	Skeletal muscle tissue	Transversely isotropic and hyperelastic	Tensile	Gradient-based (Quasi-Newton)
Chawla et al. (2009)	Passive muscle tissue	Linear viscoelastic	Impactor	Global search (Genetic algorithm)
Guan et al. (2011)	Bone (skulls)	Linear plasticity	Three-point bending	Response surface modeling (Kriging)
He et al. (2016)	Laminated composites	Ramberg-Osgood	Three-point bending	Least-squares

2.4 Numerical Optimization Techniques

Numerical optimization techniques attempt to find the set of input parameters which maximize or minimize of a particular function. Because optimization problems generally seek a minimum, these problems are also sometimes referred to as minimization problems. Further, any problem seeking a maximum can be easily converted to a minimization problem by simply multiplying the final result by negative one without loss of physical significance. The function which is being optimized is referred to as the cost or objective function. numerical optimization techniques make up a critical component of IMM, as they control how input parameters are tuned to match experimental and computational response.

numerical optimization can be broadly broken into two categories: local optimization algorithms and global search methods. Local optimization algorithms are capable of precisely determining a minimum of a function. However, they are unable to determine if the minimum they have found is the global minimum of a function or a local minimum, the difference between the two is depicted in Figure 2.6. Global search methods utilize different types of algorithms to sample the entire solution space to find the global optimum of a function.

One feature common to all optimization techniques is that many evaluations of the objective function are required. As such, optimization can be a numerically and computationally expensive process.

This research uses both local optimization techniques and global search methods. To that end, this section will provide an overview of both categories. However, all optimization algorithms used in this work were commercially produced. As such, this section only provides an overview of the methods used. For a more detailed discussion of the operation of these algorithms, please refer to the sources referenced in each section.

2.4.1 Local Optimization Techniques

Local optimization algorithms can be broken into two types, those which utilize the gradient information of the objective function, known as gradient-based algorithms, and those which do not, which are referred to as derivative-free methods. While both types of methods cannot distinguish between a local and global minimum, local optimization algorithms generally provide better performance at finding the exact location of a given minimum than global search algorithms. Another feature of local optimization techniques is that they require an initial starting point to be specified. The selection of the starting location can have a significant impact on the efficiency of the algorithm and whether the algorithm finds a local or global optimum.

2.4.1.1 Gradient-Based Methods

As the name suggests, these optimization techniques take advantage of the derivative of the objective function to aid in finding the optimum. Their operation can be described with the following analogy. If a mountaineer wants to get down a mountain as fast as possible, it behooves them to find the steepest part of the mountain and descend in that direction. During their decent, the mountaineer should continuously monitor the slope of the mountain and adjust their track to follow the steepest route. While this is obviously not true for a real mountaineer, for whom sheer slopes may impede a swift descent, it is an accurate description of how gradient-based optimization algorithms operate.

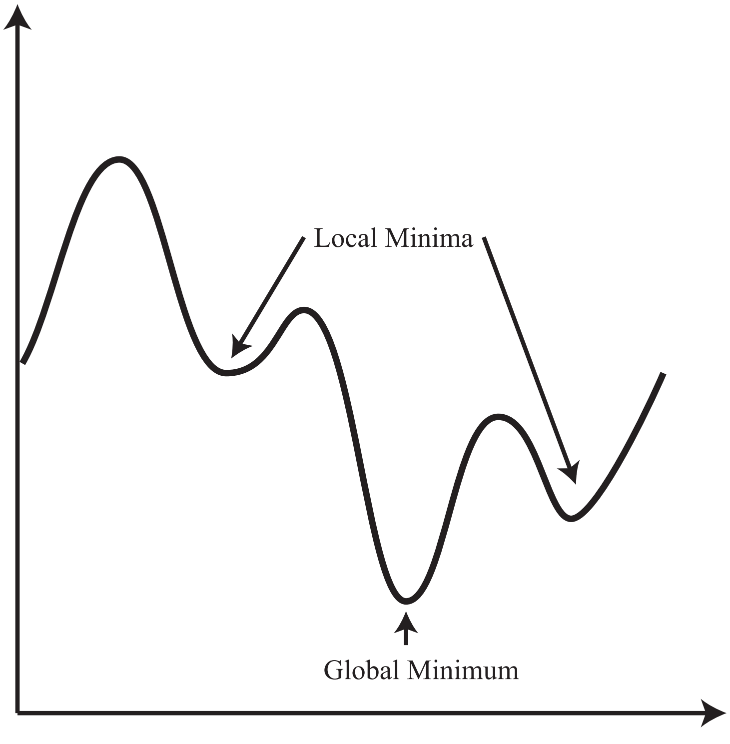

Figure 2.6: A demonstration of a multi-modal function with a two local minima and a single global minimum.

This method is formalized in the appropriately named steepest descent method. Compared to more complex gradient-based optimization methods (which will be presented later), the steepest descent method has very little computational expense associated with it. The algorithm only needs to determine the derivative of the function at the current point and an appropriate step size to take for each iteration (Eiselt et al., 1987). The step size can either be fixed in the most simple form of steepest descent or can be adaptive depending on the gradient of the function. For example, it makes more sense that if the derivative is large, indicating a very steep gradient, a larger step size would likely allow the algorithm to approach a minimum faster than a small step.

An extension of steepest descent type algorithms are known as conjugate gradient methods (Eiselt et al., 1987; Press et al., 2007). These methods not only use gradient information, but also the second derivative of the function, which provides information about the curvature, or rate of change of gradient, at a particular point. While such methods allow algorithms to converge on an optimal point faster than methods which rely on gradient information alone, they require that second derivative information of the objective function be provided at every point in the solution space. A more commonly seen variant of conjugate gradient methods are quasi-Newton methods, which do not calculate the second derivative at each iteration but instead build an approximation of the second derivative based on derivative information retained from previous steps in the algorithm. The approximation of second derivative information can provide better optimization performance as the algorithm maintains a history of where it has been (Press et al., 2007).

Gradient-based methods require, at minimum, the first derivative of the objective function to be known at all points in the solution space, which implies that the analytic derivative of the objective function must be provided. However, there are many cases in which the objective function does not have an analytic derivative which can be calculated. A pertinent example of this would be IMM, as a derivative cannot be extracted from an FE model. In these cases, the gradient can be approximated numerically through the use of finite difference methods. However, the numeric approximation of the derivative comes with an additional computational cost, as calculation of the derivative requires one evaluation of the objective function for each dimension of the problem. For problems with high dimensionality or that have a high computational cost per evaluation, such as a long-running FE model or a constitute model with a large number of tunable parameters, this drastically increases the expense of gradient-based optimization algorithms.

2.4.1.2 Derivative-Free Methods

Derivative-free methods, sometimes also referred to as direct search methods, are optimization techniques which do not use the gradient information of the objective function to determine an optimal solution. These types of methods are more commonly seen in global search algorithms, as will be discussed in Section 2.4.2, although one particular direct search algorithm has proven itself to be a very effective local optimizer.

The Nelder-Mead method is a derivative-free optimization technique developed by Nelder and Mead (1965) while working as statisticians at the National Vegetable Research Station in the United Kingdom. This method consists of creating a simple convex hulled polygon, known as a simplex, in the solution space with one more vertex than there are dimensions in the problem. At each iteration of the algorithm, the objective function is evaluated at all vertices in the simplex. Then, following a series of predefined rules, the simplex expands, contracts, or translates through the solution space towards a minimum. As it approaches the minimum, the simplex will begin to contract, which provides a useful stopping criterion for the algorithm.

Direct search methods are appropriate for objective functions for which an analytic derivative cannot be supplied. However, they can converge slower for some functions, as the use of gradient or conjugate gradient information can allow gradient-based algorithms to find an optimum faster (Press et al., 2007).

2.4.2 Global Search Algorithms

Global search algorithms explore the entire solution space to find the most optimal solution. In comparison to local optimization techniques, global search methods are almost exclusively direct search methods because while gradient information will aid in the determination of a minimum, derivative information cannot be used to differentiate between a global and local minimum. While this may imply that global search methods are superior to local optimization techniques, the trade-off is that global search methods require significantly more evaluations of the objective function to fully explore the solution space. Furthermore, global search algorithms do not perform as well as local optimization techniques at homing in on the exact final optimum.

While a very large number of global search algorithms exist, this section looks at two methods: the genetic algorithm and the particle swarm optimizer. These two methods were selected due to their prominent use in the literature.

2.4.2.1 Genetic Algorithms

Genetic algorithms attempt to replicate the "survival of the fittest" phenomena seen in evolutionary biology. Genetic algorithms begin by sampling the solution space of an objective function to develop what is known as the population. Based on their objective score, a set number of the best scoring individuals of the population "survive" each iteration. A new population is then created by combining information from the surviving population through the use of predefined rules. These rules, in essence, replicate how the best traits of an individual or set of individuals are passed on to their offspring. This process, referred to as crossover, allows the population to slowly converge on an optimal solution. In addition, random mutations are introduced in a small fraction of the population at each iteration. These mutations help the algorithm explore the solution space and prevent the algorithm from converging prematurely on a local optimum (Hassan et al., 2005).

Genetic algorithms are one of the most common global search techniques seen in literature, leading to their prevalence in commercial optimization or mathematics packages such as MATLAB. However, due to the randomized nature of crossover at each iteration of genetic algorithms, they can be slow to converge on an optimal solution, as well as experience difficulty predicting the exact location of a minimum solution (Hassan et al., 2005).

2.4.2.2 Particle Swarm Optimization

An alternative to genetic algorithms for global optimization is the particle swarm optimizer (PSO) (Kennedy and Eberhart, 1995). Like genetic algorithms, PSOs are biologically inspired. However, whereas genetic algorithms model the evolution of a population, PSOs are based on the swarming behavior of birds and insects. An initial population of individuals is created. Each individual is also given a random initial velocity vector. To determine each individual's location at the next timestep, three factors are considered: 1) the individual's current velocity, 2) the most optimum location the individual has already visited, and 3) the swarm's most optimal location. Each factor results in a separate velocity vector, the magnitude of which is controlled by a predefined coefficient. The three vectors are summed to produce a final velocity vector used to calculate the particle's position in the next iteration.

The behavior of PSOs is largely controlled by the coefficients for each velocity vector. For example, if a slow convergence with significant exploration of the solution space is desired, the coefficients modifying the individual's current velocity and history of it's best location could be increased. For faster convergence, the coefficient associated with the swarm's best location is increased (Hassan et al., 2005). Furthermore, PSOs can dynamically adjust their coefficients, allowing the individuals more freedom to explore the solution space during the first few iterations before forcing them to converge on the swarm's optimum (Venter and Sobieszczanski-Sobieski, 2003).

When compared to genetic algorithms, the literature suggests that PSOs can have better convergence behavior than genetic algorithms for real-value problems (Hassan et al., 2005; Venter and Sobieszczanski-Sobieski, 2003). This could be a result of PSOs using the velocity information of swarm in much the same way as a gradient-based algorithm. As the velocity of the swarm decreases, the swarm converges on a single location. However, due to its relative youth compared to genetic algorithms, fewer mathematics packages offer PSOs with the same type of features seen in genetic algorithms. For example, MATLAB offers both a genetic algorithm and a PSO. However, the PSO they offer is unable to accept linear inequality and non-linear constraints, while the genetic algorithm they offer can do both.

Chapter 3

Tool Development

This research uses two custom-built software tools to accomplish two key aspects of the research in this thesis. The primary tool used throughout this document is COMPCAM, an IMM framework which executes FE models, parses and analyzes the responses of experimental and computational datasets, and executes numeric optimization. COMPCAM is developed within MATLAB, which allows it to take advantage of built-in libraries of optimization algorithms and other mathematics techniques.

The second tool developed for this work performs optical densitometry. DEAD, or Density by Element Averaged Downsampling, allows one to generate density maps from tiled micrographs of a specimen's cross section. With the exception of imaging stitching, DEAD is also developed and implemented in MATLAB.

This chapter provides a detailed overview of the development and implementation of each tool as well as limitations encountered.

3.1 COMPCAM

As previously mentioned, Compcam (COnstitutive Model Parameters from CAmera Measurements) performs automated fitting of material model parameters using IMM. This tool consists of three major components: the experimental data to which the constitutive model is being fit, an FE model of the experimental system assigned the constitutive model of interest, and a non-linear optimization algorithm.

As noted in Section 2.3.2, work by Roux and Bouchard (2015) found that a rich dataset is required to allow IMM to determine a globally optimum set of input parameters for a given constitutive model. As such, Compcam uses Specs to acquire multiple datasets acquired from a single test when performing model fitting. For fitting constitutive models using the cold upsetting test, two datasets are used, the force-displacement curve and the mean deformed diameter of the specimen as a function of its vertical displacement. To be clear, both datasets use the displacement data of the specimen. Both of these datasets are measured using Specs.

Force-displacement is arguably the most important dataset used by Compcam, as it provides direct information about the material's plastic behavior. While a stress-strain curve could have been used instead, force-displacement was selected because it was the most direct measurement. Creating a stress-strain curve requires both values to be computed, which in turns relies on force and displacement data. Furthermore, true stress measurements require knowledge of the deformed diameter of the specimen throughout a test. While Specs can provide this data, the calculation of stress from two measured datasets increases measurement uncertainty. Force-displacement can also be easily extracted from the FE model.

Measurements of how the specimen deforms radially provide information pertaining to friction between the specimen and platen, Poisson's effects, and material densification. Two datasets were considered to capture these effect, both shown in Figure 3.1. The first option was to compare the final deformed profile of the specimen to that of the FE model. While this metric was effective, it posed several issues. First, it was discovered that minor variations between the initial, undeformed diameter and height of the specimen and FE model had a large impact on the final fit metric. Second, the amount of data describing radial deformation measured by Specs decreases as the specimen deforms due to the platens occluding the specimen. It was found that in cases of extreme deformation, such as the copper specimens tested in Chapter 5, the

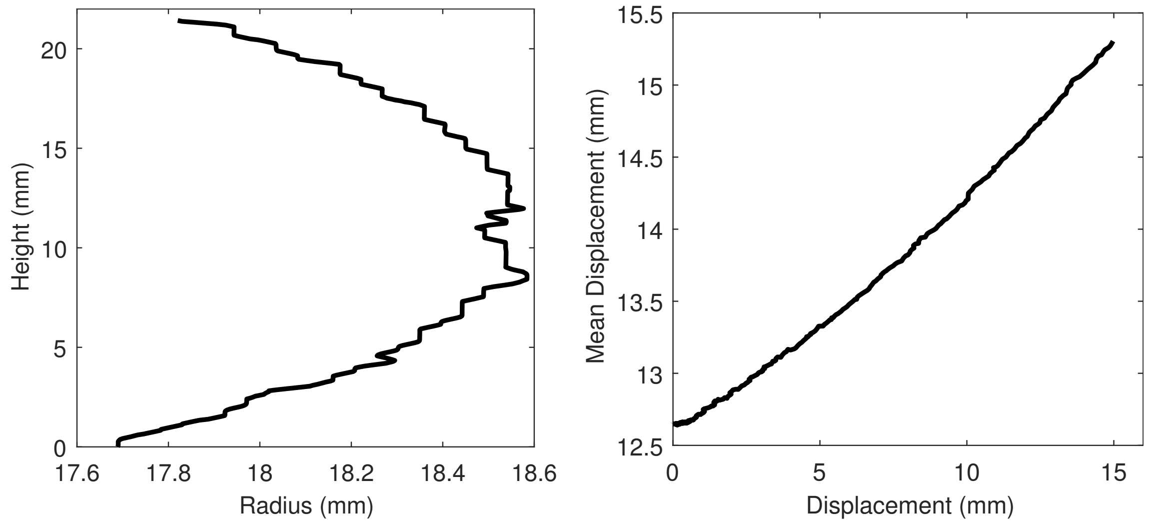

(a) Radius-Height (Barreled contour) (b) Mean Diameter-Displacement

Figure 3.1: Two potential barreling related datasets evaluated for use in Compcam. Both plots are generated from real experimental material behavior.

amount of profile data remaining at the end of the test was very limited. Finally, this metric was sensitive to ensuring the FE model and experiment were loaded to the exact same vertical deformation. It was found that varying the deformation imposed on the FE model by less than the uncertainty of Specs measurements could affect the model fit.

The metric that was adopted for final use was the mean deformed diameter of the specimen with respect to its vertical displacement. This metric had several advantages over comparing the final deformed radial profile. First, matching the entire history of radial deformation presents a more challenging metric for the optimization algorithm and the constitutive model. Second, because the deformed radial profile is averaged at each time of measurement, issues such as lack of profile data and measurement noise are mitigated. Finally, it was found that this metric was much less sensitive to the minor variations between the initial diameter and height of the FE model as well as the final amount of deformation imposed on the specimen.

The FE model used in this work was simple from a geometric perspective. The model consisted of a two-dimensional, axisymmetrical representation of a cold upsetting test, with two rigid platens compressing a deformable specimen, as shown in Figure 3.2. Friction between the platens and specimen was accounted for using a single parameter friction model at the interface between platen and specimen. The specimen had a

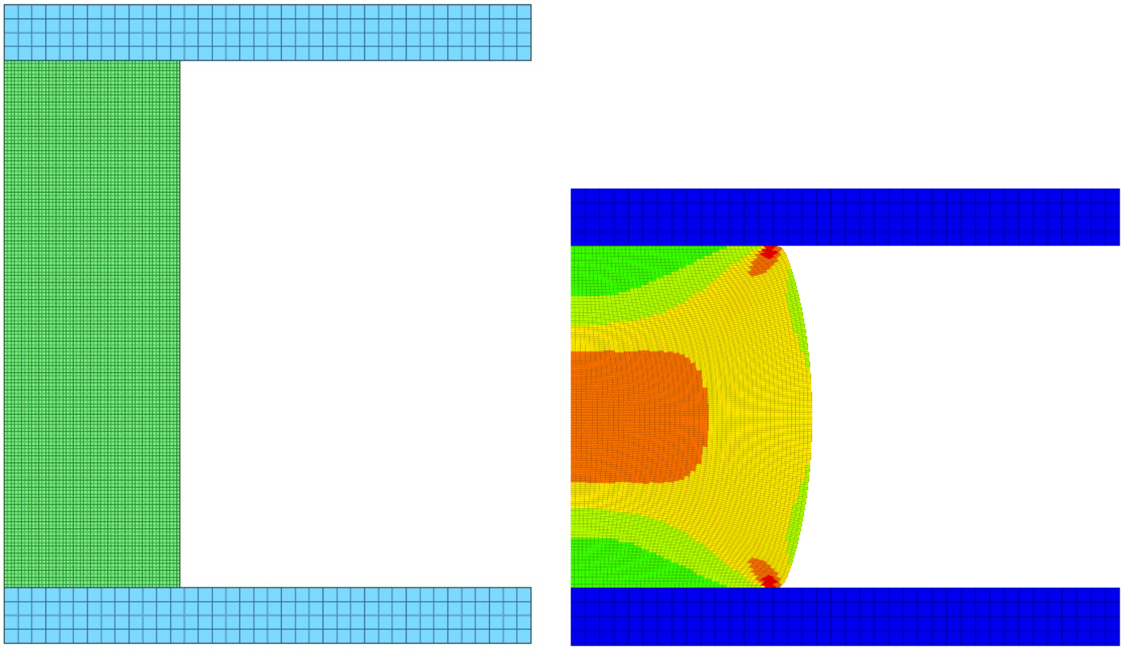

(a) FE mesh Geometry

(b) Example von Mises stress distribution and the deformed model

Figure 3.2: FE model used by COMPCAM

uniform mesh size of 0.25 mm with a larger mesh size applied to the rigid platens. In total, the model consisted of approximately 10,000 elements.

The commercial hydrocode Ls-Dyna R9.1.0 was selected as the solver for this work owing to its ability to model large deformation, robust contact algorithms, and large library of built-in material models. To load the specimen, the upper platen was held fixed while the displacement of the lower platen was controlled to load the specimen. Displacement control was selected for this work due to its innate stability with both implicit and explicit time integration routines. It is important to note that this does break with experimental testing, wherein load control was utilized. However, the use of displacement control has been used in literature to successfully model load controlled phenomena (Felling and Doman, 2018).

Two time integration schemes were utilized in this work. This was due to how certain built-in material models were programmed in Ls-Dyna. Implicit time integration was used when fitting the isotropic linear plasticity model and the Swift hardening law. Implicit time integration is the preferred technique when modeling quasi-static processes such as the cold upsetting technique as the timestep can be much bigger than explicit time integration (LSTC, 2017b).

While implicit time integration is the preferred method, many material models in Ls-Dyna are not available for use in implicit simulations. This is because material models used in implicit simulations require different stress integration techniques to accommodate the large time steps. As such, explicit time integration was used when fitting parameters to the GTN and Johnson-Cook models. The major disadvantage of using explicit time integration for the modeling of quasi-static processes such as the cold upsetting test is runtime. The timestep of an explicit model is determined by the Courant criterion, which specifies the timestep must be smaller than the time required for an elastic wave to propagate through the smallest element to guarantee stability. As this is a function of element size, material density, and Young's modulus, the Courant timestep for this work would have been extremely small, forcing the simulation to run for weeks to replicate the experiment.

To alleviate runtime issues, time and mass scaling were applied. The application of time scaling meant the load was applied in a fraction of the time needed for the experiment. This was deemed acceptable as none of the models used in this work had strain rate effects or had their strain rate effects disabled. Mass scaling was also applied to reduce runtime by artificially increasing the mass of all components. Mass scaling can be dangerous to use in simulations which rely on inertial effects as the added mass results in increased energy in the system. This can lead to unrealistic stresses, non-physical oscillations in the FE model's energy, and the propagation of elastic waves in the FE model which should not exist. However, the FE models used in this work ran stably with mass scaling without measurable numeric artifacts or the need for dampening to eliminate non-physical vibrations.

Force-displacement data was extracted from the FE model using the contact force between the platen and specimen and by tracking the displacement of the controlled platen. Measurements pertaining to the deformed radial profile of the specimen were done by extracting the displacement of all nodes along the outer edge of the specimen. The coordinates of these nodes could be used to provide the deformed radial profile directly or could be averaged to determine the mean deformed radius at each timestep. Data extraction was the same for implicit or explicit time integration.

In order to perform optimization, an error metric was required to compare the fit of the FE model against experimental data. For this work, the coefficient of determination or R-squared value, given by (3.1) was adopted for two reasons. First, as the fit of the FE model against the experimental data improves, the value of the coefficient of determination approaches 1 from below. Second, the built-in scaling associated with the coefficient of determination negates the large difference in the magnitude between force measured in kilonewtons and displacement measured in millimeters. The downside of using the coefficient of determination as an error metric for this work is the coefficient of determination was developed for linear models. As such, it can struggle with non-linear data. Despite this, the coefficient of determination has been used successfully in literature, even with non-linear material models (Morrow et al., 2010).

$$R^2 = 1 - \frac{\sum(y_i - f_i)^2}{\sum(y_i - \bar{y})^2} \tag{3.1}$$

where y is the experimental response, f is the response of the FE model, and $\bar{y}$ is the mean of the experimental dataset.

Using two datasets resulted in the calculation of two coefficients of determinations. For optimization purposes, these two values were averaged to produce a single final value. Once again, the literature suggests that this is an appropriate method for IMM applications (Morrow et al., 2010). Further, to convert the coefficient of determination into a minimization problem, one minus the coefficient of determination was used instead. This meant that a perfect fit between the model and experiment approaches zero from above instead. This change was made as the optimization algorithm used in this work only worked on minimization problems.

MATLAB's 'fmincon', a quasi-Newton, interior-point algorithm (MathWorks Inc., 2017a) was used to perform all optimization in COMPCAM. It is important to note that this is a local optimizer, and as such, can lead to issues such as local minima. It also requires the user to specify an initial condition. The selection of an initial condition can affect how long the optimizer takes to solve a problem, as an initial condition close to the optimum of the problem will allow the algorithm to converge much faster than an initial condition much further away.

The inputs to the optimization algorithm were the parameters for the constitutive model of interest and the coefficient of friction between the specimen and platens. Bounds were placed on each input parameter to ensure the optimization algorithm converged a realistic final parameter set and to ensure the stability of the FE model. Further, linear inequality constraints were placed on some parameters to ensure realistic results and a stable FE model. Finally, all input parameters were scaled from their input bounds to [0,1]. Recommended by Forrester et al. (2008), scaling eliminated issues associated with the large variation in magnitudes between input parameters. This can be exemplified by examining yield strength, generally measured in hundreds of megapascals, and Poisson's ratio, generally around 0.3. The optimization algorithm, which lacks the real-world context the researcher has, sees two parameters which are at least eight orders of magnitude apart. This scaling technique allowed the optimization algorithm to converge to a final answer faster without compromising the final parameter set.

The operation of Compcam is summarized graphically in Figure 3.3. Experimental tests are run, using the cold upsetting test exclusively in this work, to garner data about material behavior. The two experimental datasets used for model fitting are extracted. An FE model replicating the experimental test and assigned the constitutive model of interest is then executed with arbitrary input parameters. The experimental and computational responses are then compared and fit score computed. If the fit score falls below a pre-defined termination tolerance, indicating a good fit between experiment and the FE model, Compcam terminates. Otherwise, the local optimization algorithm computes parameters for the next iteration. Because 'fmincon' is a gradient-based algorithm, the FE model must be evaluated repeatedly by the optimization algorithm to determine a gradient to compute the next set of parameters. The new set of parameters is fed into the FE model and the cycle continues until the fit score falls within the termination criteria.

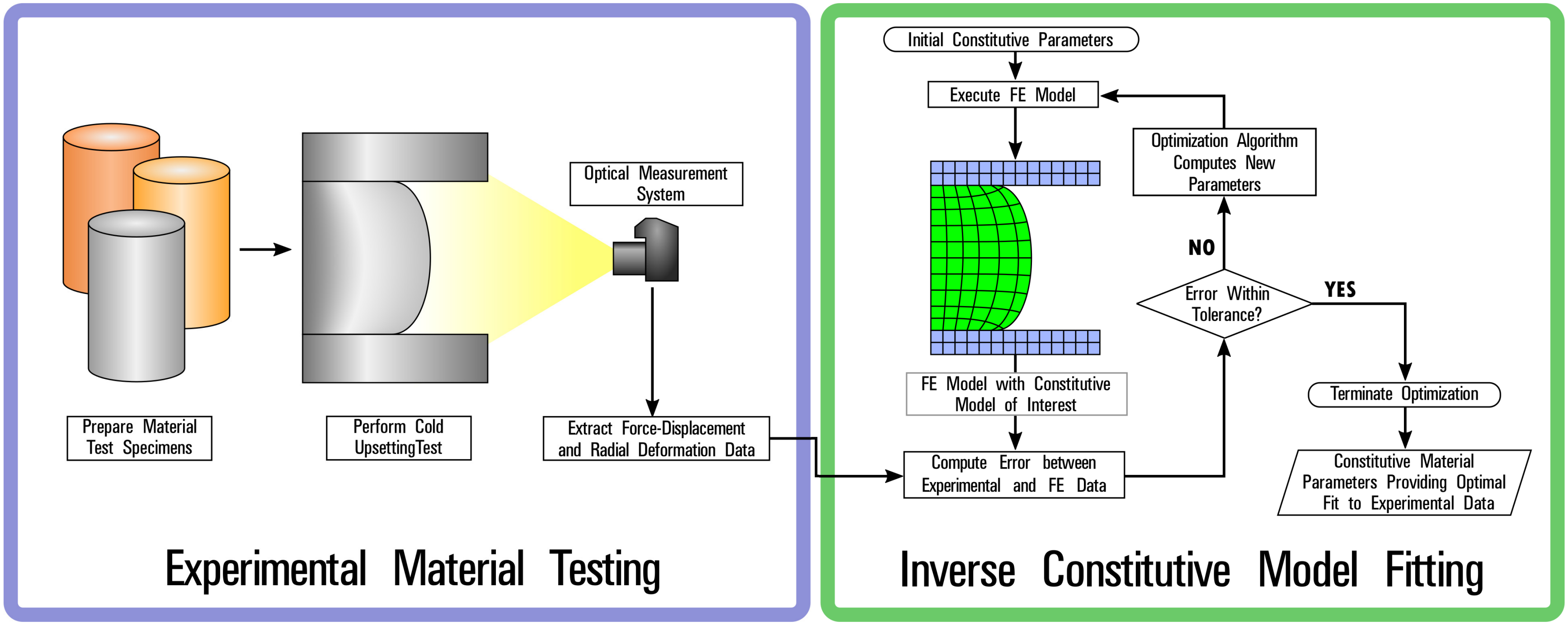

Figure 3.3: A graphical depiction of COMPCAM's operation..

3.2 DEAD

Optical densitometry is the process of measuring density gradients which develop within a specimen using non-contact, optical methods. Unlike other density mapping methods such as hardness testing, optical densitometry is not destructive to the polished specimen. Optical densitometry works by measuring the degree of porosity of a specimen sectioned about its midplane. By relating this degree of porosity to the amount of non-porous material in the specimen, relative density can be computed. It is important to note that this methodology does make the assumption that porosity is the sole contributor to a specimen being not being fully dense and the porosity in the measured plane is representative of the full specimen.

Prior to performing optical densitometry, regardless of the tool used, the specimen in questions must be prepared. First, the bulk density of the specimen must be measured using traditional means, such as the Archimedes methods laid out by MPIF standards (Metal Powder Industries Federation, 2010a). Bulk relative density is used to calibrate image processing during optical densitometry. After bulk density measurements, the specimen is sectioned about its midplane and polished to a mirror finish using appropriate polishing techniques for the material in question. The specimen is not be etched, as optical density methods rely on having a clear contrast between pores and base metal. However, specimens can be etched if desired after imaging has taken place without any additional prep work, which again sets it apart from other density mapping techniques.

Following polishing, the entire polished cross-section of the specimen is imaged using optical microscopy. Given the size of most specimens and the typical field of view of most microscopes, many individual images will be required to generate a tiled image of the specimen's cross section. In this work, a magnification of 50x was used, generating over 200 images for a single specimen. Image stitching is accomplished using Fiji (Schindelin et al., 2012). The final stitched image is used to measure the density gradients within a specimen's cross section.

The optical densitometry tool developed for this work, Dead, is based on an older tool successfully used for optical densitometry on green compacts (Beck, 2012; Selig, 2012). However, while the mapping resolution of that tool was limited to the number of images taken during microscopy, Dead allows the user to generate maps of almost infinitely variable resolution through a technique referred to in this work as element averaged downsampling.

Prior to performing downsampling, the tiled image must first be converted to black and white using binary thresholding. This step in the process is critical, as it ensures the accuracy of the density maps generated. The binary thresholding of the image must be calibrated to ensure the relative percentage of pores, which appear black against the white base metal, is the same as the relative bulk density of the specimen in question. At present, this step is accomplished by manual iteration, however, it could be modified in the future to use a simple, one-dimensional root finding algorithm.

Once the image is converted to black and white, element averaged downsampling takes place. Based on an element size inputted by the user, DEAD overlays a grid of uniformly sized elements onto the tiled image. DEAD then averages the value of all pixels within each element, generating a single value for the entire element. This not only provides the spatial average of the underlying image in a particular area, it drastically reduces the amount of data which needs to be processed. The grid of averaged elements becomes the final density map.

One as yet unresolved issue with DEAD is the appropriate selection of an element size. If the size of an element is too small, such as when the element size approaches the size of a pore in the specimen being mapped, the final map will appear disjointed and non-smooth, making it hard to interpret trends in the specimen's density gradients. Alternatively, if the element's size is too large, the final map lacks detail. Unlike other computational methods which rely on meshing, such as FE modeling, convergence studies are difficult to run as determining an appropriate final density map is primarily qualitative in nature. Because the density maps used in this work are being compared to FE models, the element size inputted into DEAD was selected to match FE models. While appropriate for this work, it does not resolve the issue of selecting an appropriate mesh size for general purpose density maps.

In addition to density mapping, DEAD has several other features which are currently in their infancy. The most impactful of these is a pore counting tool. Through the use of image segmentation techniques, individual pores can be isolated. Not only does this allow for the counting of individual pores, but this technique can also provide information about the size and morphology of each pore. At present, only the equivalent diameter of each pore is measured by DEAD, allowing for the generation of histograms showing pore size distribution. However, with relatively little additional work, information such as pore morphology could be incorporated.

Chapter 4

Experimental and Computational Methodology

This chapter is broken into two sections. The first details the experimental methods used to characterize each material. This includes sample geometry, preparation, and testing methods. The second section describes the computational methods used throughout this research, with particular focus on the specific implementation of the material models used in this work.

4.1 Experimental Methods

All experimental characterization of mechanical behavior in this work was conducted through the use of the compressive cold upsetting test and the friction ring test. However, due to minor variations between the procedures used for wrought metals and PM alloys and the densification behavior of the PM alloys, the procedures used for the two types of metals are discussed separately.

4.1.1 Ductile, Wrought Metals

Five ductile, wrought metals, shown in Table 4.1 with known material parameters, were used in this research. These metals were selected as the wide range of expected material responses would be a suitable means to validate the operation of COMPCAM. Furthermore, aluminum 2024-T351 and AISI 4340 were selected due to the large amount of material characterization work seen in the literature. AISI 4140 was selected as its elemental composition proved to be the closest, commercially available wrought alloy available to that of Stackpole powder blend SP6664. All wrought alloys used in this work underwent two forms of mechanical testing; cold upsetting to characterize mechanical behavior and friction ring testing to estimate the coefficient of friction between the material and pressing platens.

Material	Young's Modulus (GPa)	Density (g/cc)
Aluminum 2024-T351	70	2.7
C36000 brass	97	8.6
C11000 copper	115	8.9
AISI 4140 steel	205	7.8
AISI 4340 steel	200	7.8

Table 4.1: List of known material parameters for each alloy used

Five cold upsetting specimens were created for each material from one-inch nominal diameter, wrought, round bar stock. Specimens were cut to length from the rod stock then faced on a lathe to ensure the ends were flat and perpendicular to the cylindrical sides. The final height of all specimens was 50 mm, providing an aspect ratio of 2:1. Aspect ratio defined as the ratio of height to diameter for this work. The cylindrical surface was not altered from its wrought finish. The top and bottom faces of all specimens were finished using light file strokes and a non-woven abrasive to remove machining artifacts.

An Instron 600RD compressive test frame was used to carry out the cold upsetting of all test specimens. Ground, hardened, and unlubricated platens were used to apply the load. Each specimen was compressed to 75% engineering strain or until fracture at a constant load rate of 1.0 kN/s. Additionally, safety limits were imposed to ensure that at no point did a specimen exceed 2 GPa of engineering stress during testing. Force measurement was provided by the Instron test frame. SPECS was used to provide measurements of vertical deformation of the specimen as well as radial deformation. As a physical extensometer was not used, specimens could be taken all the way to fracture without interrupting a test to remove fragile equipment. The platens were cleaned between each test specimen of the same material using a non-woven abrasive pad. Between the testing of different materials, the platens were polished with 600 grit abrasive paper then cleaned with a small amount of acetone.

Six friction ring test specimens were created for each material. As laid out by Male and Cockcroft (1964), the specimens had an outer diameter of 19.1 mm (3/4”), an inner diameter of 9.5 mm (3/8”), and a height of 6.4 mm (1/4”). Rings were compressed by the Instron 600RD test frame at a constant load rate of 1.0 kN/s until the specimens were deformed to 75% their initial height. The same platen preparation done with all cold upsetting testing was done between friction ring tests. All specimen dimensions were then measured using a Mitutoyo CD-6” ASX digital caliper.

4.1.2 Sintered, Ferrous PM Alloys

As part of a research contract with Stackpole International, four ferrous PM alloys at three sintered densities each were provided to Dalhousie University for material characterization. These alloys are identified by the Stackpole designation 2140, 4420, 6664, and E2148. These codes do not follow MPIF or AISI alloy designation and as such, this report prepends “SP-” to all Stackpole designators to avoid confusion. The three sintered densities provided for each alloy were 6.8, 7.1, and 7.4 g/cc. Sintered density is indicated in the material code by appending two digits to represent density. For example, a specimen consisting of Stackpole alloy 2140 with a sintered density of 6.8 g/cc is given the code SP-2140-68.

Six specimens from each alloy-density combination were tested. These specimens were created through the use of dual action compaction. However, specifics of the process parameters and sintering procedures used to generate for specimens for each alloy and density were not provided by Stackpole. Dalhousie University simply received the final, sintered specimens. The ends of each specimen were faced to ensure the specimens were flat and perpendicular. While it was assumed that the sintered specimens would have appropriate faces without secondary machining, an initial investigation determined that the ends of each specimen were not flat. This warpage was likely caused by the sintering process, as the die-compacted green compact likely had flat and perpendicular faces upon ejection from the die.

All specimens had a nominal aspect ratio of 2:1. However, two specimen diameters were provided. All specimens made from SP-E2148 had a 25.8 mm nominal diameter while specimens from the remaining alloys had a nominal diameter of 28.8 mm. The height of each specimen was roughly constant at 50 mm.

As with the wrought metals, an Instron 600RD compressive test frame was used to conduct the cold upsetting. Unlubricated, hardened, and ground platens were used to load the specimen at a constant load rate of 1.00 kN/s. However, unlike the wrought metals which were loaded until failure or extreme deformation, all tests with sintered PM alloys were limited to a maximum engineering stress of 650 MPa. While the Instron 600RD has the ability to apply 3 MN of compressive force, fixturing used to test these specimens restricted the ability to apply loads which would exceed 650 MPa. This constraint introduced significant limitations on the ability to test these ferrous alloys. Once again, SPECS was used to provide measures of vertical deflection and radial deformation.

4.2 Computational Methods

This section discusses the specifics of the computational methods used in this work. The operation of Compcam is not discussed as it is presented in Section 3.1, but rather, the details pertinent to the specific implementation of constitutive material models used in Ls-Dyna. Also detailed in this section is how volume, and hence density, is computed from Specs data.

4.2.1 Optical Bulk Density Measurements

Bulk density measurements of a material can be conducted in two ways. The widely accepted industry practice follows MPIF standard #42 (Metal Powder Industries Federation, 2010b). This procedure uses Archimedes method to compute the density of a material by measuring the weight of a specimen in air and water. While this is an accurate and efficient means of measuring density, it cannot be conducted in-situ. This generally limits density measurements to initial and final density.

Specs provides the radial profile of a specimen throughout a test. This profile can be used to calculate the volume of a specimen by constructing a solid of revolution based on the radial profile and integrating to determine volume. In this work, the disk method was used to integrate that radial profile, as shown in (4.1), where $r(h)$ is the specimen's radius with respect to its height and H is the specimen's total height.

$$V = \int_0^H \pi r(h)^2 \, dh \tag{4.1}$$

Changes in volume, based on the initial volume of the test specimen, correlate directly to changes in density and can provide a measure of bulk relative density, as shown by (4.2). As a result, Specs can be used to measure the bulk densification of a material with respect to the vertical strain imposed on the specimen without pausing and unloaded a test specimen.

$$\rho = \rho_{initial} \frac{V_{initial}}{V} \tag{4.2}$$

4.2.2 Constitutive Material Models

As discussed in Section 2.2, this work does not investigate or develop any new constitutive material models. Instead, it uses pre-existing models implemented in Ls-Dyna R9.1.0. While Section 2.2 discusses these models from a theoretical perspective, this section details the specific material parameters which are used by Ls-Dyna and documents what specific parameters Compcam tunes. It is important to note at this juncture that this work limits itself to fitting plasticity parameters. Where possible, elastic parameters such as Young's modulus are held fixed at literature values, with the exception of Poisson's ratio. This is not the case in some material models, such as the Johnson-Cook model used in this work.

4.2.2.1 Swift Hardening Law

The Swift hardening law allows for the modeling of plastic behavior which is best described exponentially. Discussed in detail in Section 2.2.4.2, the model's flow rule is reproduced below.

$$\sigma_y = K(\epsilon_0 + \epsilon^p)^n \tag{2.13}$$

Implemented in Ls-Dyna as *MAT_POWER_LAW_PLASTICITY, the Swift hardening law had five free parameters to be tuned by Compcam. These parameters are listed below. Two parameters were held fixed, the material density ρ and Young's modulus E, as the initial density of the material is a known value and elastic parameters were not the subject of this work.

- Poisson's ratio, ν
- Hardening coefficient, K
- Hardening exponent, n
- Initial yield strength, σ_0 (converted by Ls-Dyna to initial yield strain ϵ_0)
- Coefficient of friction, μ

*MAT_POWER_LAW_PLASTICITY is compatible with Ls-Dyna's implicit solvers, which allowed the FE model running this constitutive model to be solved in approximately 30 seconds. While the Swift hardening law can model linear plastic behavior as the value of n approaches 1, FE models in this work which used *MAT_POWER_LAW_PLASTICITY exhibited numeric instabilities at large values of n. As such, an additional constitutive model was required to model linear plastic behavior. Further, because this constitutive model uses a von Mises yield surface, it is incapable of modeling densification behavior.

4.2.2.2 Isotropic Linear Plasticity

The isotropic linear plasticity model was used in this work owing to the instabilities associated with the Swift hardening law discussed previously. While this model is discussed in detail in Section 2.2.4.1, the flow rule for the linear plasticity model is repeated below.

$$\sigma_y = \sigma_0 + E_p \epsilon^p \tag{2.12}$$

Implemented in LS-DYNA as *MAT_PLASTIC_KINEMATIC, this material model has the capacity to model both isotropic and kinematic hardening effects by altering the parameter β. To limit the model to isotropic plasticity only, β was held fixed at 1.0. As with the Swift hardening law, material density and Young's modulus were held fixed for this material model. The four tunable parameters used by *MAT_PLASTIC_KINEMATIC are listed below.

- Poisson's ratio, ν
- Plastic tangent modulus, E_{tan}
- Initial yield strength, σ_0.
- Coefficient of friction, μ

As with *MAT_POWER_LAW_PLASTICITY, *MAT_PLASTIC_KINEMATIC is compatible with LS-DYNA's implicit solvers. As such, FE models using *MAT_PLASTIC_KINEMATIC had a runtime of 30 seconds, comparable to the Swift hardening law. Like the Swift law, *MAT_PLASTIC_KINEMATIC used a von Mises yield surface, making this constitutive model unable to account for material densification.

4.2.3 Gurson-Tveergard-Needleman Model

The GTN model attempts to model the nucleation, growth, coalescence, and collapse of pores in a material's microstructure through the use of a specialized yield surface. While the GTN model's derivation is presented in detail in Section 2.2.4.4, its yield surface model is repeated below.

$$\Phi = \frac{\sigma_v m^2}{\sigma_y^2} + 2q_1 f^* \cosh\left(\frac{3q_2\sigma_H}{2\sigma_y}\right) - 1 - (q_1 f^*)^2 = 0 \tag{2.18}$$

Available in Ls-Dyna as *MAT_GURSON, this particular implementation of the GTN model has several features not commonly seen in other GTN implementations. One of the most prominent features is the option to select from several different hardening rules such as perfectly plastic, linear hardening, and a very basic power law hardening rule. Unlike the Swift hardening law or Johnson-Cook model, the power law hardening rule used by *MAT_GURSON only has one input parameter, the hardening factor N. The hardening coefficient is a function of yield strength and Young's modulus, as shown by (4.3). By limiting the hardening rule's input to one parameter, the GTN model cannot match the flexibility of other models when predicting plastic stress-strain behavior. *MAT_GURSON's power law hardening rule was used exclusively in this work.

$$\sigma_y = \sigma_0 \left(\frac{\epsilon^p + \sigma_0/E}{\sigma_0/E}\right)^{\left(\frac{1}{N}\right)} \tag{4.3}$$

The GTN model used in Ls-Dyna has a large number of input parameters. However, several input parameters could be held fixed or nulled out based on the circumstances of this work. For example, parameters relating to the material's initial and theoretical full density could be held fixed based on experimental measurements. A list of parameters held fixed in this work is given below.

- Full density of the material was fixed at 7.8 g/cc.
- Gurson parameters q_1 and q_2 were held at 1.5 and 1.0 respectively, as recommended by the overwhelming majority of literature on the GTN model (Malcher et al., 2012; Mirajkar et al., 2011; Slimane et al., 2015).

- Initial void fraction f_0 was held at an appropriate value based on initial sintered density. Fixed values of f_0 were 0.128, 0.090, and 0.051 for sintered densities of 6.8, 7.1, and 7.4 g/cc, respectively.
- Failure void volume fraction f_f, which controls element deletion was nulled out with a value of 1.0.
- Void collapse was enabled by setting the void growth flag, VGTYP, to 2.

By holding the above parameters fixed, *MAT_GURSON's large number of input parameters was reduced to nine. These parameters are listed below. Unlike the Swift or linear plasticity model, Young's modulus in *MAT_GURSON was selected as a tunable parameter for this work. While only plastic behavior was fit, Young's modulus needed to be tunable as it had an effect on the model's power law hardening rule.

- Young's modulus, E
- Poisson's ratio, ν
- Coefficient of friction, μ
- Initial yield strength, σ_0 (denoted in Ls-Dyna as SIGY)
- Hardening factor, N
- Critical void fraction, f_c
- Void fraction of nucleation, f_N
- Mean nucleation strain, ϵ_N
- Standard deviation of mean nucleation strain, s_N

Several challenges were encountered when fitting *MAT_GURSON. The largest of which was encountered in the initial modeling approach. Literature from LSTC, the developer of Ls-Dyna, stated that *MAT_GURSON was available for implicit time integration when used with solid elements (LSTC, 2017a). As implicit analysis is the most appropriate solution method for modeling quasi-static situations, an eight-symmetric solid model was created.

However, all attempts to use MAT_GURSON with implicit simulations were plagued by serious stability issues. These issues ranged from impossible material behavior such as negative void fractions to spontaneous element deletion. An investigation into the cause of these instabilities indicated that the plasticity algorithm implemented in *MAT_GURSON was likely to blame. It is the author's suspicion that despite being advertised as available for implicit analysis, the plasticity algorithms were not modified to account for the significantly different mechanics of implicit analysis compared to explicit analysis. This suspicion was backed up by the fact that the model's stability improved when the implicit timestep was forced to be very small. Such a small timestep made the use of implicit analysis unfeasible, as the simulation would run for days.

Having exhausted options to make an implicit model run execute successfully, the decision was made to switch to an explicit model, as *MAT_GURSON was initially developed for and proven to work with explicit analysis. This resolved the majority of stability issues. Further, switching to an explicit model allowed for the use of axisymmetric elements, reducing the size and complexity of the FE model. However, the use of explicit analysis increased the runtime of a single model to many hours, making it impossible to use with COMPCAM. As described in Section 3.1, time and mass scaling were applied to reduce runtime, with significant care taken to ensure stable and realistic outputs.

Unlike the implicit FE models used by the Swift and linear plasticity models, the explicit FE model used by the GTN model took approximately five minutes to solve per evaluation. That, in concert with the nine free parameters which COMPCAM was attempting to optimize, lead to much longer COMPCAM runtimes. While COMPCAM could determine optimal Swift and linear plasticity model parameters within one or two hours on average, determination of GTN parameters took between 18 and 24 hours, depending on the material and the initial input guess. Despite the lengthy runtime, this is still an improvement on traditional fitting methodology as no user interaction was needed during those hours.

4.2.3.1 Johnson-Cook Model with a Bi-linear Equation of State

The Johnson-Cook model allows for the modeling of strain rate and temperature dependent plasticity behavior. While the full definition is given in Section 2.2.4.3, the flow rule is repeated below.

$$\sigma_Y = (A + B\epsilon^{pn})(1 + c \ln \dot{\epsilon})(1 - T^{*m}) \tag{2.14}$$

The full Johnson-Cook model with damage modeling is available in LS-DYNA as *MAT_JOHNSON_COOK. However, for this research, only the power law hardening portion of the Johnson-Cook model was used. Rate, thermal, and damage effects were nulled out, leaving only the hardening rule shown in (4.4).

$$\sigma_y(\epsilon_p) = A + B\epsilon_p^n \tag{4.4}$$

With the removal of rate and thermal effects, the Johnson-Cook flow rule becomes very similar to the Swift hardening law. However, *MAT_JOHNSON_COOK affords much greater flexibility by allowing a researcher to specify an equation of state. Two equations of state were selected for this work, and as such, the two variants of the Johnson-Cook model are referred to by their equation of state for clarity.

The first variant of the Johnson-Cook model utilized EOS_TABULATED_COMPACTION, which allows one to input a piecewise linear curve representing the material's hydrostatic pressure-volumetric strain behavior. This equation of state is also capable of altering bulk modulus behavior to allow the constitutive model to have different elastic properties depending on the degree of compaction. This feature was not used, however, as unloading and hysteretic data were not available. *EOS_TABULATED_COMPACTION works by specifying individual control points on a hydrostatic pressure-volumetric strain curve, with linear interpolation and extrapolation used to determine values between and outside the points specified.

Despite a seemingly straightforward mode of operation, implementation of this equation of state proved to be perplexing due to minimal and incorrect documentation. LSTC provided the figure reproduced in Figure 4.1a to describe a bi-linear curve (LSTC, 2017a). Based on the documentation, it is implied that *EOS_TABULATED_COMPACTION automatically enforces a point at (0,0), with the first user-defined point $(\epsilon_{V,1}, C_1)$ being used to define the elastic properties of the material.

However, after encountering errors attempting to implement *EOS_TABULATED_COMPACTION in the manner indicated in the documentation, an investigation discovered that this equation of state actually operated in a very different fashion. It turned out *EOS_TABULATED_COMPACTION did not enforce a point at (0,0) and was only active during plastic deformation. The real mode of operation is depicted in Figure 4.1b. All control points needed to be explicitly defined by the user, with the

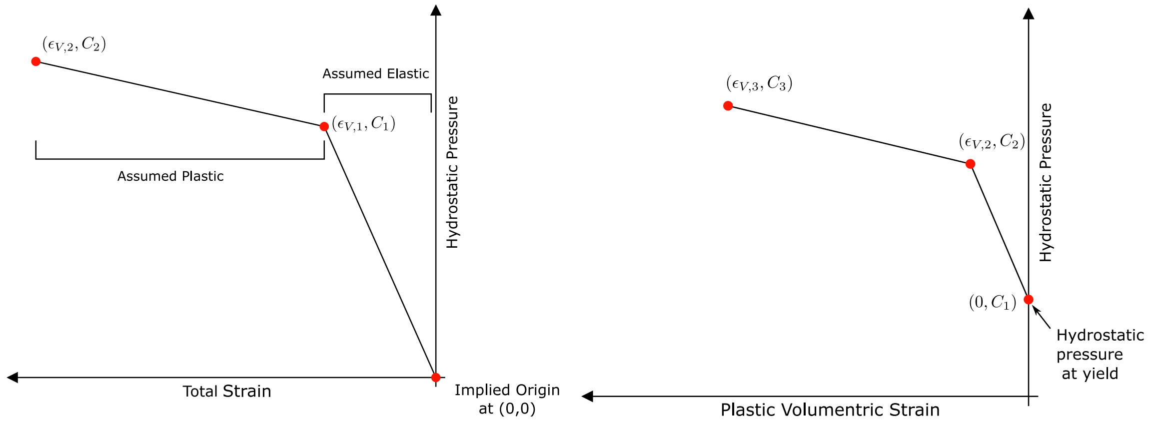

(a) Description of a bi-linear curve as reproduced from LS-DYNA documentation (LSTC, 2017a).

(b) Actual description of a bi-linear curve determined by investigation.

Figure 4.1: Variance between documented and actual operation of the equation of state used in this work.

first point being placed at zero plastic volumetric strain and the hydrostatic pressure of the material at yield.

The impact of this discovery is significant. While a bi-linear curve implemented based on LSTC documentation (LSTC, 2017a) would allow one to model the linear elastic behavior of a material and a linear pressure-volume behavior during plastic deformation, a bi-linear curve based on LS-DYNA's actual operation is modeling a more complex plastic behavior and is not active during elastic deformation. Further, parameters between the two modes of operation are not generally transferable.

While *EOS_TABULATED_COMPACTION has the ability to model plastic pressure-volume behavior using up to eight control points, only a three are used in this research, producing a bi-linear curve. As such, this implementation of the Johnson-Cook model will be henceforth referred to as the bi-linear variant. Early stage testing showed that three control points afforded greater flexibility than a linear equation of state while being more stable and determining parameters significantly faster than a three-part linear curve. The ten free parameters fit for the bi-linear variant of the Johnson-Cook model are as follows.

- Shear modulus, G
- Hardening constant, A
- Hardening coefficient, B

- Hardening exponent, n
- Volumetric strains $\epsilon_{V,2}$ and $\epsilon_{V,3}$. $\epsilon_{V,1}$ fixed at zero.
- Hydrostatic pressures, C_1, C_2 and C_3, corresponding to the volumetric strains above.
- Coefficient of friction, μ

4.2.3.2 Johnson-Cook Model with $P - \alpha$ Compaction Curve

Using the same reduced Johnson-Cook constitutive model described in Section 4.2.3.1, a $P-\alpha$ compaction curve is used here instead of the bi-linear curve to control pressure-volume behavior. The main advantage of this equation of state over the piecewise linear curve is the ability for this equation of state to cap porosity at full density. This prevents the equation of state from modeling a density greater than physically possible. The volumetric response of the material stiffens dramatically as the material approaches full density, allowing the equation of state to behave more like a pressure-independent material model.

For completeness, the equation relating porosity and pressure is reiterated below. Further, this particular equation of state uses a linear Hugoniot curve to compute hydrostatic pressure as a function of density. It is important to note that porosity α is not the same as material density ρ, although they are closely related.

$$\alpha = 1 + (\alpha_0 - 1)\left(\frac{P_s - P}{P_s - P_e}\right)^N \tag{2.17}$$

$$P_H(\alpha, \rho) = \left(\frac{\alpha\rho}{\alpha_0\rho_0} - 1\right) \tag{4.5}$$

Another advantage of the $P - \alpha$ compaction curve the fewer fitted parameters. Furthermore, unlike the control points used by the bi-linear variant, the parameters used by the $P - \alpha$ curve have a more physical meaning. The eight free parameters fitted for the reduced $P - \alpha$ variant of the Johnson-Cook model are listed below.

- Shear modulus, G
- Hardening constant, A
- Hardening coefficient, B

- Hardening exponent, n
- Pressure at elastic limit/yield point, P_e
- Pressure at full density threshold, P_s
- Exponential densification factor, N
- Coefficient of friction, μ

Chapter 5

Investigation of Wrought, Ductile Metals

This chapter deals with the investigation of five wrought metals, specifically aluminum 2024-T351, C36000 brass, C11000 copper, AISI 4140 steel, and AISI 4340 steel. This work was undertaken as a means to test the performance of the experimental setup and COMPCAM prior to moving to the more challenging PM alloys discussed in Chapter 6. This chapter includes a discussion of the experimental results of the cold upsetting tests including plastic behavior and material failure, the final fits as determined by COMPCAM, and discussions regarding experimental and numerical coefficients of friction and COMPCAM's limitations.

5.1 Experimental Results

The experimental testing regime of each ductile alloy used in this work consisted of cold upsetting tests to characterize the plastic behavior of each material and friction ring tests to estimate the coefficient of friction between each material and the platens used by the compressive test frame. The results of each test are presented and discussed below.

5.1.1 Results of Cold Upsetting

As noted in Section 2.1, the use of SPECS allows a researcher to measure the deformed barreled contour of a specimen throughout a test. This allows one to calculate true stress based on the actual cross-sectional area of the specimen at any given time in the experiment. Contrasted with traditional methods, which include approximating the deformed specimen diameter by assuming a constant volume throughout the test (Bao, 2003), the use of SPECS removes the need to make such assumptions, which is particularly valuable in materials which may change volume or density throughout a test. In fact, the only assumption that needs to be made to use SPECS is that the deformation of the specimen is axisymmetric in nature.

For all stress calculations used in this work, the mean deformed diameter was used to calculate stress. Work by Felling and Doman (2018) investigated the use of both the minimum and maximum deformed diameter to calculate true stress. They found that using the minimum diameter slightly increased the measured stress, while the maximum diameter slightly decreased stress. However, in both cases, the deviation was very low. To that end, Felling and Doman found that the mean diameter gave a good measurement of bulk stress which agreed well with other datasets from the literature.

True stress-strain curves for all five ductile metals tested are given in Figure 5.1. Each curve given in Figure 5.1 is constructed from the stress-strain curves of each of the five test specimens used for each material. As one would expect, each alloy had unique deformation behavior.

The deformation behavior of aluminum 2024-T351 is remarkable given the degree of material softening at large deformation and prior to fracture. This softening is likely not a behavior of the bulk material itself, but rather it likely the accumulation of

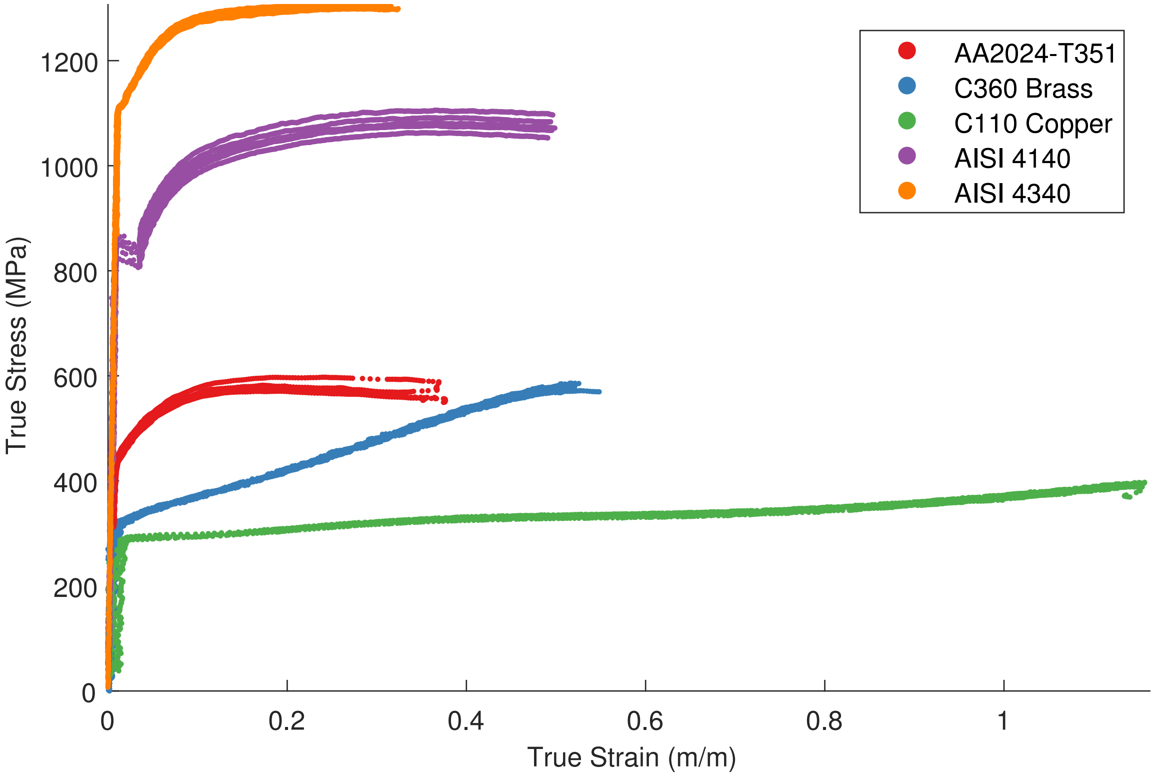

Figure 5.1: Experimental true plastic stress-strain curves for all three wrought metals tested.

material damage through void nucleation and growth within the specimen. This void growth is likely a direct contributor to the fracture of this material. Scanning electron microscopy was attempted on the fracture surface of the aluminum specimens, however, due to the mode of failure the fracture surface was smeared. As such, no definitive conclusions can be drawn as to the exact cause of fracture and the softening behavior seen in Figure 5.1.

Both copper based alloys, C36000 brass and C11000 copper, exhibited linear plastic deformation behavior, although the stiffness of each material was markedly different. Brass, which not only exhibited a higher yield point, also displayed much stiffer plastic deformation behavior. Furthermore, one can note a slight softening trend just prior to fracture. Similar to aluminum, it is likely this softening is a result of void nucleation and growth. However, scanning electron microscopy of the fracture surface of the brass specimens was inconclusive as the fracture surface of these specimens was also smeared. Copper, on the other hand, exhibited a less stiff plastic response, lower yield strength, and did not fracture. The increased yield strength and decreased ductility of brass compared to copper is a direct result of the addition of alloying ingredients.

Both AISI 4140 and AISI 4340 specimens exhibited high yield strengths. Later examination revealed that the rod stock used to make the specimens for both materials was quenched and tempered, which contributed to their high yield strength. As a result of their high strength and somewhat surprising ductility, testing was halted when the load imparted on the specimens reached an engineering stress of 2 GPa for safety reasons. This is in contrast to the 75% engineering strain imparted in copper and the fracture experienced by both aluminum and brass. Nonetheless, both steel alloys exhibited similar plastic behavior including a double yield point and hardening behavior which grew less stiff at large deformation. However, the double yield point of AISI 4140 was significantly more pronounced than that of 4340.

Of the five metals tested, only aluminum and brass underwent ductile fracture. This occurred at true strains of 36% and 52% for aluminum and brass, respectively. The fracture plane of each specimen, shown in Figure 5.2, is consistent with the region of maximum shear stress which develops within each specimen during cold upsetting (Narayan and Rajeshkannan, 2012). However, the actual fracture surface of each

Figure 5.2: Fractured aluminum (left) and the two halves of a fractured brass specimen.

metal was different. Fractured aluminum specimens exhibited a flat fracture surface. However, in the case of all specimens, the two fractured halves cold welded back together after fracture. Unlike aluminum, brass specimens did not cold weld together after fracture. Furthermore, the fracture surface of brass was conic in nature, matching cone of maximum stress which developed in each specimen more closely.

As previously noted, the copper and both steel alloys did not undergo engineering fracture. Copper was pancaked to 75% engineering strain while material testing of both steel alloys was limited to 2 GPa . It is interesting to note that all three metals did slough off particulate from their outer surface. This is shown for the case of AISI4140 in Figure 5.3. Despite the lower deformation imparted on them, the steel specimens displayed this behavior more than the copper. This is likely due to the hardened nature of the specimens. The outer surface of a quenched and tempered specimens would have decreased ductility compared to the inner material. As a result, the material on the outermost surface could undergo failure without leading to global specimen failure. In the case of copper, this sloughing behavior is likely a result of the extreme stress state and deformation imparted to the outer surface of the material.

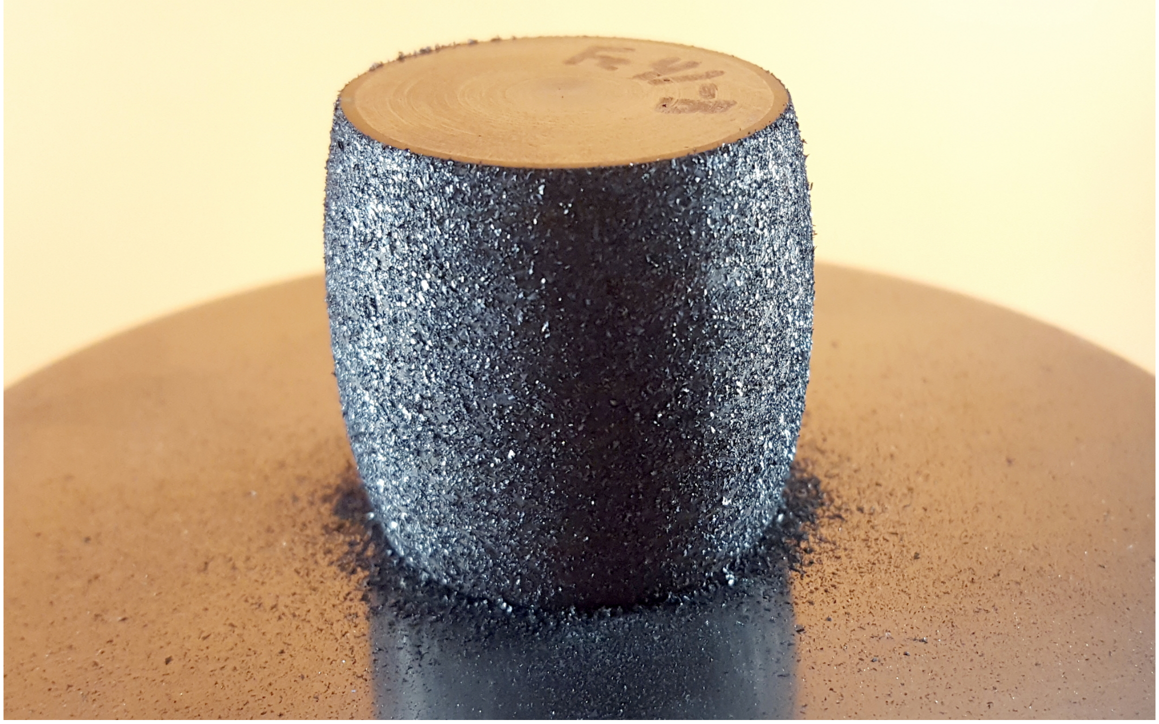

Figure 5.3: An AISI 4140 specimen directly after testing. Note the particulate matter on the platen and adhering to the specimen.

5.1.2 Results of Friction Ring Tests

As noted in Section 4.1.1, six friction ring tests per material were carried out, each deformed to 25% the ring's initial height before spring back. The average coefficient of friction as well as the 95% confidence interval (calculated using Student's T-test), are given in Table 5.1. To reiterate, the coefficients presented here are for dry, lubricated contact between the ground and hardened steel platens and the test specimen.

Table 5.1: Coefficients of friction for each material as determined by the friction ring test

Material	Mean Coefficient	95% Confidence Interval
AA2024-T351	0.1431	[0.1340, 0.1499]
C36000	0.07902	[0.07134, 0.08470]
C11000	0.07190	[0.07035, 0.07346]
AISI 4140	0.05892	[0.05566, 0.06218]
AISI 4340	0.07938	[0.07690, 0.08186]

The results of the friction ring test reveal an interesting distribution in values for the coefficient of friction for each material. The coefficient of friction for aluminum 2024-T351 is the greatest by a large margin. As one might expect, the frictional coefficients for copper and brass are low and somewhat similar in nature. This is one of the reasons these materials are used for bushings. The most interesting result is the disparity in coefficient of friction calculated for AISI 4140 and AISI 4340 compared to the remaining metals. The coefficient of friction for AISI 4140 is statistically lower (using a one-way ANOVA test) than the coefficient for AISI 4340. Furthermore, the coefficient for AISI 4140 is even lower than the copper and brass. It is not known why the coefficient of friction for AISI 4140 is so low.

5.1.3 Disparity in Aluminum 2024-T351 Data

Aluminum 2024-T351 was selected for this work owing to a large amount of published data on its plastic behavior. After testing, the stress-strain behavior of the aluminum tested in this work was compared to that of Bao (2003) and Felling and Doman (2018). It is important to note that both works used the cold upsetting test. Further, Felling and Doman (2018) also used SPECS. The true stress-strain curves from both works are shown with experimental data from this work in Figure 5.4. While the datasets

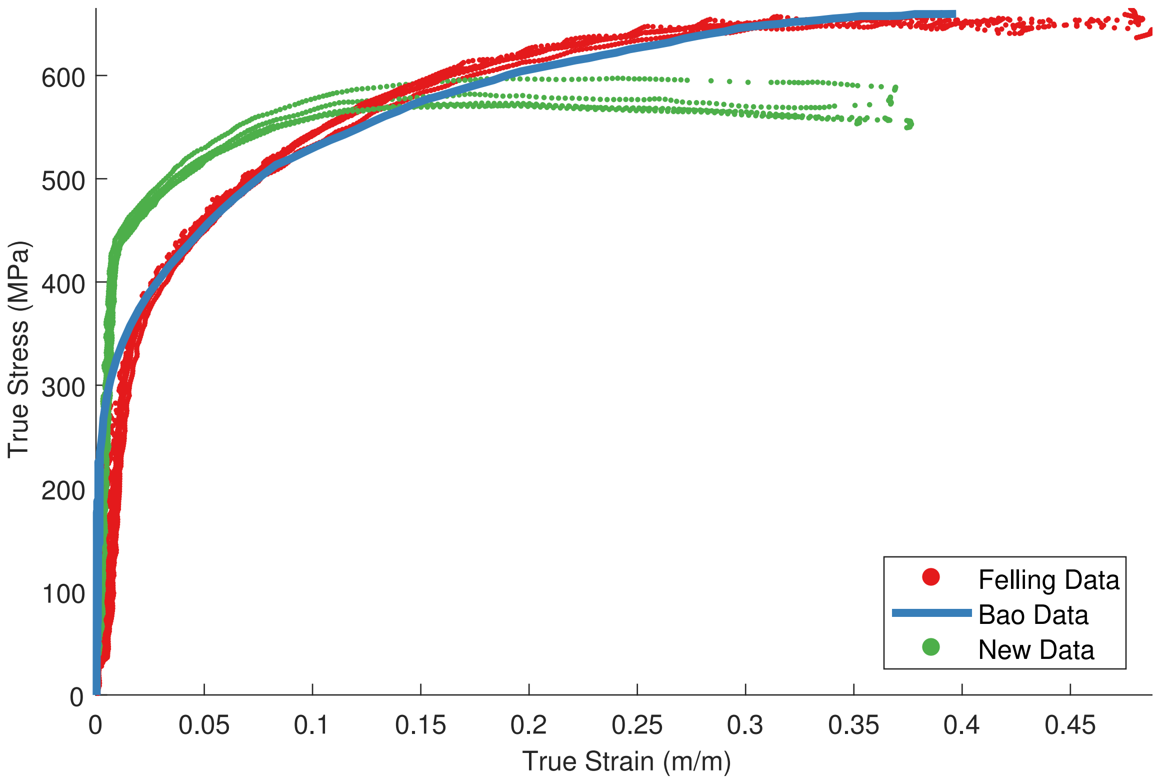

Figure 5.4: Experimental and literature data for 2024-T351. Literature data is from Bao (2003) and Felling and Doman (2018).

from Bao and Felling and Doman agree well, the stress-strain data from this work does not agree well at all. The material used in this work has a higher yield strength, lower ductility, and different plastic behavior.

To confirm that the material tested in this work was indeed aluminum 2024-T351, several material tests were undertaken. Energy-dispersive X-ray spectroscopy was performed on the material specimens from this work and the work of Felling and Doman to provide approximate elemental concentrations of Copper, Manganese, and Magnesium. The composition of these elements, in addition to the composition limits laid out by ASTM standard B211-12 (2012), are listed in Table 5.2. While there were differences between the two batches of material, both batches fall within the ASTM standard for 2024. To estimate whether the temper of the new batch was indeed T351, hardness testing was undertaken. The T351 temper is only required to have a minimum hardness of 66 HRB, with no upper bound on hardness specified by the standard. The batch of material used in this work had a hardness of 76 HRB, further showing that this batch of material did fulfill the minimum specifications laid out by ASTM. A literature view was undertaken to discover if other researchers have

Table 5.2: Partial elemental composition of two batches of AA2024-T351 with limits laid out by ASTM Standard B211-12

Material	Cu	Mn	Mg
ASTM Standard	[3.8, 4.9]	[0.3, 0.9]	[1.2, 1.8]
Felling & Doman	4.0	0.7	1.5
Current Work	4.2	0.5	1.4

reported a similarly high yield stress as measured in this work. While there was a significant variation in yield strength values reported in the literature with most being lower, there was at least one source which quoted a similarly high yield strength (Fratini et al., 2009).

The discrepancy in behavior must be a result of the small differences in composition and processing between the two batches tested. Further, it could be considered almost coincidental that the material used by Felling and Doman did match the behavior of Bao. The increased strength and decreased ductility seen in the material used in this work is likely a result of the increased copper concentration, which would increase promote the growth of precipitates.

This unexpected discovery of inter-batch variability in elemental composition yields a rather interesting conclusion for constitutive model fitting. The different plastic behaviors for the same nominal material shown in Figure 5.4 clearly require different sets of material parameters for a particular constitutive material model. This raises the question of whether one set of constitutive model parameters is actually valid for one material. If one is particularly concerned with the plastic behavior of the material, such as in the case of manufacturing process simulations or high-end modeling work, this result means that one has to refit constitutive model parameters for every batch of material, even if the simulation in question uses the same material in two different places, but from different batches.

This conclusion highlights the necessity of a tool like COMPCAM. If material characterization and fitting have to be performed on not just every different material, but every batch from every material, there is a decided need to accomplish characterization faster and cheaper than currently used methods. COMPCAM could be an ideal tool to fulfill those stringent requirements.

5.2 Constitutive Model Fitting

Fitting of constitutive material models to the five materials tested here is broken into to portions. First, the operation of COMPCAM is validated by fitting two simple, but very different constitutive models to all five alloys, which represent a range of material behaviors. The two models used in this portion are the Swift hardening rule and the isotropic linear plasticity model. The influence and sensitivity of tuning the coefficient of friction with constitutive material parameters are also explored here.

The second portion of this section uses COMPCAM to fit two more complex constitutive models, the GTN model and the $P-\alpha$ variant of the Johnson-Cook model. While the fitting of sintered PM alloys in Chapter 6 includes the bi-linear variant of the Johnson-Cook model, that constitutive model was not included for this work. Because these are wrought allows with little or no porosity, the bi-linear pressure-volume equation of state would not be appropriate. Furthermore, the numerical implementation of the bi-linear variant in LS-DYNA becomes unstable when one tries to force zero plastic volumetric deformation out of the bi-linear equation of state. The $P-\alpha$ variant has no problem accepting parameters to enforce little to no initial porosity.

5.2.1 COMPCAM Validation

Validation will explore the two different sets of responses used by COMPCAM to determine optimal material parameters, specifically force-displacement and mean radius-displacement. The goal of showing these responses is to examine what COMPCAM determines as optimal based on the information provided to it. The second set of responses which will be explored are the true stress-strain curves for each optimum constitutive model. As stress-strain behavior is not directly fitted, examination of this response will garner insight into how well COMPCAM can fit the actual material behavior from relatively unprocessed experimental data. The number of evaluations of the FE model for each material and model is not specified, as it was found that this number was extremely susceptible to the initial condition. However, on average both models used for validation required between 100 and 150 evaluations of the FE model. With a model runtime of approximately 30 seconds, this lead to an average COMPCAM runtime of around one to two hours.

Figures 5.5 to 5.9 show force-displacement and radius-displacement behavior for each material tested. These curves are overlaid with the responses of the best Swift hardening law and linear plasticity fit for each material. The characteristics of each model's fits are detailed for each material below. Tables 5.3 and 5.4 provide the final best parameters for each material model as well as the final R^2 for each fit. Recall that this R^2 value is average of the separate R^2 values for force-displacement and mean radius-displacement. Also included in Table 5.3 is the set of Swift hardening parameters determined by Felling and Doman. When contrasted with parameters determined for the different batch of material used in this work, one will note there is significant variation, further reinforcing the statements made in Section 5.1.3.

The plasticity behavior of aluminum 2024-T351 proved to be a good fit to the Swift hardening rule, as seen in Figure 5.5, with a decent agreement to material behavior at low deformation when looking at force-displacement data. The quality of the fit does decline at larger deformation as the Swift model does not have the ability to model material softening. The Swift model also showed a good fit to radius-displacement data. Comparing the coefficient of friction determined by COMPCAM in

Table 5.3: Optimal Swift hardening parameters for ductile metals determined by COMPCAM

Material	ν	K (MPa)	n	σ_y (MPa)	μ	R^2_{avg}
AA2024-T351	0.3087	662.6	0.0839	391.4	0.1456	0.9953
Felling & Doman	-	829.4	0.1960	-	0.1890	-
C36000 Brass	0.3004	717.9	0.4058	277.4	0.1418	0.9957
C11000 Copper	0.3078	279.4	0.3134	288.8	0.07091	0.9989
AISI 4140	0.3006	1324	0.2239	908.3	0.1595	0.9914
AISI 4340	0.3103	1498	0.3949	1198	0.1892	0.9802

Table 5.4: Optimal linear plasticity parameters for ductile metals determined by COMPCAM

Material	ν	σ_0 (MPa)	E_{tan} (MPa)	μ	R^2_{avg}
AA2024-T351	0.3040	446.4	553.6	0.1679	0.9400
C36000 Brass	0.3009	306.2	565.8	0.1393	0.9984
C11000 Copper	0.3093	295.9	59.98	0.1433	0.9969
AISI 4140	0.2743	921.0	619.3	0.07468	0.9750
AISI 4340	0.3039	1113	1116	0.1680	0.9802

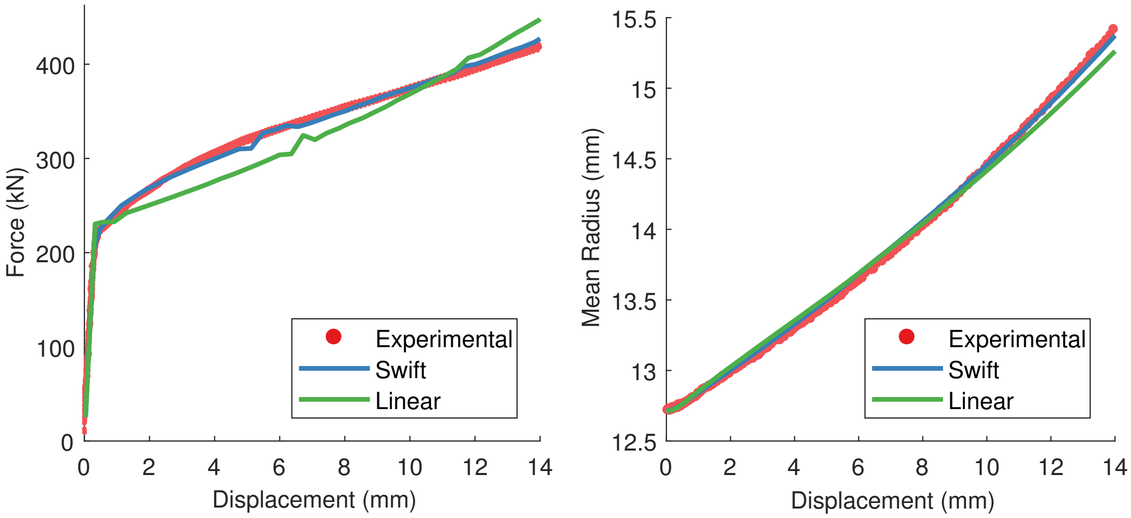

(a) Force-displacement (b) Mean radius-displacement

Figure 5.5: AA2024-T351 experimental and FEM results for optimal material parameter for Swift and linear hardening laws.

Table 5.3, one will note that a coefficient of friction of 0.1451 falls within the confidence interval presented in Table 5.1. Unsurprisingly, the linear plasticity model proved to be a very poor fit to aluminum, particularly when observing force-displacement data. Additionally, the coefficient of friction determined by Compcam falls outside the interval suggested by friction ring tests.

Both constitutive models proved to be a good fit to experimental force-displacement and radius-displacement data for brass, despite the variation in model formation. Experimental data and fits are shown in Figure 5.6. However, one will note the linear plasticity model does fit plastic behavior and yield strength slightly better. Interestingly, both set of parameters determined by Compcam suggests a coefficient of friction which is much greater than that suggested by friction ring tests.

Like brass, both constitutive models were good fits to copper's force-displacement and radius-displacement behavior, as shown by Figure 5.7. However, the linear plasticity model exhibited a slightly better fit to the yield strength and plastic behavior portrayed by force-displacement data and an overall slightly better fit to radius-displacement data. Despite this, the coefficient of friction determined for the Swift hardening rule (0.07091) falls within the experimental bounds suggested by friction ring testing while the coefficient fit to the linear plasticity model was significantly higher (0.1433).

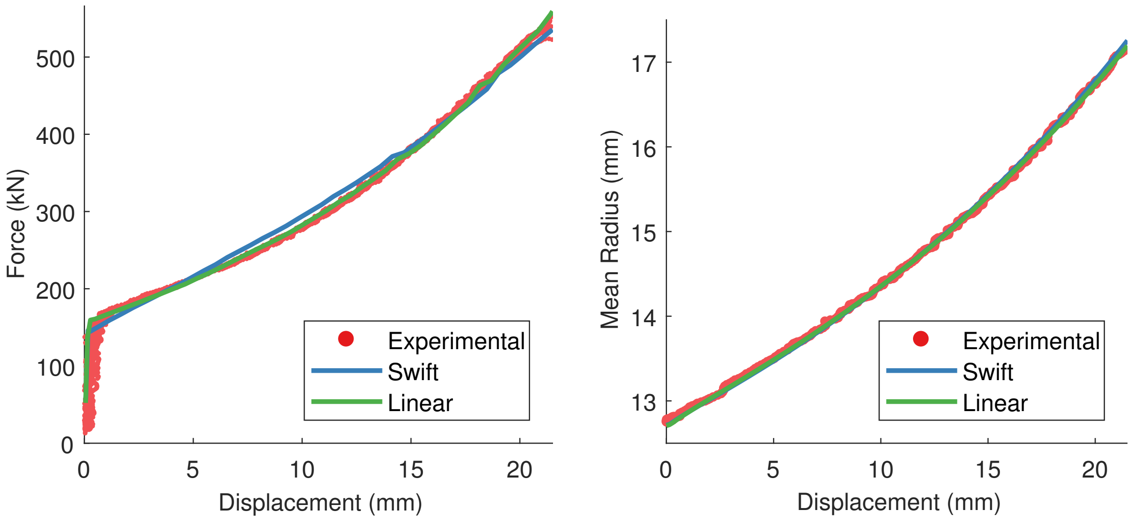

(a) Force-displacement

(b) Mean radius-displacement

Figure 5.6: C36000 brass experimental and FEM results for optimal material parameter for Swift and linear hardening laws.

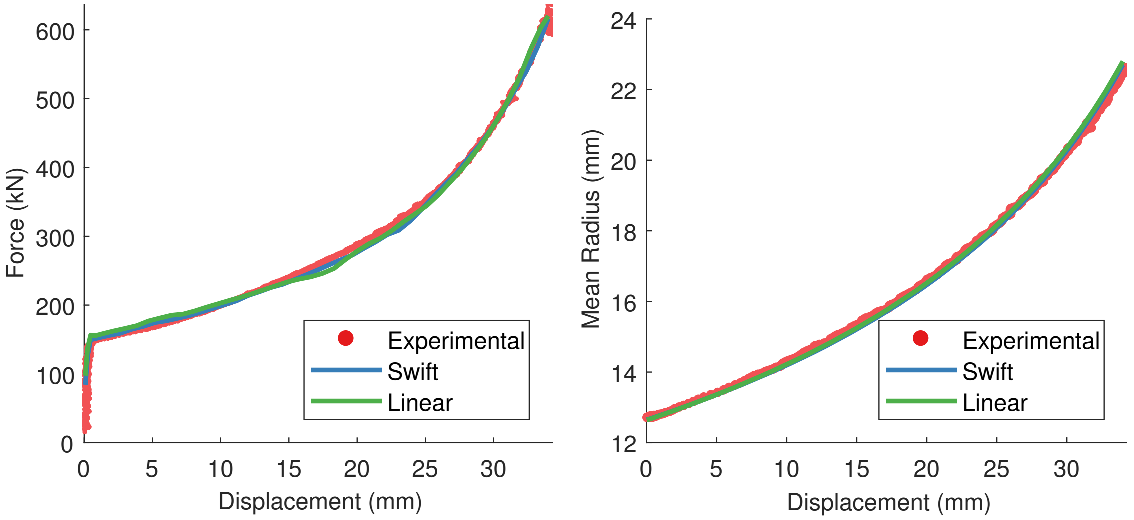

(a) Force-Displacement

(b) Mean radius-displacement

Figure 5.7: C11000 copper experimental and FEM results for optimal material parameter for Swift and linear hardening laws.

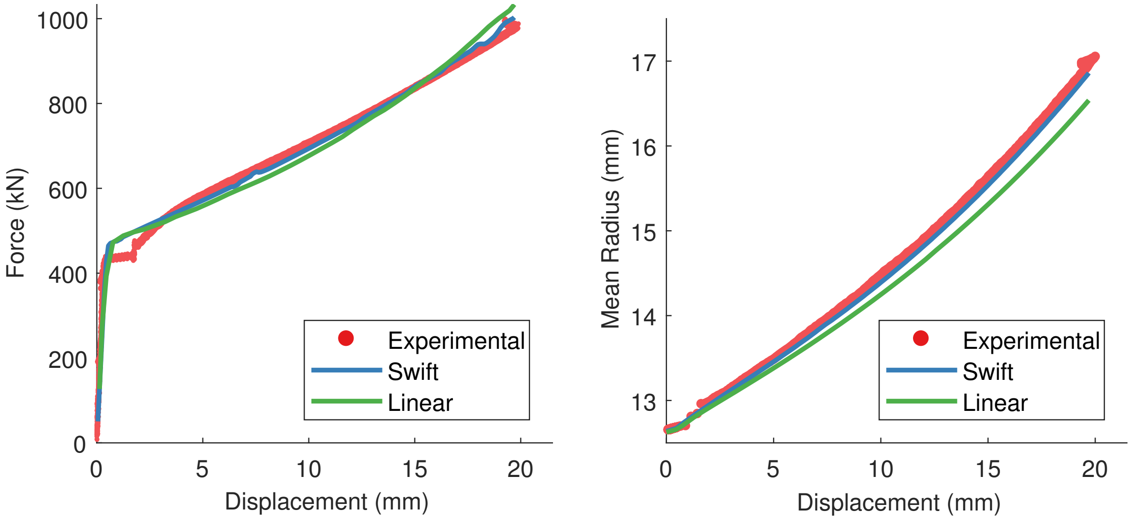

(a) Force-displacement (b) Mean radius-displacement

Figure 5.8: AISI 4140 steel experimental and FEM results for optimal material parameter for Swift and linear hardening laws.

Both constitutive models struggled to match the force-displacement behavior of AISI 4140. This is most likely due to the prominent double yield point, which leads to a prolonged period of near-zero material stiffness. As neither constitutive models can account for this phenomenon, both experienced difficulty fitting plastic behavior. Regardless, the Swift hardening law was a significantly better fit to radius-displacement data than the linear plasticity model. However, while neither model estimated coefficient of friction to fall within the bound of friction ring experiments, the linear plasticity model was significantly closer than the Swift law, which was almost three times the experimental mean coefficient of friction.

Despite having a less prominent double yield point than AISI 4140, once again both models struggled to fit the force-displacement behavior of AISI 4340. While it is clear that the from Figure 5.9 that the Swift law fits is a better fit, it is not as good a fit, especially when compared to some of the other fits presented in this section. As with AISI 4140, the Swift law was a better fit to radius-displacement data than the linear plasticity model. However, the coefficients of friction determined for both models were well above the confidence interval determined from friction ring testing.

While fitting was accomplished using force-displacement and radius-displacement, a far more important metric is how well a constitutive model predicts a material's true stress-strain behavior. For ease of viewing, the stress-strain behavior of each material compared to actual material behavior is shown in Figure 5.10 for the three non-ferrous

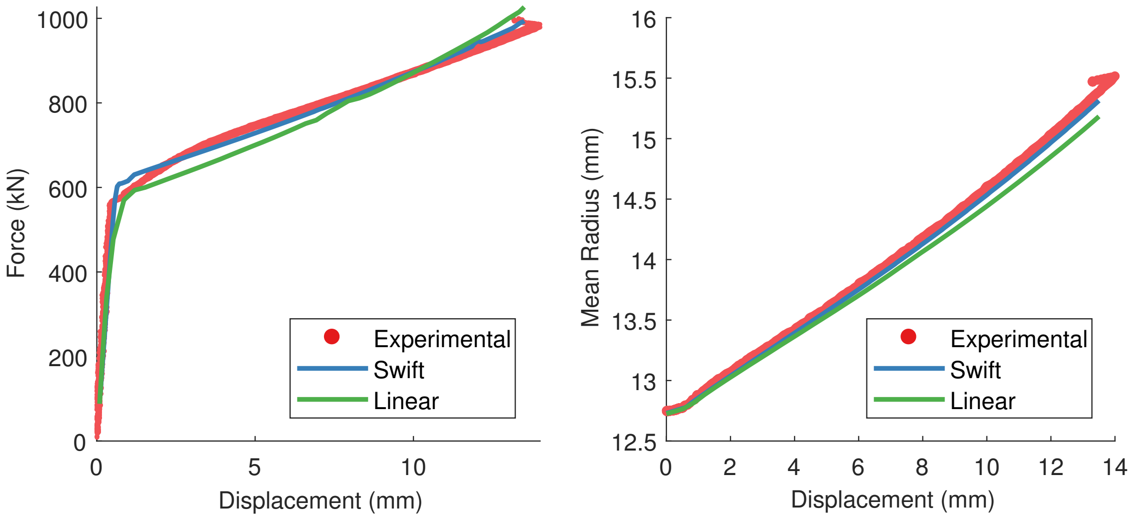

(a) Force-displacement (b) Mean radius-displacement

Figure 5.9: AISI 4340 steel experimental and FEM results for optimal material parameter for Swift and linear hardening laws.

alloys used in this work and Figure 5.11 for the two steel alloys tested. The stress-strain curves used to represent constitutive model fits are taken from the centermost element of each FE model. Von Mises stress and effective strain are used here. True stress-strain data is used to portray experimental material behavior. Experimental material curves are identical to those portrayed in Section 5.1.

Beginning with aluminum, one will note, as expected, the Swift hardening rule provided a much better fit to experimental behavior than the linear hardening rule. However, as the Swift hardening law cannot account for the softening effect of material damage, the quality of the fit is somewhat limited, especially at moderate to large deformation. However, at low levels of deformation, the Swift law predicts true-stress strain behavior well.

Referring back to the force-displacement behavior of both constitutive models for brass presented in Figure 5.6, one will recall that both the Swift and linear models presented good fits. However, it is clear from Figure 5.10 that the linear plasticity model is much more appropriate for this material. The Swift model greatly underestimates yield strength and does not exhibit the same trend in plastic stress-strain behavior.

Like brass, both the Swift and linear models were good fits to copper's force-displacement data. Interestingly, both models are also good fits to copper's plastic stress-strain behavior. The somewhat wavey behavior seen in copper's experimental stress-strain

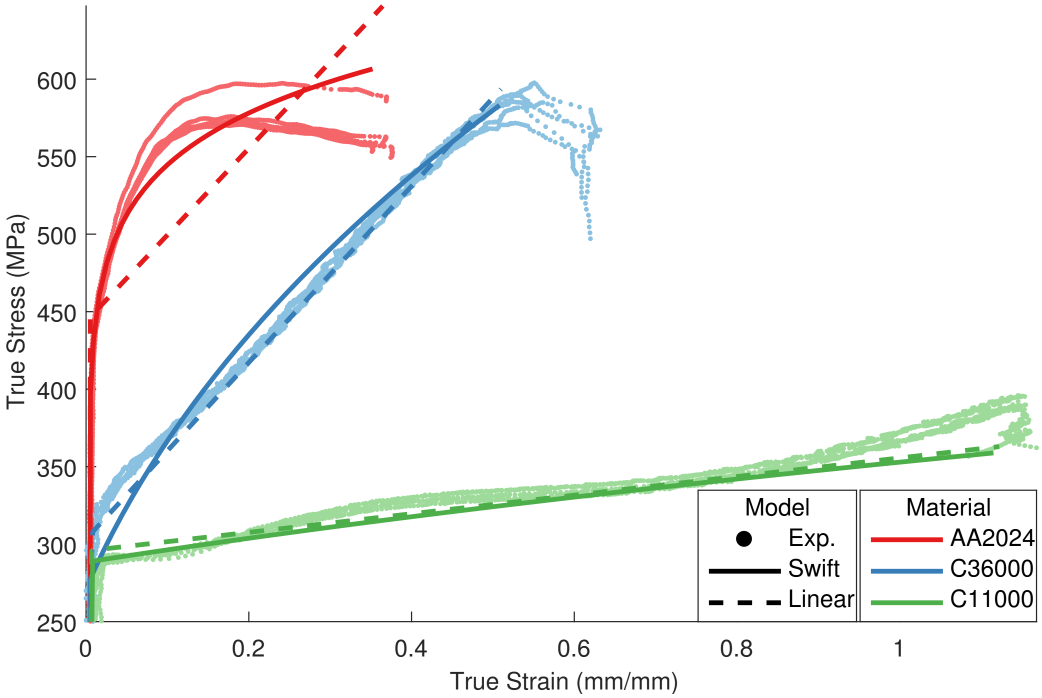

Figure 5.10: Comparison of experimental stress-strain data to optimal model fits for the non-ferrous metals tested

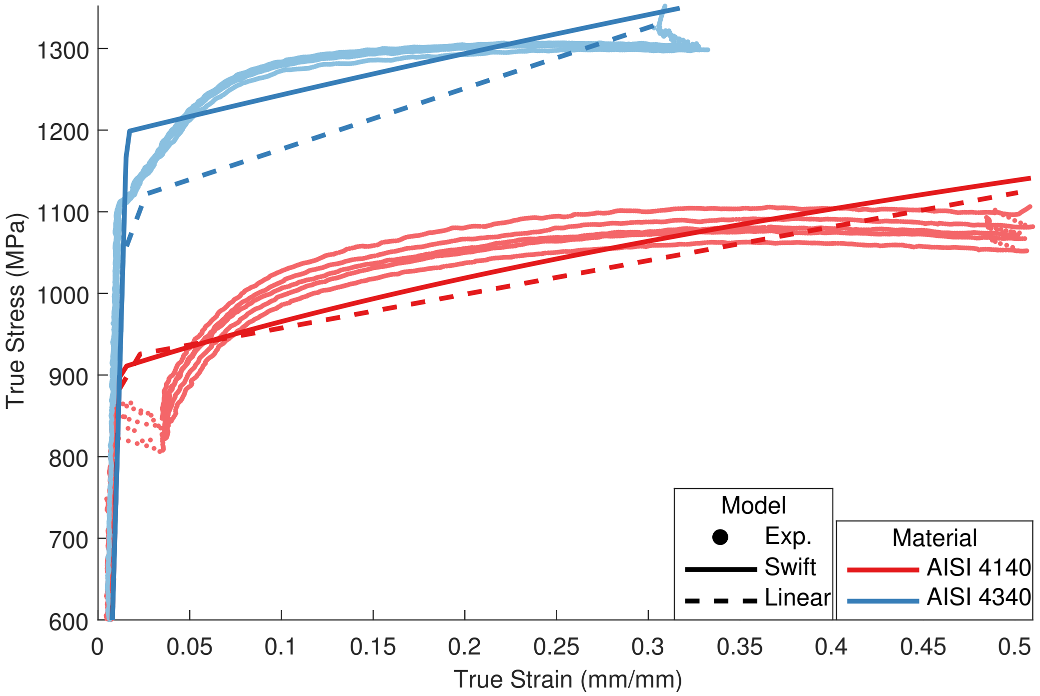

Figure 5.11: Comparison of experimental stress-strain data to optimal model fits for the ferrous metals tested

curve does make fitting more challenging, as neither model can account for such behavior. However, the linear plasticity model does present do a slightly better job predicting overall behavior. Although in this instance, both model fits would be considered appropriate for predicting copper's plastic behavior.

AISI 4140 exhibited some rather interesting fit behavior. As noted above, the prominent double yield point made the fitting of force-displacement data challenging. This observation holds true for stress-strain behavior, as shown in Figure 5.11. Both the linear and Swift models cannot account for the period of very low stiffness associated with the double yield point. While a swift model a better fit to stress-strain behavior than the linear model, it is not what one would refer to as exceedingly good.

As with AISI 4140, the yield point phenomena present in AISI 4340, although far less prominent, also result in poor quality fits both the Swift hardening law and linear plasticity model. In this case, however, the linear model produced an extremely poor quality fit. While the swift model does not capture the gradually reducing stiffness of the AISI 4340's actual behavior, it does at least overlap with the material's stress-strain curve.

The comparison of stress-strain and force-displacement responses yields an interesting conclusion. Although a constitutive model may fit well to force-displacement data, it may not fit the stress-strain behavior. Because optimization algorithms are naive to the nature of the objective function they are solving, Compcam will attempt to tune parameters of a constitutive model to minimize the error between numeric and experimental responses, regardless of the physical reality of such parameters or formulation of the constitutive model. A key example of this is the fitting of the Swift hardening law to brass. While Compcam minimized the error between the force-displacement curve, the final parameters determined resulted in an unrealistic portrayal of stress-strain behavior. This leads to the conclusion that while IMM's effectiveness is limited by how appropriate a constitutive model is to describe a material's actual behavior. A model which predicts linear plastic behavior would not be appropriate for a material whose plastic stiffness behavior changes as a function of deformation. Further, constitutive models which cannot account for yield point phenomena may struggle to predict the behavior of material with a double yield point, as showcased by the fitting of AISI 4140 and AISI 4340 to both constitutive models.

While not a conclusion, another point of interest raised in this work is the final fitted value for the coefficient of friction for each constitutive model fit and material. The coefficients of friction determined by Compcam do not reliably align themselves with the values suggested by friction ring testing. While there are cases, such as aluminum and the Swift hardening law and copper and the Swift hardening law where the model and material are a good fit to one another and the coefficients of friction fall within experimental values, it is not always the case. While one should not expect an accurate prediction of friction for a model which is not appropriate for a given material, based on the conclusion made above, there does appear to be additional factors causing the deviation between experimental and computational coefficients of frictions.

One possibility is that as a result of the numerical algorithms used by Ls-Dyna, the coefficient of friction used by the FE package may not have the same physical meaning as the coefficient of friction determined by the friction ring. Investigating the algorithms used by Ls-Dyna to account for friction (LSTC, 2017b), one will observe that while Ls-Dyna does base its friction model on Coulomb friction, there are several notable features which may change the physical interpretation of both the friction model and the coefficient used in the FE package. These include a truncated iterative approach to calculating frictional forces at a contact interface based, in part, on material stiffness and the limiting of the maximum possible frictional force at a contact interface in order to improve overall numeric stability. Both factors could contribute to differences in the coefficients determined experimentally and used by FE packages, as well as differences in coefficients determined between constitutive models.

Another possibility is that the coefficients of friction determined through the use of the friction ring test may not be correct. Coefficients of friction are difficult to publish as they depend on many different factors such as surface finish, lubricating condition, and testing method. For example, Mark's handbook (Avallone and Baumeister, 1996) gives a coefficient of friction for dry contact between steel and aluminum to be about 0.6 and dry steel on steel to be 0.74. These values are far in excess of the values determined in this work and seem excessive in nature. In their work developing the friction ring test, Male and Cockcroft (1964) made estimates of the coefficient of friction which do lie closer to the values found here, such as 0.18 for aluminum on a smooth steel die, 0.10 for brass on a smooth steel die, and 0.17 for copper on a smooth steel die. While there would likely be variations depending on how the dies were prepared, it does suggest that the coefficients determined in this work are somewhat low.

Between the numerical implementation of contact and friction in Ls-Dyna, as well as the variation and disparity in coefficients of friction suggested by literature sources, it is difficult to make a conclusive statement on the matter of friction in constitutive model fitting without further investigation.

5.2.1.1 Investigation of Frictional Effects

To explore the effects of friction on the fitting process, both constitutive models were fit once again to all five alloys. However, instead of allowing friction to be tuned by Compcam, the coefficient of friction was held fixed at the mean experimental coefficient determined by the friction ring test. If friction has a significant physical effect on barreling, which is a well known physical phenomenon, holding friction fixed should also have some effect on the fit score and final fitted parameters.

Tables 5.5 and 5.6 provide the final parameters determined by Compcam. The value of friction provided in these tables is fixed and is equal to the mean coefficient of friction determined by friction ring testing. Table 5.7 summaries the fit scores for the parameter sets tuning and holding friction constant.

Table 5.5: Optimal Swift hardening parameters for ductile metals holding friction constant

Material	ν	K (MPa)	n	σ_y (MPa)	μ (fixed)	R^2_{avg}
AA2024-T351	0.2945	661.4	0.08754	445.4	*0.1431*	0.9921
C36000 Brass	0.3015	683.9	0.3599	303.4	*0.07902*	0.9941
C11000 Copper	0.3116	277.9	0.2762	301.0	*0.07190*	0.9985
AISI 4140	0.3281	1266	0.1145	898.9	*0.05892*	0.9840
AISI 4340	0.3002	1498	0.3266	1204	*0.07938*	0.9661

Table 5.6: Optimal linear plasticity parameters for ductile metals holding friction constant

Material	ν	σ_0 (MPa)	E_{tan} (MPa)	μ (fixed)	R^2_{avg}
AA2024-T351	0.3054	484.6	399.2	*0.1431*	0.9674
C36000 Brass	0.3007	312.6	542.6	*0.07902*	0.9966
C11000 Copper	0.3037	290.6	63.11	*0.07190*	0.9988
AISI 4140	0.3029	944.7	542.2	*0.05892*	0.9754
AISI 4340	0.3035	1134	1098	*0.07938*	0.9802

Table 5.7: Comparison of fit scores with friction tunable and held fixed

Material	Swift		Linear	
	Tunable	Fixed	Tunable	Fixed
AA2024-T351	0.9953	0.9921	0.9400	0.9674
C36000 Brass	0.9957	0.9941	0.9984	0.9966
C11000 Copper	0.9989	0.9985	0.9969	0.9988
AISI 4140	0.9914	0.9840	0.9750	0.9754
AISI 4340	0.9802	0.9661	0.9802	0.9466

Comparing the final fit scores from fixed and tunable coefficients of friction found in Table 5.7, one will note that with a few exceptions, the fit score associated with a set of parameters determined by COMPCAM is improved by tuning friction. This result was expected, because as stated before, COMPCAM tunes parameters naively with the goal of maximizing fit score, regardless of the physical meaning of the parameter. This means COMPCAM will find the best coefficient to maximize fit score and that this coefficient may not correspond to any physically realistic value. This lends credence to the possibility that the coefficient of friction used in the FE solver may be physically different than experimental values.

There were a few instances where the physical coefficient of friction provided a higher fit score than the one determined by COMPCAM. In two of these cases, specifically the case of fitting the linear plasticity model to aluminum 2024 and AISI 4140, the underlying model is inappropriate for predicting the actual materials behavior. As discussed in Section 5.2.1, COMPCAM's ability to accurately tune parameters depends on the constitutive model being an appropriate representation of actual material behavior. Otherwise, the quality of the fitted parameters will suffer. Observing Figures 5.10 and 5.11, one should note that the linear plasticity model is not a good fit for either aluminum or steel.

The other exception found in Table 5.7 is rather more interesting. When fitting the linear plasticity model to copper, holding the coefficient of friction at the value suggested by friction ring testing provides a better fit score than was determined by tuning the coefficient. Unlike the aforementioned steel and aluminum, the linear plasticity model does represent a good match to copper's behavior. In this instance, the improved fit score achieved by holding the coefficient of friction constant could imply the solution space has more than one local optima. While care was taken during the fitting processes to avoid local optima, such as running COMPCAM more than once with different initial conditions as well as seeding Compcam runs with the coefficient of friction determined through experimentation, it is clear that in this case, Compcam failed to find the most optimal solution. Short of switching to a global search algorithm, which would incur a significant and almost prohibitive computational penalty, there is no way to avoid finding local optima.

However, in this instance, the difference in fit score between the two models is very small; occurring at the fourth decimal place. Interestingly, this implies that doubling the coefficient of friction resulted between the value determined by friction ring testing and using Compcam only resulted in an exceedingly small change in fit score. While this may explain why the optimization algorithm in Compcam struggled to find the global optima, it indicates that the objective function used in this work may not be the most appropriate. As it is well known that friction plays a very large part in the deformation behavior of a specimen in a cold upsetting test, why does a large change in coefficient only result in a 0.0004 change in fit score?

While effective in the majority of cases presented in this section, the fit score currently used in this work may not be the best score, as shown by the low activity associated with friction. This low activity present in the coefficient of friction would serve to make optimization more challenging and potentially reduce the accuracy to which such low activity parameters are fit. While this fit score will be used for the remainder of the present work, the investigation of an alternative fit score is recommended as a future extension of this work.

5.2.2 Application to Complex Models

Following completion of validation work, two additional constitutive models were fit to all five ductile metals; the GTN model and the $P - \alpha$ variant of the Johnson-Cook model. These models are significantly more complex than the Swift hardening rule and linear plasticity model used previously. As with validation work and as a result of the findings in Section 5.2.1.1, the coefficient of friction was tuned by Compcam.

The final fitted parameters for the GTN model and $P - \alpha$ variant are given in Tables 5.8 and 5.9, respectively. Unlike validation testing, the fit of each model to the objective function datasets of force-displacement and mean radius-displacement are excluded here. Instead, only the final fit to true stress-strain behavior is provided.

Table 5.8: Optimal GTN parameters for each ductile metal

Material ID	E (GPa)	ν	SIGY (MPa)	N	f_c	f_N	ϵ_N	s_N	μ	R^2_{avg}
AA2024	69.83	0.3093	426.7	11.17	0.4926	0.2552	0.2224	0.1745	0.1272	0.9927
C36000	94.60	0.3102	253.8	6.587	0.4945	0.2604	0.2131	0.1752	0.1055	0.9675
C11000	105.4	0.3118	197.8	9.879	0.4994	0.2529	0.25523	0.1633	0.08518	0.9968
AISI 4140	200.1	03123	743.3	10.29	0.5091	0.2530	0.2339	0.17092	0.1164	0.9961
AISI 4340	200.2	0.3103	1041	13.83	0.4963	0.2130	0.2253	0.1747	0.1370	0.9966

Table 5.9: Optimal Johnson-Cook parameters using a $P - \alpha$ compaction curve

Material ID	G (GPa)	A (MPa)	B (MPa)	n	P_e (MPa)	P_s (MPa)	N	μ	R^2_{avg}
AA2024	28.36	425.4	298.0	0.3831	170.7	1171	4.977	0.1596	0.9880
C36000	33.46	289.4	504.7	0.7274	84.70	949.0	4.743	0.08244	0.9974
C11000	44.50	226.0	152.6	0.3670	100.1	897.4	5.114	0.1512	0.9977
AISI 4140	80.15	736.8	611.2	0.3425	523.2	1953	5.417	0.1786	0.9965
AISI 4340	80.17	846.9	698.3	0.1851	481.4	1942	4.768	0.1760	0.9973

These fits are shown in Figures 5.12 and 5.13 for non-ferrous and ferrous alloys, respectively.

As with the models used for validation work, the fit of the GTN and $P - \alpha$ variant depended greatly on how appropriate the model's behavior matches actual material behavior. In particular, the GTN model proved to be a bad fit for brass's behavior and while both constitutive models did not predict copper's behavior well. That said, in some cases, these models predicted material behavior significantly better than the Swift or linear plasticity models. In particular, both models proved to be a much better fit to aluminum's plastic behavior than Swift model in Figure 5.10. Further, while not as good as the linear fit presented in Figure 5.10, the $P - \alpha$ variant proved to be a surprisingly good fit to brass's mostly linear behavior. In terms of the steel alloys tests, both constitutive models provided excellent fits to experimental true stress-strain curves, as shown in Figure 5.13.

As with the previously discussed constitutive models, the coefficient of friction does not always align with the values measured using the friction ring test. Nonetheless, the quality of the fits does not suffer as a result of this. A key example of this statement is the fit of both these models to AISI 4140 and 4340. Despite providing an excellent fit to experimental stress-strain behavior, the final coefficients of friction do not align with the friction ring test. Furthermore, there is variation between the

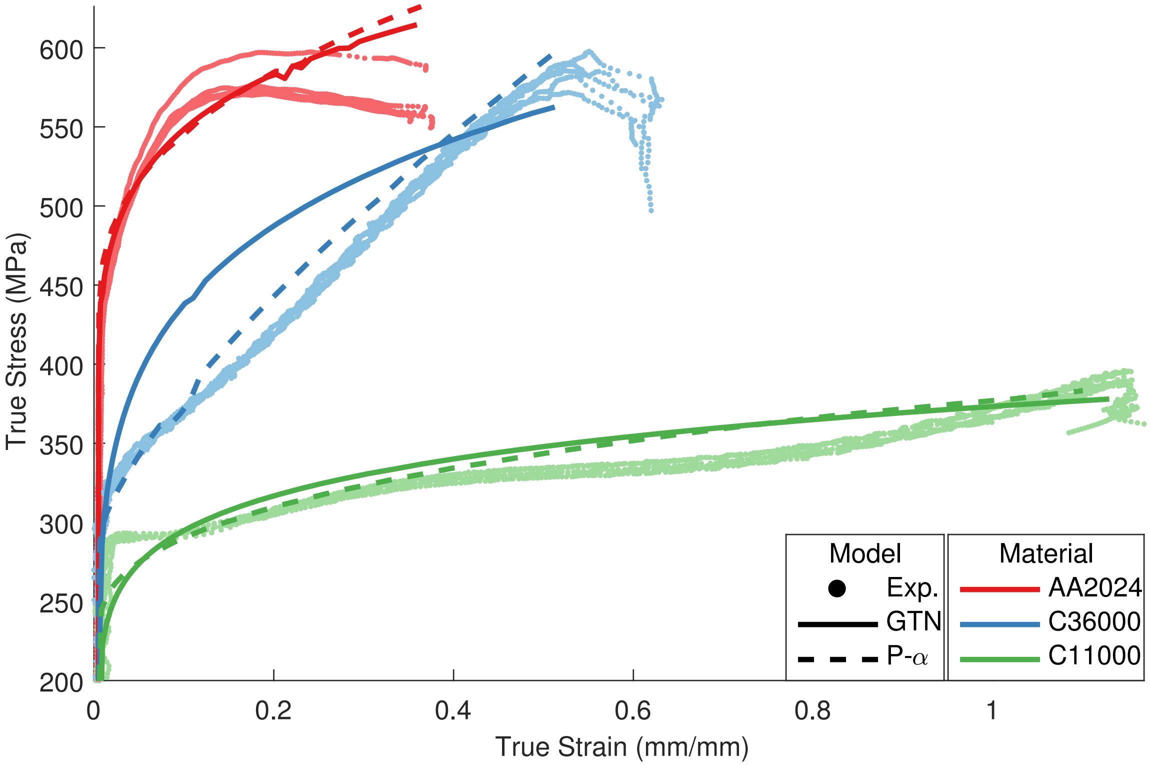

Figure 5.12: Comparison of experimental stress-strain data to optimal model fits for additional constitutive models fitted to non-ferrous alloys

coefficient of friction determined by Compcam for each constitutive model. Given that, as already mentioned, friction algorithms in the FE model which are influenced by material stiffness and plastic behavior, such variation is not surprising. Indeed it further strengthens the argument that the coefficient of friction used by the FE solver may not be completely physical in nature.

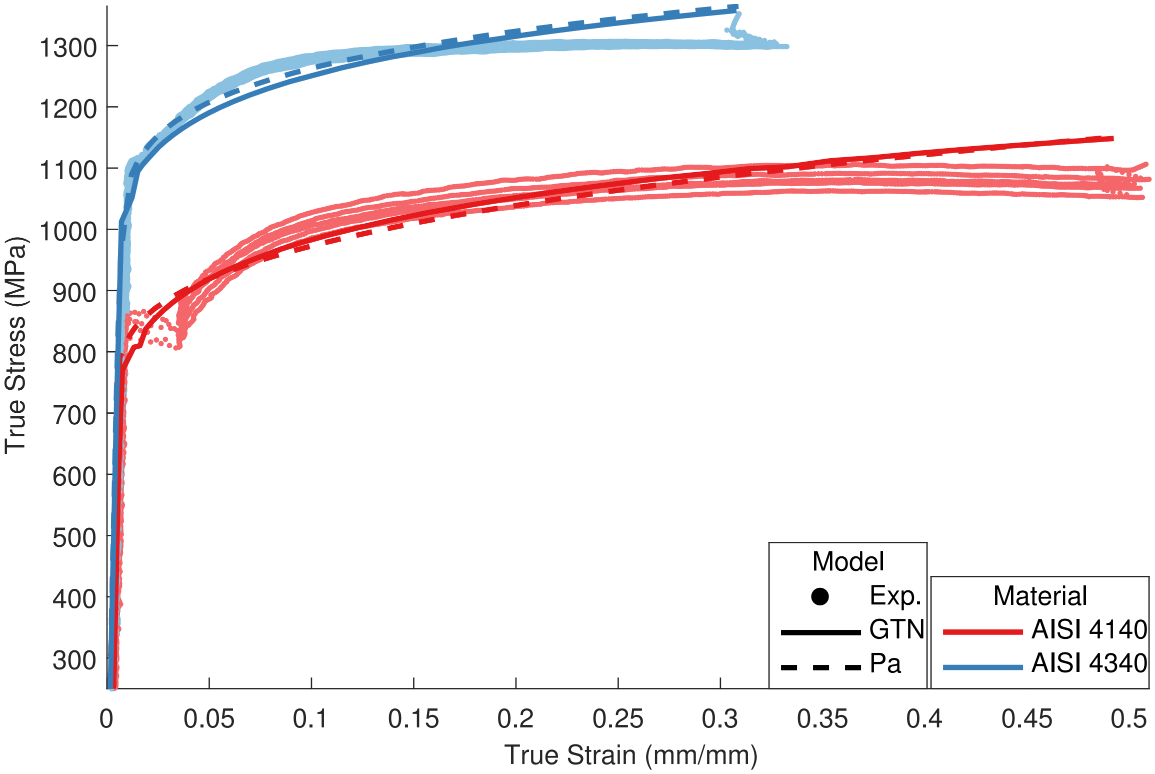

Figure 5.13: Comparison of experimental stress-strain data to optimal model fits for for additional constitutive models fitted to ferrous alloys

Chapter 6

Investigation of Sintered, Ferrous PM Alloys

This chapter deals with the experimental characterization and subsequent model fitting to twelve ferrous, sintered PM alloys provided by Stackpole International. These alloys consisted of four elemental compositions and three sintered densities. Unlike the ductile metals discussed in the previous chapter, true stress-strain behavior is not the only behavior which is being fit. The densification behavior of these alloys is a key area of interest for these alloys. As such, in addition to evaluating the fit of each constitutive model to each alloy's stress-strain behavior, the progression of bulk densification is also compared for each alloy and model.

6.1 Experimental Results

As noted in Section 4.1, all sintered PM alloys were tested compression to an engineering stress of 650 MPa owing to equipment limits related to the Instron 600RD test frame. As such, the amount of deformation imposed on each alloy varied depending on the material's composition and sintered density. For example, Figure 6.1 shows SP-4420 specimens from each sintered density which have been loaded to 650 MPa. As sintered density increased, material strength increased and the amount of deformation imparted in the specimen decreased. While only SP-4420 is shown in Figure 6.1, the same trend was seen in all alloys tested.

6.1.1 SP-2140

The true stress-strain curves for SP-2140 for all densities are given in Figure 6.2. Note that only three of the six curves tested are shown for each density to allow for a cleaner presentation. However, all alloys and densities exhibited highly repeatable behavior. This style of presentations will be used throughout this chapter.

Figure 6.1: SP-4420 specimens of all three densities (decreasing to the left) after testing compared to an untested specimen (far left)

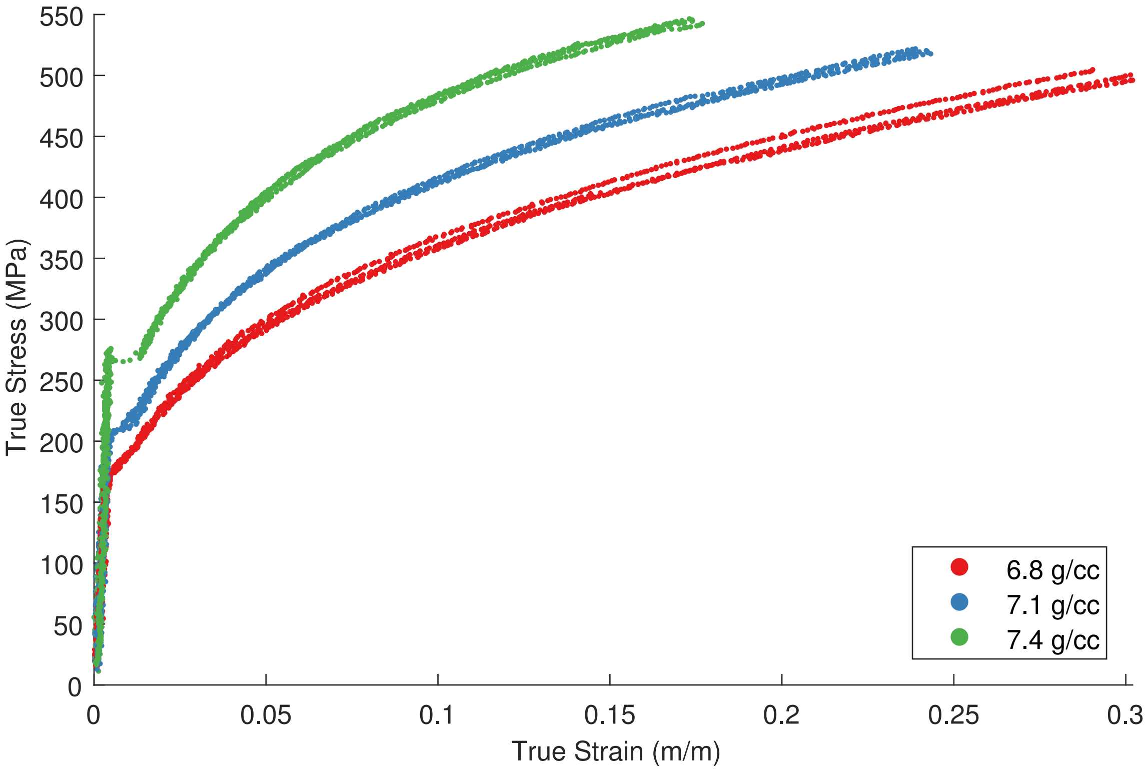

Figure 6.2: True stress-strain curves for SP-2140, all densities

As stated earlier, it is clear that the yield strength of the material increases with increasing density. However, for SP-2140, this increase does not appear to be linear despite a linear increase in density. One will note the difference in yield point between 7.4 and 7.1 g/cc appears to be much larger than the difference between the yield points for 7.1 and 6.8 g/cc.

Another interesting feature of note is the post-yield behavior of each specimen. The 6.8 g/cc specimens appear to smoothly transition from elastic to plastic behavior. Both the 7.1 and 7.4 g/cc specimens exhibit a double yield point, although the prominence of such yield point phenomena in the 7.4 g/cc specimens was much greater than the 7.1 g/cc alloy.

A final observation is each density exhibits the same decaying exponential hardening behavior. Further, as the sintered density increases, the slope of the plastic stress-strain curve, akin to the plastic stiffness of the material, also increases. Relating this to a Swift hardening law or similar power law hardening rule, this would result in an increase in the hardening coefficient. However, fitting later in this section will be needed to corroborate this observation.

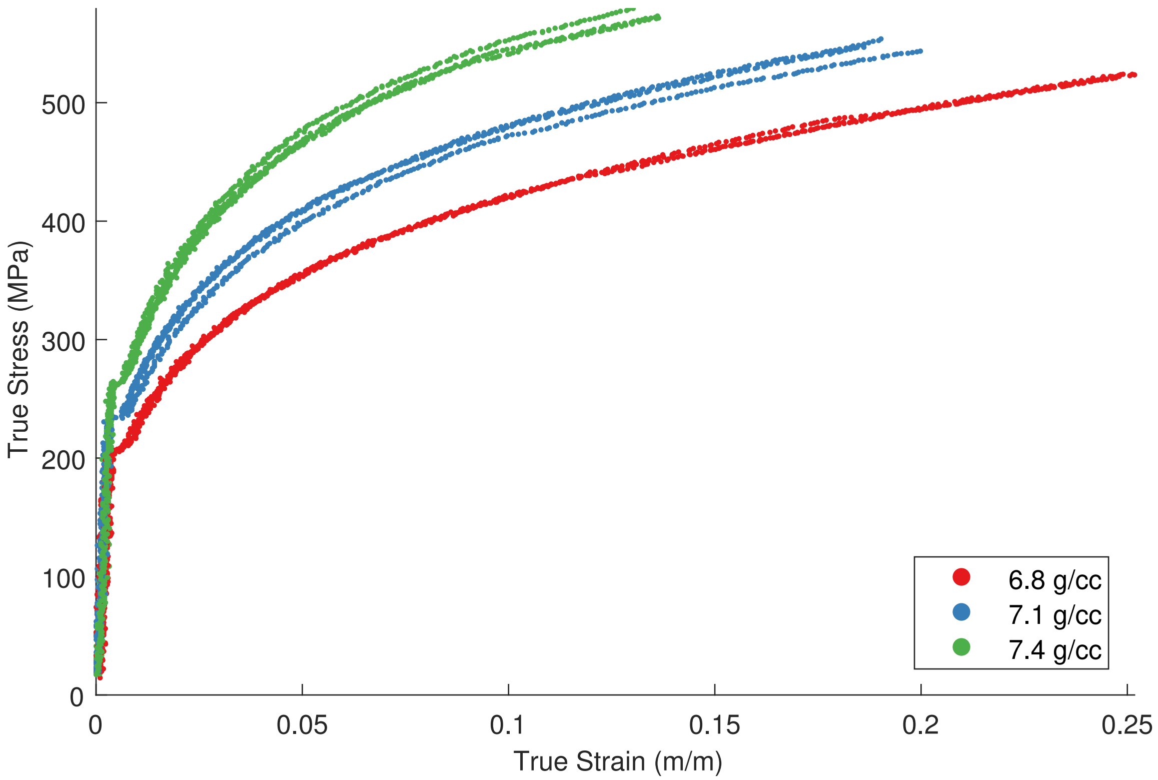

Figure 6.3: True stress-strain curves for SP-4420, all densities

6.1.2 SP-4420

The true stress-strain curves for all densities of SP-4420 are shown in Figure 6.3. As with SP-2140, yield strength increased with increasing density. However, unlike SP-2140, it appears as though the increase was somewhat linear with increasing density.

The plastic behavior of all densities was quite uniform for SP-4420, much more so than SP-2140. All SP-4420 alloys exhibited a double yield point. However, unlike SP-2140, the prominence and extent of each density's yield point effects were similar in nature.

6.1.3 SP-6664

The true stress-strain curves for SP-6664 at all densities are shown in Figure 6.4. The plastic behavior was markedly different from the previous two alloys. Specifically, one will note that the elastic-plastic transition was smooth, without the double yield point of the previous alloys. However, as with the other alloys tested, the yield strength of

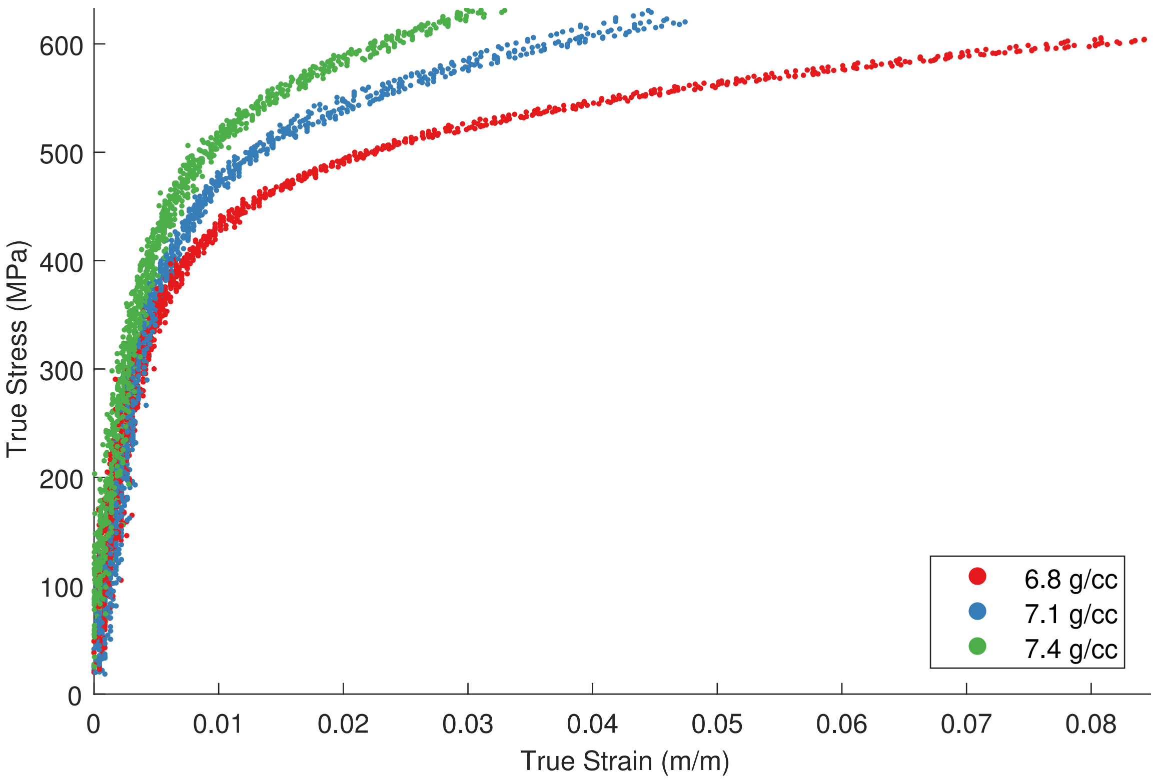

Figure 6.4: True stress-strain curves for SP-6664, all densities

the material increased commensurate with density, although not to the degree seen in the previous alloys.

This material had a higher yield point compared to the previously discussed alloys. So much so that the test end condition of 650 MPa engineering stress did not invoke significant plastic deformation, particularly at densities of 7.1 and 7.4 g/cc.

It is important to note at this juncture that one reason that AISI 4340 was used in Chapter 5 was that it was indicated by Stackpole that SP-6664 had a similar, though not identical, elemental composition. As such, it was hoped comparisons could be drawn between the behavior of AISI 4340 and SP-6664. However, given that no processing information for each alloy was released by Stackpole, coupled with the somewhat unexpected discovery that 4140 and 4340 specimens were quenched and hardened, in the end, no comparisons could be drawn.

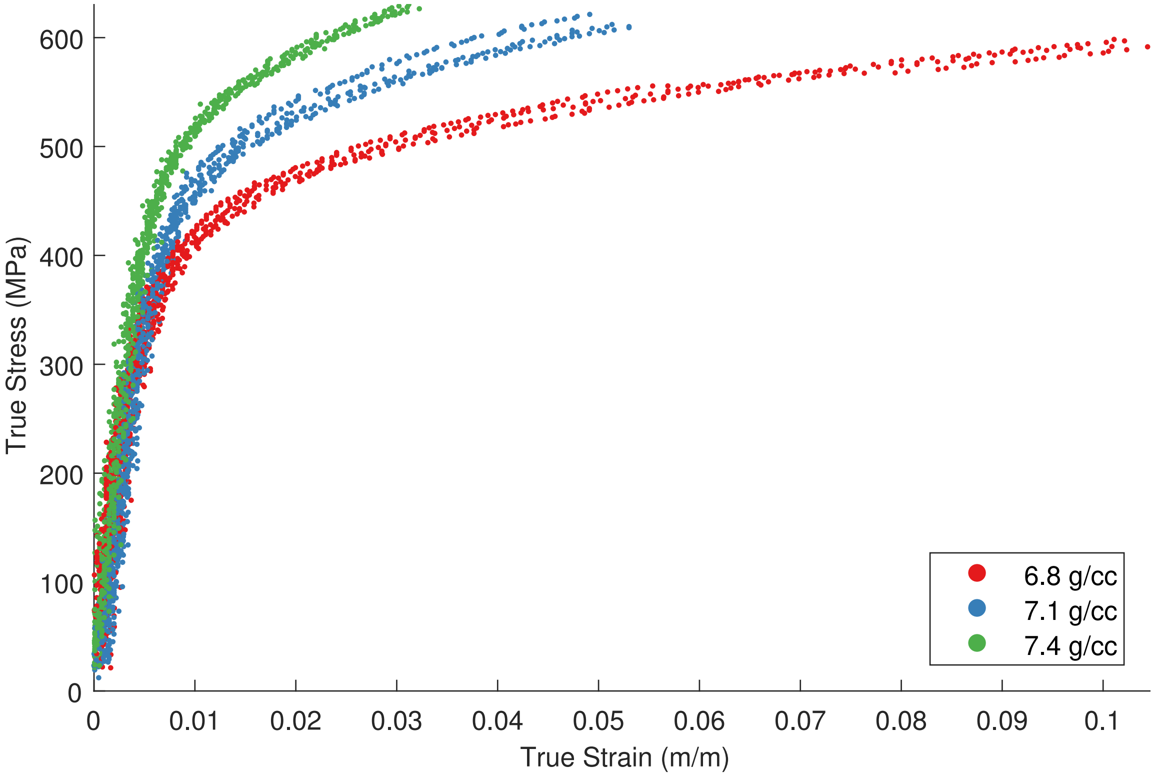

Figure 6.5: True stress-strain curves for SP-E2148, all densities

6.1.4 SP-E2148

The true stress-strain behavior for all densities of SP-E2148 is documented in Figure 6.5. Its behavior was very similar to that of SP-6664 in all aspects, particularly in terms of yield strength and plastic behavior.

6.1.5 Comparisons of Stress-Strain Behavior

Figures 6.6 to 6.8 show true stress-strain behavior for all alloys at each density, permitting observations to be made across the different alloys. First, as noted in the previous section, the behavior of SP-6664 and SP-E2148 were indeed very similar at each density. However, SP-E2148 consistently yields at a somewhat lower stress than SP-6664. Despite this, it appears as though the plastic behavior is remarkably similar despite the reduction in yield strength.

Another interesting feature is the when one compares the yield strengths of SP-2140 and SP-4420. SP-2140 yields at a much lower stress than SP-4420 at a density of 6.8 g/cc. However, as sintered density increases, the difference in yield strength

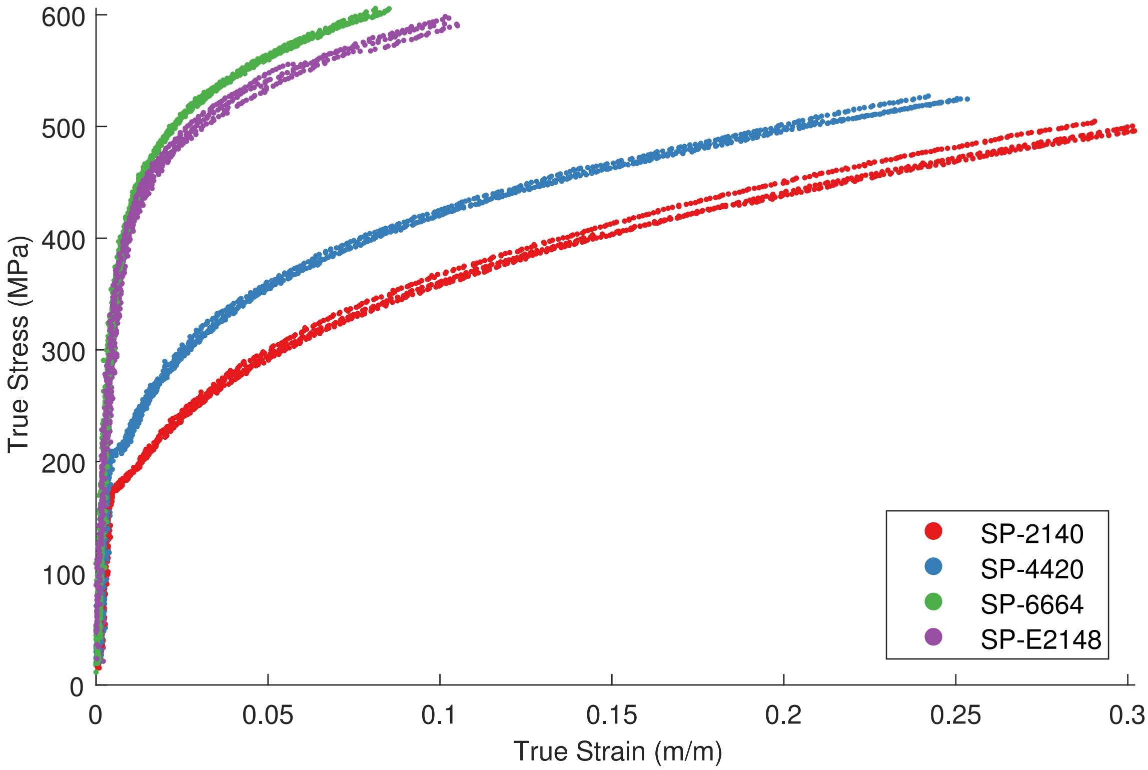

Figure 6.6: True stress-strain curves for all alloys at 6.8 g/cc

decreases. This is especially apparent at a density of 7.4 g/cc (Figure 6.8) where the yield strength of both alloys are almost identical. Assuming that SP-2140 and SP-4420 have similar initial yield strengths at full density (which is reasonable the results of Figure 6.8), this result indicates that the yield strength of SP-2140 is very susceptible to sintered density. However, despite similar yield strengths, the elastic-plastic transitions and plastic hardening behavior are still quite different.

Without knowing more about the chemical composition, sintering process and other manufacturing details associated with each alloy, any observations as to why the alloys behave differently cannot be conclusively drawn.

6.1.6 Density Measurements

In addition to work undertaken to characterize stress-strain behavior using the cold upsetting test, density measurements of all tested alloys were undertaken. Density measurements were done by two means. First, the final, compressed density was measured using a modified version of MPIF Standard #42 (Metal Powder Industries Federation, 2010b), which involves measuring the weight of a specimen in air and

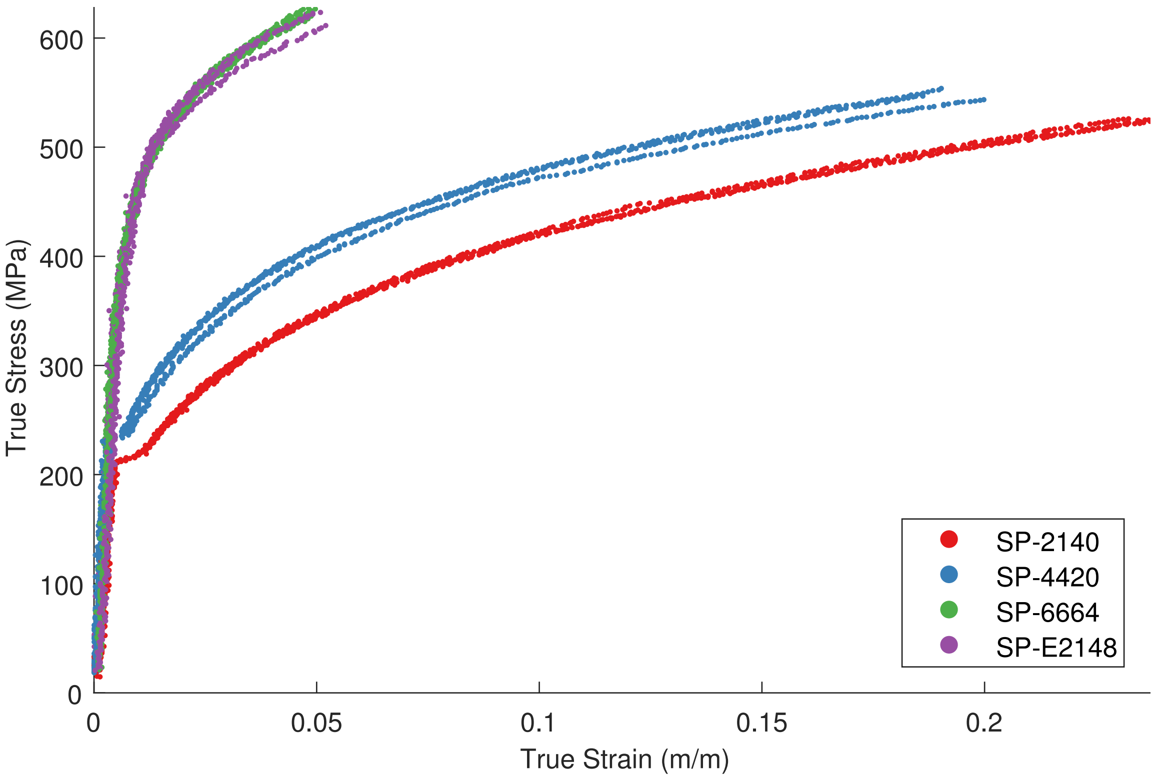

Figure 6.7: True stress-strain curves for all alloys at 7.1 g/cc

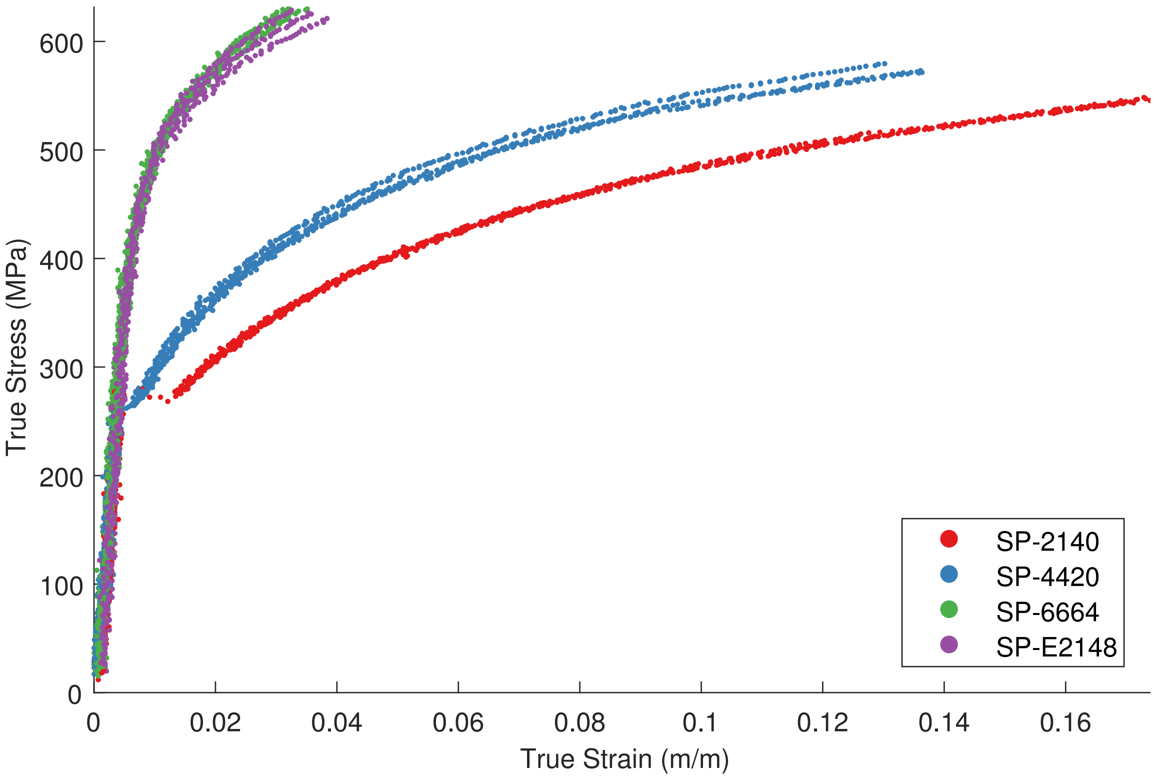

Figure 6.8: True stress-strain curves for all alloys at 7.4 g/cc

water then using Archimedes method to determined density. Deviating from the standard, this work did not impregnate the specimens with oil prior to measuring weight. Regardless, this methodology provided the means to accurately measure the final bulk density of the material without needing to consider the geometry of the specimens. The second method uses the deformed profile of the specimen measured by Specs and detailed in Section 4.2.1.

Figures 6.9 to 6.12 plot the density of the specimen with respect to vertical strain for all alloys and initial sintered densities. The final densities measured using the Archimedes method are also plotted. As one will note, there is a good agreement between the two methods at final density. Final bulk densities for each material tested as measured using the optical system and the Archimedes method with sample uncertainty are given in Table 6.1.

There is one feature of note pertaining to density data, however. There is some spread to the densities as measured by the MPIF standard in Figure 6.12. Specifically, two density measurements for SP-E2138-74 fall well below the remainder. While this is reflected in the average final density shown in Table 6.1 by a larger sample uncertainty, the exact cause of this variation is unknown. Regardless, it is rather unusual, as the repeatability of other alloys indicates that outliers should be unlikely, especially for two specimens from the same alloy/density batch.

Table 6.1: Final densities as measured using Archimedes method and using the optical measurement system

Material ID	Archimedes Final Density (g/cc)	Optical Final Density (g/cc)
SP-2140-68	7.235±0.014	7.263±0.045
SP-2140-71	7.388±0.008	7.409±0.018
SP-2140-74	7.566±0.016	7.537±0.020
SP-4420-68	7.180±0.029	7.137±0.013
SP-4420-71	7.296±0.012	7.311±0.020
SP-4420-74	7.531±0.010	7.474±0.020
SP-6664-68	6.869±0.034	6.964±0.016
SP-6664-71	7.130±0.009	7.184±0.019
SP-6664-74	7.296±0.014	7.249±0.020
SP-E2148-68	6.933±0.022	7.015±0.028
SP-E2148-71	7.145±0.022	7.207±0.018
SP-E2148-74	7.356±0.049	7.398±0.015

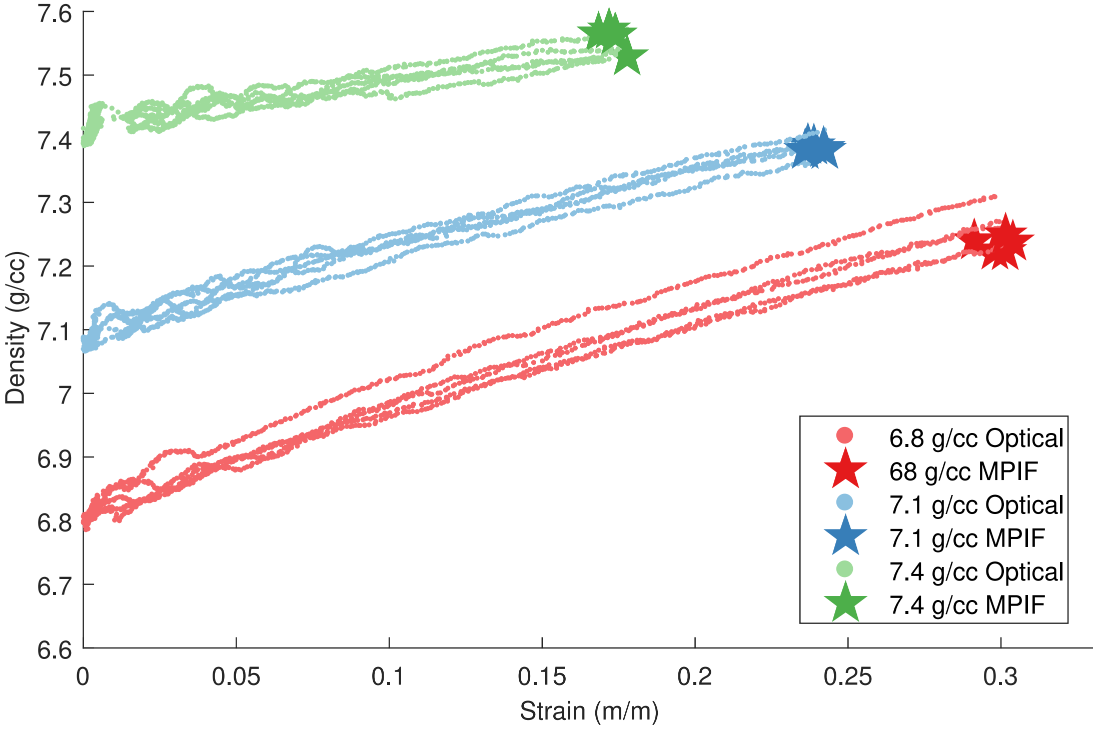

Figure 6.9: Density progression as measured with the optical system overlaid with final density measured with Archimedes method for SP-2140

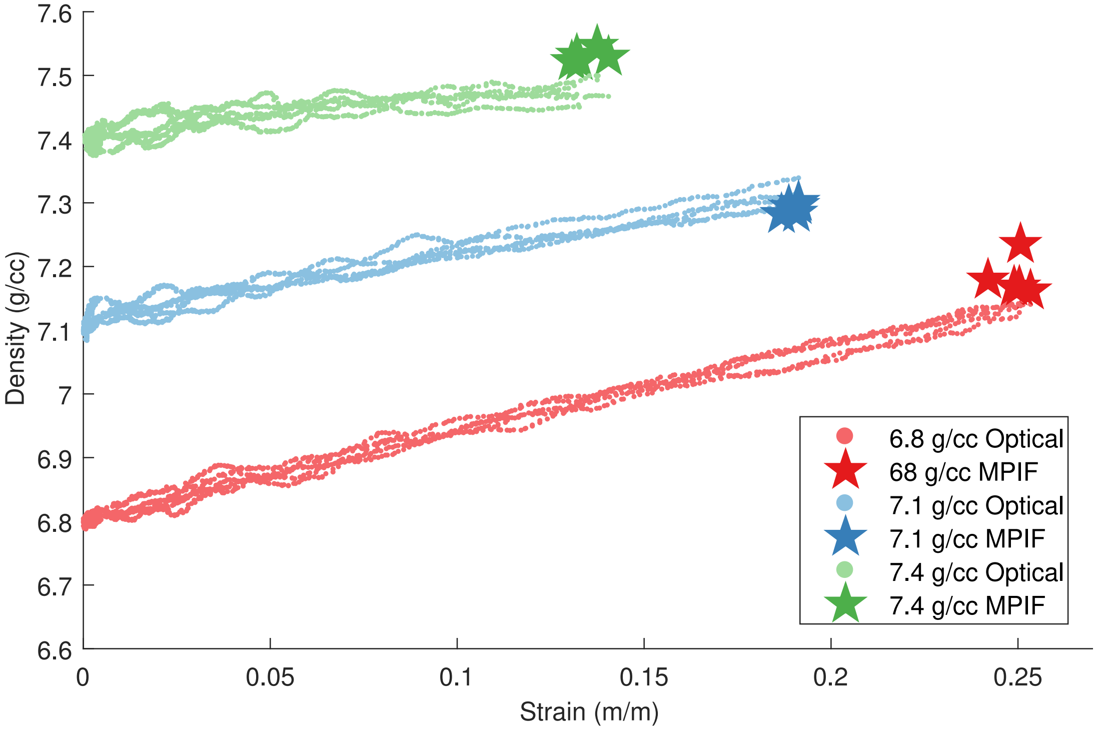

Figure 6.10: Density progression as measured with the optical system overlaid with final density measured with Archimedes method for SP-4420

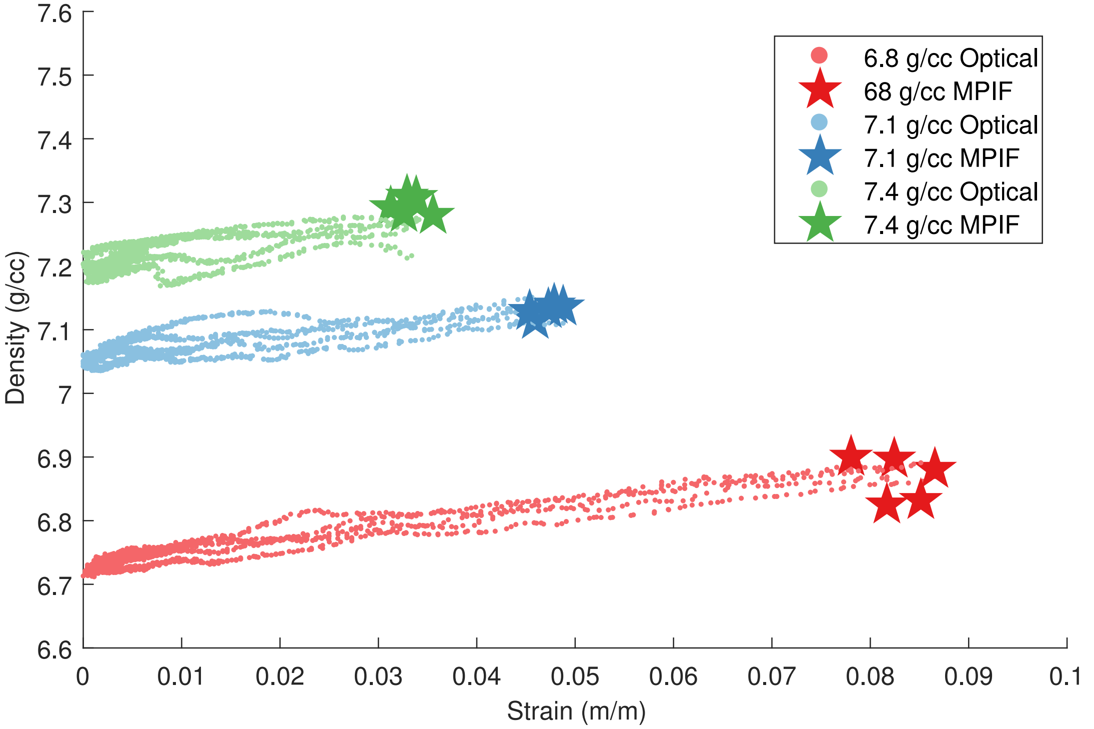

Figure 6.11: Density progression as measured with the optical system overlaid with final density measured with Archimedes method for SP-6664

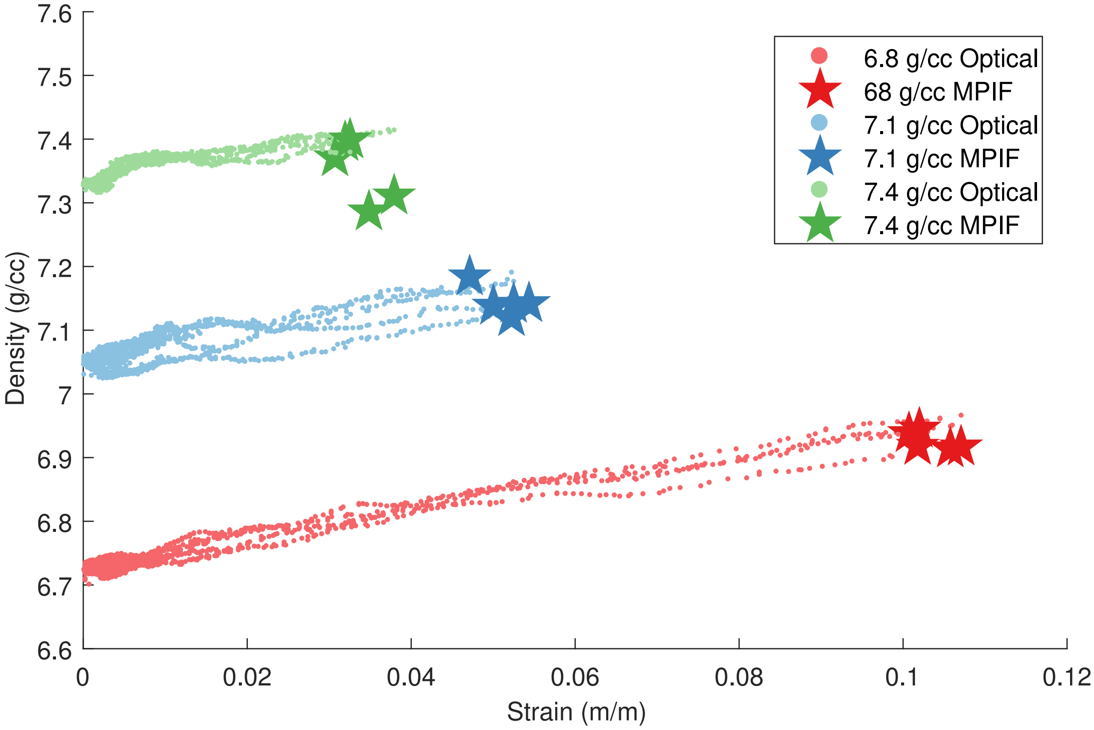

Figure 6.12: Density progression as measured with the optical system overlaid with final density measured with Archimedes method for SP-E2148

6.2 Constitutive Model Fitting

As with the ductile metals discussed in Chapter 5, Compcam as utilized to fit four constitutive material models to the behavior of all sintered materials. However, not all the same material models were used to represent the behavior of these alloys. Specifically, the linear plasticity model was not fit to these materials as the experimental plastic behavior for all sintered alloys would not be appropriate for such a model. As such, the bi-linear variant of the Johnson-Cook model was added to the Swift hardening rule, GTN model, and $P - \alpha$ variant used in Chapter 5.

Like the fitting of the GTN model and $P - \alpha$ variant in Section 5.2.2, the fit of each model to the force-displacement and mean radius-displacement curves will not be shown for fits in this chapter. Instead, the final true stress-strain curves for each alloy and density will be given. However, the fitting methodology used in this section is identical to that used for the wrought alloys.

6.2.1 Swift Hardening Law

The Swift hardening law proved to be a very good fit to plastic stress-strain data for all materials tested. Figures 6.13 to 6.16 show the experimental data overlaid with the optimal model fits. Table 6.2 provides the optimal constitutive model parameters determined for each material. As with the wrought alloys in the previous chapter, optimal Swift parameters were found in less than two hours for all alloys tested.

As already noted, there is good agreement between the Swift hardening law and all alloys tested. The only areas where the Swift hardening law struggled were with the alloys which exhibited a double-yield point, particularly SP-2140-74 and the entire set of SP-4420 alloys. As the Swift law was unable to account for this phenomenon, the final model fits tend to ignore the post-yield softening region and assume a smooth curve extending from the yield point. Given the brief duration of double yield point effects in these alloys, this is an acceptable approximation of material behavior. It is important to note this approximation was made by Compcam without any outside influence. It is also interesting to note that the Swift model was able to compensate for double yield point phenomenon significantly better than AISI 4140 and 4340 in the previous chapter.

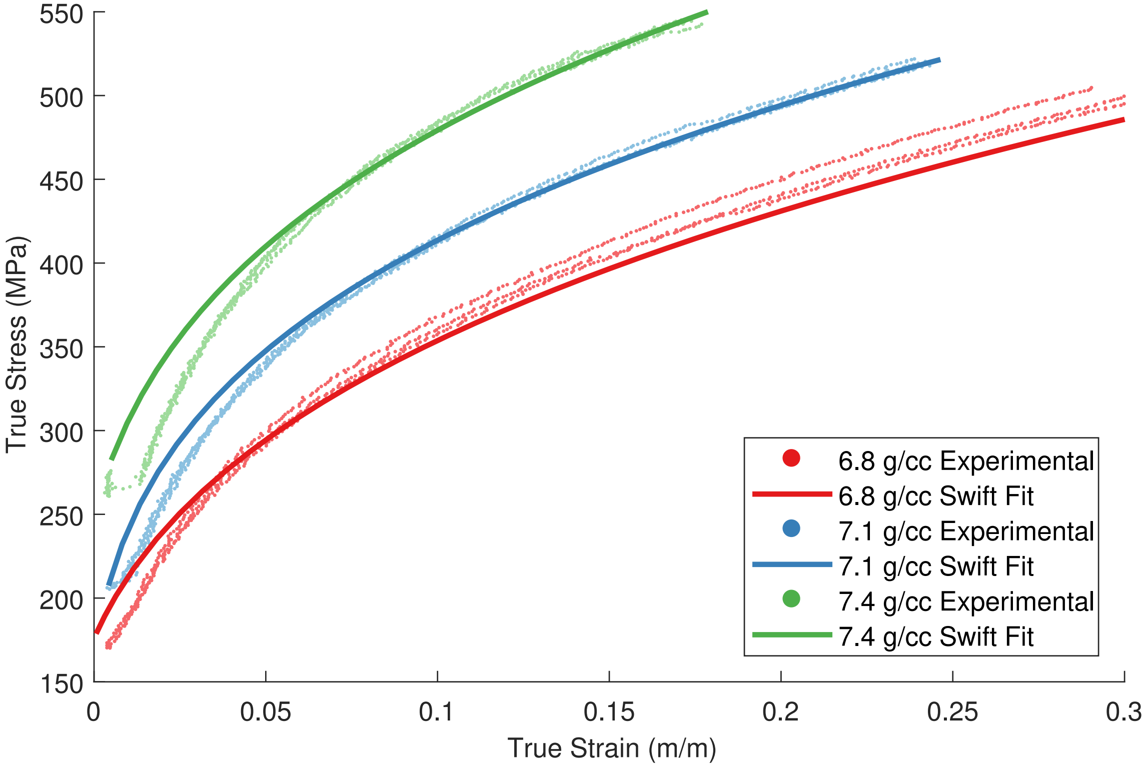

Figure 6.13: Optimal fits for the Swift model for SP-2140

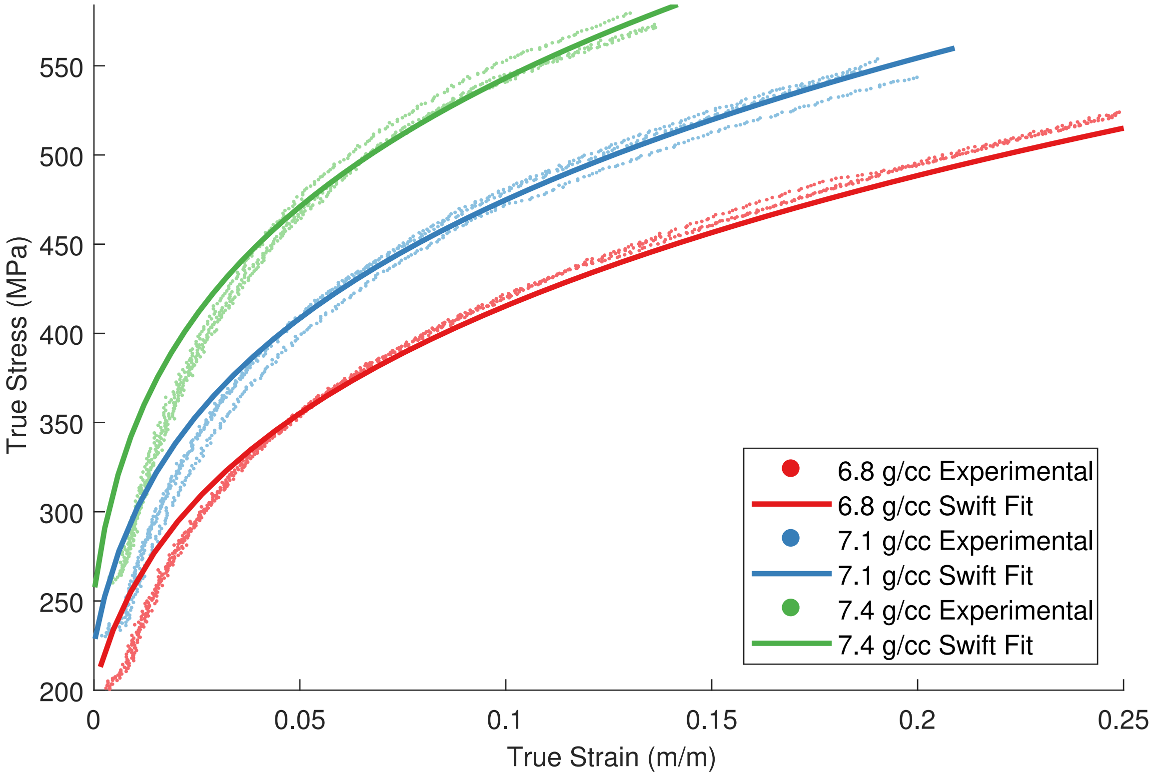

Figure 6.14: Optimal fits for the Swift model for SP-4420

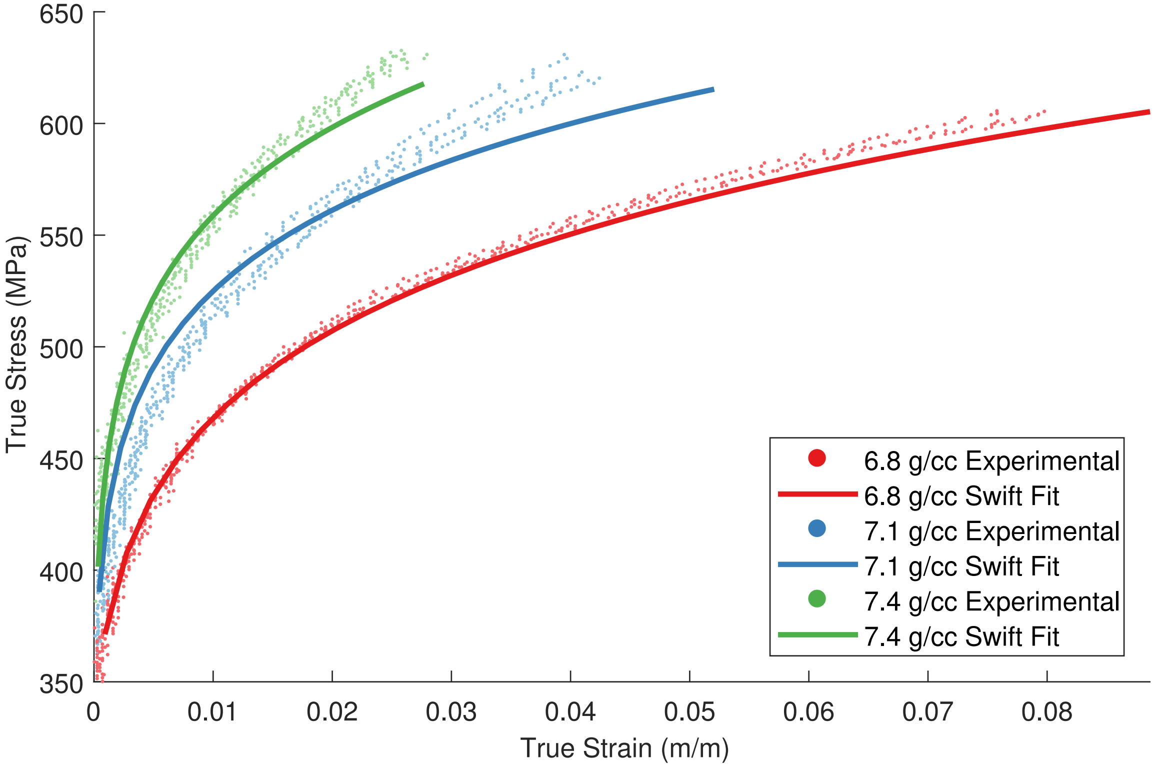

Figure 6.15: Optimal fits for the Swift model for SP-6664

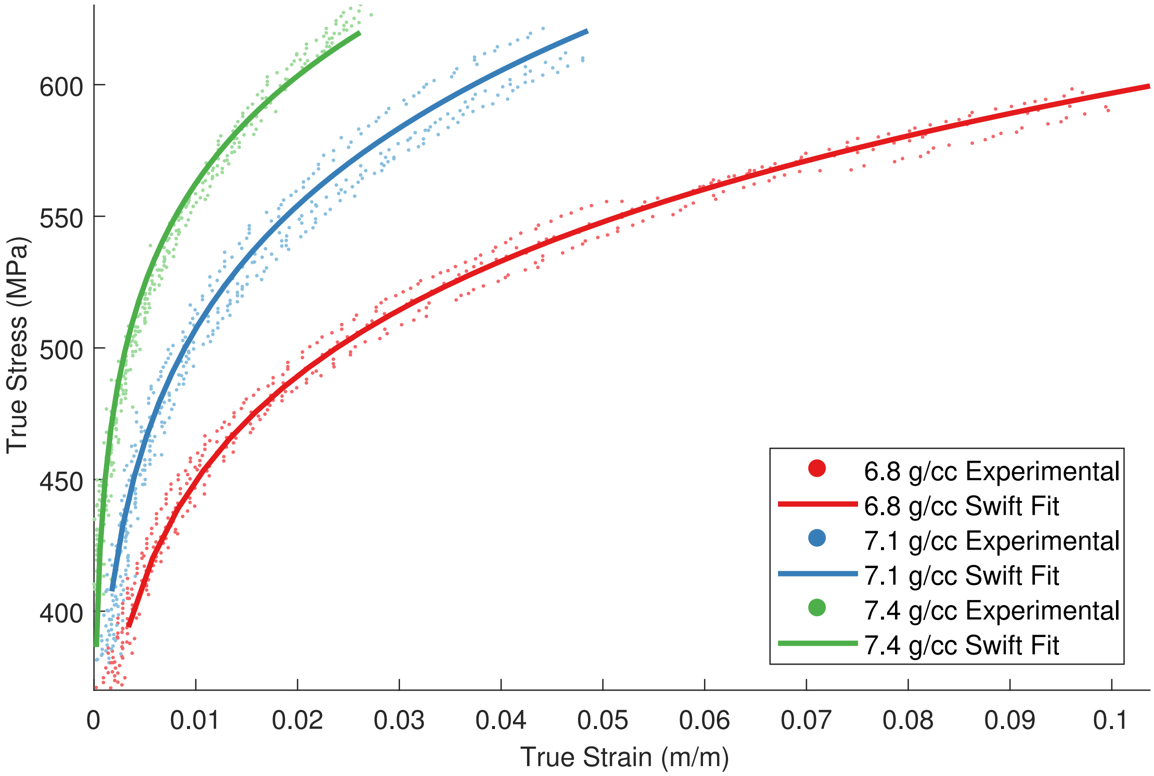

Figure 6.16: Optimal fits for the Swift model for SP-E2148

Table 6.2: Optimal Swift hardening parameters as determined through IMM

Material ID	ν	K (MPa)	n	σ_0 (MPa)	μ
SP-2140-68	0.2587	696.5	0.3090	175.9	0.0508
SP-2140-71	0.3018	750.5	0.2623	166.6	0.0550
SP-2140-74	0.2965	839.2	0.2520	250.5	0.1408
SP-4420-68	0.3054	717.3	0.2426	200.0	0.0721
SP-4420-71	0.2778	799.0	0.2300	225.5	0.0573
SP-4420-74	0.2826	884.6	0.2145	254.0	0.1151
SP-6664-68	0.2661	810.2	0.1207	333.4	0.0677
SP-6664-71	0.2886	818.1	0.0964	294.0	0.1206
SP-6664-74	0.2929	879.6	0.0985	269.4	0.0842
SP-E2148-68	0.2962	793.1	0.1236	252.4	0.0566
SP-E2148-71	0.2829	913.9	0.1280	270.5	0.1049
SP-E2148-74	0.2527	895.7	0.1010	276.7	0.0532

Despite good fits to stress-strain behavior, however, the Swift law, as with all constitutive models which use the von Mises yield criterion, was unable to account for densification of the material. Because the objective functions used by COMPCAM utilize barreling behavior to determining material parameters, the inability to account for changes in volume resulted in unrealistic values of coefficient of friction and Poisson's ratio. This is very apparent observing the values of those parameters for specimens with the lowest sintered density of 6.8 g/cc for all alloys, as lowering Poisson's ratio and coefficient of friction results in reduced barreling. However, it appears that as the sintered density increases and the densification in the material is reduced, this fitting technique was better able to determine realistic material parameters as the minor changes in volume measured experimentally agree better with the Swift model's assumption of volume consistency.

6.2.2 Gurson-Tvergaard-Needleman Model

Observing the fits provided by the GTN model to each material in Figures 6.17 to 6.20, one will note that while they are adequate at describing the stress-strain behavior of the material, they do not have the same quality as Swift hardening law. As noted in Section 4.2.3, this is due to the lack of flexibility afforded by the one-term power law hardening rule this implementation of the GTN model uses. Further, like the Swift law, the GTN model is also unable to account for the post-yield softening seen in SP-2140 and SP-4420.

Table 6.3: Optimal GTN parameters as determined through IMM

Material ID	E (GPa)	ν	μ	SIGY (MPa)	N	f_c	f_N	ϵ_N	s_N
SP-2140-68	200.3	0.3091	0.1134	158.1	4.5629	0.4729	0.1924	0.2317	0.1772
SP-2140-71	200.2	0.3129	0.1202	199.6	5.3395	0.5000	0.2546	0.2187	0.1732
SP-2140-74	199.2	0.3000	0.1219	265.8	6.5227	0.5085	0.2266	0.2129	0.1657
SP-4420-68	200.1	0.3096	0.1237	201.4	4.7896	0.4981	0.2289	0.2714	0.2272
SP-4420-71	200.2	0.3103	0.1239	205.2	4.6021	0.4917	0.2280	0.2766	0.2256
SP-4420-74	200.2	0.3105	0.1048	254.0	5.2529	0.4714	0.2272	0.2830	0.2341
SP-6664-68	200.9	0.2812	0.0576	398.8	5.5096	0.4752	0.2299	0.2711	0.2525
SP-6664-71	199.7	0.3054	0.1278	378.6	4.6466	0.4839	0.2271	0.2749	0.2199
SP-6664-74	201.9	0.3135	0.0842	375.3	4.4171	0.4845	0.2293	0.2586	0.2178
SP-E2148-68	200.1	0.3086	0.1012	414.6	6.2856	0.4896	0.2276	0.2767	0.2252
SP-E2148-71	198.4	0.2886	0.0844	378.8	4.6073	0.4846	0.2260	0.3045	0.2274
SP-E2148-74	199.4	0.3004	0.0901	383.0	4.4380	0.4943	0.2298	0.2850	0.2272

Despite the reasonable fits produced by Compcam, examining the optimal constitutive parameters in Table 6.3 yields some surprising observations. First, initial yield strength does not make physical sense, particularly for densities of 6.8 and 7.1 g/cc. However, this discrepancy is due to the power law hardening rule available in *MAT_GURSON. By forcing hardening parameters to be related to elastic parameters such as Young's modulus and initial yield strength, Compcam naively lowered yield strength to better describe plastic behavior. Trials were conducted constraining the values which SIGY to correlate with experimental data, however, this resulted in a significant reduction in the quality of the fits. In many respects, this result is similar to the issue of fitting friction discussed in Section 5.2.1.1.

Another issue experienced by primarily SP-6664 but also SP-E2148 to a lesser degree is the unusual values of coefficient of friction and Poisson's ratio, particularly for SP-6664-68. This was caused by the GTN model being unable to adequately describe the densification of the material. While this was an issue for all materials, the combination of low sintered density and the reasonably small amount of plastic deformation compared to SP-2140 and SP-4420 amplified this issue. The densification behavior of the GTN model is elaborated on further in Section 6.2.5.

A final interesting note on the final GTN parameters is the convergence of certain parameters between the alloys tested. Specifically, the critical void fraction and all three nucleation parameters showed convergent behavior. However, it is important to note no FE model actually exhibited a void fraction which approached either f_c

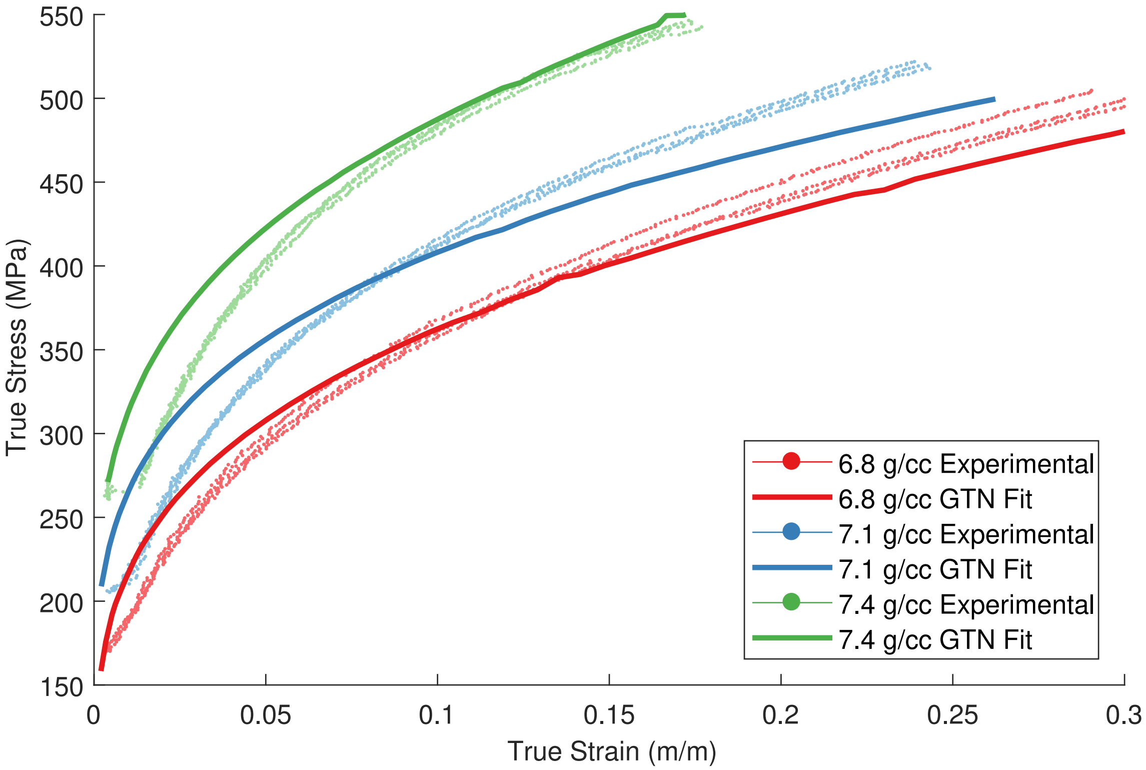

Figure 6.17: Optimal fits for the GTN model for SP-2140

or f_N due to the compressive nature of the testing and relatively low amounts of plastic deformation imparted on the specimens. However, since ϵ_N and s_N are tied to f_N, it is unknown why inactive variables converged to the same values. This finding implies the majority of GTN parameters are not active or required when modeling a cold upsetting test, at least to the reasonably small degree of deformation imparted during the experimental work conducted here.

6.2.3 Johnson-Cook Model with Bi-Linear Equation of State

The bi-linear variant of the Johnson-Cook model proved to be a good fit to experimental stress-strain data, as seen in Figures 6.21 to 6.24. While the quality of the fit is not quite as consistent as the Swift law, particularly at large deformations with alloys SP-2140 and SP-4420, it represents a distinct improvement over the GTN model. Optimal constitutive material parameters are presented in Table 6.4.

While the Swift law may outperform this implementation of the Johnson-Cook model in terms of runtime and quality of fit to stress-strain behavior, the use of an equation of state allows the Johnson-Cook model to model densification. While the ability of

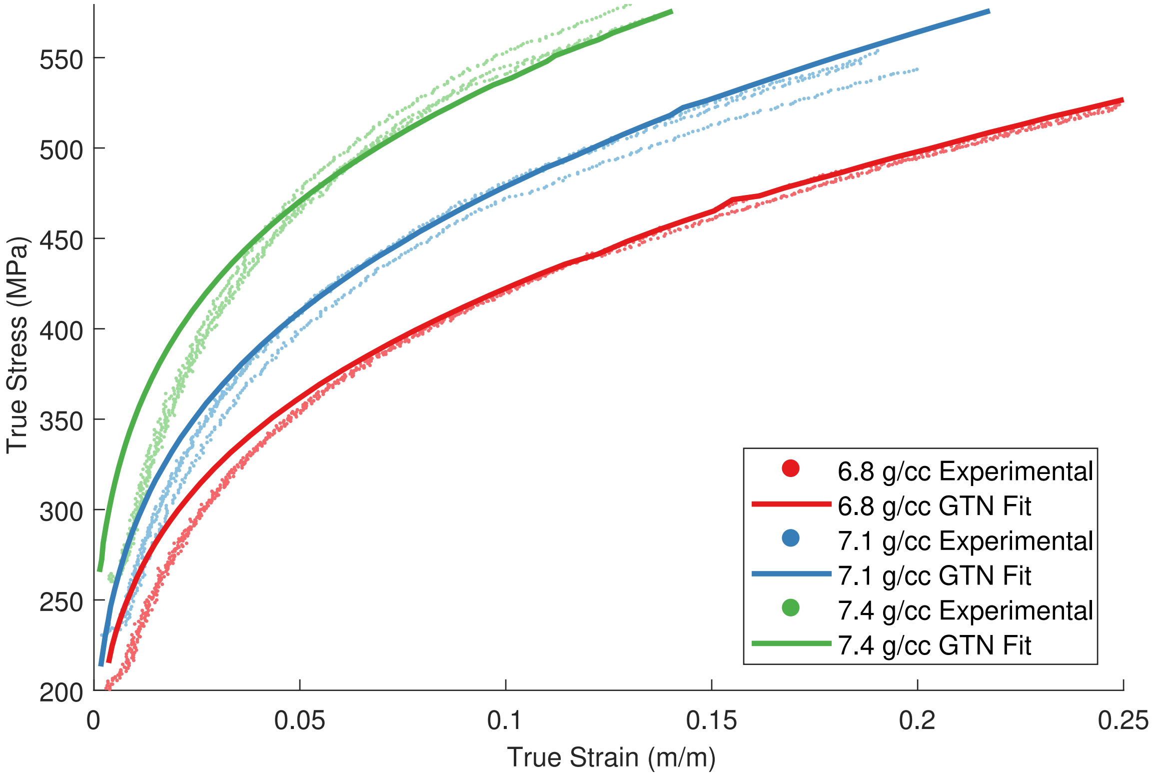

Figure 6.18: Optimal fits for the GTN model for SP-4420

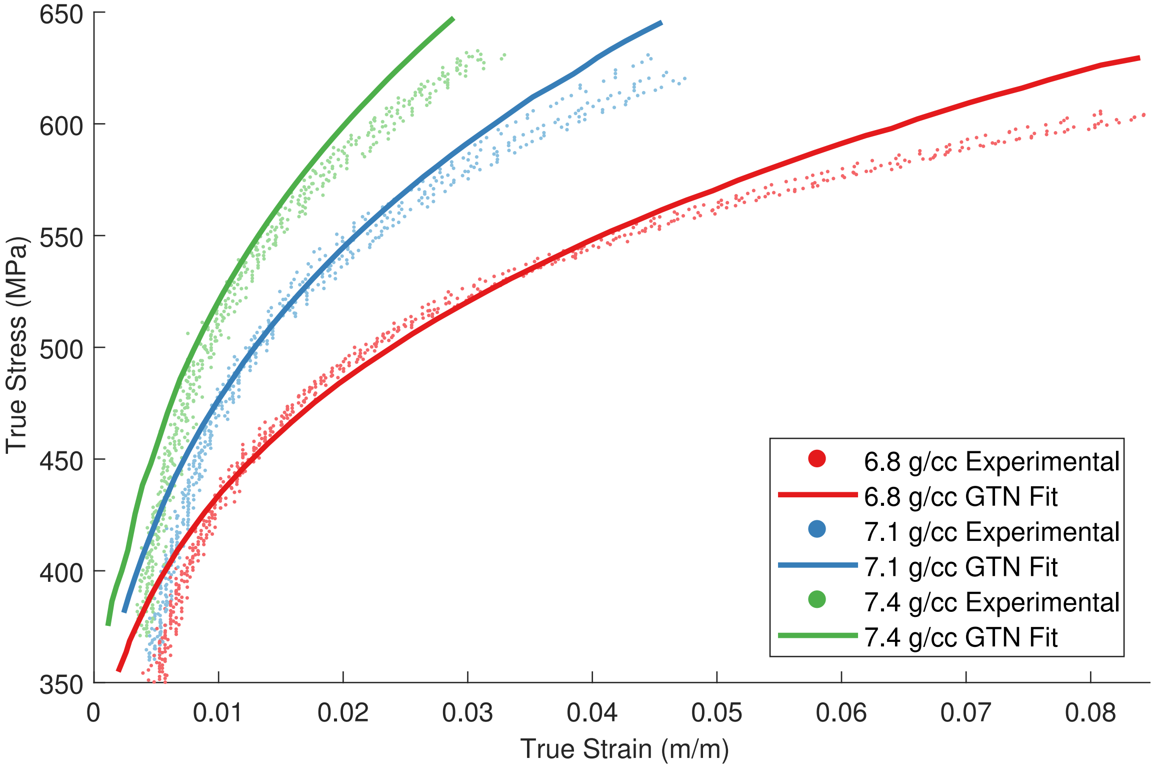

Figure 6.19: Optimal fits for the GTN model for SP-6664

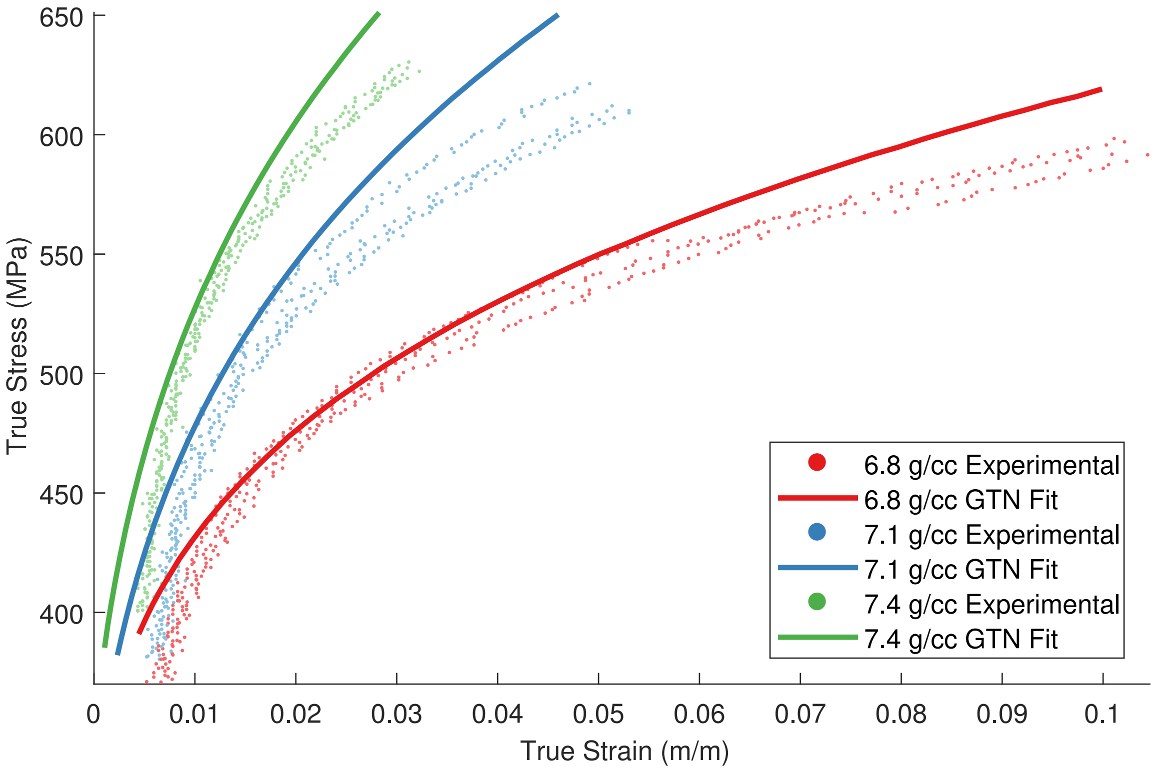

Figure 6.20: Optimal fits for the GTN model for SP-E2148

all material model used to predict the densification behavior of these sintered alloys is presented later in this section, one indication that the bi-linear variant provides a better fit to densification behavior is the consistency of the coefficient of friction tuned for each alloy. The optimal coefficient remains consistent between sintered densities, in comparison to the variation seen with both the Swift hardening law in Table 6.2 and the GTN model Table 6.3.

Like the Swift model, this Johnson-Cook model fit the double yield point present in SP-2140 and SP-4420 by effectively ignoring this region of softening behavior.

6.2.4 Johnson-Cook Model with $P-\alpha$ Compaction Curve

The $P - \alpha$ variant of the Johnson-Cook model proved to be an equally good fit to stress-stress strain behavior as the bi-linear variant. The fit of the $P - \alpha$ variant to all alloys is provided in Figures 6.25 to 6.28. Optimal constitutive model parameters are given in Table 6.5.

Table 6.4: Optimal Johnson-Cook parameters with a bi-linear equation of state.

Material ID	G (GPa)	A (MPa)	B (MPa)	n	C_1 (MPa)	$\epsilon_{V,2}$	C_2 (MPa)	$\epsilon_{V,3}$	C_3 (MPa)	μ
SP-2140-68	80.0	114.5	696.6	0.4261	64.0	-0.0415	167.1	-0.1307	252.3	0.1423
SP-2140-71	80.0	87.6	742.6	0.3373	51.2	-0.0281	181.9	-0.1222	304.6	0.1467
SP-2140-74	80.0	104.5	813.0	0.3229	69.4	-0.0228	294.3	-0.1125	386.7	0.1338
SP-4420-68	79.9	89.8	718.2	0.3133	58.6	-0.0227	162.0	-0.1222	254.7	0.1316
SP-4420-71	79.7	88.0	781.5	0.2897	58.8	-0.0195	201.8	-0.1168	293.4	0.1538
SP-4420-74	79.7	141.5	860.9	0.3215	80.8	-0.0197	281.4	-0.1379	403.8	0.1614
SP-6664-68	80.2	175.2	688.4	0.1781	116.4	-0.0359	269.8	-0.1282	396.5	0.1397
SP-6664-71	80.6	174.0	838.4	0.2038	204.2	-0.0345	330.2	-0.1459	434.0	0.1488
SP-6664-74	81.5	171.1	791.0	0.1549	205.2	-0.0726	316.3	-0.1471	404.7	0.1202
SP-E2148-68	80.0	175.5	694.3	0.1965	117.4	-0.0420	271.9	-0.1406	400.2	0.1477
SP-E2148-71	78.5	159.3	870.2	0.2004	185.0	-0.0406	311.5	-0.1464	413.1	0.1518
SP-E2148-74	80.6	183.3	771.4	0.1611	177.7	-0.0388	310.5	-0.1477	416.5	0.1654

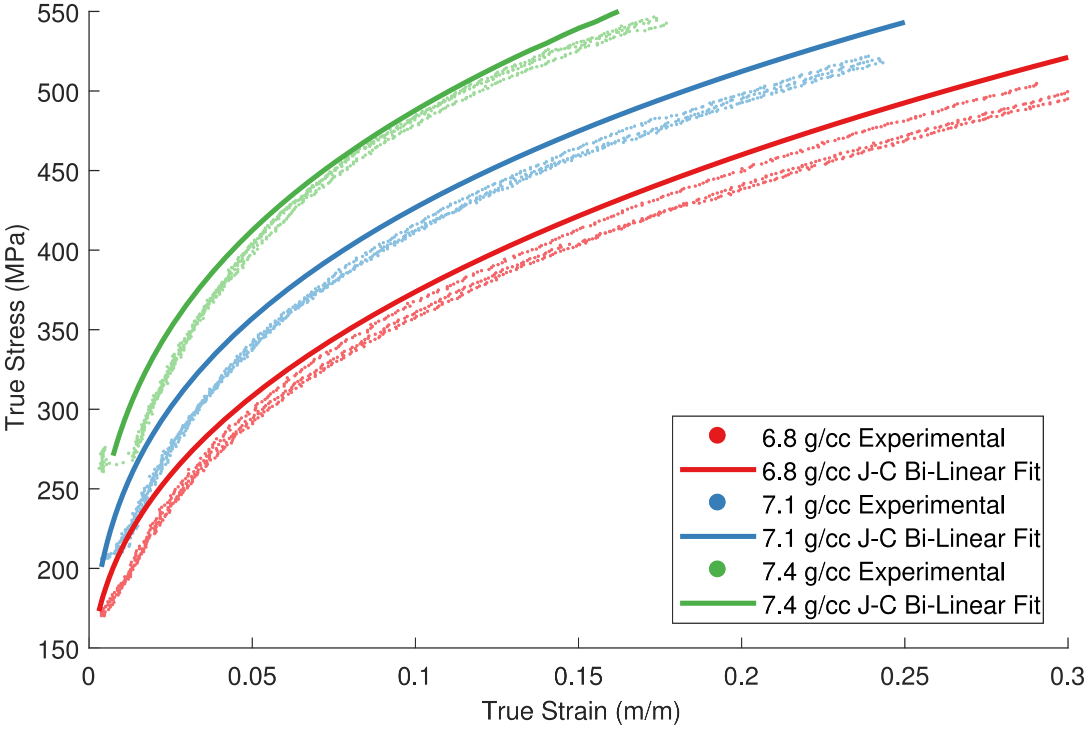

Figure 6.21: Optimal fits for the Johnson-Cook model with a bi-linear equation of state for SP-2140

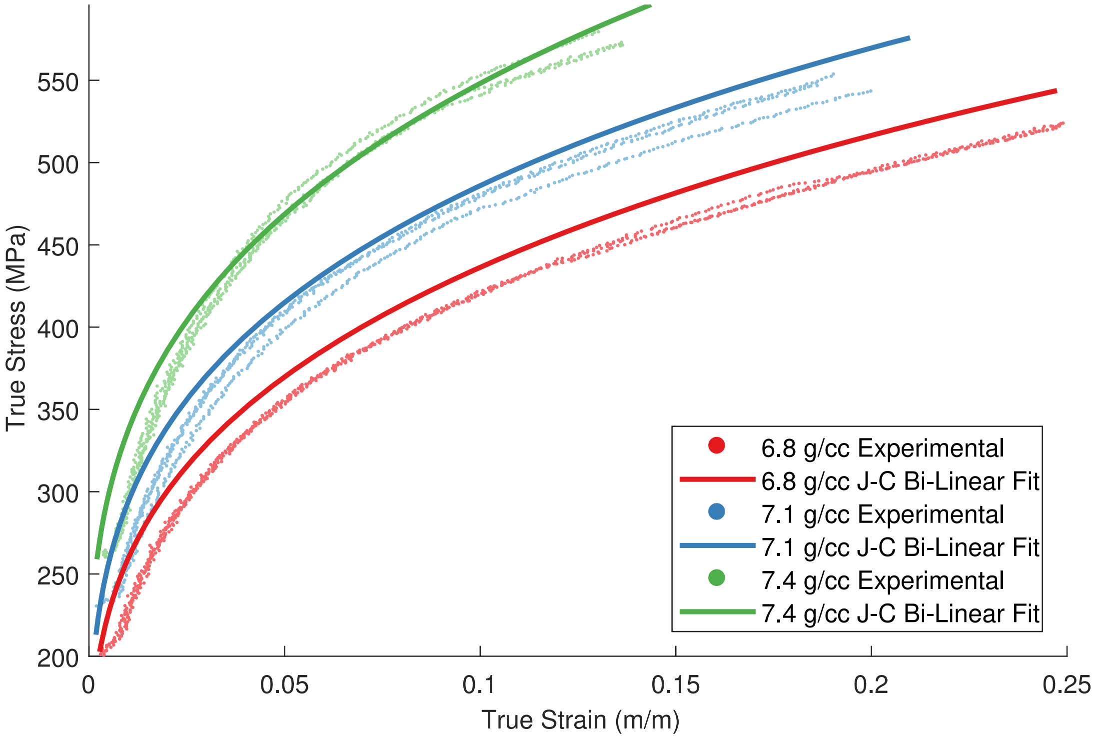

Figure 6.22: Optimal fits for the Johnson-Cook model with a bi-linear equation of state for SP-4420

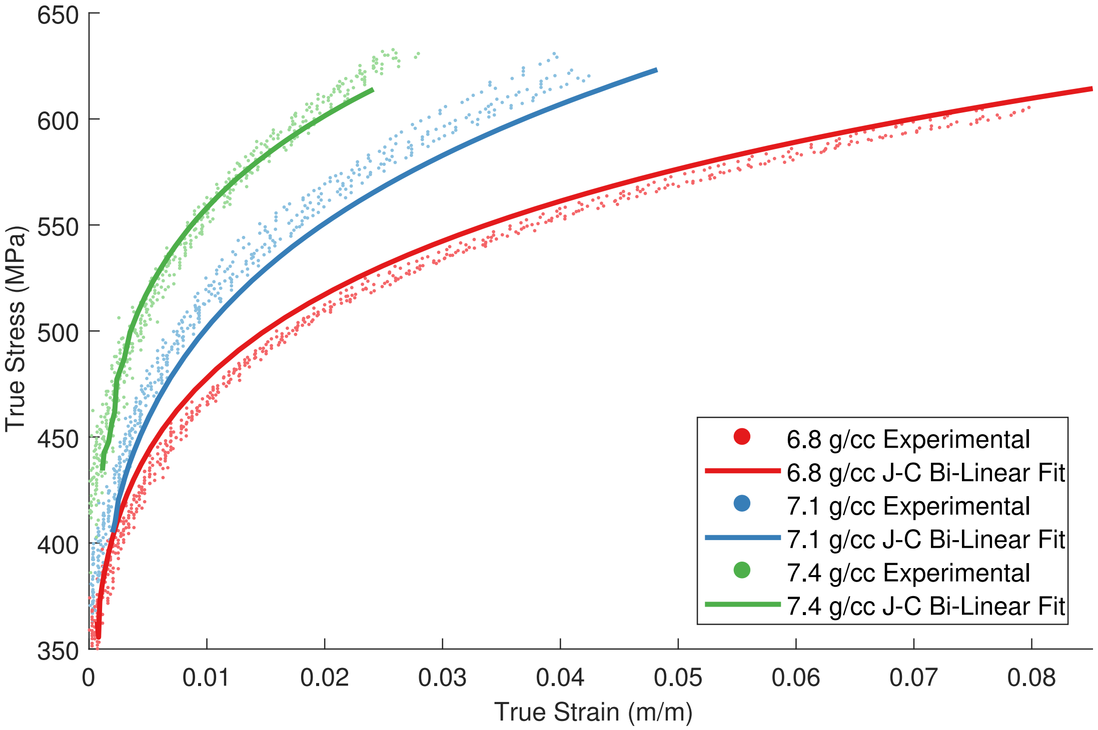

Figure 6.23: Optimal fits for the Johnson-Cook model with a bi-linear equation of state for SP-6664

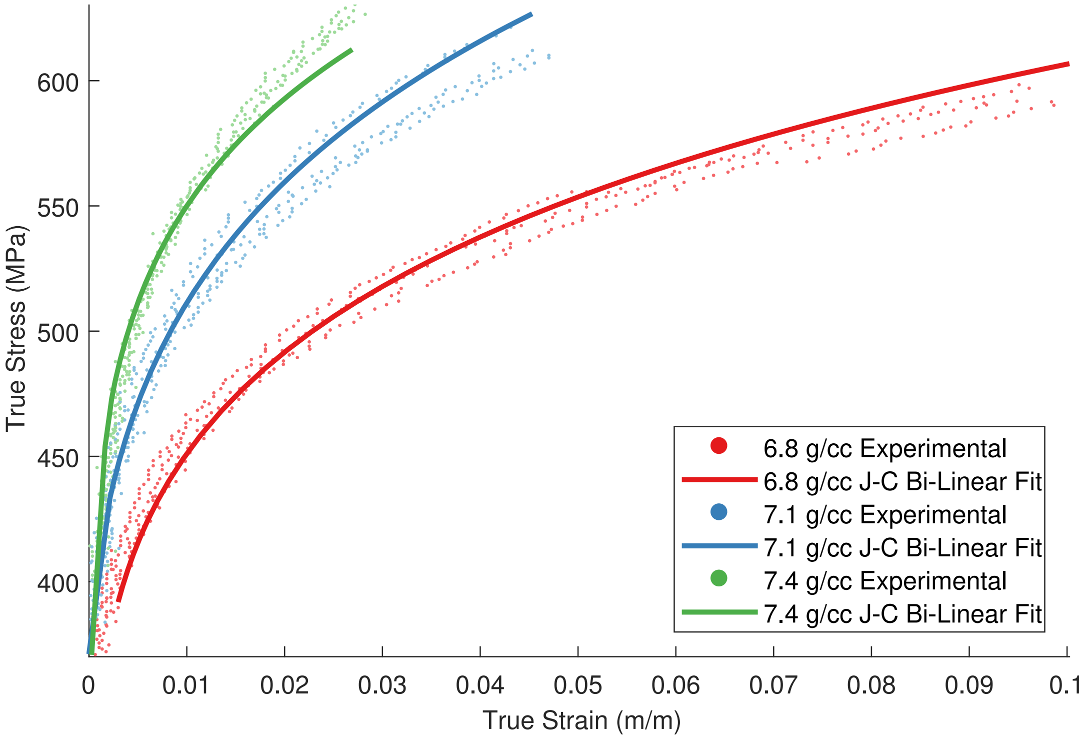

Figure 6.24: Optimal fits for the Johnson-Cook model with a bi-linear equation of state for SP-E2148

Table 6.5: Optimal Johnson-Cook parameters using a $P-\alpha$ compaction curve

Material ID	G (GPa)	A (MPa)	B (MPa)	n	P_e (MPa)	P_s (MPa)	N	μ
SP-2140-68	80.0	137.3	690.9	0.4789	92.26	567.8	2.823	0.1530
SP-2140-71	80.3	103.9	756.0	0.3759	103.4	681.2	3.046	0.1457
SP-2140-74	79.9	143.9	779.1	0.3560	84.83	571.3	1.222	0.1649
SP-4420-68	79.2	144.6	714.0	0.4034	120.0	718.3	3.641	0.1510
SP-4420-71	79.9	146.5	745.5	0.3491	92.70	583.6	1.217	0.1610
SP-4420-74	80.7	130.0	856.6	0.3050	70.90	799.4	1.475	0.1873
SP-6664-68	79.0	217.7	707.7	0.2300	126.6	749.1	1.225	0.1233
SP-6664-71	81.1	216.1	827.7	0.2384	122.8	610.2	0.2728	0.1494
SP-6664-74	79.6	198.9	882.3	0.2095	177.4	846.0	3.287	0.1431
SP-E2148-68	78.9	102.2	770.0	0.1801	176.4	787.4	3.153	0.1405
SP-E2148-71	79.7	219.2	770.1	0.2119	99.63	746.3	0.5871	0.1522
SP-E2148-74	78.4	179.0	859.9	0.1830	126.6	1005	1.308	0.1388

Comparing optimal flow rule parameters between the two Johnson-Cook variants, one will note that there are somewhat large deviations. However, owing to the different methods of modeling pressure-volume behavior, such difference in flow rule are to be expected. However, like the bi-linear variant, the values of A and B in the $P-\alpha$ variant do not exhibit a consistent increase with increasing sintered density, even though the material's measured yield strength does increase. However, such deviations are to be expected as Compcam is attempting to naively minimize the error between the model response and experimental data. As with the GTN model, attempts to force Compcam to use realistic parameters resulted in lower quality fits.

Unlike the bi-linear variant, the $P-\alpha$ model does seem to experience somewhat more variation in coefficient of friction. Based on the optimal parameters from the Swift and GTN models, this could indicate that the $P-\alpha$ Johnson-Cook model is not predicting density as well as the bi-linear equation of state. This supposition is explored more in the following section.

6.2.5 Comparison of Densification Behavior

One of the key aspects of this investigation is how well each material model used in this chapter captures the densification effects of the alloys tested. Of the four material models used in this chapter, all but the Swift hardening law are able to account for changes in a material's volume during plastic deformation. The GTN model can

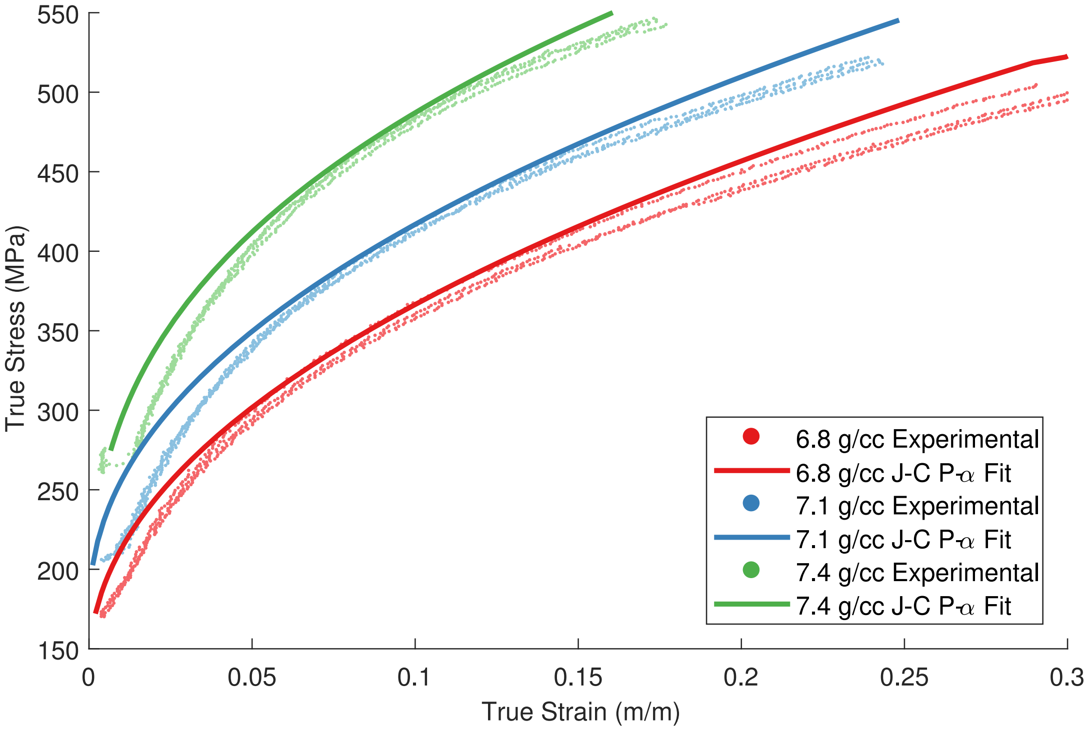

Figure 6.25: Optimal fits for the Johnson-Cook model with a $P - \alpha$ for SP-2140

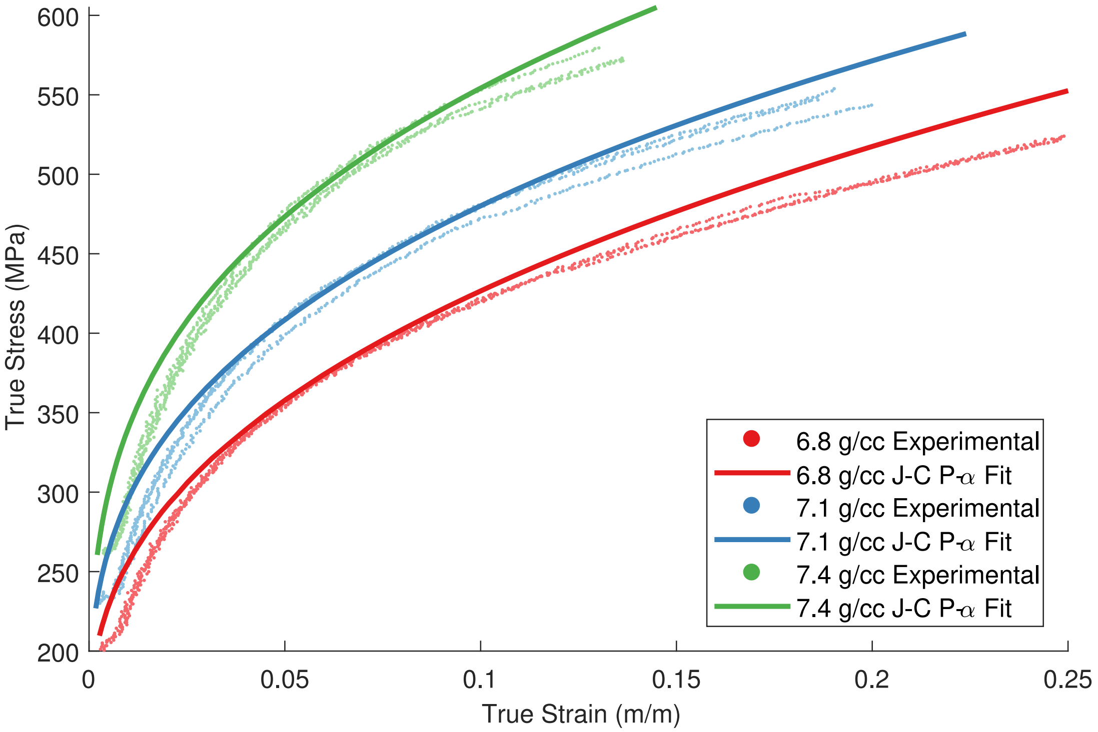

Figure 6.26: Optimal fits for the Johnson-Cook model with a $P - \alpha$ for SP-4420

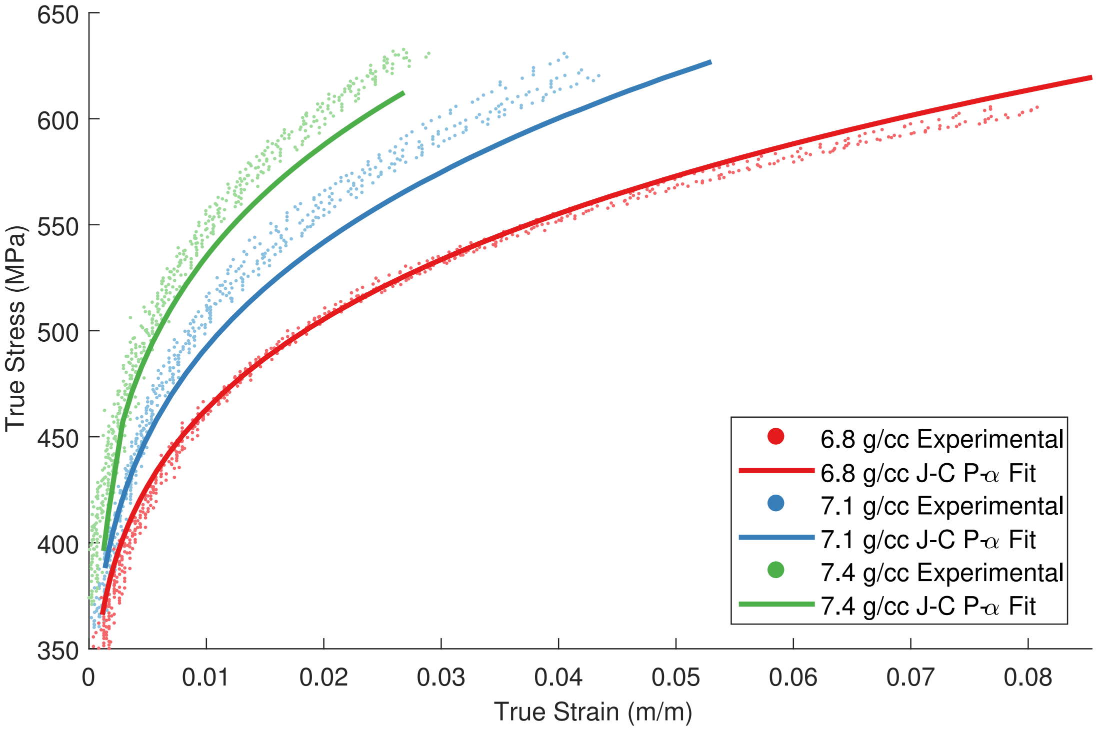

Figure 6.27: Optimal fits for the Johnson-Cook model with a $P - \alpha$ for SP-6664

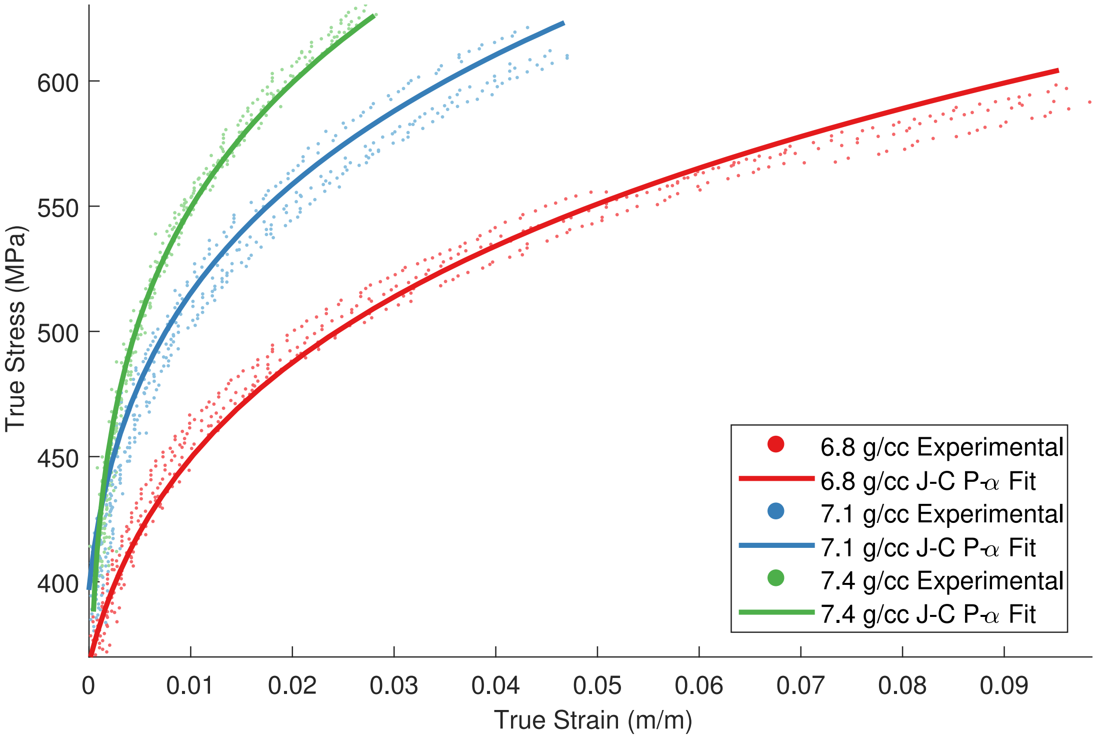

Figure 6.28: Optimal fits for the Johnson-Cook model with a $P - \alpha$ for SP-E2148

account for changes in material density internally due to the formulation of its yield criterion while the two Johnson-Cook model variants rely on an external equation of state. To compare the effectiveness of these models, Figures 6.29 to 6.32 present the density-strain behavior of each material. The Swift hardening law is not included on these plots as the density remained constant.

For each alloy and density tested, the experimental density-strain curves are approximately linear. While the GTN model is the only model used which predicts a linear increase in density with strain, the GTN model consistently underestimates the degree of densification in the material. This underestimation is a direct result of the formulation of the GTN model used by Ls-Dyna. Ls-Dyna uses the original formulation of the GTN model in *MAT_GURSON. The original GTN model was used primarily to model drawing and forming of sheet metal (Chu and Needleman, 1980; Tvergaard, 1981), where biaxial tension is the most prevalent state of stress, with shear stress being a secondary concern. As a result, the original GTN model only allows for the growth or contraction of pores as a result of hydrostatic stress.

While effective for sheet metal forming, the assumption of minimal shear stress does not apply to the cold upsetting test where shear stress, which primarily influences the deviatoric component of stress, is by far the biggest factor. As a result, the original GTN formulation, and the formulation within Ls-Dyna, cannot accurately model densification of a cold upsetting test. While several modifications and extensions to the GTN model exist to account for the effects of a highly deviatoric stress state, either through the use of a second set of damage parameters (Malcher et al., 2014; Xue, 2008) or by considering anisotropic pore deformation Gologanu et al. (1993), they are not available as a stock material model in Ls-Dyna nor were they explicitly developed to model densification behavior. While these extensions could be added as a user-defined material model, it as decided not to develop a custom material model for three reasons. First, development of a user-defined material model takes significant time, even for constitutive models which are well documented in the literature. Second, while it may prove interesting and perhaps even effective, implementing a material model developed by another researcher does not have the same scientific novelty as developing one's own version. Third and finally, the industry client for this work, Stackpole International, wanted a turnkey solution, not a custom user-defined material.

Both variants of the Johnson-Cook model proved to be a good fit to experimental densification behavior. However, one variant does not seem to reliably model density better than the other. Interestingly, despite the disparity in optimal coefficients of friction seen for the $P-\alpha$ variant, this variant predicts densification behavior well for all alloys, even when the bi-linear variants provides a slightly better fit. This could imply that when using the $P-\alpha$ variant of the Johnson-Cook model, the coefficient of friction has much less impact on the quality of fit than the equation of state and flow rule parameters.

In both variants of the Johnson-Cook model, the disparity in fit to densification behavior seems to appear during the low deformation region of plastic behavior. Perhaps the best example of this is seen in Figure 6.29 for SP-2140-71. While the bi-linear variant predicts initially trends steeply upward before leveling off, the $P-\alpha$ variant trends upward slowly before beginning to match experimental behavior. This trend is seen for several other fits presented here. It is possible this behavior is a result of a local minimum found by COMPCAM. However, resolving this issue with the current objective function could be challenging, as this densification is not fit directly, but is instead inferred through the use of the radius-displacement data extracted from SPECS. This finding further substantiates suggestions made in Section 5.2.1.1 that while largely effective for this work, an alternative objective function should be investigated to improve performance.

While both Johnson-Cook variants predict bulk densification well, bulk density provides little information about the density gradient which develops within a specimen. The different stress states which develop within a cold upsetting specimen will result in a non-uniform density gradient within the specimen. To that end, work was carried out to map the density gradient with a specimen using DEAD.

This work was hampered by several factors. First, the specimen preparation required for optical density measurements was very time-consuming, particularly with the large surface area which needed to be polished. Further, microscopy was also challenging. In order to capture an image of high enough resolution for a high-quality density map to be produced by DEAD, a mosaic of over 200 images was acquired at 50X magnification. This process was extremely time-consuming using a microscope with a manual translation stage. As a result, only one alloy and density was mapped, specifically SP-2140-68. This material was selected as it experienced the largest degree of densification, which would make density gradients within a specimen the most pronounced.

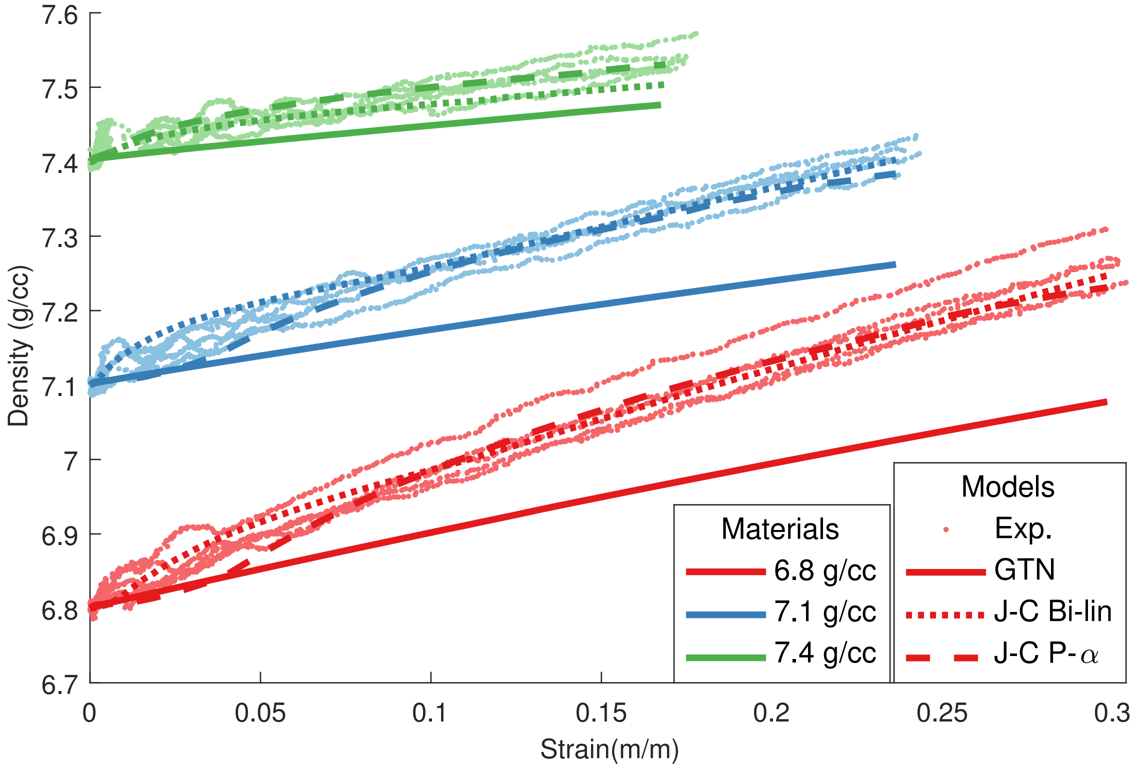

Figure 6.29: Densification of SP-2140 as predicted by three material models.

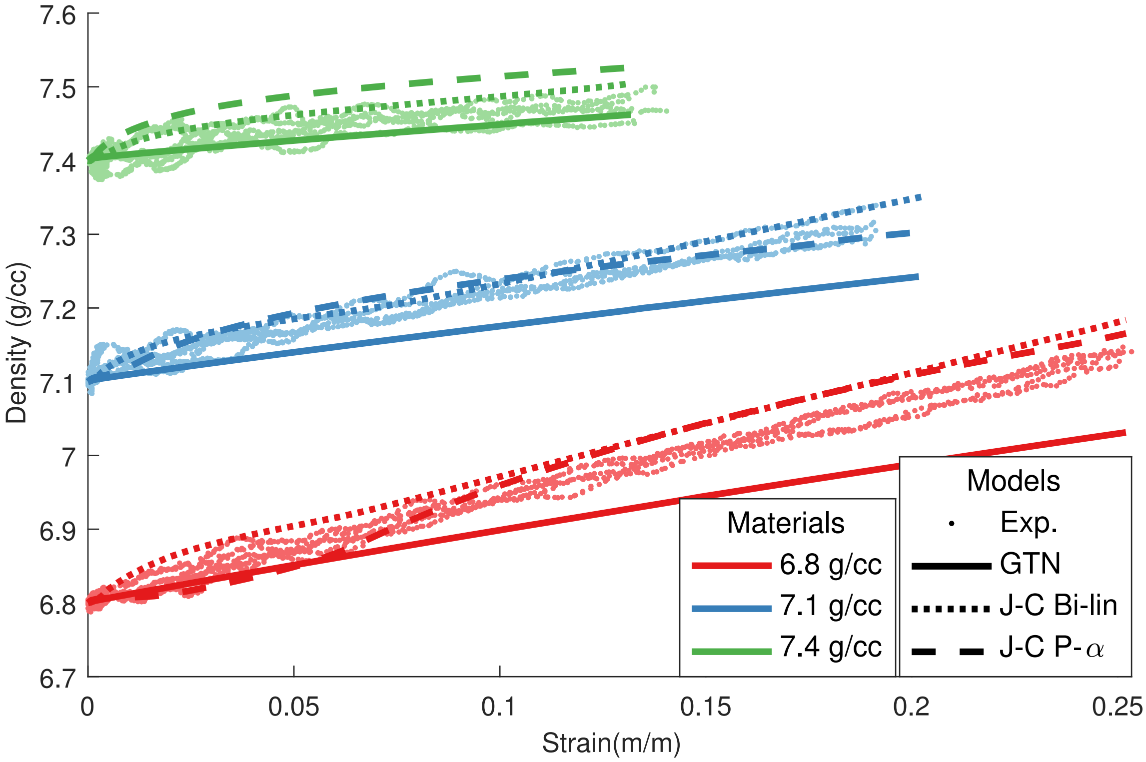

Figure 6.30: Densification of SP-4420 as predicted by three material models.

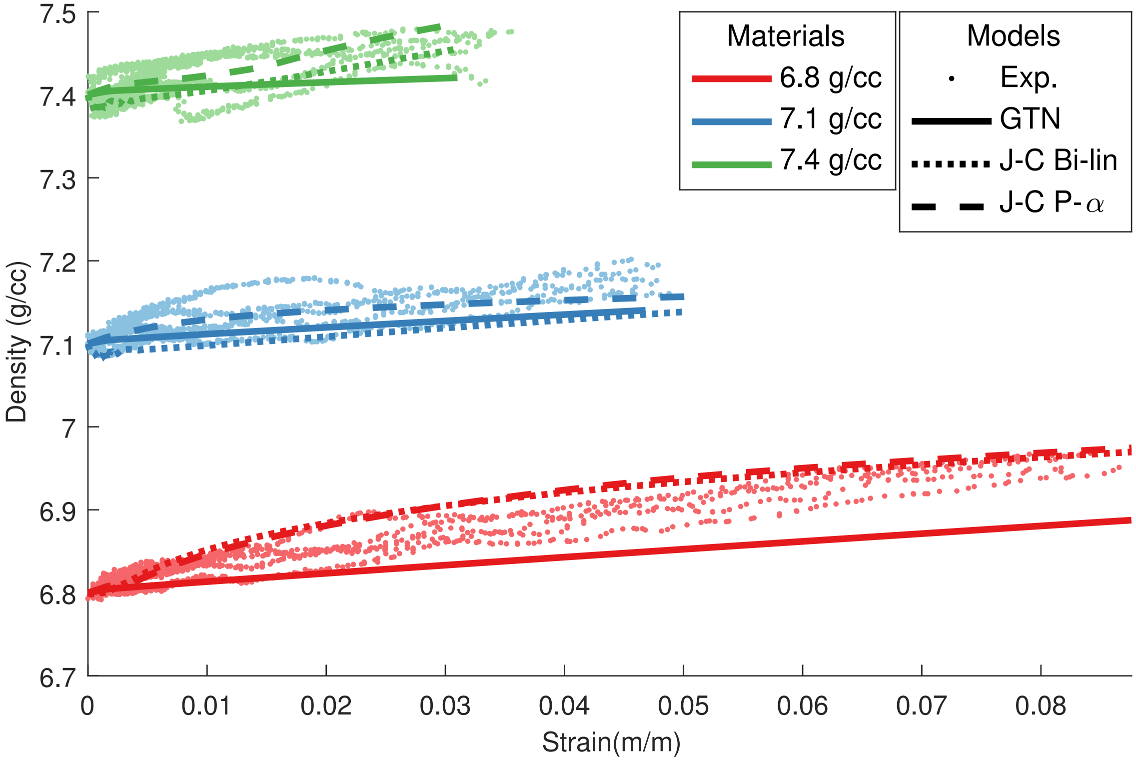

Figure 6.31: Densification of SP-6664 as predicted by three material models.

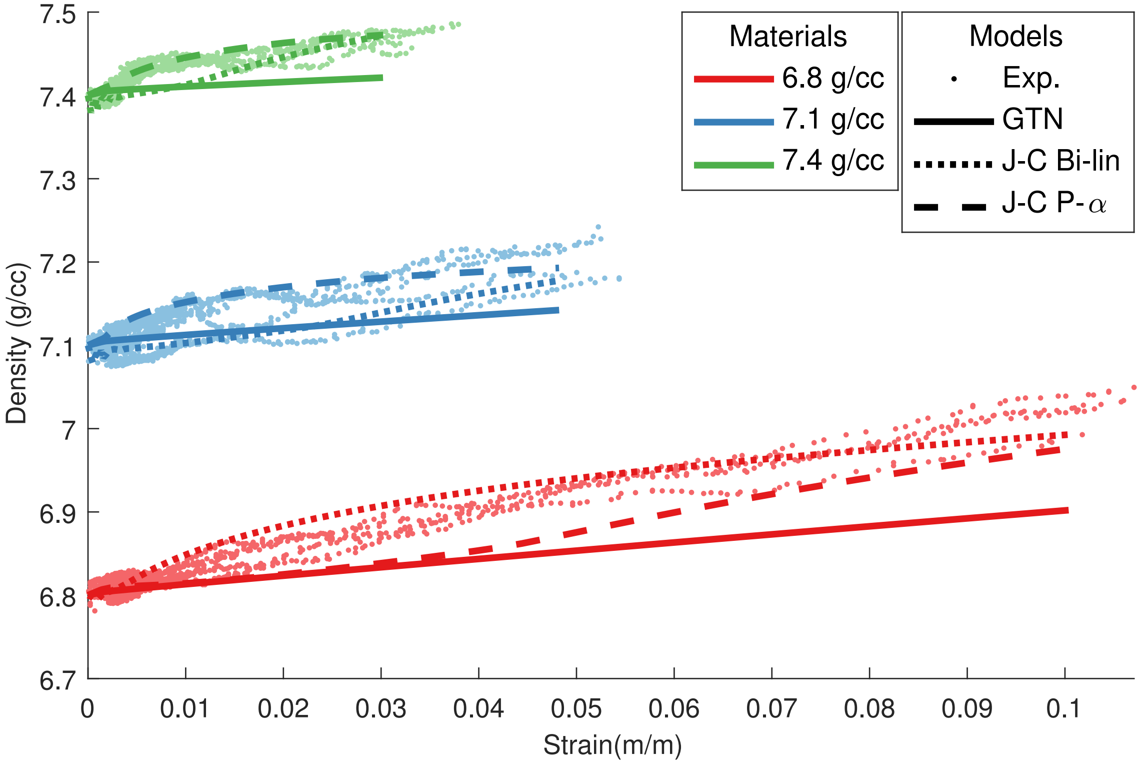

Figure 6.32: Densification of SP-E2148 as predicted by three material models.

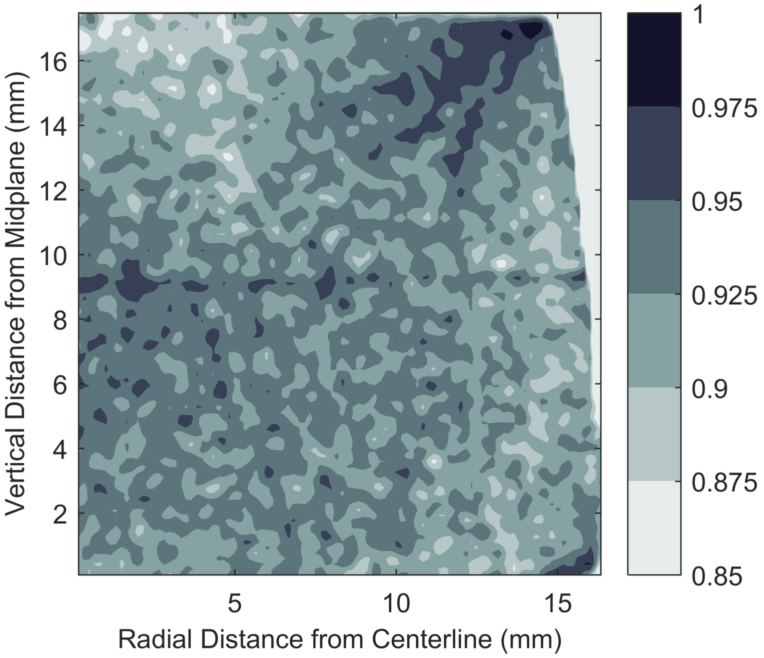

Figure 6.33: Optical density map of SP-2140-68 using a 0.35 mesh size

Figure 6.33 shows the density map of the top quarter of a specimen of SP-2140-68 captured with a mesh size of 0.35mm. This allowed for approximately 100 elements along both dimensions. The final map was filtered through convolution using a 3x3 Gaussian kernel to smooth mapping noise and make trends more pronounced. Even with filtering, there is significant spatial noise. Nonetheless, one will note that relative density is highest at the outer corner of the specimen where the barreling of the material causes the edge to fold over. This area of the specimen is experiences significantly higher stresses than the rest of the specimen, as such high densification is to be expected.

The area of lowest density in the specimen occurs near the top of the specimen near its centerline. This is the area of the specimen which is in direct contact with the platen. The low densification seen here may be a result of frictional forces mitigating the degree of deformation this area of the specimen undergoes, hence reducing the degree of density. Another area of low density is the near the outer surface of the specimen between the specimen's midline and outer corner. Note that the high density seen at the specimen's midline is actually an artifact caused by incomplete polishing and should be disregarded.

While material density increases moderately along the specimen's centerline toward its midplane, the largest areas of densification are along a diagonal connecting the outer corner of the specimen and the very center of the specimen. Interestingly, this diagonal corresponds with both the area of maximum shear stress in the material as well as the fracture plane seen in both aluminum and brass specimens detailed in Section 5.1.1. It is likely the high degree of both shear stress and stress triaxiality along this diagonal is a direct contributor to increased densification. Work by Yazici et al. (2008) helps to validate that the density maps produced here as well as the overall trends in density gradient which develop when performing cold upsetting on sintered PM alloys.

Drawing direct comparisons between the FE models used in this chapter and the density maps was not possible without significant modification to the constitutive models or element formulations used, both of which were beyond the scope of this project. Ideally, the relative density in an FE model can be extracted by tracking an element's volumetric strain. However, none of the material models or element formulations used save volumetric strain as a history variable. Further, the axisymmetric nature of the simulations prevented the use of nodal displacements to approximate volumetric strain. This is because axisymmetric formulations account for the circumferential components of displacement and stress, also known as the hoop components, internally and do not allow for the type of access which would be required to resolve volumetric strain.

As relative density could not be compared directly between experimental density maps, a qualitative comparison between the FE models and optical density maps can be made using an approximation of volumetric strain. This approximation, given in (6.1), relies on principal strains. While only truly valid at small deformations, this approximation remains useful for showing trends, if not absolute values, at large deformation. The fringe plots of the FE models running optimal parameters for the GTN model and $P-\alpha$ Johnson-Cook variant for SP-2140-68 are shown in Figure 6.34. Both fringe plots constrain upper and lower bounds of approximate volumetric strain to allow for direct comparison between the models.

$$\tilde{\epsilon}_V = (1+\epsilon_1)(1+\epsilon_2)(1+\epsilon_3) - 1 \tag{6.1}$$

While there are significant differences in the degree of volumetric strain incurred by the GTN model and $P-\alpha$ variant, this is to be expected given the differing final bulk densities. Nonetheless, both models exhibit the same patterns of volumetric strain. Further, while exact values cannot be compared, these patterns agree well

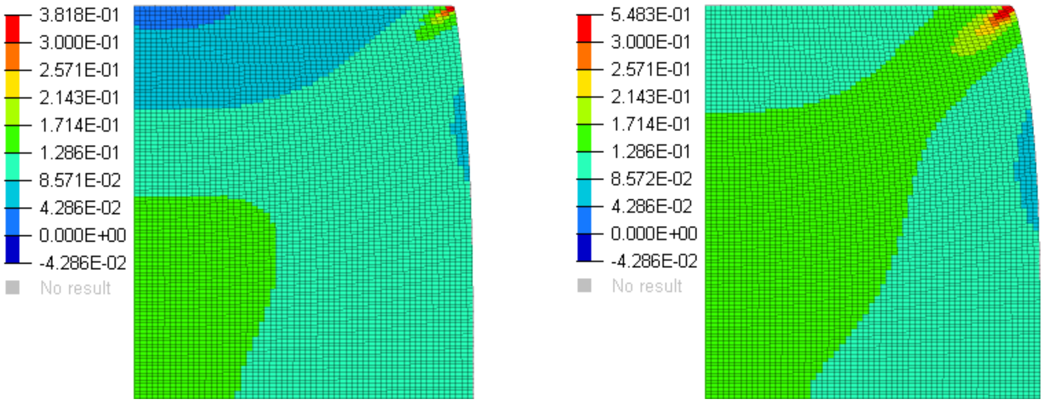

(a) GTN Model

(b) $P - \alpha$ variant

Figure 6.34: Approximate volumetric strain contours used to qualify densification.

with the experimental density map in Figure 6.33. While this result cannot be used to prove that the experimental and computational density maps agree, it does seem to suggest it. Further work is required in order to make quantitive comparisons of FE and experimental density maps

Chapter 7

Conclusions and Recommendations

7.1 Conclusions

Constitutive model fitting is a challenging and time-consuming proposition. IMM is a promising method to save time and cost in the fitting process. Compcam, a custom developed IMM framework has been the primary focus of this report. Additionally, research in this thesis has used the compressive cold upsetting test in conjunction with a specialized optical measurement system to characterize the plasticity behavior of various materials. This testing method, which is not generally used for the characterization of plastic behavior due to the combined effects of friction between specimen and platen as well as the significant stress triaxiality which develops within the test specimen, was shown to be quite effective when used with IMM to fit constitutive models.

To demonstrate the effectiveness of Compcam, two investigations were undertaken. In the first, five wrought, ductile metals alloys of varying composition and behavior were characterized using the cold upsetting test and subsequently fit to four constitutive models to predict the material's stress-strain behavior. This investigation yielded two important conclusions. First, the effectiveness of Compcam and IMM is heavily dependant on how well the constitutive model being fit describes a given material's behavior. For example, a constitutive model designed to model linear plastic behavior is not appropriate for materials which do not exhibit such linear behavior. While Compcam will produce model parameters which minimize the error between the FE model's response and experimental behavior regardless of the appropriateness of a given model, fits for inappropriate models may be poor and produce final material parameters which do not make physical sense. To that end, while Compcam is a valuable tool for model fitting, knowledgeable judgment is still required to select appropriate constitutive models and verify final model fits.

The second conclusion is that the frictional effects in the cold upsetting test can be difficult to characterize. While friction ring testing was undertaken to experimentally determine the coefficient of friction, the optimal coefficient of friction determined by Compcam rarely aligned with experimental values. In fact, in most cases, fixing the coefficient of friction used by Compcam and the FE model resulted in a lower quality fit than allowing friction to be tuned. There are several reasons for this, however, the two largest are the uncertainties in the friction ring test used and the fundamental physical differences between the experimental coefficient of friction and the numerical algorithms used by FE solvers to model friction.

Keeping these findings in mind, the first investigation in wrought alloys showed that Compcam and IMM were very effective at fitting constitutive models to experimental behavior, provided the constitutive model was appropriate for a given material. Furthermore, fitting was accomplished in under 24 hours at most, with user interaction only required at the beginning of that period to initialize Compcam and the end to confirm the quality of the final fitted model. Compared to manual fitting techniques, which require generally require manual iteration and significant degrees of user interaction, Compcam presents large savings in terms of both time and personnel utilization.

In the second investigation, Compcam's ability to fit constitutive models to significantly more complex material behavior was tested using twelve ferrous, sintered PM alloys of four different compositions and three sintered densities. In this trial, four constitutive models were fit to each alloy's behavior with the goal of predicting the material's stress-strain and densification behavior. This investigation proved once again that the quality of the final constitutive model fit was highly dependant on how well the constitutive model described material behavior. Interestingly, this lead to the interesting finding that the GTN model, which was developed to model the nucleation, coalescence, and collapse of pores in a material, was unable to accurately predict bulk densification for the cold upsetting specimens used in this work. It is hypothesized that this is because the formulation of the GTN model, wherein pores only morph under hydrostatic pressure, cannot cope with the high degrees of triaxiality and shear stress which develop within a constitutive model. It was found instead that the utilization of an equation of state to control a constitutive model's volumetric deformation was more successful at predicting bulk densification.

In addition to fitting bulk densification, a qualitative analysis was undertaken using optical densitometry to compare the density gradients which develop within test specimens to those which developed within the FE models using the fitted constitutive models. While the qualitative nature of this analysis prevented definitive conclusions from being drawn, this early work indicated that the density gradients which develop within experimental and numerical cold upsetting tests are similar, despite the fact that density gradients were not directly used in the fitting process. This indicates that COMPCAM has the ability to fit material behaviors not directly utilized in the fitting process, provided a sufficiently large and relevant dataset of experimental behaviors is used.

Overall, this work has shown that IMM and, specifically, COMPCAM is an effective tool for constitutive model fitting that is both material and constitutive model agnostic. While this work has shown that COMPCAM has decided limitation in its capability, the breadth of the investigations described within this thesis shows that given appropriate constitutive models are used and limitations are understood, quality constitutive model fits can be obtained with less effort and time than traditional fitting techniques.

7.2 Recommendations

In many respects, the development of COMPCAM is still in its infancy. Due to the time limitations inherent in academia, there was a decided limit to the extent to which COMPCAM's applications could be explored. As such, there is a significant number of improvements which can be made to the tool as well as future research avenues which stem from its use.

Two improvements should be immediately investigated to improve COMPCAM's performance. The first is the utilization of an alternative objective function used by the optimization algorithm. As discovered in Section 5.2.1.1, large changes in the coefficient of friction can result in very small changes in the current objective function's value. This is despite the fact that the effects of friction are known to have a large influence. Work should be undertaken to develop a new objective function which accounts for the physical activity of each constitutive model parameter more accurately. This should improve both optimization efficiency as well as the quality of the final fitted parameters.

The second immediate improvement would be to investigate alternative optimization methods to reduce the computational expense of IMM. These optimization methods would serve to reduce the number of FE model evaluations needed to fit a given model. This improvement would allow COMPCAM to use FE models which have a significantly longer runtime to fit constitutive models without excessively long COMPCAM runtimes. It is the author's recommendation that Kriging surrogate models be investigated as an alternative fitting technique. Appendix C provides an overview of the author's early investigations into Kriging models and the development of a software tool known as MIKE. While it was the author's intent to utilize Kriging surrogates more prominently in this thesis, work had to be abandon due to time constraints. It is recommended that this work is reactivated and, in conjunction with the revised objective function discussed previously, be implemented into COMPCAM.

While not directly related to COMPCAM's functionality, another item of work should be undertaken in the short term is to determine how to extract a quantitative measure of densification from FE models. As presented in Section 6.2.5, the lack of a quantitative data limits the effectiveness of comparisons between FE models and experimental density maps. For certain application discussed later in this section, the ability to quantitatively measure deformation is a requirement for accurate model fitting.

On a longer time horizon, work should be undertaken to expand Compcam to use material tests other than the cold upsetting test. This would allow Compcam to accommodate a far wider range of materials and behavioral phenomena. One area of research which is quite pertinent is the fitting of constitutive models to the compaction of metal powders, which is of great concern to the manufacturing sector. Constitutive models used to model powder compaction are generally quite complex and current fitting methodologies require specialized equipment and intensive testing. It is the author's opinion that Compcam can be applied to this problem to overcome many of the challenges in fitting powder models. Exploratory work into this field completed by the author (not detailed in this thesis) did show promise but was ultimately abandoned due to time constraints.

In addition to the fitting of powder models, Compcam should be expanded to other forms of material test for bulk materials, such as the ubiquitous uniaxial tension test as well as some less common tests such as the short beam bending test/transverse rupture strength test, the Brazilian disc test, and ideally, the split Hopkinson bar test. Expansion into these material tests would require somewhat significant work to modify or develop appropriate instrumentation systems for such tests. In particular, it is the author's suggestion that Compcam be modified to accommodate experimental data from DIC, as this measurement system is becoming increasingly prevalent in material characterization across all forms of testing methodology.

By expanding Compcam's reach to more material testing techniques, it will allow Compcam to not only fit constitutive models to materials which may not be compatible with the cold upsetting test, but it would also allow Compcam to fit new material phenomena. One of the most promising applications, in the author's opinion, is the utilization of Compcam to fit damage models. Material tests such as the Brazilian disc test and the short beam bending tests would be ideal for this purpose, as the fracture can be controlled much easier than with the cold upsetting test.

One concrete application of Compcam which would cement its fitting ability would be to utilize Compcam to fit the full Johnson-Cook model, including strain-rate and temperature dependent behavior. Currently, the fitting of the Johnson-Cook test requires a very large test matrix to fully characterize material behavior. In the proposed work, Compcam would be used in conjunction with material tests which combine several material behaviors, such as elevated temperature cold upsetting tests where the temperature of the specimen is tracked over the duration of the test. It is the author's hypothesis that such a methodology could fully characterize material behavior with a significantly smaller test matrix. If this hypothesis were to be proven true, it would have potentially significant ramification across the field of constitutive modeling.

Bibliography

Abbasi, M., Ketabchi, M., Izadkhah, H., Fatmehsaria, D., Aghbash, A., 2011. Identification of GTN model parameters by application of response surface methodology. Procedia Engineering 10, 415–420.
URL `http://linkinghub.elsevier.com/retrieve/pii/S187770581100258X`

ASTM Standard B211-12, 2012. Standard Specification for Aluminum and Aluminum-Alloy Rolled or Cold Finished Bar, Rod, and Wire. Annual Book of ASTM Standards, 1–10.

ASTM Standard E9-09, 2012. Standard test methods of compression testing of metallic materials at room temperature. Annual Book of ASTM Standards 3.01 (1), 92–100.
URL `www.astm.org`

Avallone, E. A., Baumeister, T., 1996. Mark's Standard Handbook for Mechanical Engineers, tenth Edition. McGraw-Hill, New York, NY.

Bammann, D. J., 1990. Modeling Temperature and Strain Rate Dependent Large Deformations of Metals. Applied Mechanics Reviews 43 (5S), S312.
URL `http://appliedmechanicsreviews.asmedigitalcollection.asme.org/article.aspx?articleid=1394297`

Banerjee, J. K., 1985. Barreling of solid cylinders under axial compression. ASME Journal of Engineering Materials and Technology 107 (2), 138–144.
URL `http://materialstechnology.asmedigitalcollection.asme.org/article.aspx?articleid=1423548`

Bao, Y., 2003. Prediction of ductile crack formation in uncracked bodies. Ph.D. thesis, MIT.
URL `https://dspace.mit.edu/handle/1721.1/17634`

Bao, Y., Wierzbicki, T., 2004. A comparative study on various ductile crack formation criteria. Journal of Engineering Materials and Technology 126 (3), 314.

Beck, G., 2012. On a Novel Method of Incorporating an Internal Structure into Green Powder Metallurgy Compacts Using Die Compaction. Ph.D. thesis, Dalhousie University.

Benson, D. J., 1990. Computer Methods in Lagrangian and Eulerian Hydrocodes 99, 235–394.

Bondy, M., Altenhof, W., Jensen, M. R., 2016. Finite element modelling of a novel cutting deformation mode of AA6061-T6 tubes employing higher order element formulations and GPU computing technology. In: ICILSM 2016. No. August. Politecnico di Torino, Turin, pp. 1–6.

Booker, A. J., Dennis J.E., J., Frank, P. D., Serafini, D. B., Torczon, V., Trosset, M. W., 2 1999. A rigorous framework for optimization of expensive functions by surrogates. Structural and Multidisciplinary Optimization 17 (1), 1–13.
URL `http://link.springer.com/10.1007/BF01197708http://dx.doi.org/10.1007/BF01197708`

Chait, R., Curll, C. H., 1976. Evaluating engineering alloys in compression. In: Schmleder, A. (Ed.), Recent Developments in Mechanical Testing. ASTM International, West Conshohocken, PA, pp. 3–19.
URL `https://www.astm.org/DIGITAL_LIBRARY/STP/PAGES/STP27852S.htm`

Chawla, A., Mukherjee, S., Karthikeyan, B., 2 2009. Characterization of human passive muscles for impact loads using genetic algorithm and inverse finite element methods. Biomechanics and Modeling in Mechanobiology 8 (1), 67–76.
URL `http://link.springer.com/10.1007/s10237-008-0121-6`

Chen, F. K., Chen, C. J., 2000. On the nonuniform deformation of the cylinder compression test. Journal of Engineering Materials and Technology (Transactions of the ASME) 122 (2), 192–197.

Cho, H., Shin, Y., Hwang, S. W., Gu, J. H., Baek, J. H., Kim, J. H., Chung, S. T., Chung, S. H., Park, S. J., 7 2015. Finite element simulation of PM gear rolling

process. Powder Metallurgy 58 (3), 202–208.
URL http://www.tandfonline.com/doi/full/10.1179/1743290115Y.0000000011

Chu, C. C., Needleman, A., 1980. Void Nucleation Effects in Biaxially Stretched Sheets. Journal of Engineering Materials and Technology 102 (3), 249.
URL http://materialstechnology.asmedigitalcollection.asme.org/article.aspx?articleid=1422824

Chuzhoy, L., DeVor, R. E., Kapoor, S. G., Beaudoin, A. J., Bammann, D. J., 2003. Machining Simulation of Ductile Iron and Its Constituents, Part 1: Estimation of Material Model Parameters and Their Validation. Journal of Manufacturing Science and Engineering 125 (2), 181.
URL http://manufacturingscience.asmedigitalcollection.asme.org/article.aspx?articleid=1446164

Cooreman, S., Lecompte, D., Sol, H., Vantomme, J., Debruyne, D., 2008. Identification of mechanical material behavior through inverse modeling and DIC. Experimental Mechanics 48 (4), 421–433.

Couckuyt, I., Forrester, A., Gorissen, D., De Turck, F., Dhaene, T., 2012. Blind Kriging: Implementation and performance analysis. Advances in Engineering Software 49, 1–13.

Cressie, N., 4 1990. The origins of kriging. Mathematical Geology 22 (3), 239–252.
URL http://link.springer.com/10.1007/BF00889887

Cuesta, I. I., Alegre, J. M., Lacalle, R., 6 2010. Determination of the Gurson-Tvergaard damage model parameters for simulating small punch tests. Fatigue & Fracture of Engineering Materials & Structures 33 (11), no–no.
URL http://doi.wiley.com/10.1111/j.1460-2695.2010.01481.x

Eiselt, H. A., Pederzoli, G., Sandblom, C.-L., 1987. Continuous Optimization Models, 1st Edition. de Gruyter, Berlin.

Felling, A. J., Doman, D. A., 4 2018. A New Video Extensometer System for Testing Materials Undergoing Severe Plastic Deformation. Journal of Engineering Materials and Technology 140 (3), 031005.
URL http://materialstechnology.asmedigitalcollection.asme.org/article.aspx?doi=10.1115/1.4039291

Forrester, A., Sobester, A., Keane, A., 2008. Engineering Design via Surrogate Modeling, 1st Edition. John Wiley & Sons, West Sussex, United Kingdom.

Forrester, A. I., Sóbester, A., Keane, A. J., 2007. Multi-fidelity optimization via surrogate modelling. Proceedings of the Royal Society of London A: Mathematical, Physical and Engineering Sciences 463 (2088).

Fratini, L., Pasta, S., Reynolds, A., 3 2009. Fatigue crack growth in 2024-T351 friction stir welded joints: Longitudinal residual stress and microstructural effects. International Journal of Fatigue 31 (3), 495–500.
URL `https://www.sciencedirect.com/science/article/pii/S0142112308001151`

Fung, Y., 1977. A First Course in Continuum Mehanics. Prentice-Hall, Inc., Englewood Cliffs, NG.

Gologanu, M., Leblond, J.-B., 1997. Recent extensions of Gurson's model for porous ductile metals. In: Suquet, P. (Ed.), Continuum Micromechanics. Springer-Verlag Wien, Vienna, Austria, p. 61–130.

Gologanu, M., Leblond, J. B., Devaux, J., 1993. Approximate models for ductile metals containing non-spherical voids-Case of axisymmetric prolate ellipsoidal cavities. Journal of the Mechanics and Physics of Solids 41 (11), 1723–1754.

Guan, F., Han, X., Mao, H., Wagner, C., Yeni, Y. N., Yang, K. H., 1 2011. Application of Optimization Methodology and Specimen-Specific Finite Element Models for Investigating Material Properties of Rat Skull. Annals of Biomedical Engineering 39 (1), 85–95.
URL `http://link.springer.com/10.1007/s10439-010-0125-0`

Gurson, A. L., 1977. Continuum Theory of Ductile Rupture by Void Nucleation and Growth: Part I—Yield Criteria and Flow Rules for Porous Ductile Media. Journal of Engineering Materials and Technology 99 (1), 2.
URL `http://materialstechnology.asmedigitalcollection.asme.org/article.aspx?articleid=1422194`

Hassan, R., Cohanim, B., De Weck, O., Venter, G., 2005. A comparison of particle swarm optimization and the genetic algorithm. In: Proceedings of the 1st AIAA multidisciplinary design optimization specialist conferenc. pp. 18–21.

He, T., Liu, L., Makeev, A., Shonkwiler, B., 4 2016. Characterization of stress–strain behavior of composites using digital image correlation and finite element analysis. Composite Structures 140, 84–93.
URL `http://linkinghub.elsevier.com/retrieve/pii/S0263822315011083`

Herrmann, W., 5 1969. Constitutive Equation for the Dynamic Compaction of Ductile Porous Materials. Journal of Applied Physics 40 (6), 2490–2499.
URL `http://aip.scitation.org/doi/10.1063/1.1658021`

Huang, L., Gao, Z., Zhang, D., 2013. Research on multi-fidelity aerodynamic optimization methods. Chinese Journal of Aeronautics 26 (3), 279–286.

Johnson, G., Cook, W., 1983. A constitutive model and data for metals subjected to large strains, high strain rates and high temperatures. In: Proceedings of the 7th International Symposium on Ballistics. The Hague, The Netherlands, pp. 541–547.

Jones, D. R., 2001. A taxonomy of global optimization methods based on response surfaces. Journal of Global Optimization 21 (4), 345–383.
URL `http://link.springer.com/10.1023/A:1012771025575citeulike-article-id:1113155%5Cnhttp://dx.doi.org/10.1023/a:1012771025575`

Jones, D. R., Schonlau, M., Welch, W. J., 1998. Efficient Global Optimization of Expensive Black-Box Functions. Journal of Global Optimization 13 (4), 455–492.
URL `http://link.springer.com/10.1023/A:1008306431147`

Joseph, V. R., Hung, Y., Sudjianto, A., 2008. Blind Kriging: A New Method for Developing Metamodels. Journal of Mechanical Design 130 (3), 1–8.
URL `http://mechanicaldesign.asmedigitalcollection.asme.org/article.aspx?articleid=1449652`

Kennedy, J., Eberhart, R., 1995. Particle swarm optimization. In: Proceedings of ICNN'95 - International Conference on Neural Networks. Vol. 4. IEEE, pp. 1942–1948.
URL `http://ieeexplore.ieee.org/document/488968/`

Kiran, R., Khandelwal, K., 2 2014. Gurson model parameters for ductile fracture simulation in ASTM A992 steels. Fatigue & Fracture of Engineering Materials & Structures 37 (2), 171–183.
URL `http://doi.wiley.com/10.1111/ffe.12097`

Klocke, F., Schröder, T., Kauffmann, P., 2007. Fundamental study of surface densification of PM gears by rolling using FE analysis. Production Engineering Research and Development 1, 113–120.

Le Gratiet, L., Garnier, J., 2014. Recursive Co-Kriging Model for Design of Computer Experiments With Multiple Levels of Fidelity. International Journal for Uncertainty Quantification 4 (5), 365–386.

LSTC, 2017a. LS-DYNA Keyword User's Manual Volume II - Material Models, r9.1.0 Edition. LSTC, Livermore, USA.

LSTC, 2017b. LS-DYNA Theory Manual. LSTC, Livermore, USA.

Malcher, L., Andrade Pires, F., César de Sá, J., 2012. An assessment of isotropic constitutive models for ductile fracture under high and low stress triaxiality. International Journal of Plasticity 30, 81–115.
URL `http://www.sciencedirect.com/science/article/pii/S0749641911001690`

Malcher, L., Andrade Pires, F., César de Sá, J., 2014. An extended GTN model for ductile fracture under high and low stress triaxiality. International Journal of Plasticity 54, 193–228.
URL `http://www.sciencedirect.com/science/article/pii/S0749641913001708`

Male, A., Cockcroft, M., 1964. A Method for the Determination of the Coefficient of Friction of Metals under Conditions of Bulk Plastic Deformation. Journal of the Institute of Metals1 93 (3), 38–46.
URL `http://dx.doi.org/10.1115/1.3451419`

Male, A. T., DePierre, V., 1970. The Validity of Mathematical Solutions for Determining Friction From the Ring Compression Test. Journal of Lubrication Technology 92 (3), 389–395.
URL `http://dx.doi.org/10.1115/1.3451419`

Matheron, G., 12 1963. Principles of geostatistics. Economic Geology 58 (8), 1246–1266.
URL `http://economicgeology.org/lookup/doi/10.2113/gsecongeo.58.8.1246`

MathWorks Inc., 2017a. Constrained Nonlinear Optimization Algorithms. URL `https://www.mathworks.com/help/optim/ug/constrained-nonlinear-optimization-algorithms.html`

MathWorks Inc., 2017b. How the Genetic Algorithm Works. URL `https://www.mathworks.com/help/gads/how-the-genetic-algorithm-works.html`

MathWorks Inc., 2017c. Particle Swarm Optimization Algorithm. URL `https://www.mathworks.com/help/gads/particle-swarm-optimization-algorithm.html`

Metal Powder Industries Federation, 2010a. Standard 42: Determination of Density of Compacted or Sintered Powder Metallurgy (PM) Products. In: Standard Test Methods for Metal Powders and Powder Metallurgy Products, 2010th Edition. Metal Powder Industries Federation, Princeton, NJ, pp. 59–62.

Metal Powder Industries Federation, 2010b. Standard Test Methods for Metal Powders and Powder Metallurgy Products, 2010th Edition. Metal Powder Industries Federation, Princeton, NJ.

Mirajkar, S. B., Gopinath, K., Prakash, R. V., 2011. Material characterization and modeling of high strength PM Steel. Advanced Materials Research 337, 766–769. URL `http://www.scopus.com/inward/record.url?eid=2-s2.0-80053421557&partnerID=40&md5=0d039e26a33e1b37b9885aa4fb5e9741`

Morris, M. D., Mitchell, T. J., 1995. Exploratory designs for computational experiments. Journal of Statistical Planning and Inference 43 (3), 381–402.

Morrow, D. A., Donahue, T. H., Odegard, G. M., Kaufman, K. R., 2010. A method for assessing the fit of a constitutive material model to experimental stress-strain data. Computer methods in biomechanics and biomedical engineering 13 (2), 247–256. URL `http://www.ncbi.nlm.nih.gov/pubmed/20094931http://www.pubmedcentral.nih.gov/articlerender.fcgi?artid=PMC2895688`

Muñoz-Rojas, P. A., Cardoso, E. L., Vaz, M., 6 2010. Parameter Identification of Damage Models Using Genetic Algorithms. Experimental Mechanics 50 (5), 627–634. URL `http://link.springer.com/10.1007/s11340-009-9321-y`

Narayan, S., Rajeshkannan, A., 4 2012. Some aspects of barreling in sintered plain carbon steel powder metallurgy preforms during cold upsetting. Materials Research 15 (2), 291–299.
URL `http://www.scielo.br/scielo.php?script=sci_arttext&pid=S1516-14392012000200019&lng=en&nrm=iso&tlng=en`

Nelder, J. A., Mead, R., 1 1965. A Simplex Method for Function Minimization. The Computer Journal 7 (4), 308–313.
URL `https://academic.oup.com/comjnl/article-lookup/doi/10.1093/comjnl/7.4.308`

Oh, C.-K., Kim, Y.-J., Baek, J.-H., Kim, Y.-P., Kim, W., 2007. A phenomenological model of ductile fracture for API X65 steel. International Journal of Mechanical Sciences 49 (12), 1399–1412.

Press, W. H., Teukolsky, S. A., Vetterling, W. T., Flannery, B. P., 2007. Numeric Recipes: The Art of Scientific Computing, 3rd Edition. Cambridge University Press, New York.

Primavera, V., Perillo, M., Carofalo, A., Giorgi, M. D., Nobile, R., 2015. Calibration of material models for the numerical simulation of aluminium foams – MAT 154 for M-PORE foams @ 3 loads. In: 13th International LS-Dyna Users Conference. LSTC, Deerborn, MI, pp. 1–24.

Qiao, Y., Bisagni, C., Bai, Y., 9 2017. Experimental investigation and numerical simulation of unidirectional carbon fiber composite under multi-axial loadings. Composites Part B: Engineering 124, 190–206.
URL `http://www.sciencedirect.com/science/article/pii/S1359836816310824#fig3`

Queipo, N. V., Haftka, R. T., Shyy, W., Goel, T., Vaidyanathan, R., Kevin Tucker, P., 2005. Surrogate-based analysis and optimization. Progress in Aerospace Sciences 41 (1), 1–28.

Roux, E., Bouchard, P.-O., 9 2010. Ductile Damage Material Parameter Identification: Numerical Investigation. In: Topping, B., Adam, J., Pallares, F., Bru, R., Romero, M. (Eds.), Tenth International Conference on Computational Structures Technology. Civil-Comp Press, Valencia, Spain, pp. 1–10.
URL `http://www.ctresources.info/ccp/paper.html?id=5842`

Roux, E., Bouchard, P.-O., 10 2015. On the interest of using full field measurements in ductile damage model calibration. International Journal of Solids and Structures 72, 50–62.
URL `http://linkinghub.elsevier.com/retrieve/pii/S0020768315003170`

Sacks, J., Welch, W. J., Mitchell, T. J., Wynn, H. P., 1989. Design and analysis of computer experiments. Statistical Science Statistical Science 4 (4), 409–423.
URL `http://www.jstor.org/stable/2245858http://about.jstor.org/terms`

Schindelin, J., Arganda-Carreras, I., Frise, E., Kaynig, V., Longair, M., Pietzsch, T., Preibisch, S., Rueden, C., Saalfeld, S., Schmid, B., Tinevez, J.-Y., White, D. J., Hartenstein, V., Eliceiri, K., Tomancak, P., Cardona, A., 7 2012. Fiji: an open-source platform for biological-image analysis. Nature Methods 9 (7), 676–682.
URL `http://www.nature.com/articles/nmeth.2019`

Schonlau, M., 1997. Computer Experiments and Global Optimization. Ph.D. thesis, University of Waterloo.
URL `https://uwspace.uwaterloo.ca/bitstream/handle/10012/190/nq22234.pdf`

Selig, S. G., 2012. Finite Element Simulation of the Compaction and Springback of an Aluminum Powder Metallurgy Alloy. Ph.D. thesis, Dalhousie University.

Simo, J. C., Hughes, T., 1998. Computational Inelasticity, 1st Edition. Springer-Verlag, New York.

Simpson, T. W., Mauery, T. M., Korte, J. J., Mistree, F., 12 2001. Kriging models for global approximation in simulation-based multidisciplinary design optimization. AIAA Journal 39 (12), 2233–2241.
URL `http://arc.aiaa.org/doi/abs/10.2514/2.1234`

Slimane, A., Bouchouicha, B., Benguediab, M., Slimane, S.-A., 2015. Parametric study of the ductile damage by the Gurson–Tvergaard–Needleman model of structures in carbon steel A48-AP. Journal of Materials Research and Technology 4 (2), 217–223.

Sóbester, A., Leary, S. J., Keane, A. J., 9 2005. On the design of optimization strategies based on flobal response surface approximation models. Journal of Global Optimization 33 (1), 31–59.
URL `http://link.springer.com/10.1007/s10898-004-6733-1`

Springmann, M., Kuna, M., 2005. Identification of material parameters of the Gurson-Tvergaard-Needleman model by combined experimental and numerical techniques. Computational Materials Science 33 (4), 501–509.

Stander, N., Craig, K., 2002. On the robustness of a simple domain reduction scheme for simulation-based optimization. Engineering Computations 19 (4), 431–450.

Swift, H., 1952. Plastic instability under plane stress. Journal of the Mechanics and Physics of Solids 1 (1), 1–18.
URL `http://linkinghub.elsevier.com/retrieve/pii/0022509652900021`

Theil, H., 1983. Linear algebra and matrix methods in econometrics. In: Griliches, Z., Intriligator, M. D. (Eds.), Handbook of Econometrics, 1st Edition. New Holland Publishing Company, p. 771.

Tvergaard, V., 8 1981. Influence of voids on shear band instabilities under plane strain conditions. International Journal of Fracture 17 (4), 389–407.
URL `http://link.springer.com/10.1007/BF00036191`

Umbrello, D., M'Saoubi, R., Outeiro, J. C., 2007. The influence of Johnson-Cook material constants on finite element simulation of machining of AISI 316L steel. International Journal of Machine Tools and Manufacture 47 (3), 462–470.

Vaz, M., Cardoso, E. L., Munoz-Rojas, P. A., Carniel, T. A., Luersen, M. A., Tomiyama, M., da Silva, J. O., Stahlschmidt, J., Trentin, R. G., 5 2015. Identification of constitutive parameters - optimization strategies and applications. Materialwissenschaft und Werkstofftechnik 46 (4-5), 477–491.
URL `http://doi.wiley.com/10.1002/mawe.201500423`

Venter, G., Sobieszczanski-Sobieski, J., 2003. Particle Swarm Optimization. AIAA Journal 41 (8), 1583–1589.

Welch, W. J., Buck, R. J., Sacks, J., Wynn, H. P., Mitchell, T. J., Morris, M. D., 2 1992. Screening, Predicting, and Computer Experiments. Technometrics 34 (1), 15–25.
URL `http://www.jstor.org/stable/1269548?origin=crossref`

Wierzbicki, T., Bao, Y., Lee, Y. W., Bai, Y., 4 2005. Calibration and evaluation of seven fracture models. International Journal of Mechanical Sciences 47 (4), 719–743.

Wikman, B., Bergman, G., Oldenburg, M., Haggblad, H.-A., 5 2006. Estimation of constitutive parameters for powder pressing by inverse modelling. Structural and Multidisciplinary Optimization 31 (5), 400–409.
URL `http://link.springer.com/10.1007/s00158-005-0556-7`

Xue, L., 7 2008. Constitutive modeling of void shearing effect in ductile fracture of porous materials. Engineering Fracture Mechanics 75 (11), 3343–3366.
URL `http://linkinghub.elsevier.com/retrieve/pii/S0013794407003220`

Xue, L., Wierzbicki, T., 2009. Numerical simulation of fracture mode transition in ductile plates. International Journal of Solids and Structures 46 (6), 1423–1435.
URL `http://dx.doi.org/10.1016/j.ijsolstr.2008.11.009`

Yazici, B. A., Kraft, T., Riedel, H., 9 2008. Finite element modelling of PM surface densification process. Powder Metallurgy 51 (3), 211–216.
URL `http://www.tandfonline.com/doi/full/10.1179/174329008X271682`

Appendix A

Equations of State and the Lagrangian Timestep

Underpinning all explicit FE solvers is the Lagrangian timestep, the procedure used to update the all information (stress, strain, displacement, volume, bulk viscosity, etc.) within an element from timestep to timestep. While the implementation of the Lagrangian timestep may vary from solver to solver, the basic structure remains the same. A graphical depiction of this structure is given below in Figure A.1. This description is taken from Benson's treatise on Lagrangian and Eulerian hydrocodes (Benson, 1990).

As already noted in this document, a constitutive material model using the von Mises yield criterion cannot account for a material's change in volume. However, the addition of an equation of state allows for the modeling of such phenomena. The aim of this appendix is not to discuss the full Lagrangian timestep, but rather to focus on how an equation of state effects the overall stress update procedure (steps 5-7 in Figure A.1). As will be detailed in the following sections, the introduction of an equation of state fundamentally alters the stress update portion of the Lagrangian timestep and how the constitutive material models calculate total stress. To convey this difference in operation, this appendix will present the stress update procedure for elements with and without an equation of state. The procedure detailed here is used by LS-DYNA and detailed in the LS-DYNA theory manual (LSTC, 2017b). Additional content and context are drawn from Benson (1990).

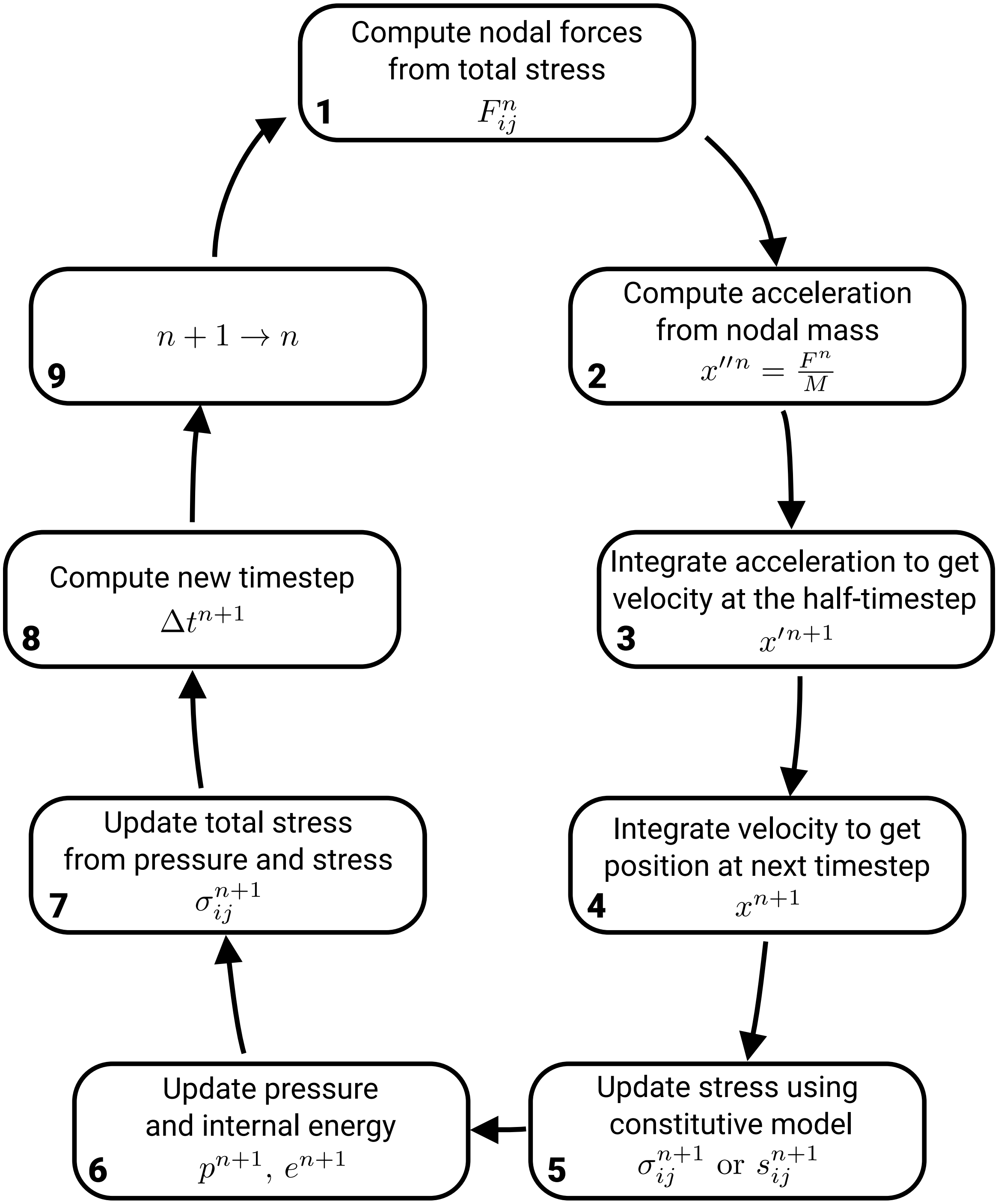

Figure A.1: Lagrangian timestep procedure

Prior to diving into the mathematics of the stress update procedure, it is important to define notation and convention. Because the stress is updated from timestep to timestep, it is important to track the timestep a particular piece of information is drawn from. The current timestep is denoted by a superscript n. The next timestep is denoted by $n+1$, and a half-timestep (used by integration algorithms for improved numerical stability and accuracy) is denoted by $n+\frac{1}{2}$. Hydrostatic pressure for these derivations is denoted as p, the deviatoric stresses are denoted as s_{ij}, and the total stress denoted as σ_{ij}. In keeping with the sign conventions used by Ls-Dyna, these three variables are defined below. It is important to note that pressure is explicitly given a negative sign following this convention. Additionally, the bulk viscosity is defined as q, although this particular parameter will not be discussed in detail in this appendix.

$$p = -\frac{1}{3}\sigma_{ij}\delta_{ij} - q = -\frac{1}{3}\sigma_{kk} - q \tag{A.1}$$

$$s_{ij} = \sigma_{ij} + (p+q)\delta_{ij} \tag{A.2}$$

Therefore:

$$\sigma_{ij} = s_{ij} - (p+q)\delta_{ij} \tag{A.3}$$

A.1 Stress Update Without an Equation of State

The most popular stress update method used by FE solvers is the Jaumann stress rate (Benson, 1990). LS-DYNA uses this method with the exception of a few specialized models. (LSTC, 2017b). While chosen for explicit FE packages for its good balance of accuracy and computational cost, it can cause problems with implicit time integration schemes as it can create non-symmetric stiffness matrices.

For materials which exhibit elastic-plastic behavior, the incremental nature of the stress update procedure is demonstrated by (A.4).

$$\sigma_{ij}^{n+1} = \sigma^{n} + \dot{\sigma}_{ij}\Delta t \tag{A.4}$$

where material time derivative, $\dot{\sigma}_{ij}$, is defined by (A.5).

$$\dot{\sigma}_{ij} = \sigma_{ij}^{\nabla} + \sigma_{ik}\omega_{kj} + \sigma_{jk}\omega_{ki}. \tag{A.5}$$

The spin tensor, ω_{ij}, is defined in (A.6), were v_i is the velocity vector.

$$\omega_{ij} = \frac{1}{2}\left(\frac{\partial v_i}{\partial x_j} - \frac{\partial v_j}{\partial x_i}\right) \tag{A.6}$$

The Jaumann stress rate, σ_{ij}^{∇}, is defined in (A.7), were C_{ijkl} is the stress-dependant constitutive matrix and $\dot{\epsilon}_{ij}$ is the strain rate tensor defined by (A.8).

$$\sigma_{ij}^{\nabla} = C_{ijkl}\dot{\epsilon}_{kl} \tag{A.7}$$

$$\dot{\epsilon}_{ij} = \frac{1}{2}\left(\frac{\partial v_i}{\partial x_j} + \frac{\partial v_j}{\partial x_i}\right) \tag{A.8}$$

With the stage now set, the stress can now be incrementally updated. This is accomplished by first calculating the rotation of stress at the current timestep, as given by (A.9). This ensures the objectivity of the stress update procedure.

$$r_{ij}^{n} = \left(\sigma_{ik}^{n}\omega_{kj}^{n+\frac{1}{2}} + \sigma_{jk}^{n}\omega_{ki}^{n+\frac{1}{2}}\right)\Delta t^{n+\frac{1}{2}} \tag{A.9}$$

Total stress is then calculated using (A.10).

$$\sigma_{ij}^{n+1} = \sigma_{ij}^{n} + r_{ij}^{n} + \overset{\nabla}{\sigma}_{ij}^{n+\frac{1}{2}} \Delta t^{n+\frac{1}{2}} \tag{A.10}$$

where

$$\overset{\nabla}{\sigma}_{ij}^{n+\frac{1}{2}} \Delta t^{n+\frac{1}{2}} = C_{ijkl} \Delta \epsilon_{kl}^{n+\frac{1}{2}} \tag{A.11}$$

and

$$\epsilon_{ij}^{n+\frac{1}{2}} = \dot{\epsilon}_{ij}^{n+\frac{1}{2}} \Delta t^{n+\frac{1}{2}} \tag{A.12}$$

The most important thing to note about the stress update procedure, from the context of plasticity and volumetric deformation, is C_{ijkl}. While noted above, it is important to reiterate that this is the stress-dependent constitutive matrix, meaning that it will change depending on the material loading and whether the material is undergoing plastic deformation. In many ways, it would be more appropriate to denote this as $C_{ijkl}(\sigma_{ij}^{n+\frac{1}{2}})$. It is also very important to note that in (A.10), C_{ijkl} accounts for the combined effects of hydrostatic pressure and deviatoric stress.

Changes in C_{ijkl} are governed by the constitutive material model used. For pressure-independent constitutive models, such as models which utilize the von Mises yield criterion, the portion of C_{ijkl} which governs volumetric deformation is not altered. As such, while components of C_{ijkl} which are affected by the deviatoric component of stress may change and allow for permanent deformation, all volumetric deformation imparted on an element is elastic and fully recoverable. However, for models which do account for changes in volume, such as the GTN model or a Drucker-Prager-type cap model, both deviatoric and hydrostatic components of C_{ijkl} are updated, which allows the constitutive models to account for permanent volumetric deformation.

A.2 Stress Update Procedure with an Equation of State

Equations of state control the pressure within an element and are generally functions of relative volume, V, and internal energy, E. This is formalized below in (A.13). When defined on an elemental bases, volume is defined as ν and energy as e.

$$p = p(V, E) \tag{A.13}$$

When an equation of state is used, the stress update changes quite significantly. Instead of incrementing total stress, pressure and deviatoric stress are handled separately. This is important because the pressure the $n+1$ timestep is dependant on the internal energy at $n+1$.

The stress update begins by using the Jaumann stress rate, however, unlike the previous section, the Jaumann stress rate is only used to calculate the deviatoric stress at the next timestep as given by (A.14), where $\dot{\epsilon}'^{n+\frac{1}{2}}_{kl}$ is the deviatoric strain rate tensor defined by (A.15).

$$s^{n+1}_{ij} = \sigma^n_{ij} + r^n_{ij} + p^n \delta_{ij} + C_{ijkl}\dot{\epsilon}'^{n+\frac{1}{2}}_{kl}\Delta t^{n+\frac{1}{2}} \tag{A.14}$$

$$\dot{\epsilon}'^{n+\frac{1}{2}}_{ij} = \dot{\epsilon}_{ij} - \frac{1}{3}\dot{\epsilon}_{kk}\delta \tag{A.15}$$

(A.14) displays the key difference between a stress update with and without an equation of state (given by (A.10)). While both methods use the stress-dependant constitutive matrix C_{ijkl}, which is controlled by the constitutive material model, when an equation of state is used, only the deviatoric components of C_{ijkl} are used to update total stress due to the use of the deviatoric strain rate tensor $\dot{\epsilon}'^{n+\frac{1}{2}}_{ij}$. This implies that however the constitutive material model may affect the hydrostatic response, the equation of state will always override it.

The calculation of pressure at the $n+1$ timestep is challenging because the pressure is also dependant on the internal energy at the $n+1$ timestep, which itself is dependant on pressure. To that end, pressure and internal energy at the $n+1$ timestep are solved implicitly. After updating bulk viscosity, q (not detailed here), a trial internal energy at the next time step, e^{*n+1} is calculated based on current pressure and change in volume, as given by (A.16). The change in volume is determined by the geometric configuration of the element.

$$e^{*n+1} = e^{n} - \frac{1}{2}\Delta\nu(p^{n} + q^{n-\frac{1}{2}} + q^{n+\frac{1}{2}}) + \nu^{n+\frac{1}{2}} s_{ij}^{n+\frac{1}{2}} \epsilon_{ij}^{n+\frac{1}{2}} \tag{A.16}$$

where

$$\Delta\nu = \nu^{n+1} - \nu^{n} \tag{A.17}$$

$$\nu^{n+\frac{1}{2}} = \frac{1}{2}(\nu^{n} + \nu^{n+1}) \tag{A.18}$$

$$s_{ij}^{n+\frac{1}{2}} = \frac{1}{2}(s_{ij}^{n} + s_{ij}^{n+1}) \tag{A.19}$$

The next step requires the assumption that the equation of state is linear in terms of energy, as shown in (A.20). For the most part, this is a valid assumption, as the overwhelming majority of equations of state used for metal plasticity are linear in terms of energy, including all equations of state used in this work. If the equation of state is not linear, an iterative procedure is used (LSTC, 2017b).

$$p^{n+1} = A^{n+1} + B^{n+1}E^{n+1} \tag{A.20}$$

where

$$E^{n+1} = \frac{e^{n+1}}{\nu_0} \tag{A.21}$$

and ν_0 is the initial elemental volume.

Because (A.16) calculates the trial energy using the pressure at the current timestep, the trial energy can be corrected knowing the pressure at next timestep to produce the actual energy at the next timestep, as shown in (A.22).

$$e^{n+1} = e^{*n+1} - \frac{1}{2}\Delta\nu p^{n+1} \tag{A.22}$$

Using (A.16), (A.20) and (A.22), the pressure at $n+1$ can be calculated implicitly, as shown in (A.23).

$$p^{n+1} = \frac{A^{n+1} + B^{n+1}E^{*n+1}}{1 + \frac{1}{2}B^{n+1}\frac{\Delta\nu}{\nu_0}} \tag{A.23}$$

Once p^{n+1} is solved for, energy is updated using (A.22). Total stress is then calculated using (A.3). Because the total stress tensor now accounts for the effects of volumetric deformation from the equation of state, volumetric deformation of the element is accounted for when the stress tensor is used to generate nodal forces and hence nodal accelerations, velocities, and finally, displacements (steps 1-4 on Figure A.1).

Appendix B

COMPCAM Organization

This appendix is written for future researchers who may need to modify Compcam's source code. As is typical with many purpose-built codes, it can be difficult for outsiders to decipher the design methodology and file structure which was developed by a single author working alone. However, code that cannot be maintained, particularly in a high turnover area such as academia, is ultimately useless.

While Compcam was written with the intent to allow for easy modifications by another researcher with some familiarity with Matlab, it became clear to the author that during collaboration with other researchers, the issue was not readability of the code, but rather the underlying system architecture. To that end, what follows is two graphical illustrations of Compcam's file structure followed by a brief overview of what each file or function does. Note that this overview only covers parameter identification using the cold upsetting test. Parameter identification for other types of tests, such as powder compaction, will follow a slightly different file structure. However, in general, these file structures generally differ only by the objective function inputted into the optimization algorithm. Further, it is highly recommended to continue using this file structure when expanding Compcam's functionality to maximize compatibility with previous releases.

B.1 System Architecture

The graphical depiction of Compcam's file architecture is broken into two figures. Figure B.1 covers Compcam's main entry point, a script titled "MainExecutionScript.m". This script handles high-level execution of Compcam, including setting initial conditions, parameter bounds, solver settings, and optimization. Figure B.2 covers the objective function inputted to the optimization algorithm noted in chart #1. The objective function handles setting up the solver deck for a particular set of parameters, executing Ls-Dyna, parsing solver output files (in the form of ASCII files), and computing the fit score.

These charts are interpreted from top to bottom, with implied data being passed downward. Items inside a box are called by that function.

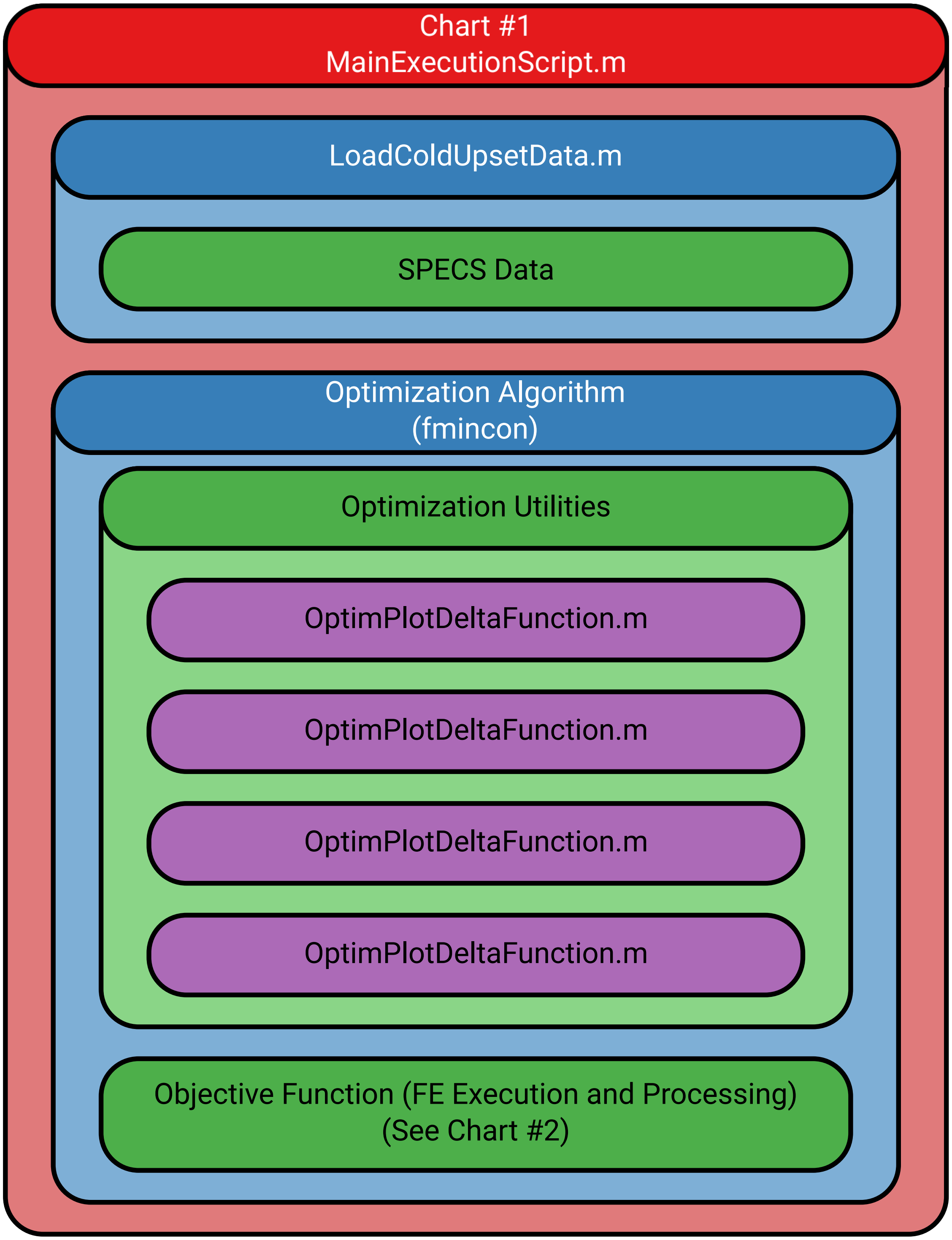

Figure B.1: Graphical overview chart #1: COMPCAM's main entry point

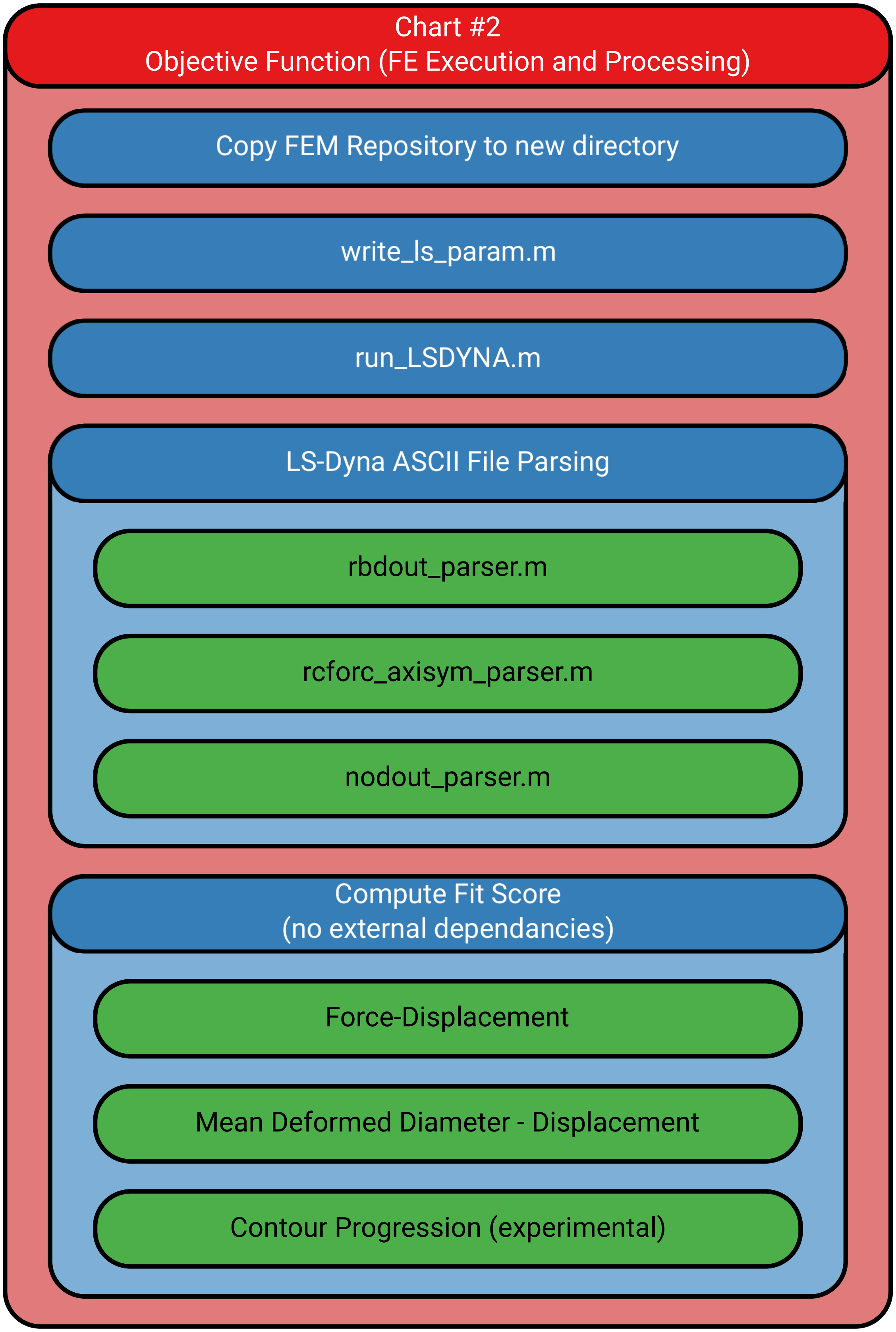

Figure B.2: Graphical overview chart #2: cold upsetting objective function

B.2 Overview of Files

This section provides context to the functions and scripts listed in Figures B.1 and B.2. Each file used in Compcam is listed below with a brief description and a note on what function is called by it. This summary is meant to supplement the graphical overview, not supplant it.

MainExecutionScript.m

The primary entry point into Compcam. Allows the user to change the constitutive model being fitted, the initial conditions and bounds for the optimization algorithm, and execute the optimization algorithm. Also used to read existing the results of previous Compcam runs, as these are saved to a folder.

LoadColdUpsetData.m

Function loads Specs data from file and extracts the information required by Compcam. Therefore, instead of saving the entire Specs dataset of a material during operation, only data such as force-displacement and radius-displacement are kept in memory during operation. Specs data is saved in the folder named “Optimization Goal”.

Optimization Algorithm

The optimization algorithm which powers Compcam. By default, it is “fmincon”, which is built into Matlab. However, this could be changed to whatever the user prefers, although care would be taken to ensure optimizer options would be valid for the new algorithm. Options to run Mike do exist in Compcam by setting a single execution flag in “MainExecutionScript.m”. In addition to optimization utilities, the main purpose of the optimization algorithm is to call the objective function repeatedly.

OptimPlotDeltaFnc.m

Optimization utility, called by the optimization algorithm directly. Allows one to graphically track the change in objective function from iteration to iteration.

PrintIntermSolution.m

Optimization utility, called by the optimization algorithm directly. Prints the parameter set solved by the optimization algorithm at that iteration to screen. This allows the researcher to easily track the convergence behavior of parameters.

RunIntermFEM.m

Optimization utility, called by the optimization algorithm directly. Runs a simulation which does not further the optimization algorithm, but instead, allow the user to see the effect of fit by the iteration's parameter set. While it increases computational cost, it provides invaluable service for tracking the progression of the optimization algorithm.

SaveIntermSolution.m

Optimization utility, called by the optimization algorithm directly. Saves the current state of the optimization in case the algorithm is interrupted by a failed simulation or power outage. Allows the user to seed a new COMPCAM run with the parameters determined by the optimization algorithm just prior to failure.

ColdUpsetObjective.m

This function serves as the primary objective function called by the optimization algorithm. This function generates new solver decks, runs simulations, parses outputs, computes fit scores, and plots experimental and numeric data. This function is also called when processing preexisting data, such as final values from a COMPCAM run or interim values outputted by the optimization algorithm.

This function creates new solver decks by copying the entire FEM repository of COMPCAM to a new folder. All modification to the solver deck occurs in this new folder so that none of the original decks are overwritten.

write_ls_param.m

Writes the constitutive material model parameters inputted to the objective function to the solver deck. As the name implies, LS-DYNA parameters are used to allow this function to write only a few lines into the solver deck in a single location, instead of trying to modify many independent numbers spread over the entire deck. The parameters used by LS-DYNA must match the parameters listed in COMPCAM's "MainExecutionDeck.m". The COMPCAM option "paramTarget" must be properly set to ensure parameters are written to the correct portion of the solver deck.

run_LSDYNA.m

Runs a solver deck. The version of LS-DYNA used and the solver directory are can be changed by modifying this file. By default, this function runs the solver without printing solver information to screen, however, this functionality can be enabled with the second input argument.

Parsing Functions

All parsing functions are found under "Dyna Utilities", and are meant to parse the ASCII files outputted by LS-DYNA. Because LS-DYNA is not internally consistent with the format of its output files, a separate parser is needed for each file type. A list of all parsers found in COMPCAM is found below, however, only those functions with an asterisk are called by "ColdUpsetObjective.m". The remainder were written for future eventualities.

- elout_axisym_parser: for element output files from axisymmetric simulations
- elout_3D_parser: for element output files from 3D simulations
- eloutDET_3D_parser: for interpolated nodal stress/strain output files from 3D simulations
- glstat_parser: for the global statistics file

- matsum_parser: for material energies and statistics
- nodfor_parser: for nodal output forces file
- nodout_parser*: for nodal displacements and rotations
- rbdout_parser*: for rigid-body displacements and coordinates
- rcforc_axisym_parser*: for contact force files from axisymmetric simulations
- rcforc_3D_parser: for contact force files from 3D simulations

Appendix C

Exploratory Work into Use of Kriging Models

One of the primary detractors of IMM and COMPCAM is that the optimization algorithms require the the FE model to be evaluated a significant number of times. While that is acceptable for FE models which solve in a few minutes, such as the ones covered the main body of this thesis, it quickly becomes prohibitive as time needed to solve an FE model exceeds 20 minutes to half an hour.

This appendix covers work which was conducted during my masters into a means to mitigate this penalty through the use of surrogate modelling techniques. The impetus of surrogate models can be summed up by the following questions:

> Can an expensive, black-box function be approximated with a cheap-to-evaluate model with sufficient accuracy be used for optimization? Furthermore, can such a model be generated cheaper than executing direct optimization on the expensive function?

These questions drive the development of a software tool known as MIKE, the MATLAB Integrated Kriging Environment. MIKE is a surrogacy modeling tool which uses a statistical modeling technique known as a Kriging model to build predictive models. Kriging models excel at making accurate interpolations from sparsely sampled datapoints, meaning, in the case of IMM, the FE model only needs to be evaluated a relatively small low of times. Furthermore, the statistical nature of the Kriging model can be exploited to allow for predictive infilling, or the use of the existing Kriging model to predict the point at which a new sampling point will provide the greatest improvement to the Kriging model's predictive accuracy. By harnessing predictive infilling, the overall accuracy of a Kriging model, particularly around areas of interest such as global and local minima or maxima, can be incrementally improved through sequential infilling. However, even with sequential infilling, the expense of developing a Kriging surrogate model tends to be less than that of standard optimization techniques, which has caused the Kriging model to be referred to as a form of efficient global optimization (EGO) method. The derivation and implementation of the Kriging model used in MIKE, as well as validation using analytic test functions, are presented in this document.

While a significant amount of progress and investigation was made into surrogate modelling MIKE, it was ultimately excluded from the main body of the thesis due to time constraints. As a result of said time constraints, throughout validation and use in IMM applications was not achieved. However, it is the author's strong believe that Kriging surrogate models and MIKE represent a very promising means to reduce the expense of IMM. As such, development and early stage investigations using MIKE is included in this appendix to aid in the future development of Kriging surrogates and eventual implementation into COMPCAM as the primary optimization method.

C.1 Kriging Model Background

The Kriging model was selected for this work due to its ability to not only provides the ability to make accurate interpolations from sparse datasets, but also because of its ability to act as a global search method using significantly fewer evaluations of the objective function compared to the genetic algorithm and PSO. While this section provides historical context and cites some significant work which use Kriging models, the actual derivation of the Kriging model, as well as their implementation in MIKE, are provided in Section C.2.

The Kriging model was developed for use in geology as a means to interpolate information such as ore yield over a large area from a sparse collection of core samples (Cressie, 1990). Prior to the development of the Kriging model (also referred to as the Kriging method), traditional interpolation methods such as splines and geometric interpolation were used. However, the majority of these fitting techniques either used only the sampling points immediately surrounding the points of interest or interpolation with fixed weights attached to each sampling point.

South African mining engineer Danie G. Krige formulated an idea for an interpolation method which varied the weighting of sampling points depending on how far a given sampling point was from the point where one was making their interpolation (Cressie, 1990). For example, when interpolating the value of any given point, it makes sense that the sampling points closest to the point of interest have a greater influence on the interpolated value than points far away. However, it is interesting to note that Krige did not name his method after himself and that his original work bears little resemblance to the Kriging models used today. The use of the term Kriging method or model was adopted by later researchers (Cressie, 1990; Matheron, 1963).

Given its origin in geology and statistics, it should not be surprising that the Kriging method remained in those fields for many years. It was not until what one could call a seminal article by Sacks et al. (1989) entitled the "Design and Analysis of Computer Experiments" that Kriging methods began to appear in other fields. In this article, Sacks et al. introduced the idea that the Kriging method could be used to generate a cheap-to-evaluate computer model which could be used as a stand-in for expensive computer simulations. Such a model, which became known as the DACE model after the title of the article (Booker et al., 1999; Jones et al., 1998), could then be utilized to perform tasks such as parametric studies and design optimizations which would have been otherwise prohibitively expensive.

It would be unfair to say the use of surrogates as suggested by Sacks et al. was adopted quickly by other researchers, because it was not. At the time the Sacks article was published, the computational costs to generate a Kriging-type model were still very high. As such, its use was limited, despite the potential advantages granted by a surrogate model, especially for optimization. However, the Kriging method did find some application in the design of helicopter blades (Booker et al., 1999), multi-physics models of rocket engines (Queipo et al., 2005; Simpson et al., 2001), and transistor design for electric circuits (Welch et al., 1992).

While the use of surrogate models remains limited, there is increased interest in their use. This is driven by reduction in computational cost to build a surrogate, the increase in complexity associated with most simulations, and the push for model-driven design (Booker et al., 1999; Jones et al., 1998). One of the prominent applications of surrogate models and, in particular, Kriging surrogates is for design optimization in the aerospace sector, which use very expensive, but accurate computational fluid dynamics models (Huang et al., 2013). In some cases, the original Kriging methodology is being adapted to work with what is known as multi-fidelity modeling. Multi-fidelity modeling couples two separate computer simulations: one simulation is reasonably cheap, but not accurate enough for design optimization; the other is expensive but accurate. Multi-fidelity Kriging or Co-Kriging (Forrester et al., 2007; Le Gratiet and Garnier, 2014) uses the cheap simulation, which can be evaluated many times for the time required for one expensive simulation, to help fill in the gaps in the widely spaced expensive simulation data by essentially providing an estimate of how the expensive function should trend.

While the Kriging model is most commonly used as a computationally inexpensive surrogate for a computationally expensive function, it can be used to perform a global optimization. This is accomplished through a process called infilling, where the statistical nature of the Kriging model is exploited to successively add new sampling points to improve the predictive ability of the model near a global optimum. Infilling is described in detail in Section C.2.1. This type of optimization is sometimes referred to as an EGO method, as the significantly fewer evaluations of the objective function are required to build and infill a Kriging model. Excellent examples of the use of the Kriging model as an EGO method are seen in the works of Roux and Bouchard (2010,

2015) when performing IMM to determine parameters for damage and constitutive material models.

C.2 Mike Development

Mike, the Matlab Integrated Kriging Environment, is a tool for the construction and use of Kriging models for interpolation and optimization. Owing to their ability to created accurate and cheap-to-evaluate approximations of expensive functions, Kriging models are often referred to as surrogate models, with the computationally expensive function referred to as the parent function. While used by Compcam in this work, Mike is completely independent and could be used to create surrogate models for any arbitrary dataset.

Kriging models do not themselves act as optimizers, despite being referred to as an EGO technique. A global search method is still required to search the Kriging model for an optimum solution. However, the use of predictive infilling allows Kriging models to intelligently sample the solution space of an expensive function in order to improve the surrogate's accuracy in areas around the global optimum of the parent function. While other EGO techniques exist, such as successive response surfacing modeling (Stander and Craig, 2002), one benefit of Kriging surrogates is that even when used as an EGO method, the Kriging model still allows for interpolation anywhere in the solution space.

This section provides a full derivation of the Kriging model in Mike as well as derivation and discussion of predictive infilling. Programming considerations are discussed, particularly those related to computational efficiency. Finally, validation of Mike against analytic test functions is presented.

C.2.1 Model Derivation

The derivation and formulation of the Kriging model used here draw heavily from the works of Jones (2001; 1998) and Forrester et al. (2008). Many other derivations exist but approach the subject from a mathematically intensive, statistical perspective. It was found that Jones and Forrester presented the most approachable and detailed derivation with a particular focus on real-world applications. Throughout this derivation, bold variables represent a vector of individual variables, as shown explicitly in (C.1).

$$\boldsymbol{x} = [x_1, x_2, \ldots, x_n]^{\mathrm{T}} \tag{C.1}$$

Prior to beginning the derivation, it is important to understand, from a conceptual standpoint, what a Kriging model is. Consider the following situation: you are given an set of sampling points. These sampling points can be scattered or gridded. There are two common means of extracting information from such as situation. One can fit a function to the data using regression. While this methodology allows for a simple analytic function to be used with further data processing, regression suffers from two drawbacks. First, there is no guarantee that the fitted function will pass through the sampled points. If we know that there is no error in our measurements, such as with the deterministic nature of computer models, then a function that does not pass through sampled points adds error to the surrogate. Second, if the underlying physics of the system are not known, selection of the interpolation function becomes arbitrary.

Alternatively, one can use methods to interpolate values between sampling points. This also presents issues. First, one can to select the type of interpolation function used. This could be linear, polynomial, or a spline. The selection of interpolation function greatly influences the value at a given point, especially for sparsely sampled data. Second, interpolation can be very expensive. Not only does sorting through the existing data points present a large computational expense, but the cost of interpolation increases dramatically with higher dimensionality, making such problems prohibitively expensive.

The Kriging model attempts to split the difference between the two methodologies. Making a prediction with a Kriging models can be described by (C.2), which is often referred to as the Kriging predictor. The Kriging predictor can be considered the combination of a regression function $\mu(\boldsymbol{x})$ which predicts the underlying trends inherently in the data, and a stochastic function $Z(\boldsymbol{x})$, which accounts for the deviation of data away from the underlying trend. This is depicted graphically in Figure C.1.

$$y(\boldsymbol{x}) = \mu(\boldsymbol{x}) + Z(\boldsymbol{x}) \tag{C.2}$$

The form of the Kriging predictor shown in (C.2) is known as the universal Kriging model. It is given this name because the regression component of the predictor $\mu(\boldsymbol{x})$ is to takes whatever form is required to accurately represent the underlying physics of the situation. However, the selection of $\mu(\boldsymbol{x}$ has the same issues as selection of a regression function detailed above, namely that if the underlying trend is not known, the regression function is difficult to choose. To that end, the majority of Kriging

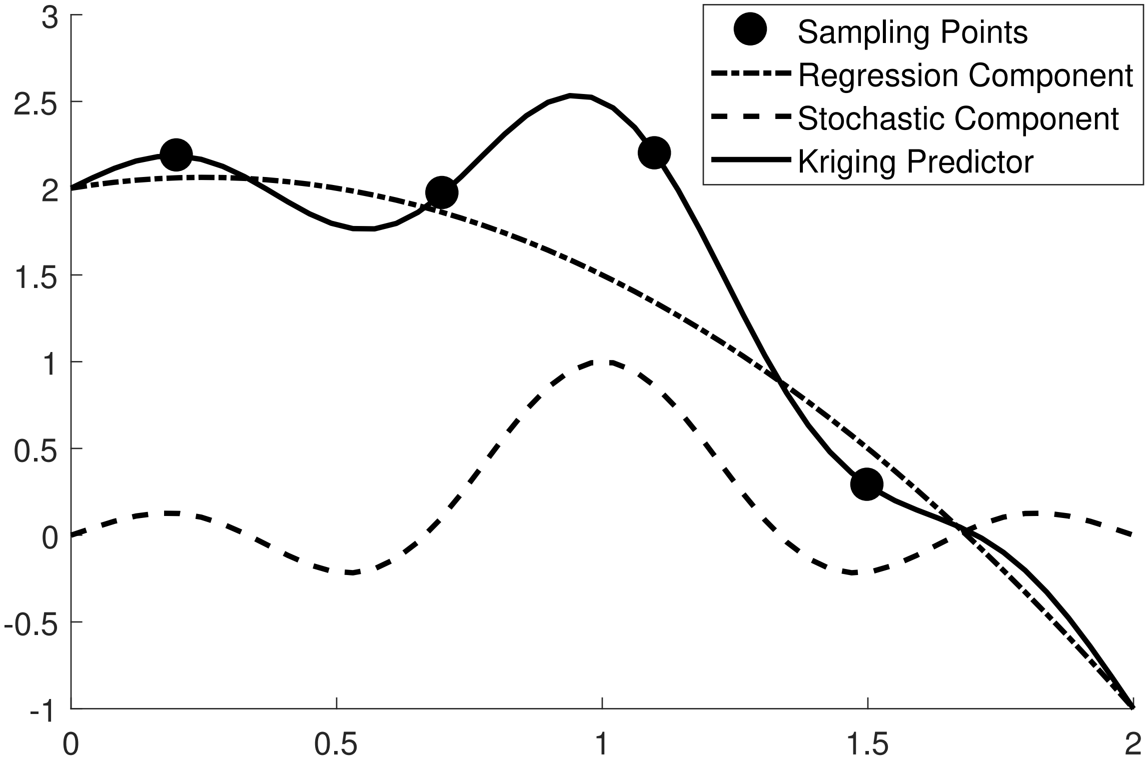

Figure C.1: Graphical representation of the Kriging predictor's regression and stochastic components.

model implementations, including MIKE, use what is known as the Ordinary Kriging, where the regression function $\mu(\boldsymbol{x})$ is replaced with a single mean value μ_0, as shown in (C.3).

$$y(\boldsymbol{x}) = \mu_0 + Z(\boldsymbol{x}) \tag{C.3}$$

While a large body of work has shown the ordinary Kriging is sufficient for the majority of applications, one will note that the replacement of a regression function with a simple mean value does significantly reduce the flexibility of the Kriging model, placing a much higher importance on the tuning of the stochastic function, which makes up the bulk of the derivation provided below. To alleviate this, one promising alternative has been suggested. Known as blind Kriging (Couckuyt et al., 2012; Joseph et al., 2008), this methodology uses Bayesian forward selection to select the best regression function for any given constitutive model. In this way, the necessity of selecting appropriate regression functions is removed, reducing the critically of fitting an accurate stochastic portion of the model. While some work was undertaken to implement a blind Kriging model into MIKE, this work was abandon due to time constraints, although early testing showed promising results.

To construct a Kriging surrogate, the parent function must be evaluated using an initial sampling plan to gather determine enough information to build the surrogate. For a high-quality surrogate, the sampling plan should be random and uncorrelated, with $\boldsymbol{x}^{(i)}$ and $y^{(i)}$ representing the i-th sampling point and value at that point, respectively. However, because we assume the underlying system to be random or stochastic in nature, each evaluation at a given sampling point is also random. Each evaluation is also a stochastic process and are represented by $Y(\boldsymbol{x}^{(i)})$. This creates the vector of stochastic processes $\boldsymbol{Y} = (Y(\boldsymbol{x}^{(1)}), \ldots, Y(\boldsymbol{x}^{(n)})^{\mathrm{T}}$. This vector has a mean value of $\mathbf{1}\mu$, where $\mathbf{1}$ is a $n \times 1$ unity vector.

From this field of stochastic processes, one can determine the statistical correlation between any two sampling points in the field. In keeping with the assumption of a stochastic system with normally distributed noise, we can say the two points become more correlated as the distance between them, $||\boldsymbol{x}^{(i)} - \boldsymbol{x}^{(j)}||$, decreases. While many correlation metrics exist, the Kriging model used in this work computes correlation using (C.4), where k is the number of dimensions or design variables in the problem, and θ and p are correlation parameters. These correlation parameters are discussed in detailed later in this derivation.

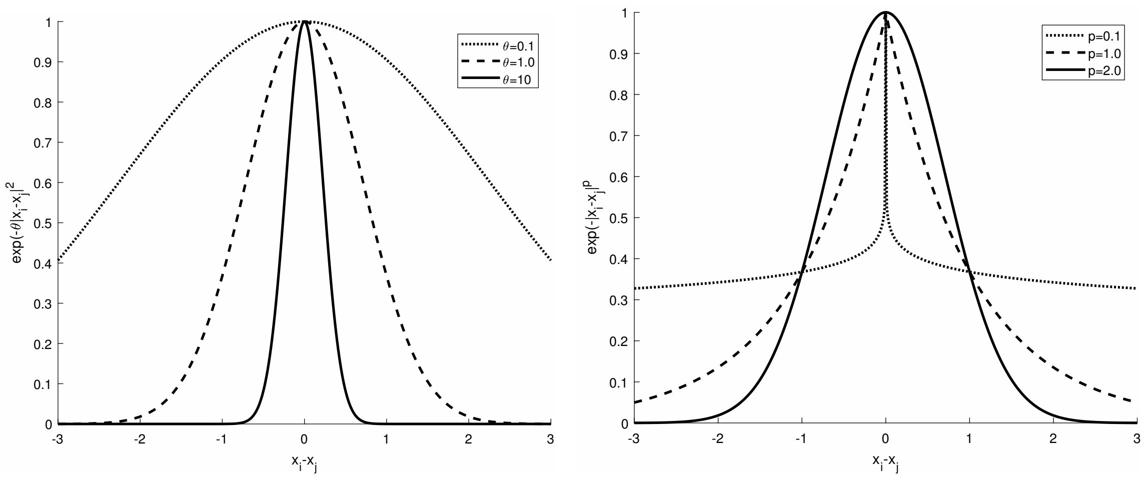

(a) The effect of θ on correlation (b) The effect of p on correlation

Figure C.2: The effect of θ and p on correlation between sampling points.

$$\mathrm{Corr}\left[Y(\boldsymbol{x}^{(i)}),\, Y(\boldsymbol{x}^{(j)})\right] = \exp\left(-\sum_{l=1}^{k} \theta_l \,|x_l^{(i)} - x_l^{(j)}|^{p_l}\right) \tag{C.4}$$

Individual correlations are then assembled into an $n \times n$ correlation matrix $\boldsymbol{\Psi}$, as shown in (C.5). $\boldsymbol{\Psi}$ is the most important variable in the development of Kriging models as it contains the correlation between every sampling point. The correlation matrix is used in all aspects of the Kriging model, from prediction to infilling.

$$\boldsymbol{\Psi} = \begin{bmatrix} \mathrm{Corr}\left[Y(\boldsymbol{x}^{(1)}),\, Y(\boldsymbol{x}^{(1)})\right] & \dots & \mathrm{Corr}\left[Y(\boldsymbol{x}^{(1)}),\, Y(\boldsymbol{x}^{(n)})\right] \\ \vdots & \ddots & \vdots \\ \mathrm{Corr}\left[Y(\boldsymbol{x}^{(n)}),\, Y(\boldsymbol{x}^{(1)})\right] & \dots & \mathrm{Corr}\left[Y(\boldsymbol{x}^{(n)}),\, Y(\boldsymbol{x}^{(n)})\right] \end{bmatrix} \tag{C.5}$$

Directing one's attention back to (C.4), one will note two sets of parameters $\boldsymbol{\theta}$ and $\boldsymbol{p}$ which adjust the correlation between each sampling point for each design variable. The correlation parameter θ is a Gaussian width parameter which serves to model the influence or "activity" of each design variable. Design variables with a high θ or influence imply that sampling points far from where an interpolation is being made will have a large impact on the interpolated value. Conversely, design variables with a low influence and small θ mean that only sampling points close to the point of interpolation will affect the interpolated value. This is depicted graphically in Figure C.2a.

The correlation parameter p serves to alter the smoothness of the correlation function between sampling points for a particular design variable, as shown in Figure C.2b. As p approaches 0, the correlation between two points becomes sharp and discontinuous while as p approaches 2, the correlation becomes smooth. As shown by Sacks et al. (1989), when $p = 2$ the correlation function is infinitely differentiable, which sets the bounds of p to be between zero and two. Altering p aids in the modeling of design variables whose responses may not be smooth in nature.

Selection of appropriate values for each design variable's θ and p are critical to the accuracy of the Kriging model. However, there is no analytic method of determining these parameters as they are a function of not only the parent function being approximated but also how the parent function was sampled. As such, correlation parameters are determined numerically through the use of optimization techniques.

As noted in Section 2.4, an objective function is required in order to perform optimization. The objective function used to determine correlation parameters takes advantage of our assumption that the process is stochastic. A stochastic process implies that the errors, ϵ, in the system are independent and normally distributed. This further implies the error in the system is associated with the evaluated sampling point, specifically $\{(\boldsymbol{x}^{(1)}, y^{(1)} \pm \epsilon), \ldots, (\boldsymbol{x}^{(n)}, y^{(n)} \pm \epsilon)\}$. Using this assumption, we can determine the probability of the whole dataset, as seen in (C.6) where σ is the standard deviation of the system.

$$P = \frac{1}{(2\pi\sigma^2)^{(n/2)}} \prod_{i=1}^{n} \left\{ \exp\left[-\frac{1}{2} \left(\frac{y^{(i)} - f(x)}{\sigma} \right)^2 \right] \epsilon \right\} \tag{C.6}$$

The underlying assumptions of stochastic processes and probability inherent in Kriging models raise some interesting implications. First, it implies that the Kriging model perfectly replicates the parent system and the only source of error ϵ is due to the evaluation of the sampling points, $\boldsymbol{y}$. However, as surrogate models rely on deterministic models, we know there is no error in the evaluation of $\boldsymbol{y}$ and that any error in the surrogate must be due to the surrogate itself. Regardless, we can still use the probability of the system, expressed instead as the likelihood L, as seen in (C.7), which now contains the field of stochastic processes $\boldsymbol{Y}$, as well as the mean μ and standard deviation σ of the system.

$$L = \frac{1}{(2\pi\sigma^2)^{(n/2)}} \exp\left[-\frac{1}{2} \left(\frac{\sum(\boldsymbol{Y}^{(i)} - \mu)^2}{\sigma^2} \right) \right] \tag{C.7}$$

(C.7) is a difficult function to evaluate directly as $\boldsymbol{Y}$ is not known. As such, likelihood is often expressed as a function of the sampled data points $\boldsymbol{y}$ and the correlation matrix $\boldsymbol{\Psi}$, as seen in (C.8).

$$L = \frac{1}{(2\pi\sigma^2)^{(n/2)}|\boldsymbol{\Psi}|^{1/2}} \exp\left[-\frac{(\boldsymbol{y}-\mathbf{1}\mu)^{\mathrm{T}}\boldsymbol{\Psi}^{-1}(\boldsymbol{y}-\mathbf{1}\mu)}{2\sigma^2}\right] \tag{C.8}$$

Common practice is to take the natural logarithm of likelihood to remove the exponential from the function, as shown in (C.9). This makes analytic differentiation simpler, but also makes the function more amenable to numeric optimization, as a logarithmic solution space is easier to search than an exponential one.

$$\ln(L) = -\frac{n}{2}\ln(2\pi) - \frac{n}{2}\ln(\sigma^2) - \frac{1}{2}\ln|\boldsymbol{\Psi}| - \frac{(\boldsymbol{y}-\mathbf{1}\mu)^{\mathrm{T}}\boldsymbol{\Psi}^{-1}(\boldsymbol{y}-\mathbf{1}\mu)}{2\sigma^2} \tag{C.9}$$

Taking the analytic derivative of (C.9) and setting it to zero, we can obtain what is known as maximum likelihood estimates of μ and σ^2, given by (C.10) and (C.11).

$$\hat{\mu} = \frac{\mathbf{1}^{\mathrm{T}}\boldsymbol{\Psi}^{-1}\boldsymbol{y}}{\mathbf{1}^{\mathrm{T}}\boldsymbol{\Psi}^{-1}\mathbf{1}} \tag{C.10}$$

$$\hat{\sigma}^2 = \frac{(\boldsymbol{y}-\mathbf{1}\mu)^{\mathrm{T}}\boldsymbol{\Psi}^{-1}(\boldsymbol{y}-\mathbf{1}\mu)}{n} \tag{C.11}$$

Substituting these estimates back into (C.9) and removing constant terms yields what is known as the concentrated logarithmic likelihood function, given by (C.12).

$$\ln(L) \approx -\frac{n}{2}\ln(\hat{\sigma}^2) - \frac{1}{2}\ln|\boldsymbol{\Psi}| \tag{C.12}$$

The value of the concentrated logarithmic likelihood function depends solely on $\boldsymbol{\Psi}$, which in turn depends only on $\boldsymbol{\theta}$ and $\boldsymbol{p}$ as shown in (C.4) and (C.5). As such, we can now execute an optimization algorithm to maximize (C.12) and generate the optimal set of parameters for $\boldsymbol{\theta}$ and $\boldsymbol{p}$. Because (C.12) is both cheap to evaluate and multimodal, optimization is generally conducted using a global search method, with simulated annealing (Sacks et al., 1989) and genetic algorithms (Forrester et al., 2008; Sóbester et al., 2005) being used in the literature.

The process of determining optimal $\boldsymbol{\theta}$ and $\boldsymbol{p}$ parameters is also referred to as training; a term borrowed from the field of artificial neural networks. Training of artificial neural networks is the process of optimizing model parameters with the goal of minimizing the error of the neural network with respect to the input data. While developed independently, the Kriging model can be thought of as a specialized form of artificial neural network in many respects, making the term training appropriate for this work.

While optimum correlation parameters are necessary to produce an accurate Kriging surrogate, it is not yet readily apparent how one extracts the value of the surrogate at any given point in the solution space, which will be denoted as $\hat{y}(\boldsymbol{x})$. To do this, we recall the Kriging model was derived from the correlation between sampling points, for which we have just determined optimal parameters for. Therefore, we must also use correlation to when predicting from the surrogate. Further, we assume that any prediction being made is consistent with the optimal correlation parameters already determined. As such, a bias vector $\boldsymbol{\psi}$ can be created for any arbitrary location $\boldsymbol{x}$, composed of the correlation between point $\boldsymbol{x}$ and all other sampling points in the model. This bias vector is given by (C.13) and is used use augment the existing correlation matrix to form the aptly named augmented correlation matrix $\tilde{\boldsymbol{\Psi}}$, which contains all sampling points and the arbitrary point. The augmented correlation matrix is given by the partitioned matrix shown in (C.14).

$$\boldsymbol{\psi} = \begin{pmatrix} \mathrm{Corr}[Y(\boldsymbol{x}^{(1)}, Y(\boldsymbol{x})] \\ \vdots \\ \mathrm{Corr}[Y(\boldsymbol{x}^{(n)}, Y(\boldsymbol{x})] \end{pmatrix} = \begin{pmatrix} \psi^{(1)} \\ \vdots \\ \psi^{(n)} \end{pmatrix} \tag{C.13}$$

$$\tilde{\boldsymbol{\Psi}} = \begin{pmatrix} \boldsymbol{\Psi} & \boldsymbol{\psi} \\ \boldsymbol{\psi}^{\mathrm{T}} & 1 \end{pmatrix} \tag{C.14}$$

The augmented correlation matrix is then used to determine a new concentrated logarithmic likelihood shown in (C.15). However, as correlation parameters have already been determined, the only unknown value in $\ln(L)$ is $\hat{y}$, the interpolated value at any arbitrary location $\boldsymbol{x}$ calculated using maximum likelihood estimates.

$$\ln(L) \approx -\frac{\begin{pmatrix} \boldsymbol{y} - \mathbf{1}\hat{\mu} \\ \hat{y} - \hat{\mu} \end{pmatrix}^{\mathrm{T}} \begin{pmatrix} \boldsymbol{\Psi} & \boldsymbol{\psi} \\ \boldsymbol{\psi}^{\mathrm{T}} & 1 \end{pmatrix}^{-1} \begin{pmatrix} \boldsymbol{y} - \mathbf{1}\hat{\mu} \\ \hat{y} - \hat{\mu} \end{pmatrix}}{2\hat{\sigma}^2} \tag{C.15}$$

The interpolated value $\hat{y}$ can be determined by analytically maximizing (C.15). However, to accomplish this, the inverse of $\tilde{\boldsymbol{\Psi}}$ needs to be calculated. Using the method of Theil (Theil, 1983), the inverse of the partitioned matrix is given by (C.16). For the details of this calculation, please refer to Forrester et al. (2008).

$$\tilde{\boldsymbol{\Psi}}^{-1} = \begin{pmatrix} \boldsymbol{\Psi}^{-1} + \boldsymbol{\Psi}^{-1}\boldsymbol{\psi}(1 - \boldsymbol{\psi}^{\mathrm{T}}\boldsymbol{\Psi}^{-1}\boldsymbol{\psi})^{-1}\boldsymbol{\psi}^{\mathrm{T}}\boldsymbol{\Psi}^{-1} & -\boldsymbol{\Psi}^{-1}\boldsymbol{\psi}(1 - \boldsymbol{\psi}^{\mathrm{T}}\boldsymbol{\Psi}^{-1}\boldsymbol{\psi})^{-1} \\ -(1 - \boldsymbol{\psi}^{\mathrm{T}}\boldsymbol{\Psi}^{-1}\boldsymbol{\psi})^{-1}\boldsymbol{\psi}^{\mathrm{T}}\boldsymbol{\Psi}^{-1} & (1 - \boldsymbol{\psi}^{\mathrm{T}}\boldsymbol{\Psi}^{-1}\boldsymbol{\psi})^{-1} \end{pmatrix} \tag{C.16}$$

Inserting (C.16) into (C.15) and neglecting terms without $\hat{y}$ gives (C.17), which is a quadratic function dependant on $(\hat{y} - \hat{\mu})$. This quadratic can be maximized by taking the derivative of (C.17) and setting equal to zero as shown (C.18).

$$\ln(L) \approx \left(-\frac{1}{2\hat{\sigma}^2(1 - \boldsymbol{\psi}^{\mathrm{T}}\boldsymbol{\Psi}^{-1}\boldsymbol{\psi})}\right)(\hat{y} - \hat{\mu})^2 + \left(\frac{\boldsymbol{\psi}^{\mathrm{T}}\boldsymbol{\Psi}^{-1}(\boldsymbol{y} - \mathbf{1}\hat{\mu})}{\hat{\sigma}^2(1 - \boldsymbol{\psi}^{\mathrm{T}}\boldsymbol{\Psi}^{-1}\boldsymbol{\psi}}\right)(\hat{y} - \hat{\mu}) \tag{C.17}$$

$$\frac{d(\ln(L))}{d(\hat{y} - \hat{\mu})} = 0 = \left(-\frac{1}{\hat{\sigma}^2(1 - \boldsymbol{\psi}^{\mathrm{T}}\boldsymbol{\Psi}^{-1}\boldsymbol{\psi})}\right)(\hat{y} - \hat{\mu}) + \left(\frac{\boldsymbol{\psi}^{\mathrm{T}}\boldsymbol{\Psi}^{-1}(\boldsymbol{y} - \mathbf{1}\hat{\mu})}{\hat{\sigma}^2(1 - \boldsymbol{\psi}^{\mathrm{T}}\boldsymbol{\Psi}^{-1}\boldsymbol{\psi}}\right) \tag{C.18}$$

Solving (C.18) for $\hat{y}$ yields (C.19), which produces the value of the Kriging model at any arbitrary point in the solution space. As (C.19) is closed form and a function of already calculated parameters μ and $\boldsymbol{\Psi}$, it is computationally inexpensive to calculate. As such, one can use this equation for prediction, visualization, and optimization of the Kriging model.

$$\hat{y}(\boldsymbol{x}) = \hat{\mu} + \psi^{\mathrm{T}}\boldsymbol{\Psi}^{-1}(\boldsymbol{y} - \mathbf{1}\hat{\mu}) \tag{C.19}$$

Recalling the form of the ordinary Kriging model given in (C.3), one can see how the predictor relates back to that form. The regression component is the maximum likelihood estimate of the mean, $\hat{\mu}$. Instead of using the actual mean of the dataset, the mean is value is allowed to be tuned to provide the best fit, although the value does tend to the actual mean. The stochastic portion of the Kriging predictor is given by $\psi^{\mathrm{T}}\boldsymbol{\Psi}^{-1}(\boldsymbol{y} - \mathbf{1}\hat{\mu})$, where the correlation parameters $\boldsymbol{\theta}$ and $\boldsymbol{p}$ as well as all sampling points and the point of interest are found in ψ and Ψ.

C.2.2 Predictive Infilling

The Kriging model relies on sampled data points to tune correlation parameters and make predictions. As previously noted, an uncorrelated, space-filling sampling plan is required to allow the surrogate to make accurate predictions of the parent function. However, even with the best sampling plan, there may be areas of the parent function's solution space where the surrogate simply cannot make accurate predictions due to a lack of information. The simplest method to improve the accuracy of the surrogate is to add more sampling points, a process known as infilling. However, if the parent function is expensive, it is important to only evaluate the parent function at a location we know will improve the surrogate. Fortunately, the statistical nature of the Kriging model allows us to predict the best location of an infill point based solely on the Kriging model itself.

Because the Kriging model is a stochastic process which uses a Gaussian correlation function, one can calculate the estimated error in the overall process. As discussed previously, we know that the only error in the system has to be a result of the Kriging model itself, not uncertainties in the computer experiment. As such, we can compute the mean square error (MSE), $\hat{s}$, of the model at any point, as in (C.20) using only the Kriging surrogate.

$$\hat{s}^2(\boldsymbol{x}) = \sigma^2 \left(1 - \boldsymbol{\psi}^{\mathrm{T}}\boldsymbol{\Psi}^{-1}\boldsymbol{\psi} + \frac{1 - \mathbf{1}^{\mathrm{T}}\boldsymbol{\Psi}^{-1}\boldsymbol{\psi}}{\mathbf{1}^{\mathrm{T}}\boldsymbol{\Psi}^{-1}\mathbf{1}}\right) \tag{C.20}$$

The use of MSE has several useful properties for infilling. First, $\hat{s}^2$ drops to zero at each of the sampled locations, which prevents infilling points being placed at existing sampling points. Second, MSE is highly influenced by the location of the existing sampling points, indicating that MSE increases as the distance between sampling points also increases. As such, MSE is generally maximized at the largest gap between sampling points. Because the MSE criteria, and all infilling criteria which will be introduced, are reduced to zero at a sampling point, the solution landscape is highly multimodal. As a result, a global search algorithm such as a genetic algorithm or particle swarm optimizer is required to determine the optimal infill location.

MSE is a useful criterion if one is interested simply filling gaps in the initial sampling plan. This results in a more globally accurate model, but it may not improve the surrogate's ability to predict the parent's optimum values. If optimization is the goal of the surrogate, we want to place our infill points at a location which improves the estimate of the parent function's global optimum, a process which is referred to as exploitation. To do this, we can harness the statistical nature of Kriging models.

One potential infill strategy is to look at the probability that a new point will improve the estimate of the Kriging model. To do this, we consider our point of interest $\hat{y}(\boldsymbol{x})$ to be the realization of a stochastic process $Y(\boldsymbol{x})$. We can then compute the probability of improving the Kriging model where improvement is defined as $I = y_{min} - Y(\boldsymbol{x})$, where y_{min} is the sampling point with the most optimal value, as given by (C.21).

$$P[I(\boldsymbol{x})] = \frac{1}{\hat{s}\sqrt{2\pi}} \int_{-\inf}^{0} \mathrm{e}^{-\frac{(I-\hat{y}(\boldsymbol{x}))^2}{2\hat{s}^2}} \tag{C.21}$$

This criterion is known as probability of improvement and can be expressed in a closed form manner by evaluating the integral using the error function, resulting in(C.22), where erf(·) is the error function. While (C.22) is equivalent to (C.21), its closed form nature greatly simplifies its use, particularly for when implimented computationally.

$$P[I(\boldsymbol{x})] = \frac{1}{2}\left[1 + \mathrm{erf}\left(\frac{y_{min} - \hat{y}(\boldsymbol{x})}{\hat{s}\sqrt{2}}\right)\right] \tag{C.22}$$

The advantages of probability of improvement over MSE come from its use of information in the Kriging model itself, such as standard deviation and best sampling point. Instead of targeting areas of the surrogate which have widely spaced sampling points, probability of improvement primarily targets areas of the surrogate which are predicted to be less than the lowest sampling point. By placing an infill point in the lowest area of the surrogate, this infill criterion should improve the surrogate's prediction of the parent's optimium.

While probability of improvement is a dramatic improvement over MSE for exploitation of the surrogate, it can still be improved. The key drawback of probability of improvement is that it does not provide any indication how great an improvement the addition of an infill point will have. This property is desirable as it ensures the infill point will have the greatest overall improvement in the surrogate's predictive accuracy. This is accomplished with the expected improvement criterion given by (C.23), where $\Phi(\cdot)$ is the cumulative distribution function and $\phi(\cdot)$ is the probability density function.

$$E[I(\boldsymbol{x})] = \begin{cases} (y_{min} - \hat{y}(\boldsymbol{x}))\Phi\left(\frac{y_{min}-\hat{y}(\boldsymbol{x})}{\hat{s}(\boldsymbol{x})}\right) + \hat{s}\phi\left(\frac{y_{min}-\hat{y}(\boldsymbol{x})}{\hat{s}(\boldsymbol{x})}\right) & \text{if } \hat{s} > 0 \\ 0 & \text{if } \hat{s} = 0 \end{cases} \tag{C.23}$$

The advantages of expected improvement are described well by Schonlau (1997) and Sóbester et al. (2005). The first term in (C.23) is maximized when the surrogate predicts a value less than the lowest sampling point, like the probability of improvement criterion. Further, this term also increases when the difference between the lowest sampling point and an arbitrary point in the surrogate increases. The second term increases as the distance between existing sampling points increases, which would result in a greater uncertainty of the surrogate's accuracy. As a result, expected improvement harness the best parts of MSE and probability of improvement, as it is maximized in areas where the surrogate predicts a value less than the best sampling point and/or in areas of greatest uncertainty in the surrogate's accuracy. This combination allows the expected improvement criterion to be a more effective and efficient infilling algorithm for exploitation.

For the purposes of infilling, expected improvement can be expressed in the closed form equation given by (C.24).

$$\begin{aligned} E[I(\boldsymbol{x})] = \frac{(y_{min} - \hat{y}(\boldsymbol{x}))}{2}\left[1 + \operatorname{erf}\left(\frac{y_{min} - \hat{y}(\boldsymbol{x})}{\hat{s}\sqrt{2}}\right)\right] \\ + \hat{s}\frac{1}{\sqrt{2\pi}}\exp\left(-\frac{(y_{min} - \hat{y}(\boldsymbol{x}))^2}{2\hat{s}^2}\right) \end{aligned} \tag{C.24}$$

Regardless of the criterion selected, the process of infilling is as follows. First, an initial Kriging model is trained using an sampling plan. After initial training of the Kriging model, the solution space is searched with a global search algorithm with one of the infill criteria detailed above as the objective function to determine the location where the criterion is optimized. The parent function is then evaluated at this optimal location and the Kriging model is retrained with the infill location and evaluated parent function value appended to existing sampled data. This process continues until either the desired number of infill points is reached or some other form of termination criteria, such as the numeric value of the infill criterion.

While the process of infilling seems computationally expensive, one must remember that the parent function is only being evaluated once per infill point. The remainder of the time the Kriging model is searching itself, which is cheap to evaluate compared to the parent function. As such, the infilling and retraining steps generally take a fraction of the time required to evaluate the parent function. Further, because of the expense associated with evaluating the parent function, there is an advantage to spending the additional cost on the Kriging model to ensure every evaluation makes a meaningful contribution.

C.2.3 Implementation

While Sections C.2.1 and C.2.2 detail the development of the Kriging model from a purely mathematical perspective, this section provides details about the implementation of MIKE. As the name implies, MIKE is implemented in MATLAB for several reasons. Primarily, MATLAB already serves as a base for COMPCAM and SPECS, which allows for straightforward integration and sharing of data. Secondly, MATLAB is a widely available and easy to use numerical computing package, despite being a proprietary, commercial product. Finally, the large library of professionally developed and documented algorithms for optimization and matrix algebra was highly attractive as a means to reduce development time.

To develop an initial sampling plan, Morris-Mitchell sampling was used (Morris and Mitchell, 1995). This sampling methodology uses an evolutionary computing technique suggested by Forrester et al. (2008) to develop sampling plans which have very good spacing-filling properties. While some of the default sampling methods included with MATLAB were investigated, Morris-Mitchell sampling proved to provide much better results. This sampling technique was modified for this work to accommodate the use of linear inequality constraints, which many sampling algorithms cannot accommodate. This modification consisted of making multiple, independent sampling plans and removing invalid points from each. Points from each culled plan were combined until the desired number of sampling points were achieved. While this does not have the same robust space filling nature as unconstrained Morris-Mitchell sampling, the combination of two or more random, independent, should have similar space filling properties. However, the actual effect of this method is unknown, due in large part due to the lack of techniques available for quantification of space fillingness under linear inequality constraints.

MIKE is developed using object-oriented (OO) coding to allow it to be a self-contained tool. Because a Kriging model continually calls on pieces of information inherent to a specific Kriging model such as sampling points, evaluated data and the like, OO coding makes it easy to manage all this information in one place. OO coding allows MIKE to be called by any other package in MATLAB without external dependencies.

While OO coding is very efficient in languages such as C++ and Python, there are downsides using OO in MATLAB. Because MATLAB is not inherently object-oriented, there is computational overhead when calling a method, both internal and external to the object itself. Through initial development work, it was determined this overhead resulted in a 150% to 200% runtime penalty. Notwithstanding this penalty, OO code was still selected due to its versatility. To mitigate the penalty associated with OO coding, several methods were used to increase the computational efficiency of MIKE. These methods and improvements are discussed in the following paragraphs.

It is important to note that expense associated with training and making predictions from a Kriging model increase as the number of sampling points also increase. This is because each sampling point adds an additional row and column to the correlation matrix $\mathbf{\Psi}$. As such, it benefits us to ensure the methods we use to deal with our linear algebra are as efficient as possible. For example, instead of calculating all matrix entries, the symmetric nature of $\mathbf{\Psi}$ is exploited. Only the upper triangular portion of the matrix is computed, with the second half being filled in by simply flipping the matrix about the diagonal. This reduces the number of required calculations to construct $\mathbf{\Psi}$ by over half.

Another computational improvement associated with $\mathbf{\Psi}$ is the computation of its inverse. Because inverting a matrix is an expensive proposition and because the matrix must be repeatedly inverted during training, an alternative method is applied. As suggested by Forrester et al. (2008), Cholesky decomposition is used. The correlation matrix is decomposed into an upper triangular matrix through the use of Cholesky decomposition. Then, forward and backward substitution is applied to generate the pseudo-inverse. By replacing the computationally expensive process of directly inverting $\mathbf{\Psi}$ with cheap, easy to compute matrix substitutions, there is a decided computational saving, even with the optimized mathematics libraries used by MATLAB.

A final technique associated with $\mathbf{\Psi}$ and the bias vector $\boldsymbol{\psi}$ takes advantage of MATLAB applications to optimize specific portions of MATLAB code. Take for instance the creation of $\mathbf{\Psi}$, which requires three nested loops; two loops to create the matrix and the third to perform the summation. Dynamically compiled languages such as

MATLAB and Python all suffer inherent and sometimes significant computational penalties compared to statically compiled languages like C++ and FORTRAN. Given the three nested loop and that these loops are called repeatedly in a global search algorithm, the runtime penalty is significantly compounded.

To alleviate this penalty, calculation of $\boldsymbol{\Psi}$ and $\boldsymbol{\psi}$ was accomplished using a statically compiled function created using the MATLAB Coder. This tool allows a user to convert MATLAB scripts into statically compiled functions written in C or C++. These statically compiled functions, which MATLAB refers to as MEX functions, can be called in MATLAB just like any other function. While it does not make sense from a development standpoint to convert the entirety of MIKE to compiled scripts, as that defeats the point of using a dynamically compiled language such as MATLAB and hinders future modifications, components which were called repeatedly, such as $\boldsymbol{\Psi}$ and $\boldsymbol{\psi}$, were compiled. The conversation of $\boldsymbol{\Psi}$ to a statically compiled function resulted in a 6.5 times improvement in runtime, while the conversation of $\boldsymbol{\psi}$ resulted in a 2.5 times improvement. Overall, the compilation of select components of MIKE resulted in an overall speed improvement of 7.5 to 9 times.

Both training and infilling of Kriging models require the use of global search algorithms. In an effort to improve efficiency, two algorithms were investigated: a genetic algorithm and a PSO. Both algorithms were included as part of MATLAB's optimization capability (MathWorks Inc., 2017b,c). Through testing, it was found that MATLAB's PSO converged to optimal correlation parameters and infill locations with fewer evaluations than the genetic. As such, all training in MIKE uses the PSO. However, both algorithms are used for infilling depending on the constraints of the problem. The PSO implemented in MATLAB is unable to accommodate linear inequality constraints. As such, for problems with linear inequalities, the genetic was used, despite the minor increase in cost.

As noted in Section 2.4, while global search algorithms are good at approaching the global minima, they do have some difficulty in finding the exact location and value of that minima. Further, some literature suggests (Forrester et al., 2007; Jones, 2001) the Kriging surrogate is sensitive to small variations in the correlation parameters from their optimal values. As such, a hybrid optimization scheme was used, which couples a global search method to a local optimization algorithm. Once the global search algorithm locates the approximate location of the global minima, the local optimization algorithm (specifically 'fmincon' in this case) exploits gradient information to determine the best set of parameters. While this methodology does increase computational expense somewhat, it does result in better correlation parameters and estimates of infill location.

Despite the dynamically compiled nature of MATLAB and the OO programming used throughout, MIKE executes training, infilling and prediction of Kriging models in a satisfactory length of time. As will be shown in the next section, even with the techniques used here to improve runtime, these techniques do not effect MIKE's accuracy as a surrogate modeling tool and EGO.

C.2.4 Validation

With any custom built tool, validation of performance against known standards is critical. In the case of optimization tools such as the Kriging model, analytic functions are used as a benchmark as they have a known global optimum and evaluate rapidly. In this work, two analytic functions, the two-dimensional Branin function and the three-dimensional Hartmann-3 function were used to check MIKE's performance. These two functions were selection as both are multi-modal and were selected based on work by Schonlau (1997) and Forrester et al. (2008).

Validation against analytic functions also provides the means to experiment with the options available to MIKE, such as the total number of sampled points used to build the surrogate model and the ratio of initial to infill points. While there are suggestions in the literature for these parameters, there is significant variation in what researchers consider to be best. This section orovides clarification for more costly optimization in later chapters.

C.2.4.1 Branin Function

The Branin function is a two-dimensional analytic function. The original Branin function has three identical minima. However, a modified version suggested by Forrester et al. (2008) was used in this work, which added a small linear term to force the problem to have one global minimum and two local minima. This altered form, given by (C.25) makes the Branin function more representative of real-world engineering problems and a more challenging optimization benchmark.

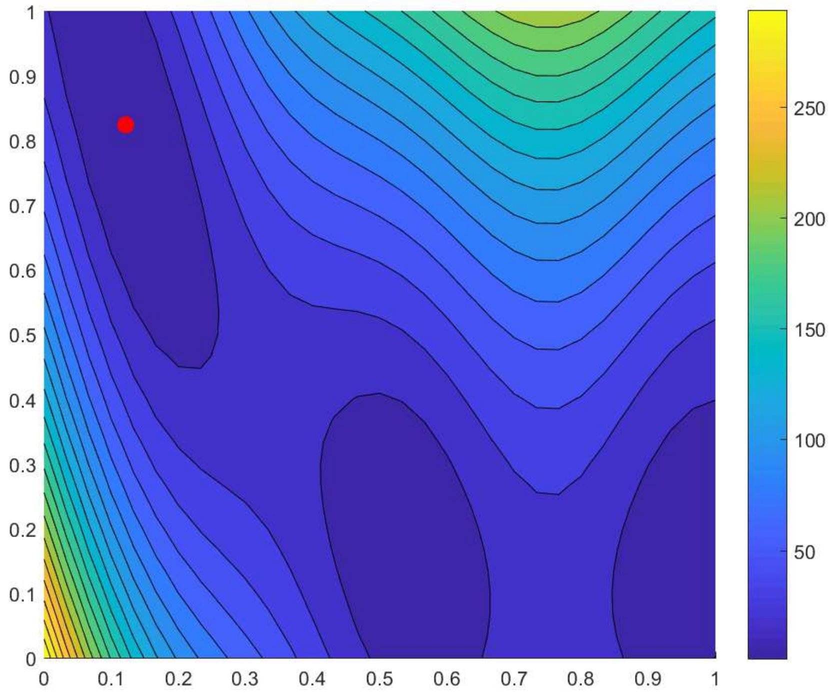

Figure C.3: Contour plot of the modified Branin function scaled onto $[0,1]^2$. Red dot marks the global minimum

$$y(x_1,x_2)=\left[x_2-\left(\frac{5.1}{4\pi^2}\right)x_1^2+\frac{5}{\pi}x_1-6\right]^2+10\left[\left(1-\frac{1}{8\pi}\right)\cos(x_1)+1\right]+5x_1 \quad \text{(C.25)}$$

The Branin function is evaluated on $x_1 \in [-5,10]$ and $x_2 \in [0,15]$ but was scaled to the $[0,1]^2$ hypercube. The global minimum of the modified Branin function is 1.0116 at $[0.12158, 0.82391]$ in the scaled hypercube. A contour plot of the Branin function with the global minima highlighted is seen in Figure C.3.

Two investigations were undertaken with MIKE. The first looked at the accuracy of a surrogate model built with only an initial sampling plan. Based on the literature, which suggests between 10 and 20 times the number of design variables (denoted by k) (Jones, 2001; Simpson et al., 2001; Sóbester et al., 2005), three trials were undertaken with $10k$, $15k$ and $20k$ sampling points. After sampling and training of the Kriging model, the same hybrid global optimization scheme used to determine optimal correlation parameters and infill locations discussed in Section C.2.3 was used to determine the global minima of the surrogate model. The results of this can be seen in Table C.1.

Table C.1: Optimal Kriging predictions built using an initial sampling plan only.

No. Sampling Points	Global Minimum Location	Global Minimum Value
True Function	[0.12158, 0.82391]	1.0116
10k = 20	[0.1429, 0.7987]	-1.0949
15k = 30	[0.1220, 0.8236]	1.1545
20k = 40	[0.1216, 0.8329]	1.0703

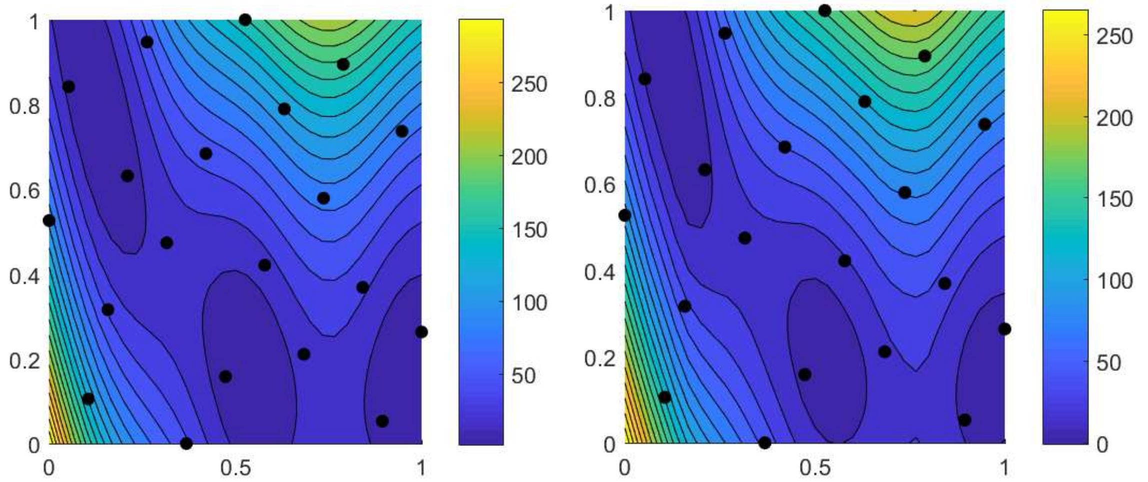

(a) Actual Branin Function

(b) Kriging surrogate train with $10k$ sampling points

Figure C.4: A comparison of the actual Branin function and a Kriging surrogate trained with 20 sampling points (black dots).

The results in Table C.1 show conclusively that as the number of sampling points increases, the surrogate model's predictive accuracy also increases. However, it is important to note that even at the fewest number of sampling points, $10k$, the surrogate predicts the location of the Branin function's global minima with reasonable accuracy. It does, however, struggle to predict the value of the parent at that location. The Kriging model built with $10k$ sampling points is compared with the analytic Branin function in Figure C.4. It is clear that while the surrogate may struggle to predict the exact value at a given point, it does predict the overall landscape quite well.

The second investigation looked at the exploitation of the surrogate as well as the optimal number of sampling points and the ratio of initial points to infill points. A good ratio of infilling to initial points is important because the two sets of points serve different purposes. The initial sampling plan develops a general prediction of the parent function while the infill points refine the surrogate in specific areas of interest. Insufficient initial points makes exploitation difficult and inefficient as the surrogate lacks sufficient knowledge of the parent to make accurate infill predictions. Conversely, overuse of infilling results results in diminishing returns in the surrogate's predictive accuracy of the parent's minima. While literature makes reference to using infilling to dramatically improve the global accuracy of the surrogate model, but few sources recommend ideal ratios (Forrester et al., 2008; Sóbester et al., 2005).

All infilling in this research made use of the expected improvement criterion. As with stage one, a hybrid global optimization scheme was used to determine the minimum of each Kriging surrogate. Table C.2 documents the trials conducted to determine both optimal infill ratio as well as the total number of sampling points. As expected, even the model generated with the fewest total sampling points was able to predict the location of the global minimum quite accurately, with the error dropping to almost nil as the number of points increased. Further, all surrogates were able to predict the global optimum better and cheaper than using pure exploration.

Table C.2: The effects of varying the number of sampling points and initial to infill ratio.

Total Points	No. Initial Points	No. Infill Points	Global Minimum Location	Global Minimum Value
True Function			[0.1216, 0.8239]	1.0116
20	10	10	[0.1257, 0.7789]	1.2070
25	10	15	[0.1238, 0.8112]	1.1495
25	15	10	[0.1216, 0.8243]	1.0140
30	10	20	[0.1214, 0.8243]	1.0115
30	13	17	[0.1207, 0.8220]	1.0022
30	15	15	[0.1218, 0.8240]	1.0116
30	17	13	[0.1215, 0.8229]	1.0050
30	20	10	[0.1215, 0.8243]	1.0101
35	20	15	[0.1215, 0.8244]	1.0096

As noted in Section C.2.3, a global search algorithm is required when predicting optimal infill location. This is exemplified in Figure C.5, which provides a contour plot of expected improvement values for a Kriging model trained with 20 sampling points. Not only does this show the multimodal nature of the expected improvement solution space, but comparing this plot with Figure C.3, one will note that three basins of highest expected improvement appear at the minima of the actual Branin function.

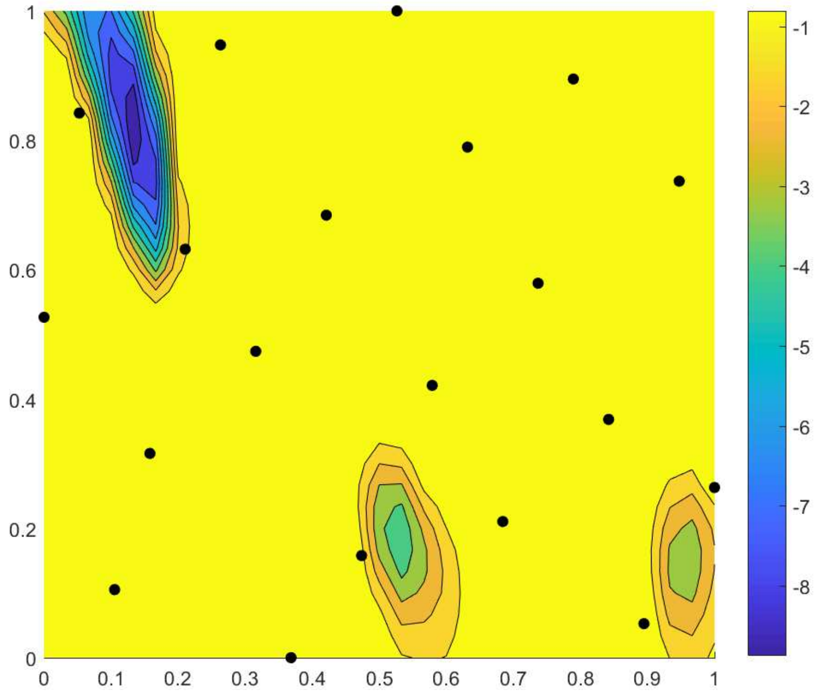

Figure C.5: Contour plot of expected improvement of a surrogate of the Branin function with 20 points. Basins represent areas of highest expected improvement (negated for optimization).

While Figure C.5 shows the landscape for 20 sampling points, it is important to note that the landscape changes with every additional infill point. As such, the location of maximum expected improvement will shift at every iteration. This is shown by Figure C.6, which shows a surrogate with an initial to infill ratio of 15:15. The boxed dots indicate those which are placed by exploitation. One will note that while infill points do cluster around the global minimum, exploitation using expected improvement will place infill points in around other areas of interest as well.

While it is impossible to draw conclusions based on the results of one test function, the results of the investigation into the Branin function indicate that infilling is essential to generating an accurate surrogate model for use in optimization. Further, these results seem to indicate that 30 sampling points were sufficient to develop such a model, implying an optimal number of sampling points of 15 times the number of design variables. While it is challenging to determine the best ratio at this point, it appears that surrogates which favour more infilling points than sampling points produce better accuracy, which supports claims by Forrester et al. (2008) and Sóbester et al. (2005). Top contenders at this point are 15:15, 13:17, and 20:10, which reduce to ratios of 1:1, approximately 1:1.618, and 3:2 respectively.

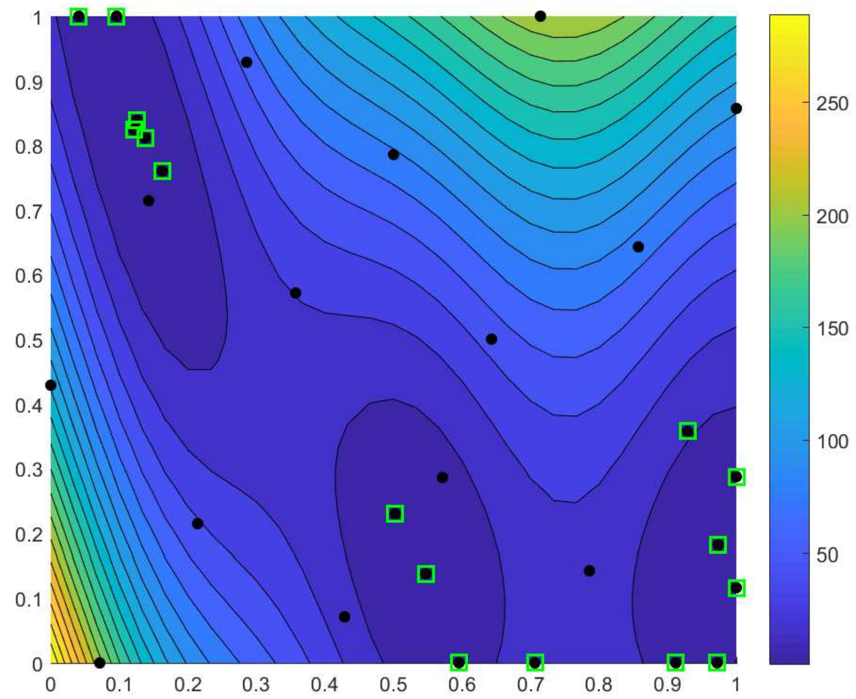

Figure C.6: A Kriging surrogate of the Branin function generated using exploitation. Boxed dots represent those added through infilling.

C.2.4.2 Hartmann-3 Problem

The Hartmann-3 function, given by (C.26) is a three-dimensional function evaluated on $[0,1]^3$ with three local minima and a single global minimum of -3.86276 at [0.11461, 0.55565, 0.85255]. A three-dimensional isosurface plot of the Hartmann-3 function is given by Figure C.7. One will note that the Hartmann-3 function is rather deceptive in the x_1 direction, as there is little change along that axis. This shallow gradient makes this function a challenging benchmark for optimization.

$$f(\boldsymbol{x}) = -\sum_{i=1}^{4} \alpha_i \exp\left(-\sum_{j=1}^{3} A_{ij}(x_j - P_{ij})^2\right) \tag{C.26}$$

$$\boldsymbol{\alpha} = (1.0, 1.2, 3.0, 3.2)^{\mathrm{T}}$$

$$\boldsymbol{A} = \begin{bmatrix} 3.0 & 10 & 30 \\ 0.1 & 10 & 35 \\ 3.0 & 10 & 30 \\ 0.1 & 10 & 35 \end{bmatrix}$$

$$\boldsymbol{P} = 10^{-4} \begin{bmatrix} 3689 & 1170 & 2673 \\ 4699 & 4387 & 7470 \\ 1091 & 8732 & 5547 \\ 381 & 5743 & 8828 \end{bmatrix}$$

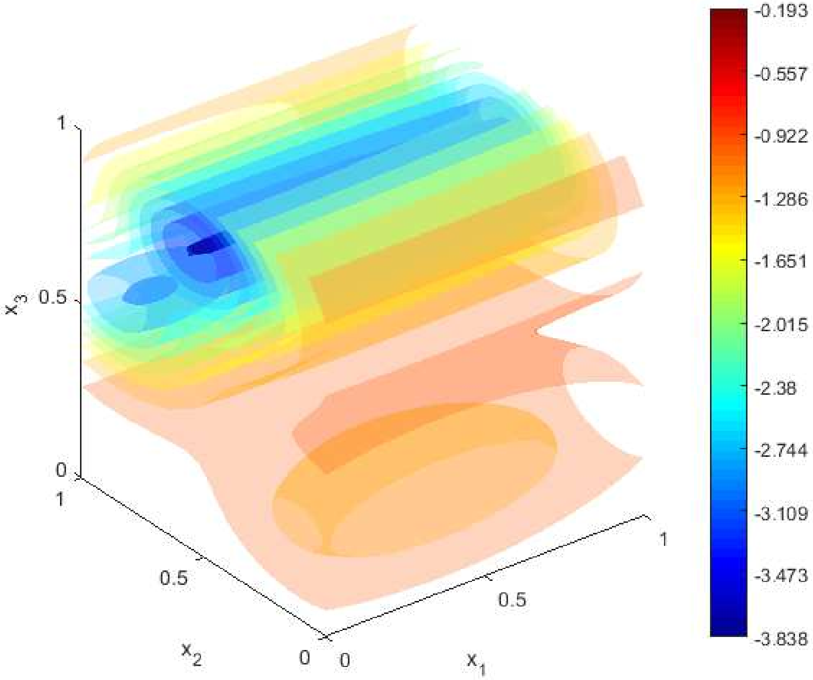

Figure C.7: Isosurface plot of the Hartmann-3 function

As with the Branin function, a series of surrogates were created using only initial sampling plans of $10k$, $15k$ and $20k$. The global minima of these surrogates are detailed in Table C.3. Unlike the Branin function, the Kriging surrogates generated with MIKE struggle to accurately predict the global minimum of the Hartmann-3

Table C.3: Optimal Kriging predictions built using an initial sampling plan only.

No. Sampling Points	Global Minimum Location	Global Min Value
True Function	[0.1146, 0.5557, 0.8526]	-3.8628
$10k = 30$	[0.5851, 0.4954, 0.8535]	-3.2977
$10k = 45$	[0.5443, 0.5309, 0.8389]	-3.6500
$10k = 60$	[0.1439, 0.5567, 0.8501]	-3.8551

Table C.4: Results of varying initial sampling points and infill points on surrogate model accuracy

No. Initial Points	No. Infill Points	Total Points	Global Minimum Location	Global Minimum Value
True Function			[0.1146, 0.5557, 0.8526]	-3.8628
30	15	15	[0.0, 0.5557, 0.8539]	-3.8552
37	15	22	[0.1768, 0.5536, 0.8552]	-3.8727
37	22	15	[0.0, 0.5558, 0.8531]	-3.8549
45	15	30	[0.1121, 0.5546, 0.8531]	-3.8627
45	17	28	[0.1118, 0.5559, 0.8533]	-3.8628
45	22	23	[0.1115, 0.5551, 0.8531]	-3.8627
45	28	17	[0.1366, 0.5519, 0.8521]	-3.8622
45	30	15	[0.1155, 0.5559, 0.8526]	-3.8628
52	30	22	[0.1152, 0.5558, 0.8526]	-3.8628

function from only an initial sampling plan due to the lack of activity along the x_1 axis. While the all surrogates converge to the proper location of the global minimum along the x_2 and x_3 axes, it is only with 60 sampling points does the Kriging surrogate properly predict the minimum location along x_1.

Table C.4 documents a series of trials which alter the number of sampling points and initial to infill ratio. The number of points and ratios are the same as those used in Section C.2.4.1 when scaled to the increased number of input variables. As with the exploratory surrogates built with only a sampling plan, these surrogates which exploit infilling also struggle to accurately predict the optimal value of x_1. Although, the use of exploitation does produce more accurate surrogate models than surrogates generated from solely initial sampling plans.

Despite the challenge the Hartmann-3 function represents, the results of the Hartmann-3 function in concert with those of the Branin function indicate that $15k$ sampling points is sufficient for an accurate surrogate model. However, further investigation is needed to determine the best ratio of initial to infill points. While work with the Branin function indicate that more infill than initial points produce a better surrogate, it has just been shown that surrogates modeling the Hartmann-3 function seem to perform better with a larger number of sampling points.

C.3 MIKE-COMPCAM Integration

In Section C.2.4, the effectiveness of Mike as a surrogate model tool was tested against analytic benchmarks. While Mike performed well, there is a large divide between analytic test functions and black-box FE models with the objective functions used by Compcam. For example, there is no analytic solution for the best parameters to a constitutive model. As such, two trials were carried out using Mike to determine optimal parameters the Swift hardening law to aluminum 2024-T351. In this set of trials, Mike used the identical objective function used for direct optimization in Chapter 5. However, unlike the five parameter problem solved by direct optimization, these two trials had their dimensionality reduced to two and three free parameters each. This makes the investigation quicker to carry out, but also allows one to visualize the output of Mike, something that would be impossible in five dimensions.

Please note that this investigation was undertaken using material data collected by Felling and Doman (2018). As noted in Section 5.1.3, there was a marked difference in material behavior between the batches of aluminum 2024-t351 used by Felling and Doman and the batch used for this work. To that end, there will be discrepancies in the final fitted parameters listed throughout this section and those tabulated in the main body of this thesis.

C.3.1 Two Parameter Trial

In this trial, Mike was used to determine optimal parameters for the Swift hardening parameters K and n, with all other parameters being held fixed. As bounds are explicitly needed to generate a Kriging surrogate of any kind, the parameter K was given the bounds $[650, 950]$ MPA while n was given the bounds $[0.1, 0.3]$. The remaining parameters, Young's modulus, Poisson's ratio, initial yield stress, and friction, were held constant at 72 GPA, 0.29, 275 MPa, and 0.18, respectively.

As there is no analytic solution to this problem, Compcam with direct optimization was executed to determine optimal parameters. To ensure a global optimum was found, Compcam was executed three times with different initial conditions. The results of these three trials are shown in Table C.5. While there was some variation in final parameters, the locations and values of the optima found were tightly grouped.

The best set of parameters was found to be $[K, n] = [812.5 \text{ MPa}, 0.1690]$ and an R^2 score of 0.99766.

As with the investigations into the two analytic test functions, a Kriging surrogate was created from three sampling plans of $10k$, $15k$ and $20k$ points and searched with a hybrid global search algorithm. The results of which are given in Table C.6 with a contour plot of the $[K, n]$ solution space generated from the Kriging model with $20k$ sampling points is given in Figure C.8. In addition to providing the minimum location and value of the surrogate, Table C.6 also provides the fit score of the surrogate's minimum evaluated directly from the objective function for comparison.

As demonstrated with the analytic benchmarks, the surrogate generated using only an initial sampling plan does a good job estimating global minimum location and value. However, it is important to note the value of the surrogate at it's minimum location does not completely correspond with the real objective function. This is to be expected, however, as the Kriging model is predicting based on a small number of sampling points. In fact, given the reasonably small number of sampling points used, Mike provides good performance, as little variation in actual fit score can be seen between the predicted minima and the actual minimum. Further, from a constitutive modeling prospective, all three parameter sets are approximately equal in terms of overall quality.

Table C.5: Results of Compcam trials to determine optimal parameters.

Trial	Optimal Parameters $[K, n]$	Objective Value	No. Evaluations
1	[811.4 MPa, 0.1685]	0.99764	39
2	[812.5 MPa, 0.1690]	0.99766	62
3	[813.3 MPa, 0.1700]	0.99765	44

Table C.6: Optimal parameters determined from the surrogate model applying exploration.

No. Sampling Points	Surrogate Minimum Location $[K, n]$	Surrogate Value	Actual Value
Direct Optim.	[812.5 MPa, 0.1690]	0.99766	-
10k = 20	[813.5 MPa, 0.1698]	0.99763	0.99766
15k = 30	[817.7 MPa, 0.1733]	0.99755	0.99761
20k = 40	[817.1 MPa, 0.1721]	0.99755	0.99763

When one compares the number of function evaluations required by Compcam to the number of sampling points required by Mike, they will note that there is not a significant advantage to generating a surrogate model. This may be due to the reasonably simplistic topology of the problem, as discussed below. However, Mike was still able to generate a surrogate which predicts the optimal set of parameters with fewer evaluations of the FE model required to execute Compcam directly.

The landscape of the $[K, n]$ solution space shown in Figure C.8 reveals some interesting results. Primarily, the contour plot shows a long, shallow valley which runs on a diagonal between K and n. This makes sense mathematically, as the one would expect there to be many similarly good pairs of K and n given the formulation of the material model. But this contour plot also shows the power of building cheap surrogate models. This contour plot required approximately 1000 function evaluations to generate, which would be computationally prohibitive using Compcam. However, using the surrogate model generated with Mike, the large number of evaluations took

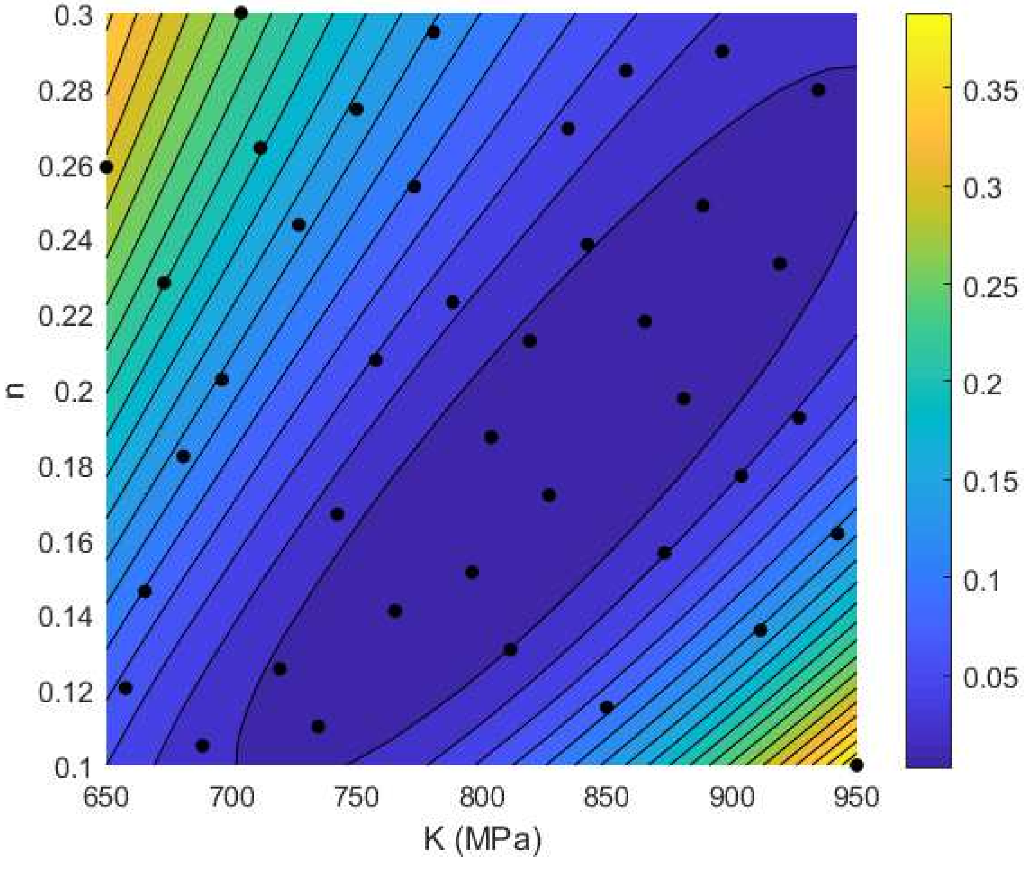

Figure C.8: Contour plot examining the variation of fit score with K and n, with small scores indicating a better fit. Generated using 40 sampling points.

only a couple of seconds to complete and provided a graphic depiction of material model fit which provides interesting insight into the constitutive model's fit.

Stage two lookd at the effect of infilling, or exploitation, to improve estimates of optimal parameters. Instead of running the full gamut of ratios as with the analytic test functions, only the most promising ratios and with a total number of evaluations less than or equal to $15k$ or 30 sampling points were used. The results of this stage can be found in Table C.7. Figure C.9 displays a contour plot of the surrogate model generated with 1.618:1 infill ratio with sampling and infilled points overlaid.

While a Kriging surrogate trained with only a sampling plan performed admirably, infilling produced better predictions of optimal parameter with fewer evaluations than a surrogate generated from solely infilling. Further, the optimal parameters predicted by each surrogate showed less variation than both direct optimization of the problem and the analytic test functions shown in Section C.2.4. This is especially apparent by observing the minimal variance between the minimum values predicted by the surrogate and the actual value at the surrogate's minimum. From a constitutive modeling prospective, all parameter sets were functionally identical.

Observing Figure C.9, one will observe that all infill locations are on the same $[K, n]$ diagonal which corresponds to the basin of parameters which provide an almost equally optimal model fit. This support the claim made above that there are many equally good pairs of K and n.

No one initial to infill ratio stood out as being the best for this problem as all tests converged to the the same minimum location and value. Further, there appeared to be no significant difference between surrogates created with 25 and 30 sampling

Table C.7: Optimal material parameters with the application of infilling

No. Initial Points	No. Infill Points	Total Points	Surrogate Minimum Location $[K, n]$	Surrogate Value	Actual Value
Direct Optim.			[812.5 MPa, 0.1690]	0.99766	-
10	15	25	[812.6 MPa, 0.1693]	0.99766	0.99766
15	10	25	[812.9 MPa, 0.1693]	0.99765	0.99766
13	17	30	[813.0 MPa, 0.1697]	0.99766	0.99765
15	15	30	[813.1 MPa, 0.1698]	0.99765	0.99765
17	13	30	[813.9 MPa, 0.1701]	0.99765	0.99765
20	10	30	[812.4 MPa, 0.1691]	0.99766	0.99766

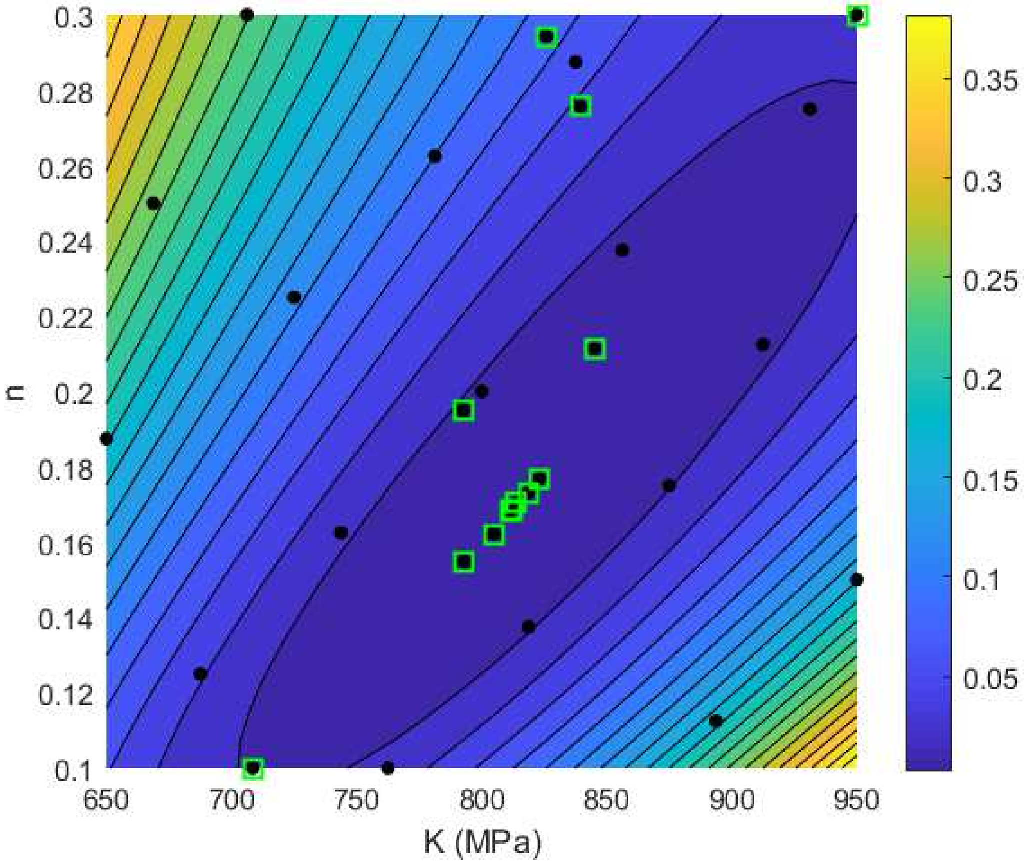

Figure C.9: Contour plot of material model fit as a function of K and n for the 17:13 trial ratio. Black dots are sampling points and boxed dots represent infilling locations.

points. As a result, the same combinations of total sampling points and ratios were repeated in the three parameter trial.

C.3.2 Three Parameter Trial

As with analytic benchmarking, a second trial was run to test the effectiveness of Mike with a three parameter problem. Hardening parameters K and n and the coefficient of friction μ were selected. The bounds of the Kriging surrogate were set to $K \in [650, 950]$ MPA, $n \in [0.1, 0.3]$, and $\mu \in [0.1, 0.3]$. The remaining three parameters were held constant with the values cited in the two parameter trial. Like the two parameter trial, Compcam was used to directly optimize the FE model to determine optimal parameters. Four direct optimization trials were conducted with varying initial conditions. The spread of optimum values and locations determined from these trials was quite small, with best set of input parameters being $[K, n, \mu] = [817.4 \text{ MPa}, 0.1730, 0.2051]$ with a fit score of 0.99787. Further, the number of evaluations of the FE model required for each trial was low, with all trials taking approximately $15k$ to $20k$ evaluations.

As with all other investigations in this work, three surrogate models were created using sampling plans of $10k$, $15k$ and $20k$ points. The optimal value and parameters of these surrogates are listed in Table C.9 along with the actual value of the objective function at each optimum.

Unlike the previous trial in the previous section, there greater variation in the optimal parameters and location as the number of sampling points increased. Further, it is not readily apparent that more sampling points actually increased the accuracy of the surrogate's estimate of global minimum. While it should be expected that accuracy will be somewhat limited by the lack of infilling, the degree of variation seen in Table C.9 was surprising given the success of the previous trial and analytic benchmarks. While the variation in estimates of K and n was not too significant, the large discrepancies seen in the estimates of coefficient of friction are dramatic. Even more surprising is how little the actual objective function changed given the spread of friction values.

Table C.8: Results of COMPCAM trials to determine optimal parameters.

Trial	Optimal Parameters $[K, n, \mu]$	Objective Value	No. Evaluations
1	[813.8 MPa, 0.1700, 0.1970]	0.99772	46
2	[812.8 MPa, 0.1683, 0.2043]	0.99784	65
3	[816.4 MPa, 0.1738, 0.2042]	0.99784	57
4	[817.4 MPa, 0.1730, 0.2051]	0.99787	67

Table C.9: Optimal material model parameters determined by MIKE using only a sampling plan.

No. Sampling Points	Surrogate Minimum $[K, n, \mu]$	Surrogate Value	Actual Value
Direct Optim.	[817.4 MPa, 0.1730, 0.2051]	0.99787	-
10k = 30	[838.0 MPa, 0.1860, 0.3000]	0.99858	0.99751
15k = 45	[814.5 MPa, 0.1698, 0.2375]	0.99960	0.99514
20k = 60	[807.3 MPa, 0.1657, 0.1644]	0.99933	0.99698

Table C.10: Optimal material model parameters determined by Mike applying exploitation.

No. Initial Points	No. Infill Points	Total Points	Surrogate Minimum $[K, n, \mu]$	Surrogate Value	Actual Value
Direct Optim.			[817.4 MPa, 0.1730, 0.2051]	0.99787	-
15	22	37	[818.9 MPa, 0.1735, 0.3000]	0.99790	0.99790
22	15	37	[818.3 MPa, 0.1724, 0.2420]	0.99788	0.99787
17	28	45	[819.6 MPa, 0.1740, 0.2433]	0.99789	0.99787
22	23	45	[818.0 MPa, 0.1706, 0.2013]	0.99780	0.99773
28	17	45	[819.5 MPa, 0.1738, 0.3000]	0.99789	0.99790
30	15	45	[819.2 MPa, 0.1734, 0.3000]	0.99789	0.99790

As with all previous investigations in this research, and in a bid to reduce the variance in estimated coefficients of friction, an exploitation study was conducted. The same ratios of total sampling points and initial to infill ratios used for the two parameter study were repeated for this trial. The optimal location and value of the resulting surrogates are given below in Table C.10 with the actual value of the objective function at the surrogate's optimum.

Unlike the improvements to optimal parameter estimates seen in previous trials, the use of exploitation with the three parameter trial raises additional questions. While infilling helped in the estimates of K and n for all surrogates shown in Table C.10, the values of friction do not improve. In fact, the estimates for best coefficient of friction hit the upper bounds placed on that variable. While this is concerning in and of itself, what is more concerning is the insignficant variation in fit score, both actual and predicted by the surrogate with the reasonably large variation in coefficient of friction. In fact, there are cases in Table C.10 where the fit score actually improves when friction hits the bounds of the problem. While the improvement is small (less than 3×10^{-5}), these results seem to imply that a more optimal set of parameters for the actual problem exists when friction is allowed to hit or perhaps exceed the upper bounds of the problem. Given the non-physicality of this situation, there is clearly an issue, and this issue likely effects the results of both direct optimization with Compcam and the use of surrogate modeling techniques.

C.3.3 Discussion of Findings

The investigation into using Mike as an optimization method for Compcam produced some interesting findings, particularly the three parameter trials. Of particular interest is the inability of Mike to accurately fit friction to experimental data. If Mike was effective at fitting the Swift law with two parameters and the analytic test functions, what makes coefficient of friction different?

Related to the Mike's inability to fit friction is the minimal change in fit score with friction, which is particularly apparent in Table C.10. Despite the significant variation in coefficient of friction (upwards of 20% of the range between upper and lower bounds of that variable), there is no significant change in fit score. In fact, the only variation in fit score seen in Table C.10 occurs at the fifth decimal place, indicating that the effect of friction on the fit score is almost vanishing small.

It is well known that friction has a major impact on the degree of barreling in cold upsetting tests. The fact that fit score used in this work shows minimal variation with changing coefficient of friction indicates that perhaps the objective function chosen for this work may not be appropriate, particularly for capturing barreling behavior. However, if this is the case, why did direct optimization yield effective and realistic results in Chapters 5 and 6?

One possible reason why direct optimization proved to be effective while Mike did not comes down to the formulation of the optimization algorithms. Compcam utilized a conjugate-gradient optimization algorithm for performing direct optimization. Such algorithms are effective at tuning parameters with very little change in objective function, such as changes at the fourth or fifth decimal place required when using the coefficient of determination as an objective function. Further, the use of gradient information in optimization allows the algorithm to account for varying influence between parameters.

The Kriging model used in Mike does not take the gradient of the objective function into account, primarily because gradient information cannot be extracted from an objective function without additional function evaluations to perform compute it numerically. Such a modification would make Mike significantly more expensive than direct optimization. Instead of relying on slope, Mike uses global search algorithms to find the best correlation parameters θ and p for each input parameter. Recalling the derivation of the Kriging model presented in Section C.2.1, it is important to

Table C.11: Variation in the correlation parameter θ across the three parameters of the Swift law problem.

K	n	μ
0.9916	0.7726	2.1451^{-4}

note that the correlation parameter θ is a measure of the activity or influence of a particular design variable in the problem. A larger value of θ implies that changing a particular input's value results in a large change in objective function.

The minimal change in fit score with large variation in coefficient of friction should result in the coefficient of friction having a small θ. To test this assertion, the correlation parameters from the three parameter surrogate model generated with 28 initial points and 17 sampling points are extracted and given in Table C.11. While the exact value or magnitude of θ for each parameter is meaningless when examined in isolation, a comparison of the three parameters provides insight into the problem's solution space. The fact that the activity parameters of K and n have the same magnitude indicate they have roughly the same effect on fit score. However, the fact that the Gaussian activity of μ is three orders of magnitude smaller than the remaining two variables imply that friction has a negligible effect on fit score. Relating this finding back to the work with analytic test functions in Section C.2.4, one will recall the difficulty MIKE had with the Hartmann-3 function due to the deceptively flat gradient along the x_1 axis. The same problem is faced by MIKE in this work, but to a larger degree.

If it can be concluded that the current objective function used to fit parameters does not account for the physical importance of friction, then the ramifications are significant, not just for MIKE, but for direct optimization as well. While such a scenario would make MIKE completely ineffective, it would also make direct optimization more difficult, likely requiring more iterations and, hence, evaluations of the FE model to find optimal parameters. As such, one recommendation for future work is to conduct further trials to investigate the sensitivity of friction on this objective function and, if necessary, find alternatives.

Completed work is not sufficient to draw complete conclusions about the objective function's sensitivity. As such, a further set of experimental trials are required. These trials will consist of friction ring and cold upsetting tests of, at minimum, aluminum 2024-T351 but may be expanded to the remaining wrought metals tested in Chapter 5. Both experiments must be repeated owing to changes in the platens between those sets of experiments and now. The friction ring tests will provide a good estimate and bounds for the actual coefficient of friction between the specimen and platens. The cold upsetting tests will provide new data which accounts for the changed platens.

Holding coefficient of friction constant at the value determined through the use of the friction ring tests, COMPCAM will fit the remaining parameters of the Swift hardening law to the data gathered from the cold upsetting test. Next, using the fitted parameters as a baseline, a parametric study will be conducted on the coefficient of friction and, perhaps, the remaining Swift parameters. The goal of this study will be to understand how changes in each input parameter effect the overall fit score, as well as to gauge the influence of each parameter. Further, this work would allow one to gauge the impact of each parameter on the force-displacement and radius-displacement objective functions independently. This would confirm supposition made earlier in this report that hardening parameters such as K and n would have a large impact on the fit score for force-displacement while μ and ν should a larger effect on radial deformation.

This parametric study will enable one to draw conclusions as to the effectiveness of the current objective function. While it is likely the use of force-displacement is effective for parameter fitting, the use of mean deformed diameter-vertical displacement may not be as effective as originally hoped. If this is the case, alternative objective functions will need to be investigated and the impact of potentially changing objective function on the results presented here will need to be considered.